A Computational and Experimental Investigation of Discrete Cell Gravure Roll Coating

By

Nicholas Raske

Submitted in accordance with the requirements for the degree of

Doctor of Philosophy

The University of Leeds,

School of Mechanical Engineering

October 2014

The candidate confirms that the work submitted is his own and that appropriate credit has been given where reference has been made to the work of others.

This copy has been supplied on the understanding that it is copyright material and that no quotation from the thesis may be published without proper acknowledgement.

The right of Nicholas Raske to be identified as Author of this work has been asserted by him in accordance with the Copyright, Designs and Patents Act 1988.

Acknowledgements

Abstract

This thesis presents an investigation of discrete cell gravure roll coating using computational and experimental techniques.

The gravure film thickness experiments conducted are similar to those presented in previous studies and show a near linear relationship between pickout ratio and speed ratio. This work adds detailed data of the gravure surface for use in computational modelling. Using a white light interferometer, surface images of the gravure topography were captured. From these images the key cell parameters, opening area, cell depth, cell volume and the cell patterning were characterised. Observations of scratches on the coated web were concluded to be caused by contact between the web and roll.

A novel computational model was derived for the discrete cell gravure coating process. The model uses a multiscale approach to address the disparate scales of the coating bead and the gravure cell. This is an extension of earlier work and is extended to a three-dimensional, realistic, topography at the small scale and at the large scale a web-to-roll contact model was added. The key topographical gravure features are included via a detailed cell scale model. The computational model was able to predict the near linear relationship between pickout ratio and speed ratio but failed to accurately predict this gradient. The model was shown to be the most accurate at speed ratios near unity.

A parametric investigation of both the coating conditions and the gravure cell geometries identified the contact pressure (the pressure caused by the web acting directly on the gravure surface) as being important to the coating process. Its magnitude was related to the web tension, wrap angle and cell size. This led the interesting result that very small cells display no contact pressure and suggests a direction for future work on the investigation of scratch free coatings.

Contents

Table of Figures

List of Tables

Nomenclature

Symbol	Units	Description
a, b, c	-	Small scale coefficients
Ca	-	Capillary number
D	m	Dimensional cell depth
F	N	Body force
G	m	Dimensional web-to-roll gap
g	-	Web-to-roll gap
g (Ch. 1)	m/s^2	Gravity
h (Ch. 1)	m	Distance separating two moving surfaces
h	-	Non-dimensional vertical distance of web from top dead centre of the gravure roll
L (Ch. 1)	m	Characteristic cell opening length
l	-	Non-dimensional length
N	-	Newtons
m	-	Meters
m_{fluid}	kg	Mass of test fluid
p	-	Non-dimensional pressure
Q	m^3/s	Dimensional volumetric fluid flow rate
Re	-	Reynolds Number
q	-	Non-dimensional volumetric fluid flow rate
q_2	-	Non-dimensional volumetric flow rate on web
R	-	Non-Dimensional and Dimensional roll radius

r	-	Non-dimensional roll radius
$r_{1,2,3}$	-	Upstream and downstream meniscus radius of curvature components
r_0	-	Characteristic cell radius used to create the cell shape
S	s	Seconds
S	-	Web-to-roll speed ratio
T	N/m	Dimensional web tension
T	s	Test time
t	-	Non-dimensional web tension
U, V, W	m/s	Dimensional velocity components
u, v, w	-	Non-dimensional velocity components
X, Y, Z	m	Dimensional Cartesian coordinates
x, y, z	-	Non-dimensional Cartesian coordinates
α (Ch. 3)	-	Steepness coefficient
α (Ch. 4)	-	Scaling variable
β	rad	Wrap angle
Γ	N/m	Surface tension
ζ	-	Coating bead mesh axis
Κ	-	Non-dimensional radius of curvature
η	Pa.s	Fluid viscosity
ρ	kg/m^3	Fluid density
Ψ	-	First order derivative of the coating bead axis (x) w.r.t. ζ
Φ	-	Pickout ratio

Acronyms

AR   Aspect Ratio

BVP   Boundary Value Problem

CFD   Computational Fluid Dynamics

ODE   Ordinary Differential Equation

Chapter 1   Introduction

Coating and printing are the process of replacing the initial fluid on a substrate/web (usually a gas) with another fluid (usually a liquid) for the purpose of altering the surface properties. This process is ubiquitous today and is involved in the production of paper products, polymer sheets, solar panels, circuit boards and even transistors etc. Coating and printing processes share much of the same fluid flow regime but differ in that coating strives to uniformly cover the web while printing typically creates specific discrete shapes such as lines, dots etc. On both fronts there is a desire to achieve a better understanding of the fluid transfer process. This task is one which has received significant interest from both industrial and academic research over the last 30 years.

Much of the early numerical representation comes from considerations that have their origins in tribology. Fluid flows where the thickness is much smaller than its width make up a sizable field of analysis commonly referred to today as lubrication. This area of numerical research was pioneered by Osborne Reynolds in his seminal paper investigating the lubrication of journal bearings (Reynolds, 1886). The hand drawn diagrams of a pressure profile between a rotating cylinder and a flat wall depict a remarkable similarity to what is discussed in the present thesis and has been reproduced in Figure 1.1. The antisymmetric pressure profile is one that is characteristic of a fluid being acted on by a roller.
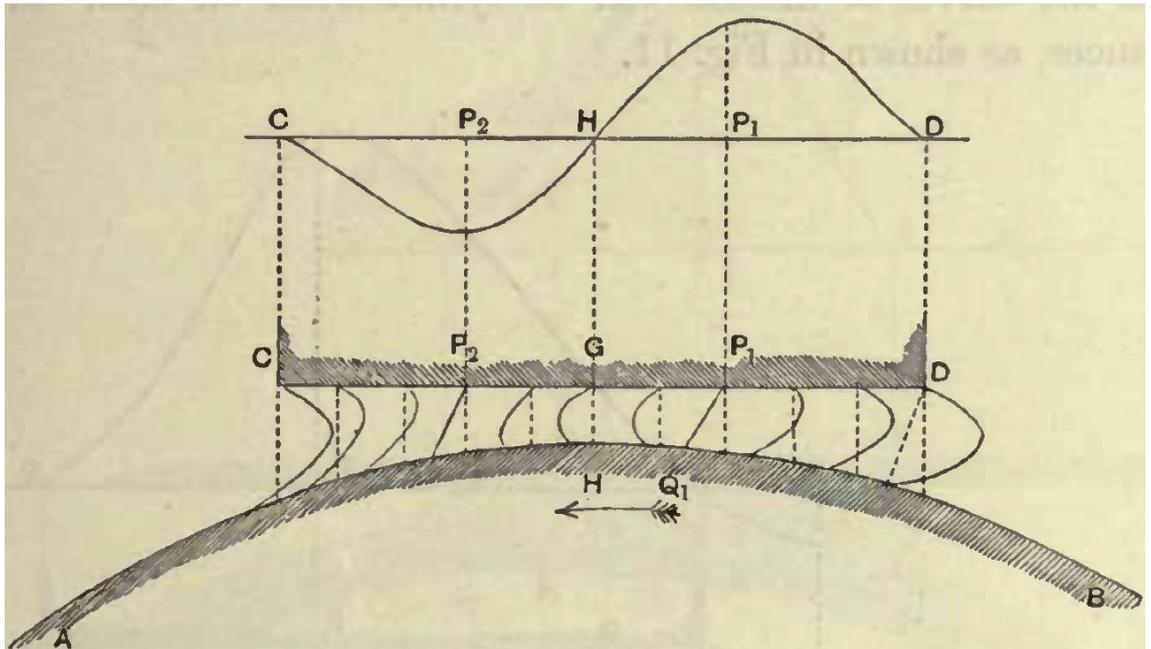
Figure 1.1: Hand drawn diagram by Osborne Reynolds showing the pressure distribution between a rotating cylinder and a flat wall.

The coating field today presents a wide range of coating systems which vary in speed and coated film thickness, some of which are shown in Figure 1.2. Curtain and slide coating control the fluid flow, Q, and speed of the web, U_w, to control the film thickness. Roll coating uses a rotating cylinder (the roll) to transfer fluid onto a web and the coated film thickness is proportional to the fluid carried by the roll and the relative velocity of the roll and web. Dip coating requires the coated object to be submerged in the coating fluid and then withdrawn.
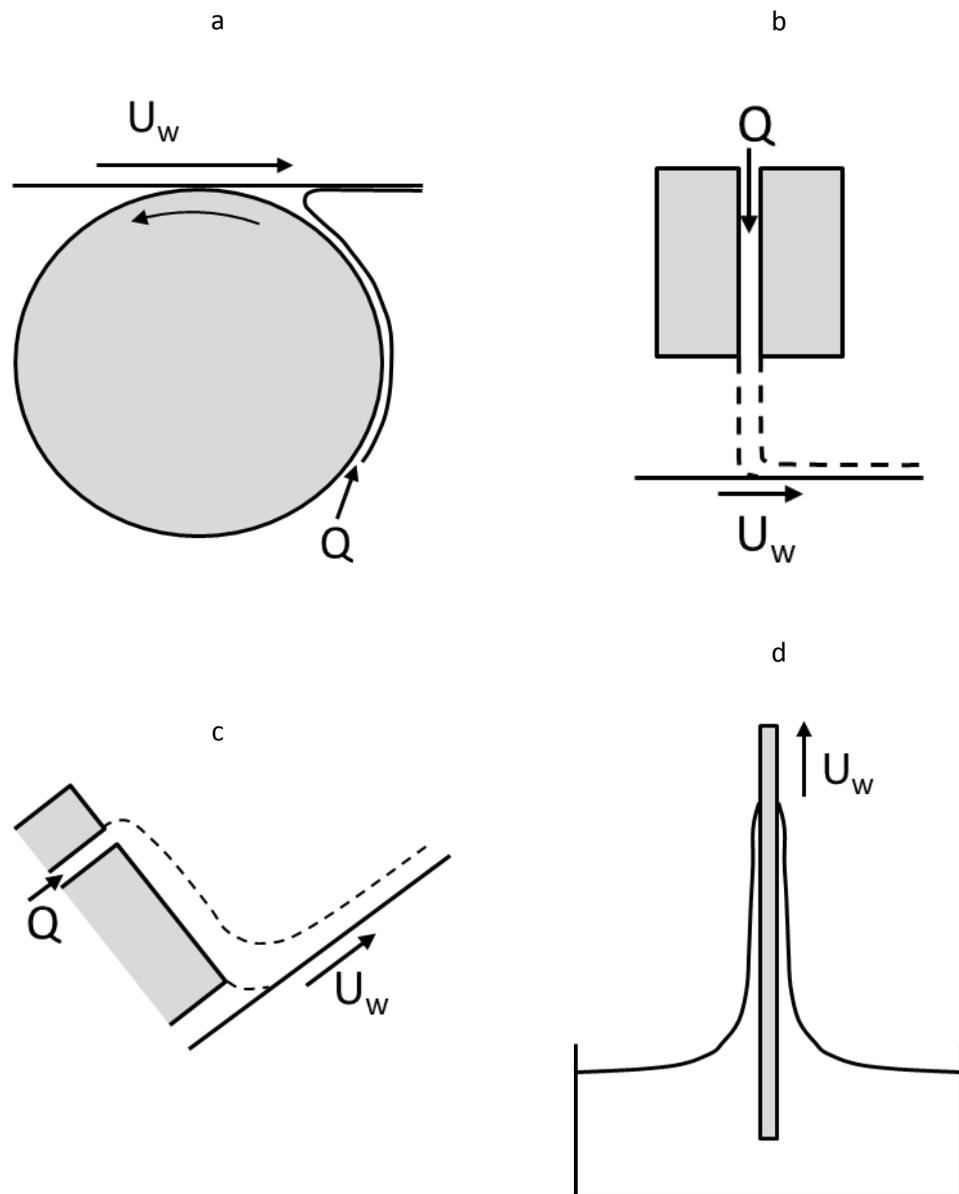
Figure 1.2: Types of coating operations: a) roll coating, b) curtain coating, c) slide coating, d) dip coating.

The focus of this thesis is on a subset of roll coating called discrete cell gravure roll coating and the relevant literature is outlined beginning in section 1.1. Results from an experimental investigation of these rolls are discussed and presented in Chapter 2. A predictive computational model is formulated in Chapter 3. Computational and experimental results are compared in Chapter 4. Results varied over a large parameter space are shown in Chapter 5. Finally, conclusions and future work are presented in Chapter 6.

1.1   Roll Coating Flows

Roll coating is a continuous reel-to-reel process that is particularly well suited for covering large areas at high speed (Benkreira, et al., 1994), (Kistler & Schweizer, 1997). Roll coaters can operate in a reverse or forward mode of operation as shown in Figure 1.3. Industrially, reverse roll coating is more common than the forward version due to the increased stability found in the reverse mode (Benkreira & Cohu, 1998).

The region of fluid transfer between roll and web is called the coating bead. For a coater operating in reverse mode the bead is bound at the upstream by one contact angle at the web-fluid-air interface and at the downstream both the roll and the web are wetted.
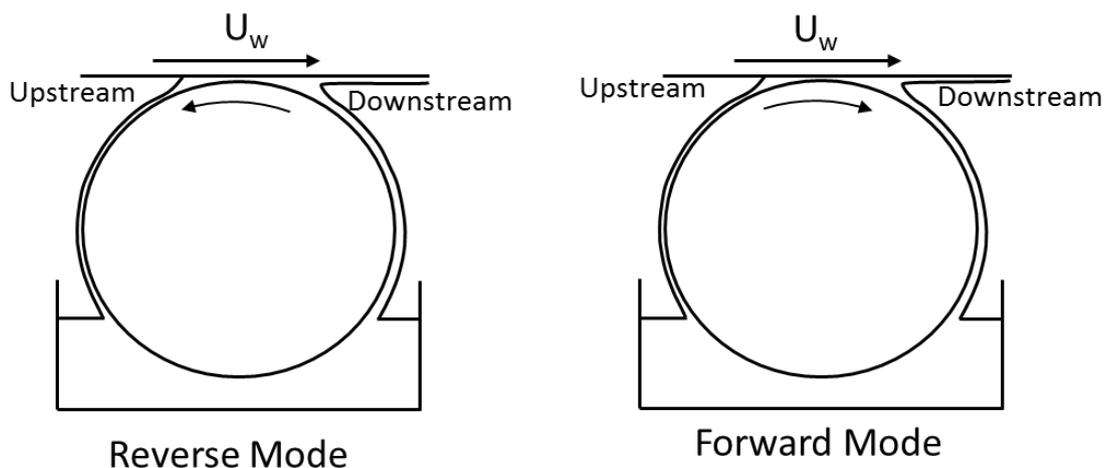
Figure 1.3: Forward and reverse mode of operation for roll coating.

In a forward roll coater at the downstream location there is a meniscus splitting region which allows for thinner films to be deposited on the web (Kistler & Schweizer, 1997) but, it also has a reduced steady operating window from that of a roll operating in reverse mode (Benkreira & Cohu, 1998). This is because the upstream meniscus is at risk of being pulled through the coating bead (Gaskell & Kapur, 2001). A steady operating window for a forward roll coater is governed by the balance of roll speed,

web speed, the fluid pressure and the rate at which the contact angle can advance along the web interface at the upstream location. The film splitting process at the downstream meniscus can be taken advantage of to produce sequentially thinner films when multiple rolls are used in an individual system (Benjamin, et al., 1995).

Multiple roll systems can be arranged in an off-set configuration (Figure 1.4) where one roll transfers the fluid to another which is then used for coating the web (there can be more than the two shown in Figure 1.4) and in this case the forward and reverse modes depend upon the roll that is transferring fluid to the web. One roll is placed in the coating fluid (metering roll), the second is placed at a fixed distance above this (applicator roll). The gap between the two rolls is referred to as the metering gap and controls how much fluid is transferred to the applicator roll (Benkreira, et al., 1994).
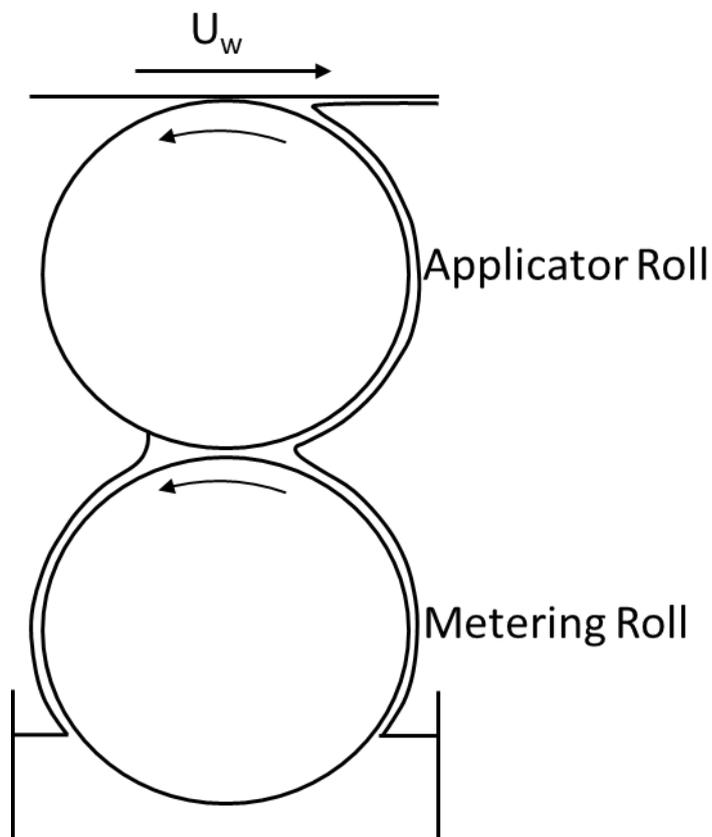
Figure 1.4: Off-set roll coater arrangement.

The roll is situated such that a portion of the surface is submerged in the coating fluid, in industry the fluid is often contained in a closed annilox chamber that encases part of the roller. Either a doctor blade or a metering roll is used to remove excess liquid from the roll surface.

1.1.1 Gravure Roll Coaters

Gravure roll coaters differ from smooth rolls by their surface topography which has patterns knurled, etched or laser engraved onto their surface (Figure 1.5). This topography is responsible for transporting the fluid from the fluid bath to the coating bead. The collective volume of the topography (i.e. the sum of the cells) dictates the volumetric fluid flow into the coating bead.

Gravure roll coaters are considered to be partially self-metering because the surface topography carries a fixed amount of fluid (Benkreira, et al., 1994). The use of a doctor blade removes excess liquid from the lands (i.e. the surface of the roll, Figure 1.6), this helps to ensure that the surface topography is the sole transport mechanism.
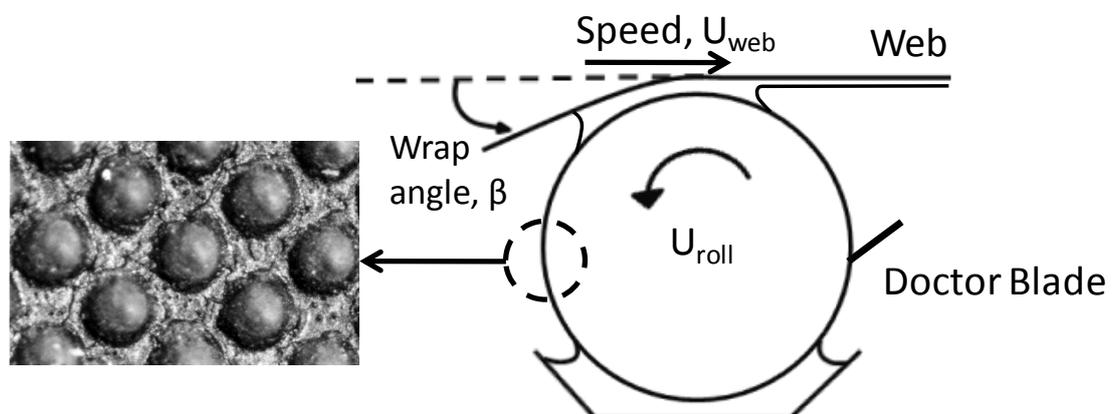
Figure 1.5: The surface topography of a discrete cell gravure roll contains cells, shown here as circular but other common shapes include hexagonal, pyramidal, etc.

Gravure roll coaters fall into two categories; discrete cell and tri-helical (Figure 1.7). Gravures that are populated with discontinuous, periodic features are called discrete cell gravures where a 'cell' refers to a unit periodic feature. Shown in Figure 1.5 there is an example with a hemispherical cell shape. The cells are aligned into off-set rows, the angle of these rows is referred to as the mesh angle or cell patterning (Figure 1.6). This describes how the position of the cells changes from one row to the next.
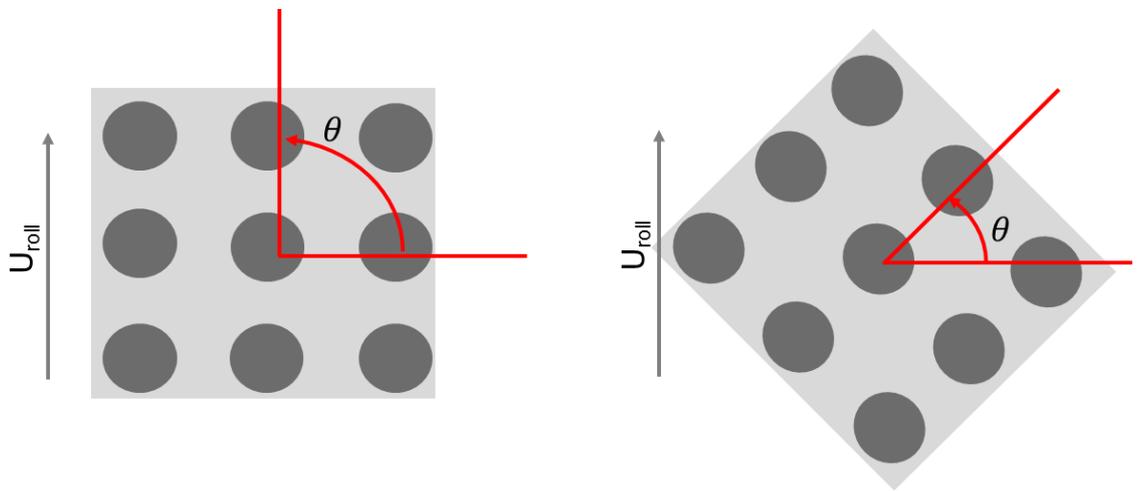
Figure 1.6: Mesh angle as seen looking down onto the surface of the roll where θ is the mesh angle. The light grey background is the land of the gravure and the circles refer to the cells.

The other common type of gravure roll has a tri-helical pattern. This is made with continuous grooves that are etched, machined or knurled around the roller as shown in Figure 1.7. The angle of these grooves is also referred to as the mesh angle of the roller.
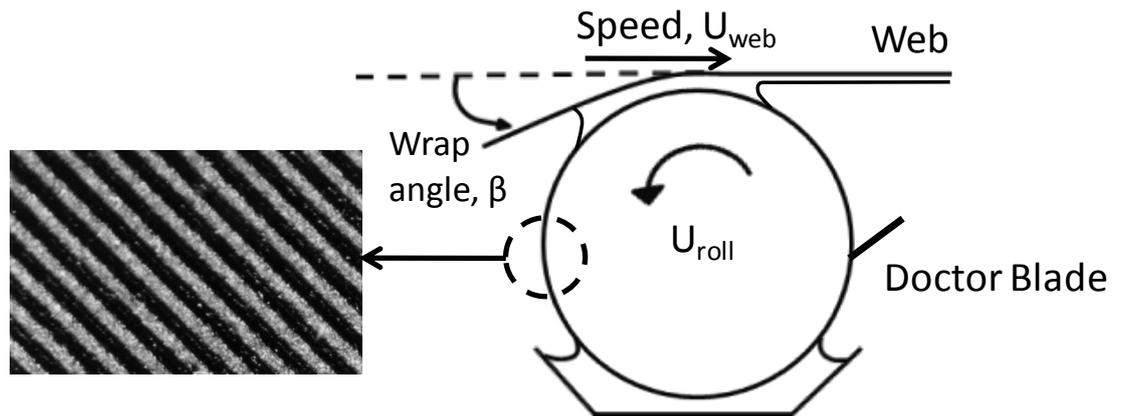
Figure 1.7: Tri-helical gravure roll coaters use continuous channels that are etched into the roll's surface.

1.1.2 Deformable Roll Coaters

Deformable rolls are smooth with an outer layer of (typically) rubber. They are commonly used with a metering device, which can be a gravure roll and hence is used in an off-set orientation as shown in Figure 1.8. When used with a gravure roller these deformable rollers can produce very thin uniform coats but the additional advantage comes from the soft nature of the outer surface. The coated web is only ever in contact with the applicator roll i.e. in off-set this is the deformable roll whereas in direct roll coating it is in contact the ceramic/metallic gravure roller. The rubber surface is much softer than the ceramic or metallic surfaces of gravure rollers. As the rubber roll is not as hard as the web scratching does not occur (Dowson, 1979).
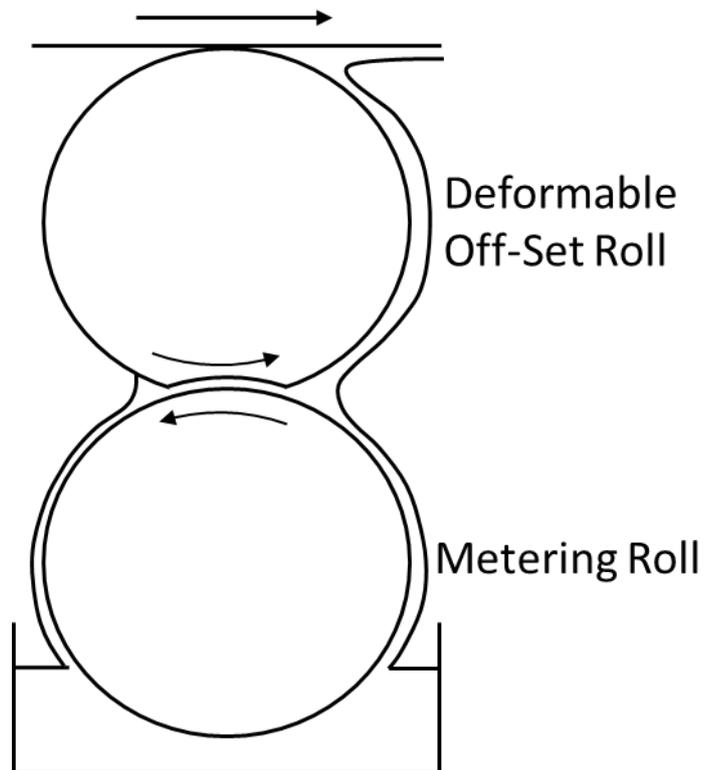
Figure 1.8: Deformable roll in off-set configuration with a metering roll.

1.2   Experimental Investigations of Gravure Roll Coating

Discrete cell gravure roll coating parameters can be divided broadly into two areas. The first is the gravure topography which includes cell shape, volume and aspect ratio. Second are coating parameters including web-to-roll speed ratio, web tension and doctor blade effectiveness, etc., and the fluid parameters viscosity, surface tension and density. The literature has offered insight to the importance of each of these areas.

1.1.3 Gravure Topography

The coated film thickness is directly linked to the volume of the cells (Kistler & Schweizer, 1997) and as such the cells act as a fluid metering device, however as the cells do not fully empty the cell shape also plays a role in the fluid transfer process. Cell shapes include (but are not limited to) circular cells forming cylinder/cone volume, quadrangular cells forming a cube/pyramid volume (see Figure 1.9). The ratio of fluid removed from a cell to its total volume is defined as the pickout ratio. It was found that the pickout ratio is related to the cell's aspect ratio, the ratio of cell length (L) to depth (D) in Figure 1.9, and the degree to which the cell tapers (Benkreira & Patel, 1992).

In a broad parametric study, it was also found that the shape of cells played a role in the fluid transfer mechanism (Kapur (2003), (Kapur, Gaskell, & Bates (2001)) noting that as volume of the cell increased so did the pickout ratio. Exceptions to this trend occurred when there were significant differences in the aspect ratio of the cells being compared (where aspect ratio was defined as the average cell width over the cell depth).
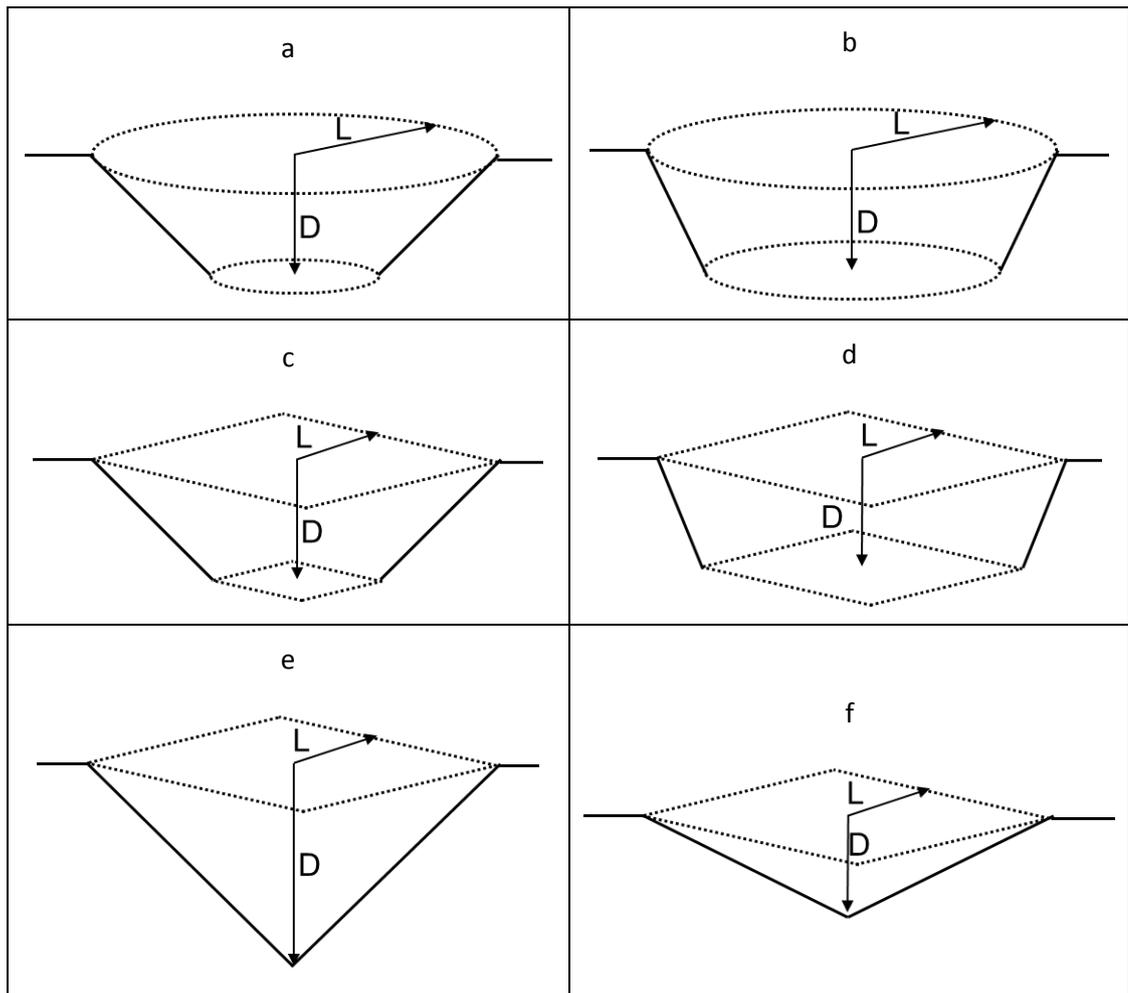
Figure 1.9: Example circular cells (a and b), quadrangular cells (c and d) and pyramidal cells (e and f). The aspect ratio, L/D, is constant for cells a, b, c and d. Cells a and c taper more than b and d. The aspect ratio is larger in cell e than cell f.

The patterning of the cells (i.e. the mesh angle) has been suggested to affect the flow structure within the coating bead by Schwartz L. W. (2002), whom numerically modelled an array of discrete cells. There is lack of experimental data relating specifically to discrete cell patterning but considering the analogous case of a tri-helical roll, the pitch angle of the channels was shown by Hewson et al (2006) to affect the pickout ratio.

1.1.4 Coating Parameters

The web-to-roll speed ratio effects the pickout ratio and the coated film thickness in both direct gravure (Benkreira & Patel, 1992) and off-set gravure modes of operation (Kapur, et al., 2001). The results documented an increase in the pickout ratio with increasing speed ratio for both discrete cell and tri-helical gravure roll coaters. Industrial applications commonly operate near a speed ratio of one. For discrete cell gravures operating at a speed ratio of one the pickout can be approximated to be one third of the total cell volume (Benkreira & Cohu, 1998).

The speed ratio is a convenient way to scale production rates, where by increasing absolute speeds of the roll and web a similar coated film thickness can be maintained. The absolute value induces changes in the fluid Capillary Number (Ca) which relates fluid viscosity, η, surface tension, γ, and the ~~velocity~~ peripheral velocity of the roll, U_{roll}, via Equation 1.1.

$$Ca = \frac{\eta U_{roll}}{\gamma} \qquad \textbf{1.1}$$

The use of a high speed ratio is limited by a steady operating window by the onset of ribbing instabilities in the forward mode of operation which will lead to a non-uniform coated film thickness (Pulkrabek & Munter (1982), Benkreira & Cohu (1998), Coyle et al (1990)). In addition, air entrainment has been observed at high speed ratios in the reverse mode of operation (Coyle, et al., 1990), (Benkreira & Cohu, 1998), (Kapur, 2003) as well as in forward operation (Gaskell & Kapur, 2001) and leads to streaking (regions of un-coated web) in the final coating.

The fluid structure within the coating bead is dependent on the transfer mechanism. For the case of two smooth rolls at a fixed gap operating in forward mode two primary eddies are formed while the reverse mode forms a single eddy (Figure 1.10, Gaskell, et al., 1998). In the smooth roll case fluid moves throughout the bead "transfer jets", which are located at regions of relatively high velocity, i.e. in the case of a reverse roller they are located at the roller surface and the web surface connected by fast flowing regions

near the bounding menisci and has been shown in Figure 1.10. The study was conducted using two smooth rolls and alludes to the macroscopic coating bead scale when a large web-to-roll gap is present.
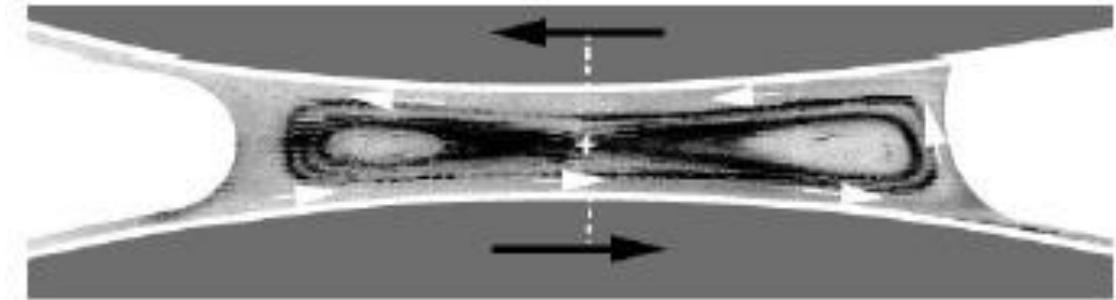
Figure 1.10: Flow visualization using a laser particle technique of rollers operating in reverse mode showing a large eddy and the primary transfer jets. (Gaskell, et al., 1998)

In the reverse mode of operation the speed ratio was found to change the coating bead structure. An increase in speed ratio (increasing the speed of the top roll) caused the coating bead to migrate downstream. The upstream meniscus was pulled down in the downstream direction as seen in Figure 1.11 (Gaskell, et al., 1998). This corresponded to a reduction in the length of the coating bead.
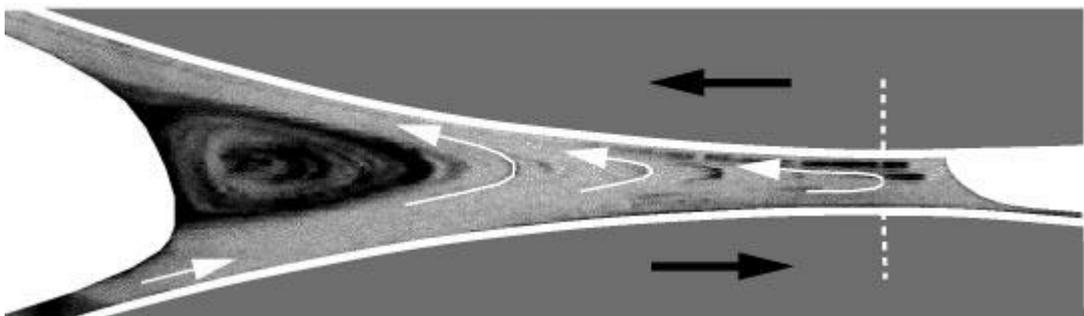
Figure 1.11: Flow visualization using a laser particle technique of rollers operating in reverse mode showing the upstream meniscus being pulled downstream. (Gaskell, et al., 1998)

A study of individual cell pickout has been undertaken on a scaled up gravure cell (Yin & Kumar, 2006) which allowed for the visualisation of the cell evacuation mechanism (Figure 1.12). It was found that the volume of coating fluid remaining in the cell after a PET (polyethylene terephthalate) coated glass top (representing a web or roller in off-set configuration) was passed over it depended on the initial volume of fluid in the cell, the distance the glass top was from the cell and the properties of the liquid (i.e. viscosity). A re-circulating flow was observed in the cell, which when considered in conjunction with the study by Gaskell et al (1998), it can be deduced that in a full gravure roller there are primary eddys forming in the coating bead but also many smaller ones in each cell indicating a very complicated flow in the domain. It has not yet been shown experimentally in the literature how the cell scale eddys affect the larger eddy in the coating bead.
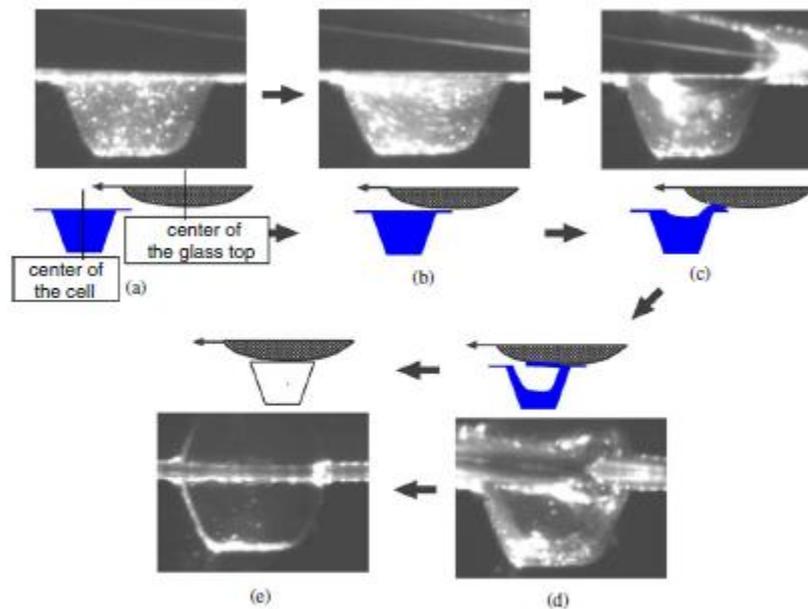
Figure 1.12: Flow visualization experiment showing the cell evacuation process. The meniscus formation can be seen as the glass top passes over the cell. (Yin & Kumar, 2006)

The addition of a flexible web to the coating bead adds the complexity of a variable web-to-roll gap which is governed by a balance of the fluid pressure and the downward force of the web. Bead structure visualisation results on a tri-helical roll (Figure 1.13, (Hewson, et al., 2006)) suggest that the web-to-roll gap collapses to a distance of zero forming a contact zone. The single eddy found by Gaskell et al (1998) separates upstream and downstream into two separate eddys either side of a central contact region.
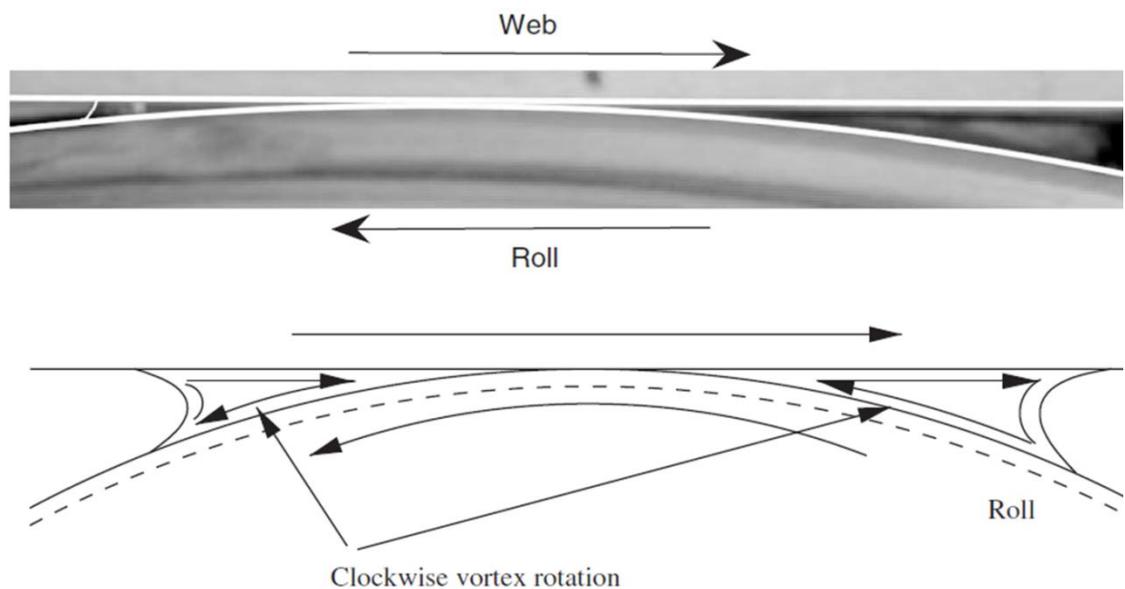
Figure 1.13: Coating bead structure (image top, schematic bottom) between a tri-helical gravure and a flexible web presented in Hewson, et al. (2006).

Using a discrete cell gravure roll Kapur (1999) observed numerous substrate scratches on an aluminium coated web (Figure 1.14). The scratches indicate that the web and roll are in contact and that web is being supported by the roll. It is unclear from the literature what impact this has on the fluid transfer mechanism.
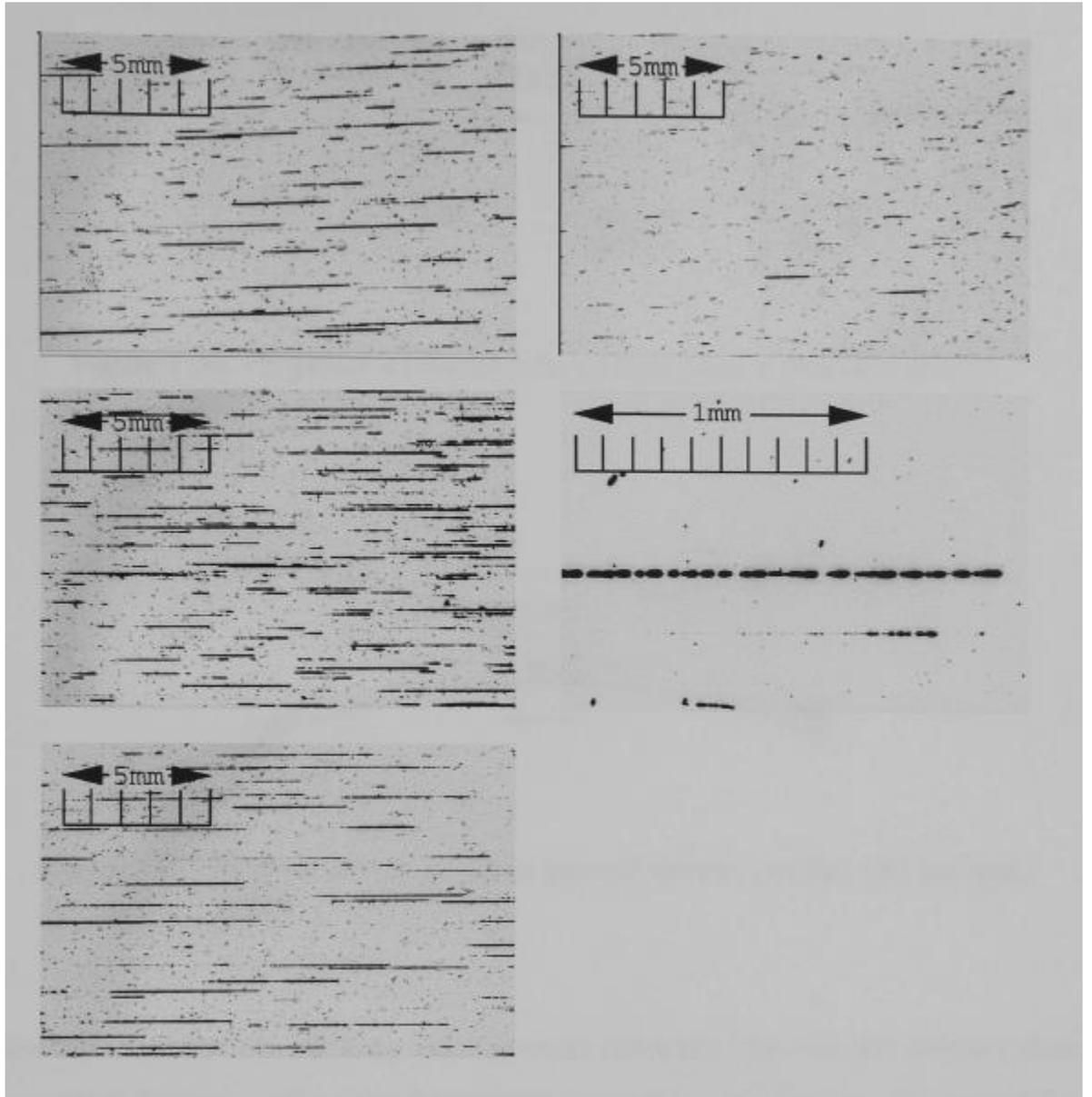
Figure 1.14: Substrate scratching presented in the PhD thesis of Kapur (1999).

1.2.1   Doctor Blade

Excess fluid is removed from the gravure surface via a doctor blade. The blade can be set in either a trailing or leading edge orientation. It can be deformed under hydrodynamic loads causing a change in the expected amount of fluid removed from the surface. In a trailing mode of operation Patel et al (1990) observed that as the angle of the blade against the gravure surface decreased the hydrodynamic loads increased, reducing the effectiveness of the blade. For leading orientation blades the resultant hydrodynamic loading pushes the blade into the roll surface.
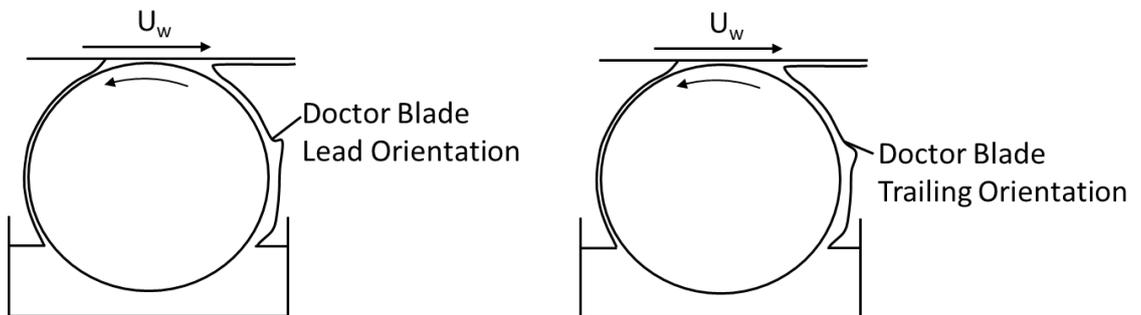
Figure 1.15: Leading and trailing orientation for doctor blades.

Hanumanthu (1999) found the blades require a wear-in period as the edges of the un-used blade form sharp corners which locally can cause a leading orientation blade to behave as if it is in a trailing orientation. During this wearing phase Hanumanthu found that the coat weight reduced by 8% before reaching a steady state, signifying that the blade was fully worn. This difference is illustrated in Figure 1.16.
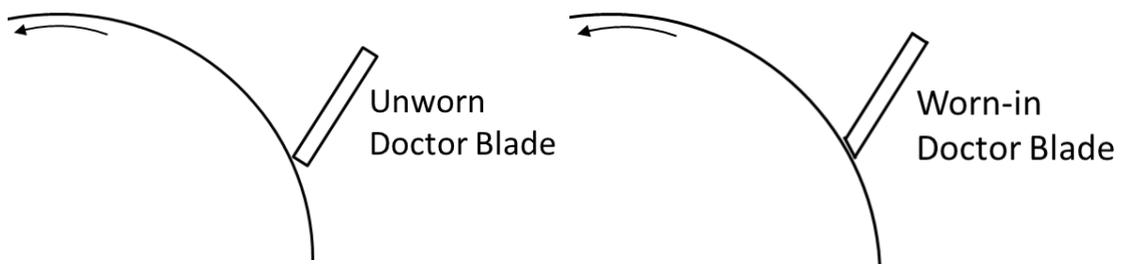
Figure 1.16: Unworn versus worn-in doctor blades. Unworn doctor blades are not parallel to the roll surface.

1.3   Gravure Numerical Modelling

The literature has presented two types of models for discrete cell gravure roll coating, these focus their attention on fluid flow through a cell or, alternatively, through the coating bead. In the analysis of roll coating the Navier-Stokes equations are often reduced to lubrication theory, therefore a derivation of this is presented at the start of this section.

1.3.1   Lubrication Theory

Reynolds equations have been used to describe simple lubricating flow and found common use in the analysis of bearing systems as well as coating applications. Equation 1.17 is the Reynolds equation subject to the following simplifications required by lubrication theory (Cameron, 1981):

1. Body forces are neglected as the field forces (i.e. gravity) applied to the lubricating liquid are much less than those applied by the surrounding surfaces.
2. Pressure through the thickness of the film is considered constant.
3. The length of the film is much greater than its thickness, $\frac{thickness}{length} \ll 1$
4. No slip conditions at all fluid to solid wall interfaces.

The problem can be simplified by limiting the scope to small where the Reynolds number $(= \frac{\rho UL}{\eta})$ flows:

5. Fluids are assumed Newtonian.
6. Fluid inertia is neglected.

Applying points 1-6 to the Navier-Stokes momentum equations (1.2, 1.3 and 1.4) results in the derivation of the Reynolds equation (Szeri, 1998).

$$\rho\left(\frac{\partial u}{\partial t} + u\frac{\partial u}{\partial x} + v\frac{\partial u}{\partial y} + w\frac{\partial u}{\partial z}\right) = -\frac{\partial p}{\partial x} + \eta\left(\frac{\partial^2 u}{\partial x^2} + \frac{\partial^2 u}{\partial y^2} + \frac{\partial^2 u}{\partial z^2}\right) + \rho f_x \qquad \textbf{1.2}$$

$$\rho\left(\frac{\partial v}{\partial t} + u\frac{\partial v}{\partial x} + v\frac{\partial v}{\partial y} + w\frac{\partial v}{\partial z}\right) = -\frac{\partial p}{\partial y} + \eta\left(\frac{\partial^2 v}{\partial x^2} + \frac{\partial^2 v}{\partial y^2} + \frac{\partial^2 v}{\partial z^2}\right) + \rho f_y \qquad \textbf{1.3}$$

$$\rho\left(\frac{\partial w}{\partial t} + u\frac{\partial w}{\partial x} + v\frac{\partial w}{\partial y} + w\frac{\partial w}{\partial z}\right) = -\frac{\partial p}{\partial z} + \eta\left(\frac{\partial^2 w}{\partial x^2} + \frac{\partial^2 w}{\partial y^2} + \frac{\partial^2 w}{\partial z^2}\right) + \rho f_z \qquad \textbf{1.4}$$

The terms in Equations 1.2 to 1.4 are defined where ρ is the fluid density, u, v, w are velocities in the x, y and z directions respectively, p is the pressure, η is viscosity of the fluid and f is the body force in the subscripted x, y or z direction. Throughout this section x will be defined as the primary flow direction, y as the thickness of the film and z as the direction across the film (on a roller this direction is axial).

For a given fluid, 1.2 to 1.4 will have four unknowns, the velocities u, v, w and the pressure, p and therefore to solve this system of equations a fourth equation is required. This is the continuity equation for conservation of volume (equation 1.5):

$$\frac{\partial u}{\partial x} + \frac{\partial v}{\partial y} + \frac{\partial w}{\partial z} = 0 \qquad \textbf{1.5}$$

With the equations for a general flow field defined, the lubrication assumptions can now be applied. First the body forces in the flow field are assumed to be negligible, $f_{x,y,z} \approx 0$. Applying assumption two, the $\frac{\partial p}{\partial y}$ term vanishes as it is assumed there is no pressure acting through the thickness of the film. From a consideration of the length scales (assumption 3) of the lubricant it can be deduced that velocities in the y direction (i.e. thickness) are very small and can be neglected which removes equation 1.3 and leaves the equations of motion as:

$$\rho\left(\frac{\partial u}{\partial t} + u\frac{\partial u}{\partial x} + w\frac{\partial u}{\partial z}\right) = -\frac{\partial p}{\partial x} + \eta\left(\frac{\partial^2 u}{\partial x^2} + \frac{\partial^2 u}{\partial y^2} + \frac{\partial^2 u}{\partial z^2}\right) \tag{1.6}$$

$$\rho\left(\frac{\partial w}{\partial t} + u\frac{\partial w}{\partial x} + w\frac{\partial w}{\partial z}\right) = -\frac{\partial p}{\partial z} + \eta\left(\frac{\partial^2 w}{\partial x^2} + \frac{\partial^2 w}{\partial y^2} + \frac{\partial^2 w}{\partial z^2}\right) \tag{1.7}$$

As a result of the constant viscosity through the thickness of the Newtonian film the fluid's velocity will only vary with its distance from the surfaces in the thickness of the film. Additionally, since the bounding surfaces are continuous, fluid velocity will not change along the length of the surface (i.e. x-direction) and similarly across the surface (i.e. z-direction).

$$\rho\left(\frac{\partial u}{\partial t} + u\frac{\partial u}{\partial x} + w\frac{\partial u}{\partial z}\right) = -\frac{\partial p}{\partial x} + \eta\left(\frac{\partial^2 u}{\partial y^2}\right) \tag{1.8}$$

$$\rho\left(\frac{\partial w}{\partial t} + u\frac{\partial w}{\partial x} + w\frac{\partial w}{\partial z}\right) = -\frac{\partial p}{\partial z} + \eta\left(\frac{\partial^2 w}{\partial y^2}\right) \tag{1.9}$$

Assuming that the inertial terms are small and can be neglected, the left hand side of the equation is set equal to zero. After rearrangement, the pressure gradients are:

$$\frac{\partial p}{\partial x} = \eta\left(\frac{\partial^2 u}{\partial y^2}\right) \tag{1.10}$$

$$\frac{\partial p}{\partial z} = \eta\left(\frac{\partial^2 w}{\partial y^2}\right) \tag{1.11}$$

Equations 1.10, 1.11 and 1.5 govern the motion of a lubricating fluid (Stokes flow). The Stokes fluid governed by Stokes flow has the properties of being instantaneous, time reversible and linear. This is useful because the flow can be solved with knowledge of the boundary conditions at only one point in time. Further, its linearity means that it is proportional to just the forces acting on it. By twice integrating 1.10 and 1.11 with respect to y to isolate the fluid velocity components, the following equation is obtained:

$$u = \frac{1}{2\eta}\frac{\partial p}{\partial x}y^2 + Ay + B \qquad \textbf{1.12}$$

$$w = \frac{1}{2\eta}\frac{\partial p}{\partial z}y^2 + Cy + D \qquad \textbf{1.13}$$

Where A, B, C and D are constants of integration. The boundary conditions for equations 1.12 and 1.13 arise from a consideration of the bounding upper and lower surfaces. In reality the surfaces would typically be a solid plate and as such only moving in one direction which is defined here as the x direction. Assuming there is no-slip at each surface:

$$u = U_{lower}, \; w = 0 \qquad \text{at} \qquad y = 0 \qquad \textbf{1.14}$$

$$u = U_{upper}, \; w = 0 \qquad \text{at} \qquad y = h$$

Where U is the velocity of the subscripted surface and h is the separation of the two surfaces. Solving equations 1.12 and 1.13 for the boundary conditions in 1.14 the following is achieved:

$$u = \frac{1}{2\eta}\frac{\partial p}{\partial x}(y^2 - yh) + \left(1 - \frac{y}{h}\right)U_{lower} + \frac{y}{h}U_{upper} \qquad \textbf{1.15}$$

$$w = \frac{1}{2\eta}\frac{\partial p}{\partial z}(y^2 - yh) \qquad \textbf{1.16}$$

A useful form of this equation is where the subject is the volumetric flow-rate. Finally the integrals $\int_0^h u \, dy$ and $\int_0^h w \, dy$ will yield the volumetric flow rates:

$$q_x = -\frac{h^3}{12\eta}\frac{\partial p}{\partial x} + (U_{upper} - U_{lower})\frac{h}{2} \qquad \textbf{1.17}$$

$$q_w = -\frac{1}{12\eta}\frac{\partial p}{\partial z} \qquad \textbf{1.18}$$

Where q_x is the volumetric flow in the x direction, h is the distance separating the two surfaces, μ is the viscosity, $\frac{\partial p}{\partial x}$ is the pressure gradient in the x direction, U is the subscripted velocity of the surface. Note that if the moving surfaces have velocity components in the z direction, equation 1.18 will have an extra velocity term similar to 1.17.

1.3.2   Numerical Gravure Cell Models

Models investigating discrete gravure cells or tri-helical channels operate on length scales of 10s-100s μm.

Early work to numerically investigate the gravure cell evacuation process was undertaken using lubrication theory to approximate a Newtonian fluid, passing over a patterned surface (Schwartz, et al., 1998), this can be seen in Figure 1.17. The result showed that the pickout ratio increased with cell volume, which agrees with other experimental work found in the literature [(Benkreira & Cohu, 1998), (Kapur, 2003)]. The model used a time-marching method, but made use of the periodic topography of a gravure surface and periodic time. Simulations were performed for both two and three dimensional cells and it was found that in three dimensions pickout ratios were smaller, suggesting that the cell walls (rather than just a cross-section) play a role in the evacuation process. The two-dimensional formulation is representative of a channel as opposed to three-dimensional formulation which describes a cell.

The effect of cell patterning was also investigated by taking the initial nine cell square domain and rotating it such that the cells were patterned at 45° from the horizontal (as one looks down on the surface of the roller) which showed a corresponding increase in pickout Schwartz (2002).
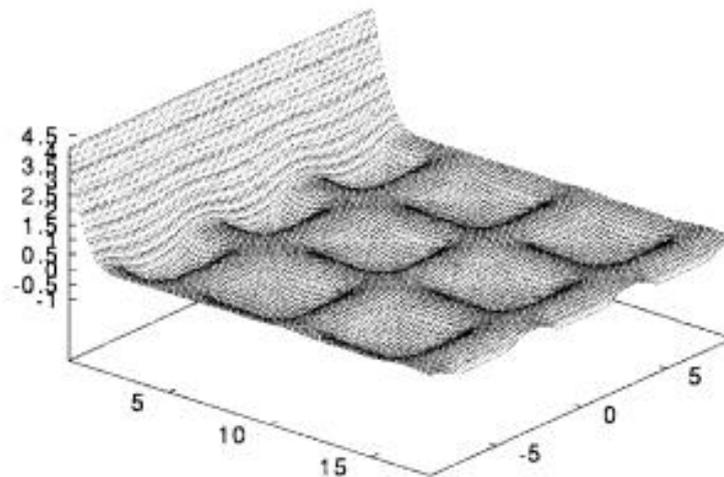
Figure 1.17: Patterned surface of the gravure roller as the meniscus passes over the surface. Fluid can be seen remaining in the cells. (Schwartz, et al., 1998)

Using the finite element method Powell et al (2000) modelled the fluid evacuation process in a two-dimensional rectangular cell (Figure 1.18). The simulation pinned a meniscus to an upper moving surface (the web) and as it travelled across the domain fluid was "pumped" out of the cell. It was found that a large aspect ratio (i.e. a long shallow cell) evacuated more completely in comparison to a low aspect ratio cell (i.e. narrow and deep cell); and for cells with a very large aspect ratios the pickout was independent of capillary number.
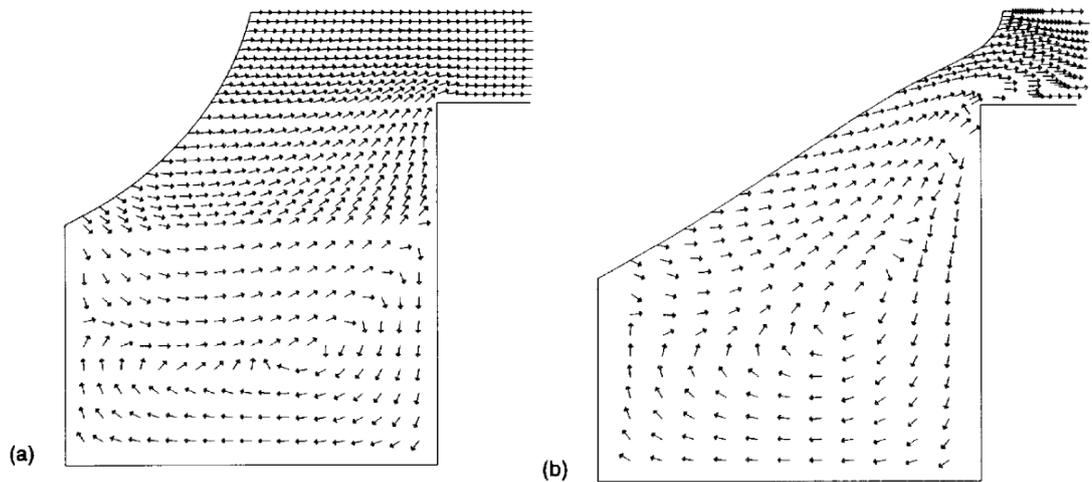
Figure 1.18 Flow field inside a gravure cell showing as the meniscus travels across the domain fluid is forced to evacuate the cell. Figure is from Powell, Savage and Gaskell (2000).

Velocity profiles in the cell also give some insight into the evacuation mechanism, whereby the eddy initially present in the cell is deformed as the meniscus travels down the cell wall. To conserve volume (and mass as the fluid is incompressible) the flow rate out of the cell near its corner greatly increases (see Figure 1.18), and it can be inferred that the meniscus is supplying a 'pumping' action to force this velocity increase.

More recently a similar study (Hoda & Kumar, 2008) using the boundary integral method concurred with the findings of Powell et al (2000) but also noted that an increase in the contact angle on the cell wall led to a reduced pickout. It could be seen that the meniscus in certain conditions can travel

along all three walls of the cell (noting that study was in two dimensions and the cell was essentially a rectangle with an open top). The contact angle of the meniscus on the cell wall was shown to affect both the rate of emptying and the degree to which a cell would empty. It is also shown how the capillary number and the cell geometry affect the evacuation process (Figure 1.19). The more significant of these two parameters is the cell geometry, specifically the ratio of the length of the cell entrance to cell depth. The model predicts what has been seen experimentally which is that shallow cells have a larger pickout ratio.
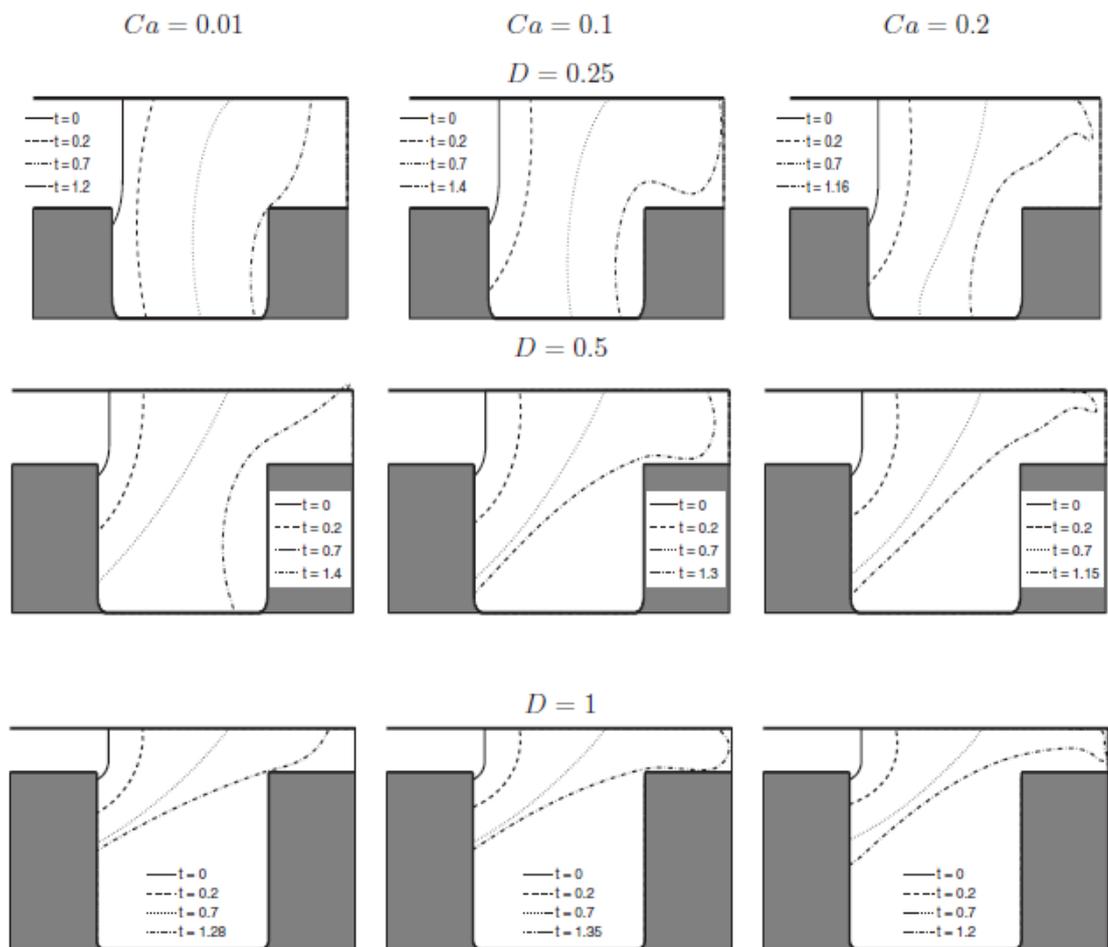
Figure 1.19 Describing the time dependent travelling meniscus for different capillary numbers and different cell geometries presented in Hoda and Kumar (2008).

Most studies that examined fluid flow in a gravure cell have neglected the influence of the web, and have considered it as a uniform rigid wall. This assumption arises from consideration of the length scale of an individual cell

(much like assuming the surface land near the cell is flat when in reality it is curved due to the cylindrical roll). This assumption was investigated by Yin and Kumar (2005) who used a lubrication model to determine the affect of a variety of tensioned webs and the case of an off-set roller which is covered in an elastic material. The results showed that webs which were only lightly tensioned severely deformed as they passed over the cell and on highly tensioned webs this effect was much less.

Following this work external pressure was incorporated into the model (Yin & Kumar, 2006) to show the effect of the web (and in this study a flexible cell base was looked at) on the streamlines in the cell and its surrounding gap. These two models do ignore the web stiffness which plays an important roll on the web deformation problem on the cell length scale (Hewson, et al., 2009). When web stiffness is included it can be concluded that the deformation, on the scale of a gravure cell level is negligible.

1.3.3   Numerical Coating Bead Models

Greener and Middleman (1979) used lubrication theory to successfully predict the film thickness produced on two parallel counter-rotating smooth rolls that were half submerged in a coating bath. Coyle et al (1990) created a numerical model on the same roll setup (Figure 1.20) operating in reverse mode and focused its attention on the flow entering and leaving the metering gap. The model applied using lubrication theory and the finite element method. Due to the experimental setup the free surface above the metering gap (i.e. where film splitting occurs) played an important role in the physics. A recirculation region was induced below this free surface but above the metering gap and it was suggested that this recirculation caused a large flow rate back through the metering gap. It was found that lubrication theory was unable to correctly predict the location of the free surface or the recirculation region.
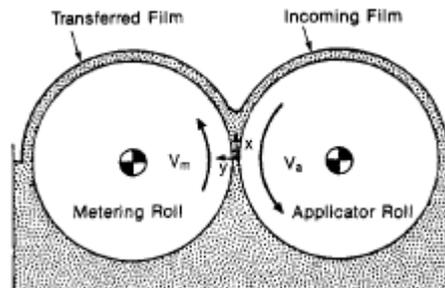
Figure 1.20 Experimental setup used by Coyle et al (1990) for the basis of their lubrication model of the metering gap.

Modelling the tri-helical coating bead on a gravure roller where the grooves are continuous and as such can be well represented with a two-dimensional model whereas discrete cells create more complex three-dimensional effects. Because of this an early predictive model was developed for a direct tri-helical gravure roller operating in reverse mode using the finite element method (Hewson, et al., 2006). In the case of a flooded coating bead these pressures would be taken at infinity where the pressure gradient would be equal to zero. As this is not ever the case since the coating bead is not infinitely long the pressure boundaries were taken to be in the menisci.

1.3.4   The Meniscus Boundary Condition

The boundary conditions applied in these coating models have largely come from considerations of free surfaces, starting with the Young-Laplace equation relating a pressure differential across a fluid boundary to the radius of curvature of that boundary. From contemplation of a dip coating experiment, Landau & Levich (1942) found that the film thickness formed as a plate was withdrawn from a liquid could be calculated. In the limiting velocity case (i.e. where velocity is much less than the ratio of surface tension to fluid viscosity) the film thickness can be found using:

$$h_0 = 2.29 \frac{(v_0\eta)^{2/3}}{\gamma^{1/2}\sqrt{\rho g}} \qquad \textbf{1.19}$$

Where the asymptotic film thickness, h_0, is related to the surface tension, γ, substrate withdrawal velocity, v_0, fluid viscosity, η, fluid density, ρ, and gravity, g. At somewhat higher rates of withdrawal the film thickness is related by the equation:

$$h = \left(\frac{\eta v_0}{\gamma g}\right)^{1/2} f\left(\frac{v_0\eta}{\gamma}\right) \qquad \textbf{1.20}$$

Where the capillary number, $f\left(\frac{v_0\eta}{\gamma}\right)$, needs to be experimentally determined. In these equations the inertial term becomes more significant as the withdrawal speed (and therefore the capillary number) increases.

Experimentally considering a liquid filled narrow horizontal tube being partially evacuated by a long bubble yields a similar result to that of Landau and Levich, however, the gravitational drainage term becomes largely insignificant and vanishes in the analysis. This becomes important for use in roll coating analysis because the bead is typically located on top of the roll and its size is such that the inertia can readily be neglected. Such work was

completed by Taylor (1960), Bretherton (1960) and Cox (1962) who considered a range of capillary numbers. Bretherton, considering capillary numbers in the range of 0.015 to 0.09, analytically derived the ratio of asymptotic film thickness (λ) over its meniscus radius of curvature (r) to equate to the product of a coefficient and the capillary number to the two-thirds power (equation 1.21). This relation was utilised as a boundary condition in Hewson, et al. (2011).

$$\frac{\lambda}{r} = 1.34 \left(\frac{\eta v}{\gamma}\right)^{2/3}$$
   1.21

1.3.5   The Multiscale Method for Discrete Cell Gravure Modelling

The multi-scale method is used to address problems that have components in disparate scales, where it is impractical to solve everything at the detail required for the small features, or alternatively there is missing information when using the larger scale (E, et al., 2003). It works by creating a homogeneous large scale solution using the small scale information to fill in the missing large scale data. The method is well suited to discrete cell gravure modelling because of the different length scales between the coating bead and the cells. This was first applied to gravure coating by Hewson et al (2011) who created a two dimensional model of a coating bead where the roller surface was populated with trapezoidal cells. The goal was to show the effect of the cells on the flow throughout the coating bead. It was noted that lubrication theory used in earlier works is not applicable to discrete cell gravure roll coating because of the sharply changing topography on the surface and since the depth of the cells can be of the same magnitude as the web-to-roll gap. In particular the multi-scale method accounted for the re-circulating within the gravure cells, a feature overlooked in earlier work.

The model was able to predict important operation parameters as identified by experimental methods on the coating bead level and the cell level.

Particularly it showed that as web-to-roll speed ratio increased so too did the pickout. The model also predicted the effect of cell geometry on pickout and film thickness, i.e. shallow cells evacuated more completely and deeper cells lead to a greater film thickness which agrees with earlier work of Kapur (2003).

1.4   Conclusions from Literature

Work on discrete cell gravure roll coating is now a well-developed field of study. Experiments over the last 25 years have identified the key parameters that influence the coating process. Some of this has been shown numerically. The fluid transfer process for a gravure roll and flexible web remains at least a partial unknown, though it is analogous to the case where a transfer bead forms between two smooth rolls. The influence of the gravure cells, the flexible web and an unknown web-to-roll gap complicate this problem. The two scale modelling technique discussed in Hewson et al (2011) has shown a method of combining a simplified cell level flow model with the larger transfer flow model. Extension of this to a predictive discrete cell gravure model is a promising path of study.

Chapter 2   Experimental Methodology and Results

2.1   Introduction

This chapter outlines film measurement experiments undertaken for two gravure rolls of different patterns. The purpose of these tests is to establish a body of results against which a numerical model can be compared. Similar experimental work has been done elsewhere in the literature [(Benkreira & Patel, 1992), (Benkreira & Cohu, 1998), (Kapur, et al., 2001), (Kapur, 2003), (Hewson, et al., 2006)] and details such as film thickness, pickout ratio, fluid properties and cell volumes are readily available. However, validation of the numerical model also requires details of the roll surface, especially pertaining to the cell shape which is typically not reported in the literature at an appropriate level.

This chapter presents both the methodology for testing and the resulting data of the measured film thickness and the calculated pickout ratio of the two gravure rolls. It also contains experimental observations of scratches formed on the web during the coating process.

2.1.1   Web Handling

The experimental roll coating apparatus used here can be seen in Figure 2.1 and Figure 2.2. It was designed to simulate industrial roll coating operations and has been used in previous work (Kapur, 1999). The apparatus replicates the coating process found on industrial production lines; it neglects the upstream web stretching processes and the downstream drying processes. A detailed description of its operation can be found in Kapur (1999). A brief description has been offered here for clarity.
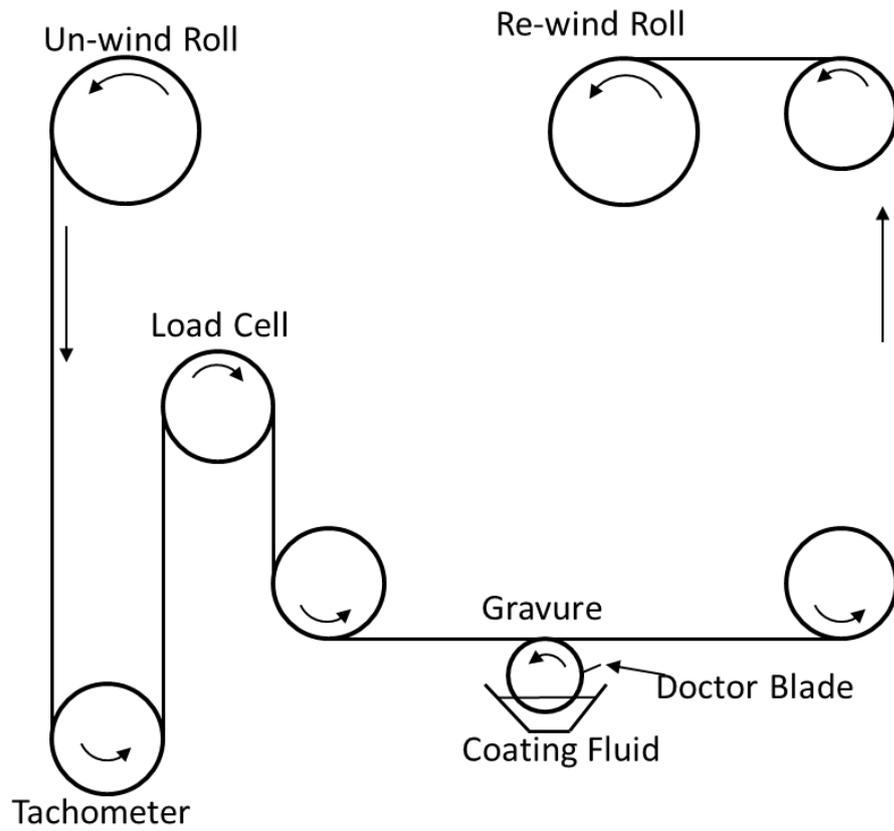
Figure 2.1: Illustraion of coating rig showing direction of web travel through the rolls.
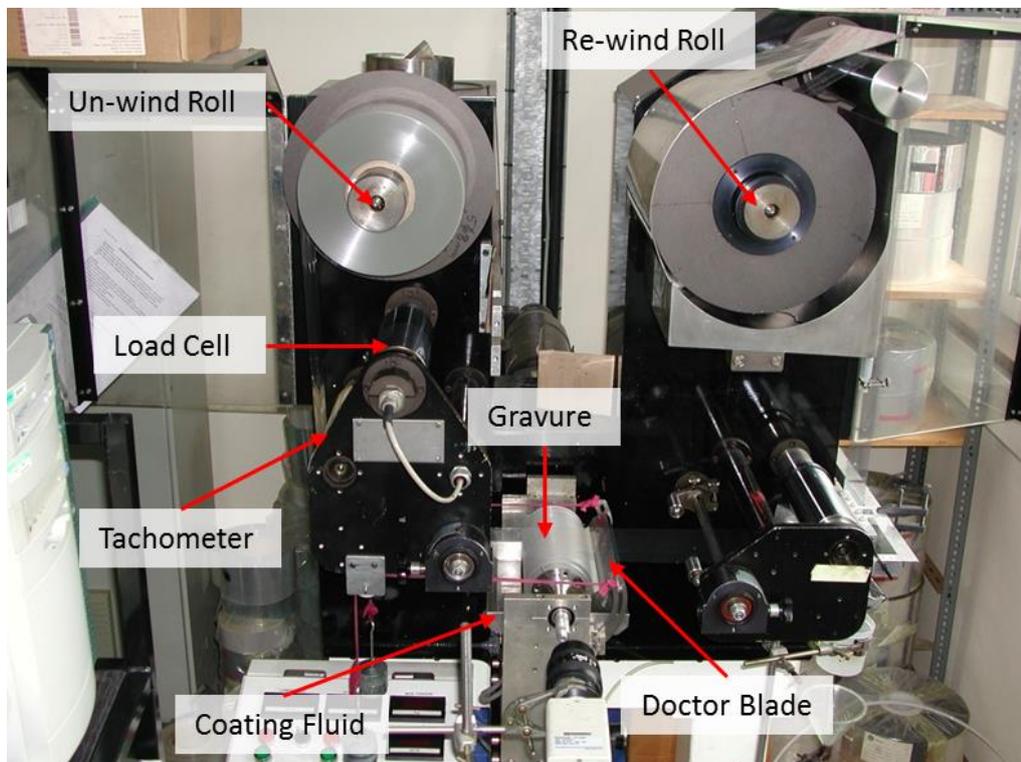
Figure 2.2: Picture of the coating rig.

2.1.2 Web Handling

Referring to Figure 2.1 the rig passes the web from the un-wind roll to a re-wind roll. These are the only two powered web handling rolls. Between these there are five idle rolls, the first of which is fitted with a tachometer for measuring the velocity of the web. The second is fitted with a load cell to measure the web tension. A third idle roll is then used to re-direct the web to ~~the coating at~~ the top dead centre of the gravure. This roll has an adjustable height such that the wrap angle upstream of the gravure can be varied. Downstream of the gravure there were two more idle rolls which are used to direct the web to the re-wind roll.

2.1.3 Fluid Handling

The coating fluid is held in an open air tray. This can be filled such that the bottom two centimetres of a 10 cm gravure roll will be submerged. Geometrically the tray is unlike the closed anilox chambers used at industrial production scales, but from an operational perspective the roll collects fluid in a similar manner.

Film thickness measurements require the fluid to be removed from the web and measured. This is accomplished using a rubber scraper which is firmly pressed against the idle roll directly downstream of the gravure (Figure 2.3). This process was described and shown to be effective in Kapur, (2003) and Kapur, Gaskell, & Bates (2001) leaving a fluid thickness of less than 0.1 μm on the web. The fluid is funneled into a beaker which is then weighed to find the mass of liquid. The coating apparatus takes several seconds to accelerate to the input speed and the fluid takes up to 30 seconds to drain from the scraper into a collection beaker. Therefore, at least 30 seconds of operation is required before steady state is reached.
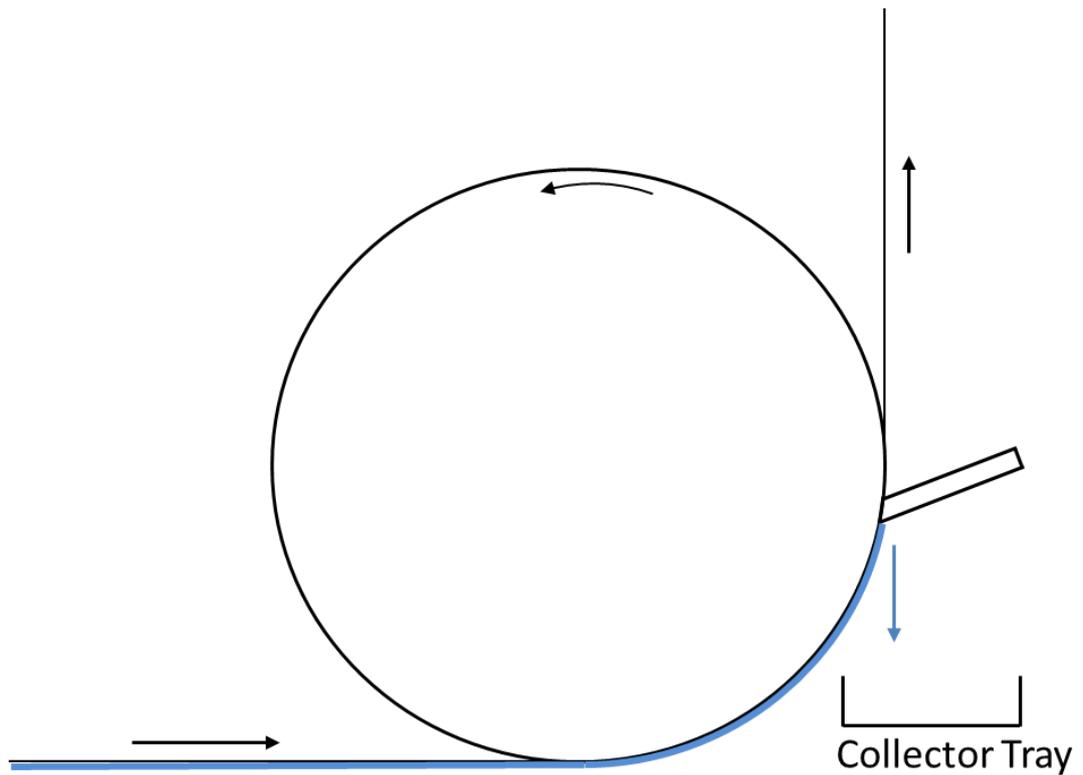
Figure 2.3: Fluid removal from web using scrapper. Fluid drips downward from the scraper to the collector tray below.

2.1.4   Gravure Handling

The gravure roll is powered by a dedicated motor and an independent speed control. The roll rotates in a tray containing the coating fluid with excess fluid being removed by the doctor blade. The gravure meshes with its drive motor using a key and channel configuration. The coating apparatus is designed to handle rolls of the dimensions shown in Figure 2.4.
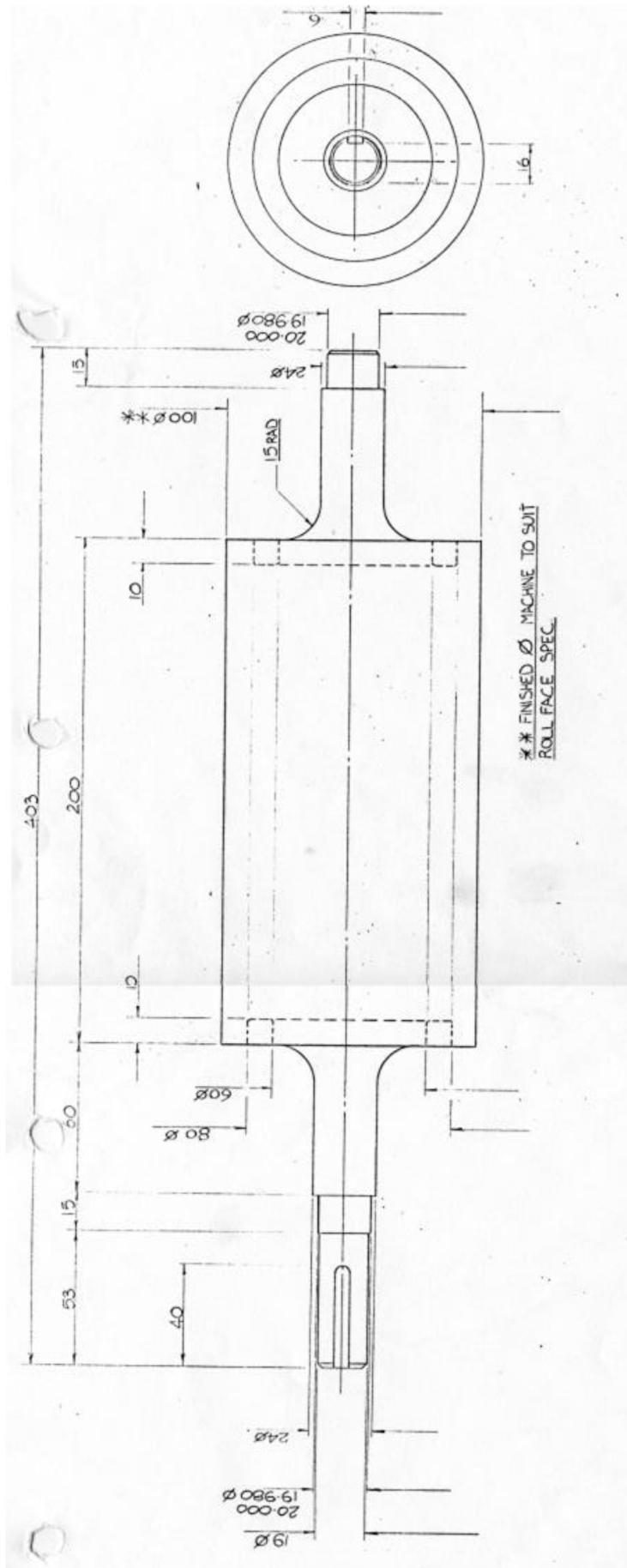
Figure 2.4: Photocopy of manufacturer's schematics for the dimensions of a gravure roll to be used in the coating apparatus.

2.1.5   Doctor Blade

A doctor blade is fitted to remove excess fluid from the roll surface. The doctor blade is loaded by suspending weights (4 kg) via a pulley system. The doctor blade angle was set to operate in a leading orientation. The blade was made from a 250 micron thick strip of PET held in a custom clamp.

New blades required a wear-in period; specifically, corners of the blade's square edge needed to be worn down. Before this wear was completed the blade could vibrate violently. This wear process was also important in allowing the coat weight to arrive at a steady state (Hanumanthu, 1999). The wear process took approximately 20 minutes while operating as intended against the gravure (speed of 0.5 m/s) and was stopped when the vibrations ceased. The wear process was conducted prior to any coating experiments using a fluid that was replaced to prevent contamination of testing fluid. This is important as PET particles from the blade will flow into the coating solution and can mechanically lock into the gravure cells. A similar process is observed in industrial coating operations where the coating fluid may already contain solid particles and over time will reduce the volume of fluid transferred to the web due to build up in the cells.

2.1.6   Coating Apparatus Control System

The apparatus is operated from a control panel allowing for the values of the gravure speed, web speed and web tension to be set.

The apparatus control uses a feedback loop comparing the input web tension and web speed to the measured tension (via the load cell) and speed (via the tachometer). The re-wind roll speed is adjusted to maintain a constant web speed/tension measured by the tachometer/load cell. These variations occur as the length of web on the un-wind/re-wind rolls changes (i.e. the radius of the web on the roll changes as it is used).

The control system does not work at web loads less than 50 N/m and is most reliable above tensions of 100 N/m. The control system fails to consistently resolve the speed when the reels have a large difference in

radius (e.g. when a new reel is added to the un-wind roll and re-wind roll is empty).

2.2   Experimental Fluid Properties

The experimental fluid used was a mixture of water and glycerol. The addition of glycerol is used to increase the fluid viscosity to bring it into line with other experimentalists and industrialists. From literature the viscosity in experimental work has been conducted over a range of 0.001-0.0134 Pa·s (Benkreira & Patel, 1992) and 0.001-0.004 Pa·s (Kapur, 2003) where at 20° C water has viscosity of approximately 0.001 Pa·s.

Numerical work typically reports capillary number as the preferred metric and often does not quote viscosity, surface tension or characteristic velocity. For the purposes here the viscosity was computed using a surface tension of 0.04 N/m and a gravure roll velocity of 0.5 m/s because these were the values eventually used in the experiment. Assuming this a value of 0.008 Pa·s was used by Hewson, et al. (2006), while Schwartz, et al (1998) reports viscosities of 0.005 Pa·s.

The surface tension of a water/glycerol solution is too high to completely wet the surface of the web (the fluid forms beads on the web leaving large areas uncoated). This was reduced using the surfactant Tween20 (polyoxyethylenesorbitan monolaurate) at a one percent concentration.

There are two properties of the coating fluid that need to be known for these experiments. These are the fluid viscosity and the surface tension of the fluid. It is worth noting that some of the boundary conditions used in the numerical model (shown in later chapters) are only applicable at low capillary numbers and a low viscosity is desirable in order to maintain their validity. The lower viscosities are also more representative of what is seen in industry.

2.2.1 Viscosity Measurement Method

Measurements of the fluid viscosity were required to determine the ratio of glycerol to water that was needed to create a test solution of viscosity 0.002 Pa·s. Four test fluids were made with 20%, 25%, 33% and 50% glycerol concentrations.

The viscosity of the coating fluids were measured using a cone on plate rheometer. This is a category of rotating shear rheometer. A sample of the test liquid is placed on the plate and the cone is lowered to a pre-set distance from the plate. This gap at the end of the cone was set to 0.25 mm (the cone is in fact slightly truncated at the tip rather than forming a point). The cone rotates and the rheometer measures the resistance to motion induced on the cone by the fluid. The viscosity can then be related to this measured value of shear force.

The rheometer also requires a calibration against a fluid of known viscosity which in this case was water.

2.2.2 Viscosity Measurement Results

Referring to Figure 2.5 the preliminary glycerol concentration tests showed that 20% glycerol would yield viscosities of approximately 0.0018 Pa·s. This concentration was carried forward to create a large batch solution for use in the experiments. The viscosity of this larger batch was measured immediately prior to conducting the experiments and was found to have a viscosity of 0.0016 Pa·s, the variation likely due to changes in fluid temperature which was ultimately controlled by the ambient room temperature.
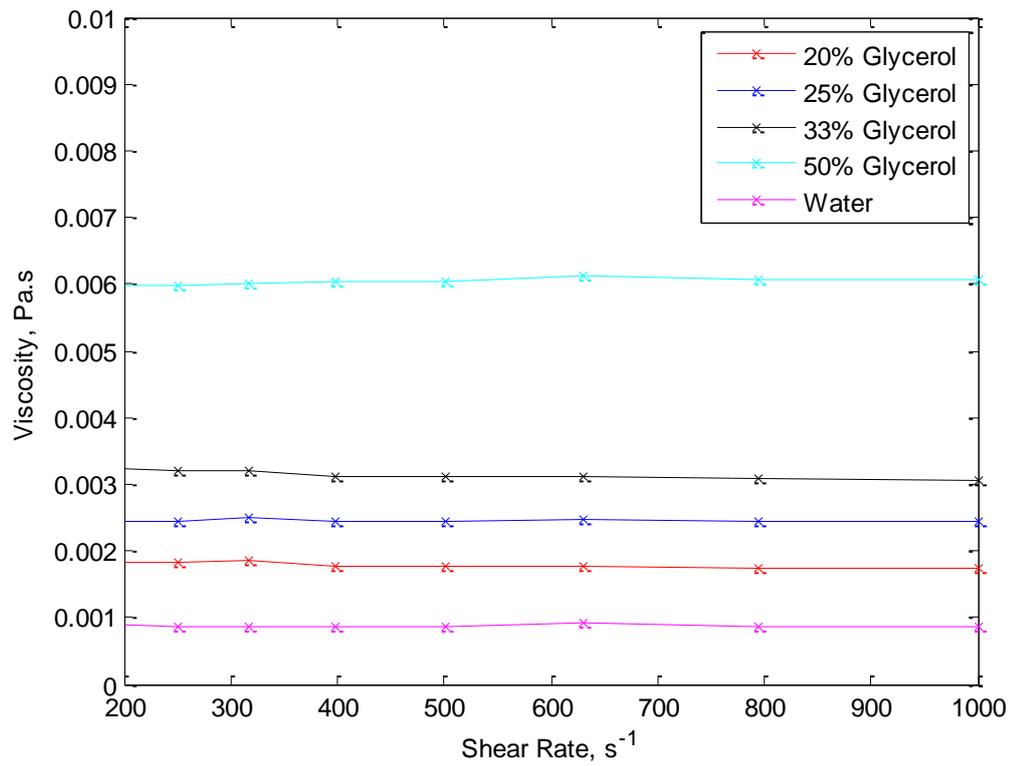
Figure 2.5: Resultant viscosity of water-glycerol test mixtures. The solution carried forward to the experiments was 20% gylcerol.

2.2.3   Surface Tension Measurement Method

A small amount of surfactant was required to ensure that the web fully wetted. The volume used to achieve this was one percent of the volume of the test solution. The surface tension of the final solution was measured using a 10mm platinum du Noüy ring fixed to a tensiometer (Figure 2.6). The ring was cleaned prior to measurements using an ultrasonic bath containing distilled water.
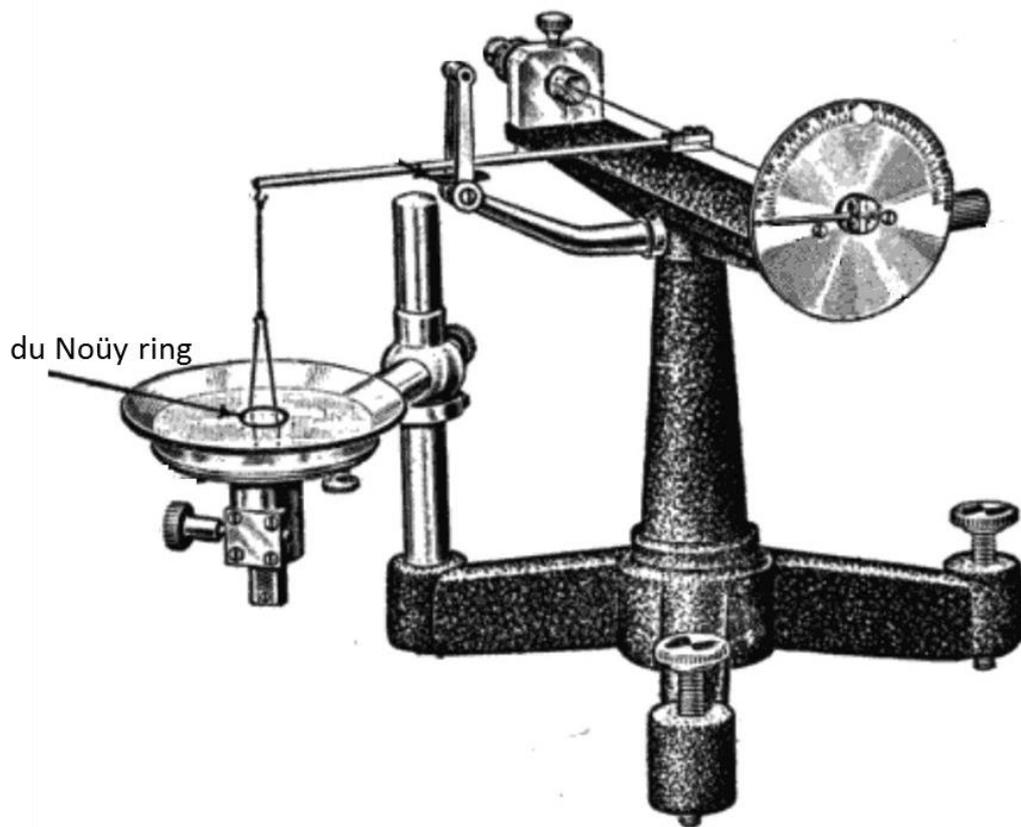
Figure 2.6: Du Noüy ring apparatus (Holmes, 1922).

2.2.3.1   Surface Tension Measurement Results

Measurement of the surface tension in the bulk test fluid used in the coating experiments was found to be 0.04 N/m. The scale on the tensiometer could read to 0.005 N/m.

2.3 Experimental Gravure Rolls

2.3.1 Introduction

The film thickness experiments were conducted using two gravure rolls which have been designated Roll A and Roll B. These are both ceramic rolls which were laser engraved with a discrete cell pattern to give the characteristics summarised in Table 2:1. The key parameters are the opening diameter, the cell depth and the characteristic length (which is equal to its periodic length), these are identified by the idealised sketch in Figure 2.7. The cell details were captured using a white light interferometry technique. This allowed for the volume of individual cells to be calculated as well as their shape characteristics such as opening diameter, depth and volume.
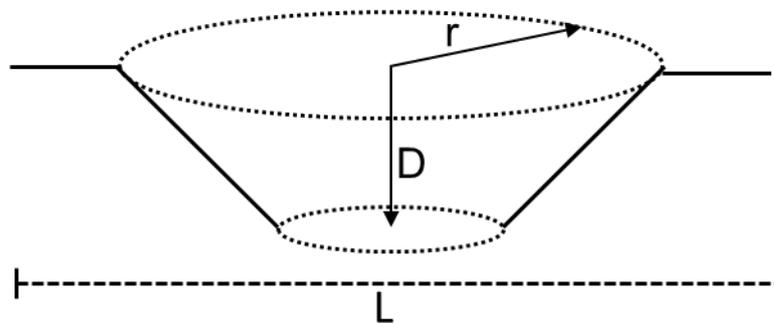
Figure 2.7: Sketch of a generic gravure cell. The cell diameter is given by 2r, the cell depth is given by D, and its characteristic length refers to its periodic length, L.

Table 2:1: Parameters for rolls A and B

Average Cell Values	A	B
Characteristic Length (L)	0.250 mm	0.450 mm
Cell Diameter (2r)	0.150 mm	0.300 mm
Cell Depth (D)	0.080 mm	0.175 mm
Cell Volume	8.9×10^{-13} m^3	7.5×10^{-12} m^3
Volume per Unit Area	1.4×10^{-5} m^3/m^2	3.7×10^{-5} m^3/m^2

2.3.2 Imaging of Gravure Rolls

The cell depth of the test rolls was on the order of tens of microns and therefore to resolve the topography an imaging technique was required to capture features on the micron scale. The cell pattern repeats on a millimetre length scale. Two pieces of equipment were tested to meet these criteria, a white light interferometer and an optical microscope.

2.3.2.1 Imaging: White Light Interferometer Method

Interferometers split a light source to create two beams of light. One beam is reflected off of a mirror and the other off the surface which is being investigated. The two beams are then recombined and interfere with each other. Due to the phase difference between the two beams of light they form fringes of lower or greater intensity. The resulting interference fringes appear on the viewing surface. The distance separating the fringes is related to how out of phase the light has become after reflecting off of the object. This can be related to the topology of the surface. The resolution for interferometers is based on the wavelength of light used making them more than adequate at measuring sub-micron features. A simple schematic of a Michelson interferometer is shown in Figure 2.8, this is one which is monochromatic (a one wavelength light source). White light interferometers operate on the same principle but are polychromatic. For further information on the operation of a white light interferometer the reader is referred to Hariharan (2006).
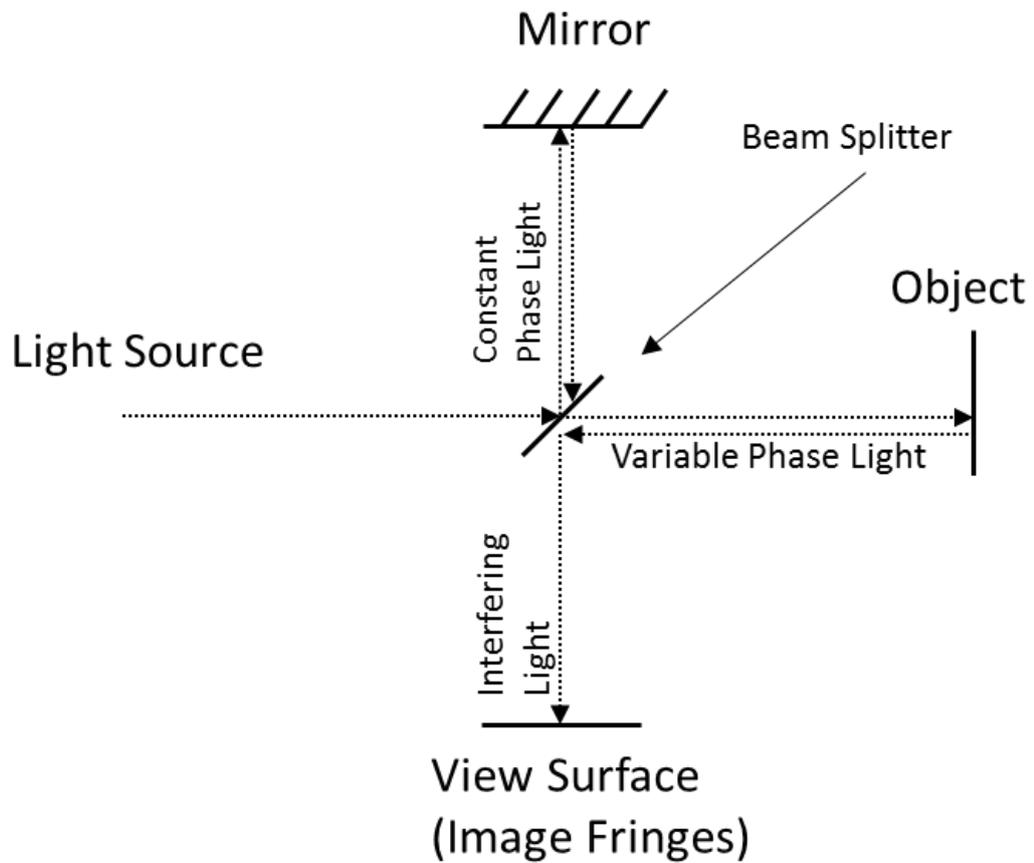
Figure 2.8: Schematic of Michelson interferometer.

The interferometer used was made by Bruker. The device was large enough for an entire gravure roll to be placed under the viewing lens. The curvature of the roll is noticeable when viewing an area of the roll. This curvature was digitally removed by approximating the roll surface to follow a parabolic curve.

Any features on the gravure roll (or any object) that have a viewing angle greater than 40° will reflect the light away from the interferometer's lens. This is relevant to rolls with steep cell walls, though the ones considered here did not exceed this criteria.

2.3.2.2   Imaging: Optical Microscope Method

An optical microscope relies on detraction of light through a lens to magnify and image. An optical three dimensional microscope operates similarly but instead of taking just one image it will take a series of images varying the

distance from the surface of the object. As the microscope has a fixed focal length there will only be one region in each image that is in focus. By digitally "stitching" these images together (this is based on interpolation between each image in the series) a single three dimensional image of the surface can be created. For further details on the theory of optical microscopes the reader is referred to Murphy (2001).

The 3D optical microscope at the University of Leeds cannot handle a large sample such as a gravure roll. Therefore in order to capture a surface image of the gravure metallic imprint strips are required (these are produced by Praxair). They are made of a soft malleable metal that can be pressed into the surface of the gravure. An image of the imprint can then be captured by the microscope.

2.3.2.3 Imaging: Conclusions

As a method for capturing an image of a gravure surface the interferometer is preferable. This is because:

- The interferometer can be focused directly on the roll without the need of an imprint strip. This reduces the number of steps required and reduces the chance of error.
- The resolution of the interferometer is related to the wavelength of white light (~400-800 nm) allowing for resolution of features on the sub-micron scale. The resolution in the vertical axis for the optical microscope is determined by, first, the accuracy of the motor and plate which move the sample; and second the number images stored that can be stitched together. The optical microscope does not achieve the resolution (in the vertical axis) of the interferometer.

However, in the event the gravure has very steep cells such that cannot be properly resolved by the interferometer the optical microscope can be used. However, none of the test rolls used here had features too steep to be captured.

2.3.3   Description of Gravure Rolls

White light interferometry images of the surface of both rolls are shown in Figure 2.9 and Figure 2.10. The cells on both rolls have approximately circular openings. The cells narrow to form a rounded base, cross-sections profiles are shown in Figure 2.11. The Figure 2.12 and Figure 2.13 compare the relative land area of each roll. In part b of these figures the all but the top layer of image pixels has been digitally removed to highlight how much land actually at the surface of the roll. Simultaneously considering all of these figures there are several key differences between the two rolls:

1. The land on Roll A is very smooth while the land on Roll B is visibly rougher (see part a of Figure 2.9 and Figure 2.10).

2. The land on Roll A occupies a larger portion of the area than the land on Roll B (see Figure 2.12 and Figure 2.13). The land on Roll A is also smooth and complete everywhere while the land on Roll B is rough and arbitrarily incomplete which exacerbates the area difference.

3. The walls on Roll A plateau to form the flat land surface while those on Roll B taper towards a point (Figure 2.11).

4. The diameter of the cell opening is approximately two times larger for Roll B than for Roll A (see Figure 2.11 and Table 2:1).

5. The depth of cells on Roll A are almost half that of Roll B (see Table 2:1).

6. The cell volume is one order of magnitude smaller for cells on Roll A than those on Roll B. Details of each roll are in Table 2:1 and the cell width can be compared directly in Figure 2.11.
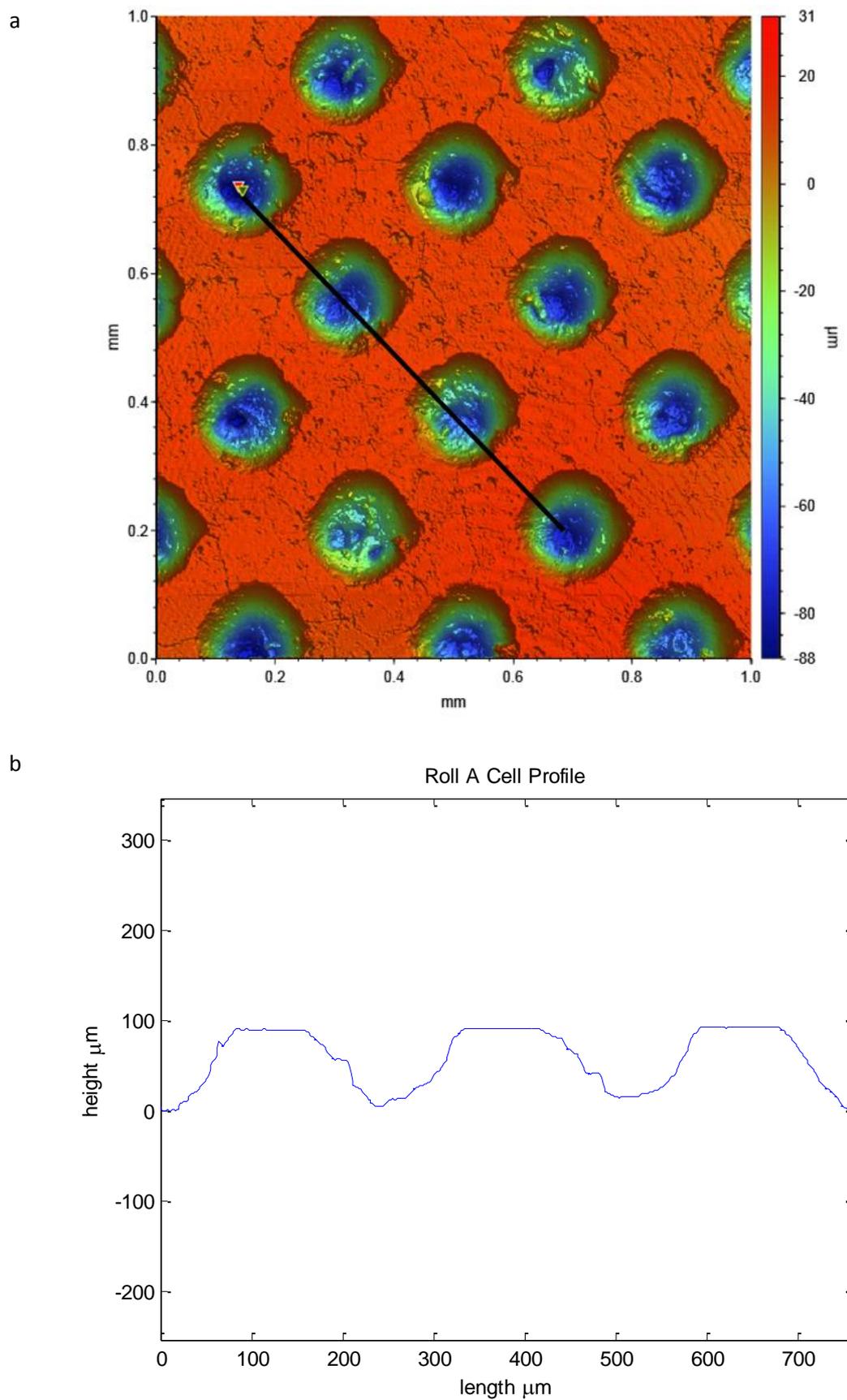
Figure 2.9: White light interferometer contour image of Roll A (a) and a profile plot of a cell row (b).
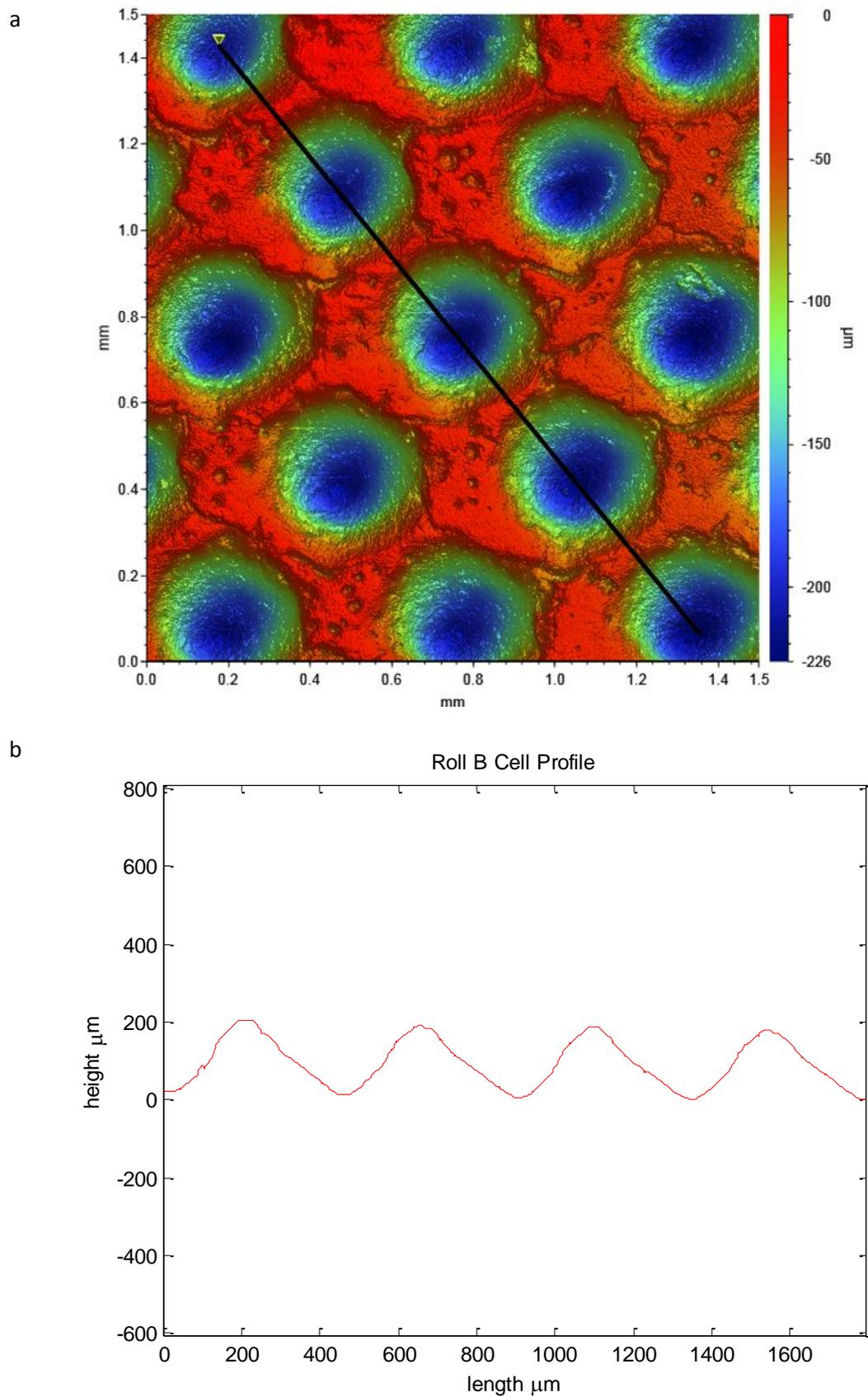
Figure 2.10: White light interferometer contour image of Roll B (a) and a profile of a cell row (b).
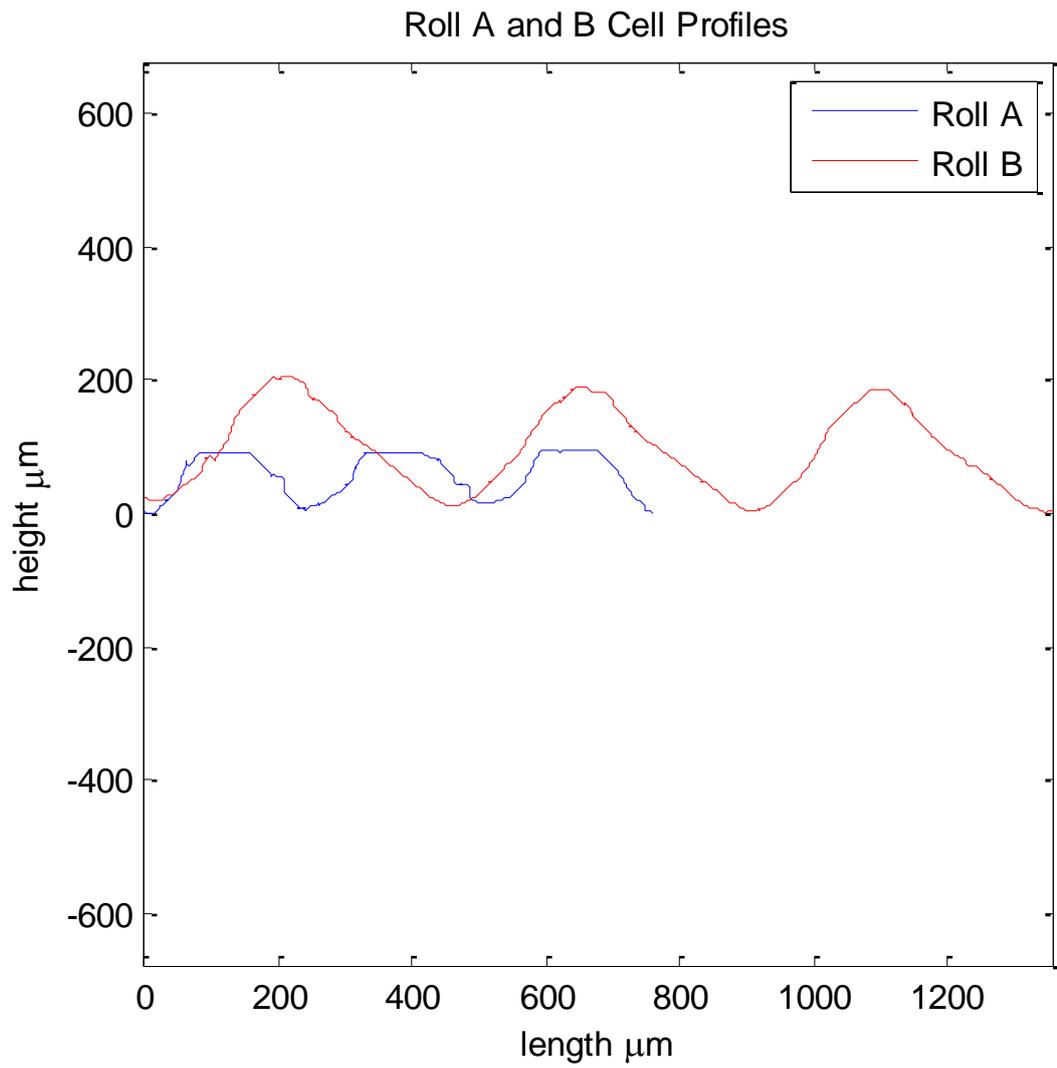
Figure 2.11: Profile plots of Roll A and Roll B spanning three cells.

Roll A
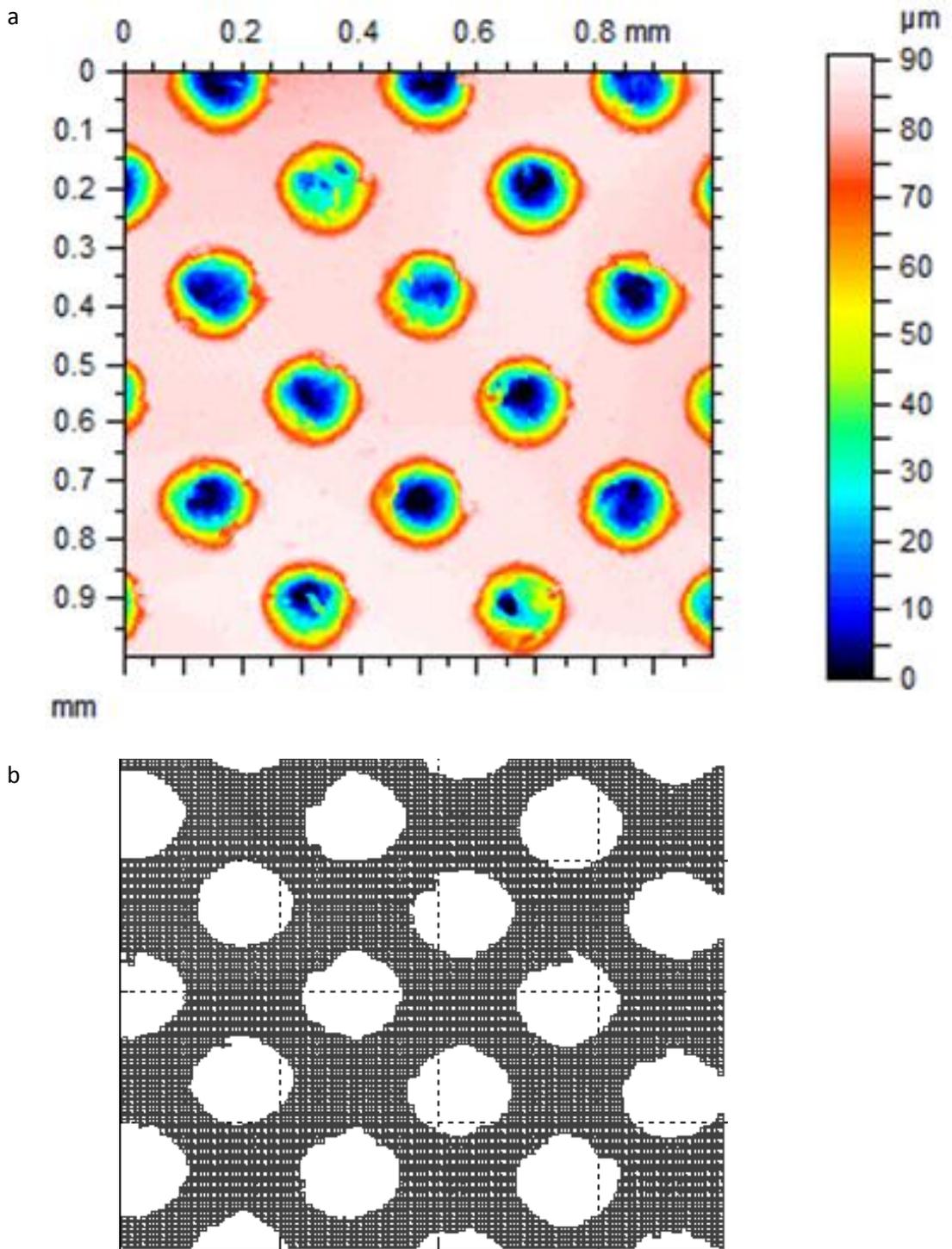
Figure 2.12: Contour plot of Roll A (a) which has been levelled such the highest point of the land is at 90 µm. Part b shows the gravure surface with all but the top layer digitally removed, note that the land is smooth and complete everywhere.

Roll B

a

b
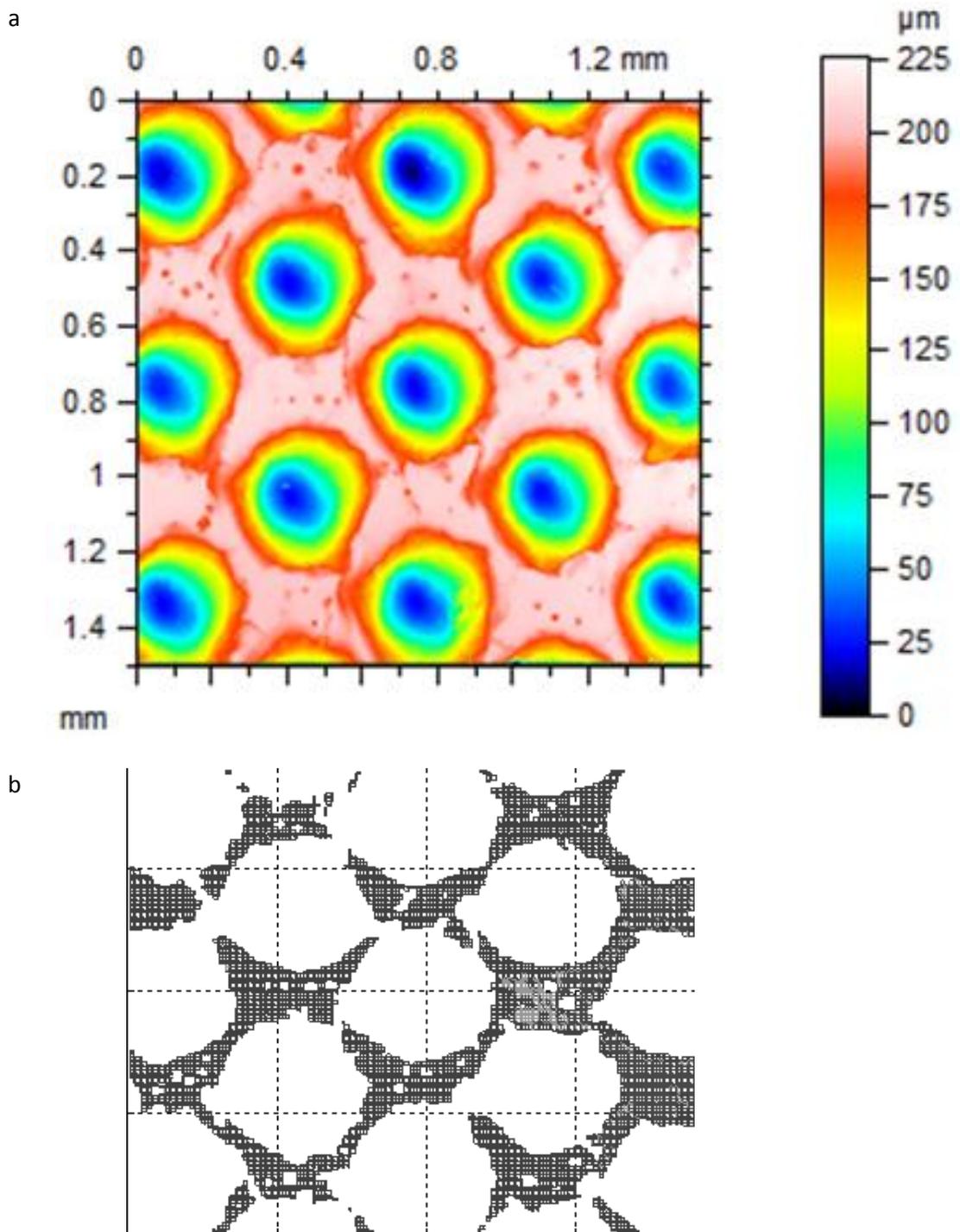
Figure 2.13: Contour plot of Roll B (a) which has been levelled such that the highest point of land is at 225 μm. Part b shows the surface with all but the top layer of land digitally removed. The land at this surface is rough and most of the space is occupied by the cell area.

2.4   Experimental Method

The experimental procedure was designed to measure the fluid transferred from the roll to the web by each gravure at a given speed ratio. The method used was similar to the one used by Kapur (2003). However, the experimental method here is linked with greater detail of the gravure surface than is found in prior literature. The gravures are not new and have an unknown amount of surface wear. The imaging data gathered in section 2.3 is used to account for this, where typically manufacturer's data would suffice.

The coating apparatus was set up with the web tension set to 1000 N/m, the roll speed 0.5 m/s, the web speed varied to achieve the desired speed ratio (0.5-1.25) and the test fluid used was a 20% glycerol/water mixture. The doctor blade was fixed in a 30° (Figure 2.3) leading orientation with the suspending weights causing a force of 4000 N/m (note that this is 400 N spread along the 10 cm web width) at the gravure surface. The web was 23 μm thick and 10 cm wide. The wrap angle was set to 2.5°.

Coat weight was measured by placing a rubber scraper against web such that the web was pushed against an idle roll. The fluid would then drain under gravity into a funnel and finally a beaker for measurement. At the start of each test a period was required for the process to reach steady state which could be visually judged. The test time (**T**) duration was two minutes. The captured fluid could then be measured to determine the transferred fluid mass along an area of web ($0.1 \times l_{web}$) and therefore the film thickness (**t**) can be calculated for a known density, ρ, (equations 2.1 and 2.2). The pickout ratio, ϕ, was then determined using equation 2.3 where the cell volume, V_{cell}, is a measured quantity. Enough repeats of each test were done to establish the experiments were in agreement with similar published data [(Benkreira & Patel, 1992), (Kapur, 2003)].

$$t = \frac{m_{fluid}}{\rho \times 0.1 \times l_{web}} \qquad\qquad 2.1$$

$$l_{web} = U_{web}\mathbf{T} = U_{roll}S\mathbf{T} \qquad\qquad 2.2$$

$$\phi = \frac{t}{V_{cell}} \qquad\qquad 2.3$$

2.5   Results

Results were obtained over a speed ratios range of 0.5 to 1.25 and have been presented in Figure 2.14 and Figure 2.15. The speed of the gravure roll was maintained at 0.5 m/s and the web speed was varied from 0.25 m/s to 6.25 m/s. Above a speed ratio of 1.5 it is likely that air entrainment effects (pockets of air being drawn into the coating bead) can occur. These were beyond the scope of the numerical model and, hence, this formed the upper limit of the experimental range.

Both rolls A and B show a linear pickout ratio against speed ratio gradient. At a speed ratio of 1 rolls A and B have a pickout of approximately 0.36 and 0.3 respectively.

The cell shape is described by the aspect ratio (cell radius at the gravure surface divided by cell depth) which for Roll A is 0.94 and Roll B is 0.86. The cell details are summarised in Table 2:1 showing that the opening diameter of A is half that of B (0.15 mm versus 0.3 mm) and likewise for the cell depth (0.08mm versus 0.175mm).

The film thickness increases with increasing speed ratio. This gradient of film thickness versus speed ratio is greatest below a speed ratio of 1 after which the gradient is reduced.

At a speed ratio of one Roll B produced a film thickness twice as large as that for Roll A. The volume per unit area for Roll B is also 2.6 times that of Roll A while a single cell of Roll B is nearly 10 times larger than one from Roll A. The film thickness, therefore, appears to be more closely related to the total volume per unit area on the roll rather than the volume of each cell.

Early experimental studies conducted by Benkreira and Patel (1993) showed that a pickout ratio of 1/3 is typical for gravure coating with deviation from this only occurring at very low Reynolds numbers. A comparison is also drawns between this work and that of Kapur (1999) which is summarized in Table 2:2. The surfaces of the compared rolls were a laser engraved ceramic and have similar cell volumes, surface volumes and characteristic length.

Table 2:2: Comparison between film thickness results in this work and in Kapur (1999) for two garvures (Roll A top row, Roll B bottom row).

This Work		Kapur (1999)	
Surface Volume	Film Thickness	Surface Volume	Film Thickness
14×10^{-6} m^3/m^2	5×10^{-6} m	26×10^{-6} m^{3}m^{-2}	6×10^{-6} m
37×10^{-6} m^3/m^2	11×10^{-6} m	31×10^{-6} m^{3}m^{-2}	9×10^{-6} m

Kapur (2003) found the most sensitive operating parameter is speed ratio which forms a nearly linear relationship with pickout ratio so long as the coating bead is not suffering from starvation/flooding effects which occur when speed ratio approaches unity/zero. This near linear trend is also observed in this work, noting as well that the bead does not reach a starvation/flooding condition over the tested speed ratio range.
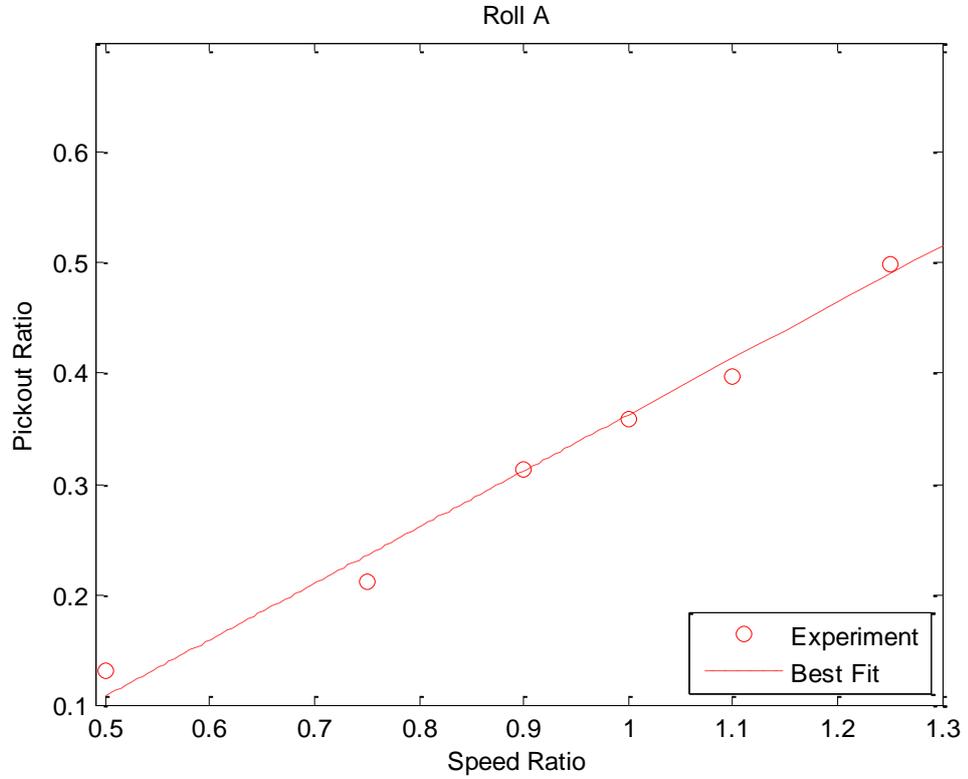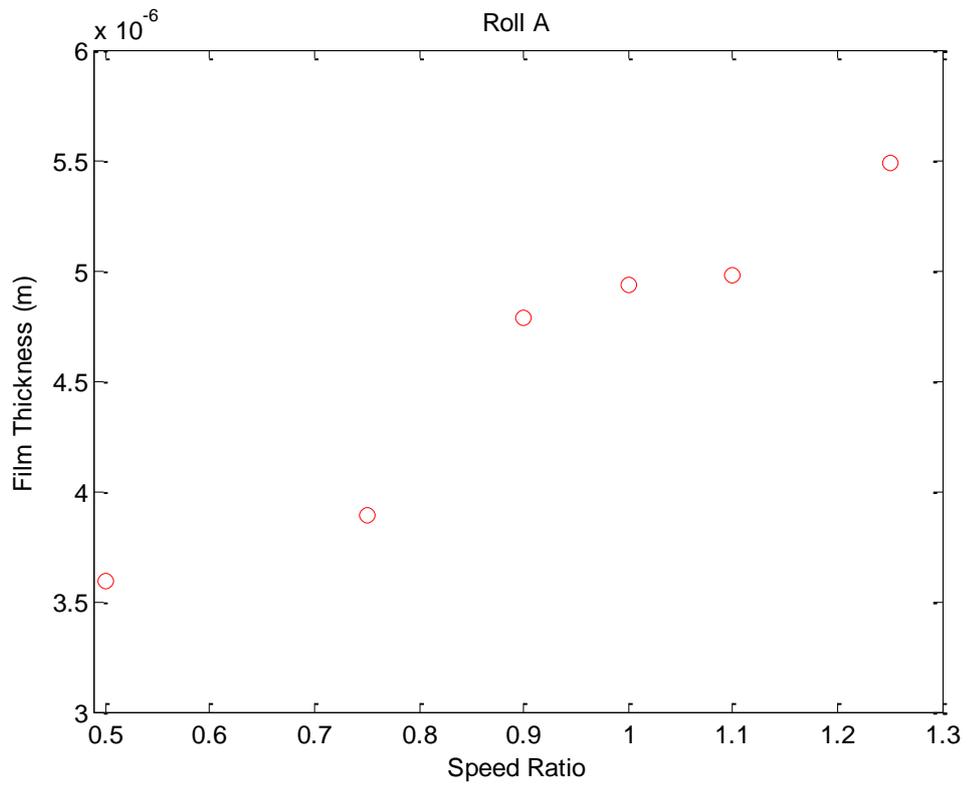
Figure 2.14: Roll A plots of film thickness (top) and pickout ratio (bottom) against speed ratio.
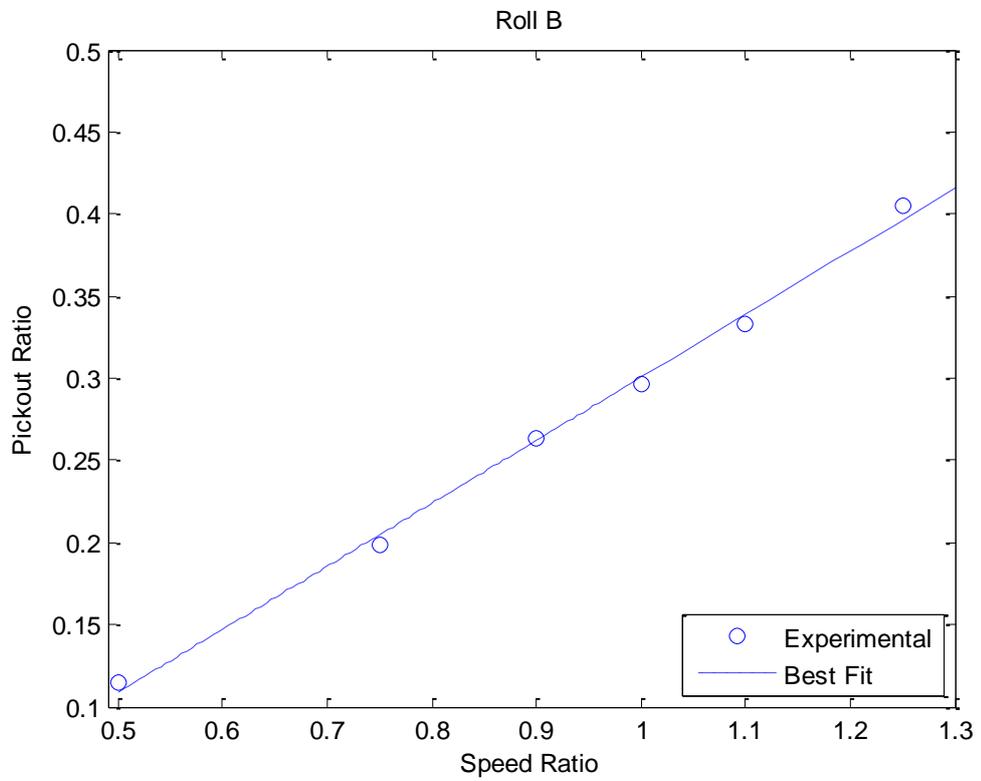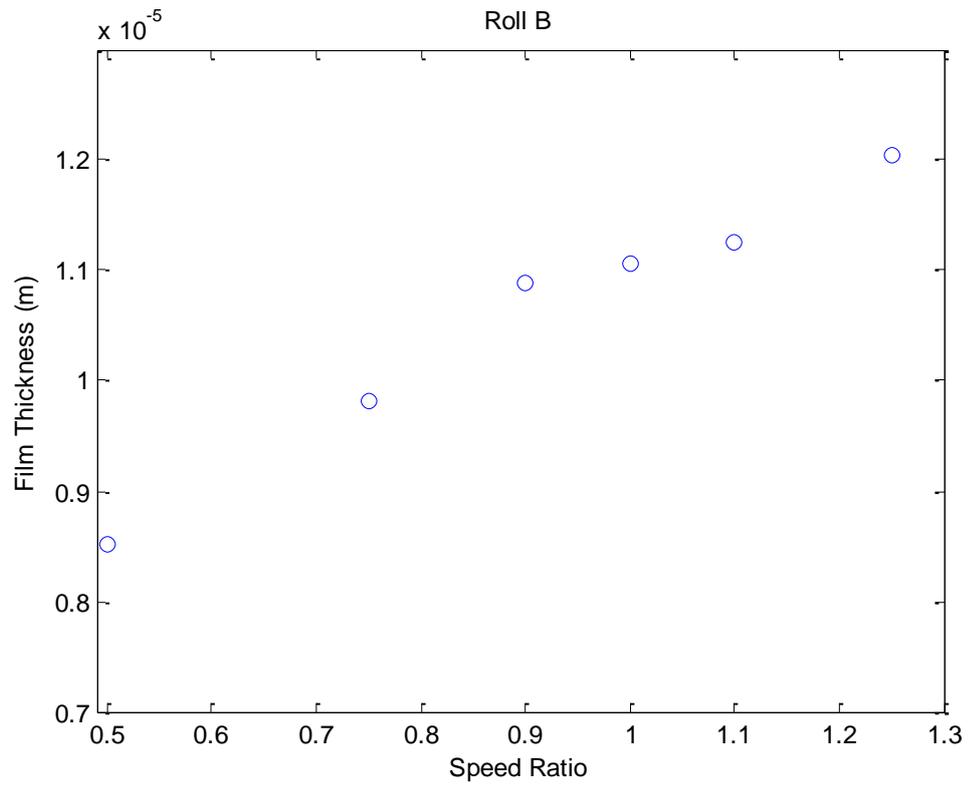
Figure 2.15: Roll B plots of film thickness (top) and pickout ratio (bottom) against speed ratio.

2.5.1 Scratching Observations

Scratches on the web appeared downstream of the coating nip. They became visible when the fluid coated onto the web was allowed to evaporate off rather than removal via the rubber scraper. In order to confirm that the scratches were not due to the web contacting any components other than the gravure the web was removed directly over the coating head such that one portion was upstream of the gravure (uncoated) and a second portion was downstream (coated). This was accomplished by using the emergency stop which applies breaks to bring the gravure and the web handling rotors to an immediate stop. A section of uncoated and coated web can be directly compared showing scratches only downstream of the gravure. The scratches were parallel to each other and could be found along the length of the coated web indicating that they have a common mode of formation (the rotating gravure). A typical length was of several millimetres with some variation between Roll A and B as well as with speed ratio.

During the coating process it was also observed that the coating apparatus was in smooth operation with no erroneous vibrations. The doctor blade was fully worn-in and the coating fluid was clean, containing no particles.

The white light interferometer image seen in Figure 2.16 depicts an arbitrary scratch. The depth was found to be very small (1-5 microns) while the length was on the millimetre length scale. It was clear that the scratch was in the web and not on the newly applied surface coating. The scratches form a trough bounded by two ridges (see Figure 2.16) suggesting that the web material was (at least partially) plastically pushed aside to form the trough rather than being mechanically removed from the web. Inspection of an un-coated web showed no signs of scratches. It was concluded that the scratches occur due to the gravure, noting as well that the ceramic gravure is several orders of magnitude harder than the web.
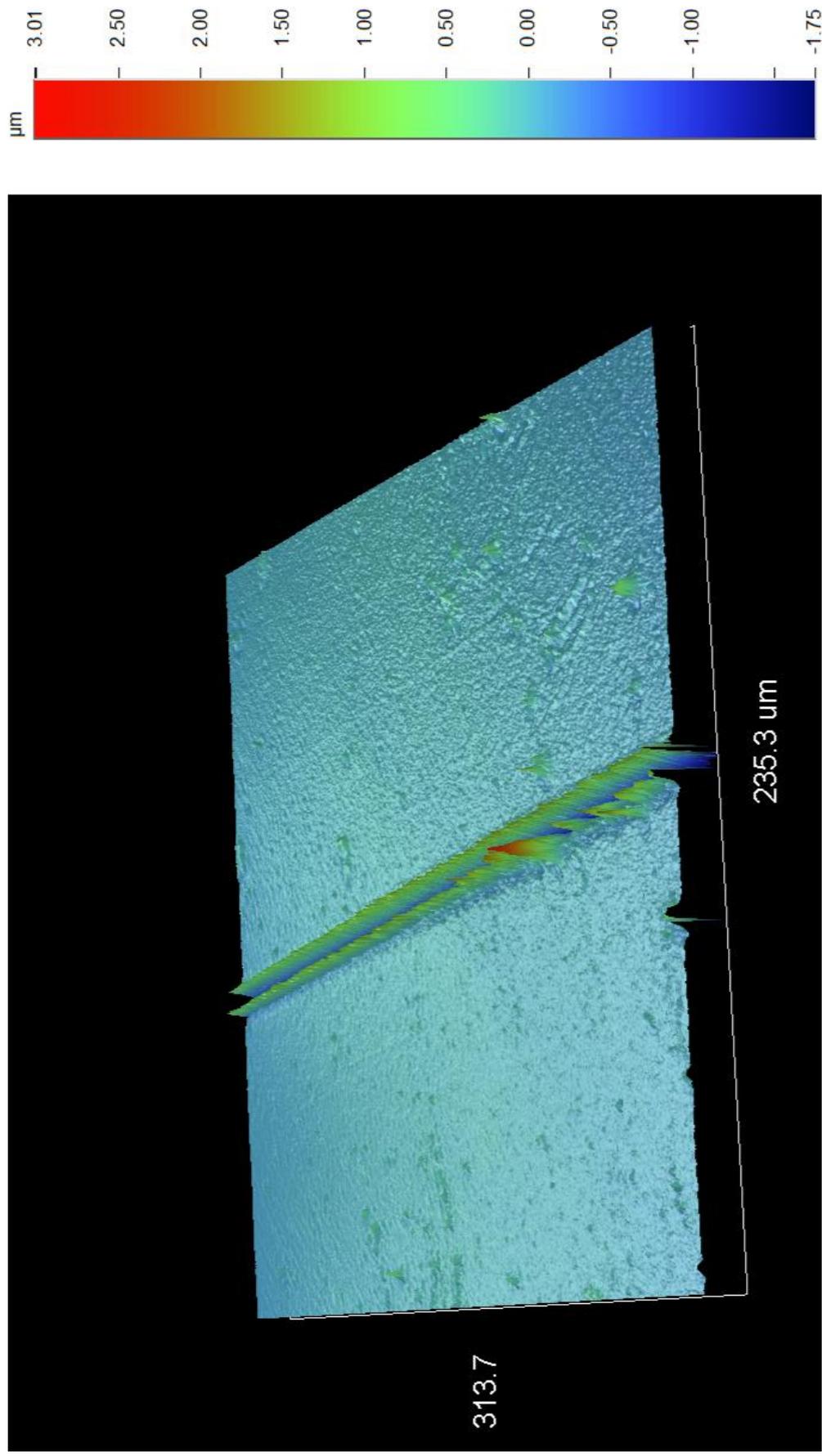
Figure 2.16: Depicts a typical scratch. The vertical displacement is stretched for visual effect.

2.6   Discussion

The results in this section confirm what was already well documented in the literature. Both rolls show a linear relationship between pickout ratio and speed ratio. Earlier work by Kapur (2003) also observed a linear relationship with some curvature appearing as pickout ratio approached both zero and one. On a cell scale this indicates that more fluid is being removed from each cell as the speed ratio increases. This corresponds to an increase in film thickness. The gradients of pickout ratio and film thickness differ due to the coated surface area increasing as speed ratio increases (i.e. more web is being drawn through the coating bead as speed ratio increases). So even though more fluid is removed from each cell, that fluid has an increased area to cover.

The pickout ratio for rolls A (0.36 at a speed ratio of 1) and B (0.3 at a speed ratio of 1) was typical of what is found in the literature (Benkreira & Patel (1993), Kapur (2003)). The aspect ratio (cell radius over cell depth) for Roll A is 0.94 and Roll B is 0.86. Much of the literature ties the pickout ratio to the cell shape and specifically the aspect ratio (Figure 2.17). Shallow broad cells have been noted to empty better which corresponds to what is seen here with Roll A having a larger aspect ratio and a larger pickout ratio.
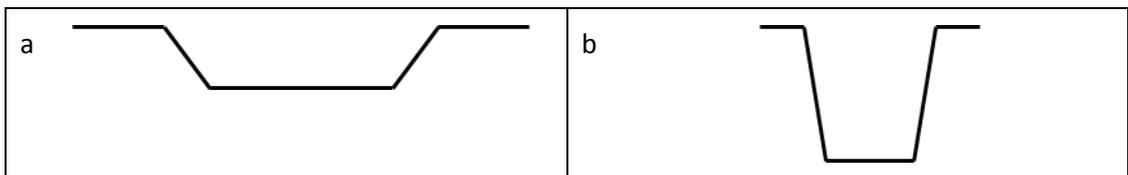
Figure 2.17: Cross-sections of a shallow broad cell (a) and a narrow deep cell (b). Cell a is an example of a high aspect ratio cell and will have a higher pickout ratio. Cell b is an example of a low aspect ratio cell and will have a low pickout ratio.

The difference in film thickness between rolls A and B is tied to the total volume per unit area rather than just the cell volume. This is supported by the change in volume per unit area correlating with the change in film thickness. Cells on Roll B had nearly 10 times more volume than those on

Roll A yet the film thickness was only two times larger from Roll B (at a speed ratio of 1). If film thickness were only related to the volume of a cell then there should be a larger corresponding difference between rolls A and B, but this is not the case.

The observed scratches were unavoidable in the direct gravure coating process. They indicate contact between the web and the gravure. The regular nature of the scratches suggests that they were not caused by large web vibrations (one would also expect periodic 'rows' in the film coating thickness which was not observed). It is likely either:

- the coating bead is sufficiently thin to allow high points on the gravure surface to periodically pierce it and scratch the web,
- or the pressure in the coating bead is insufficient to support the web and is in continuous contact with the roll with a noticeable scratch occurring due to some surface feature.

The presence of web scratching and pickout ratios that are consistent with the literature suggest that the scratching phenomena may be functional in the coating process. It also poses questions about fluid transfer in the coating bead. Contact on a smooth roll coater (assuming it is uniform and steady) would prevent any fluid flow between the up and downstream portions of the coating bead. However, the presence of gravure cells complicates this as fluid can still be transported via the cells while the roll and web are in contact.

2.7   Conclusion

The purpose of this experimental work was to provide a result against which a numerical model could be validated. Pickout ratio shows a constant near linear trend between the two rolls making it a useful metric for establishing correlations between experimental and numerical results.

The fluid transfer process is strongly tied to the surface volume of the roll rather than just the cell volume. This means an accurate measure of the characteristic length is important. The numeric model uses the characteristic length to make length units non-dimensional. Correct use of the characteristic length will remove the need to numerically represent the whole surface. When comparing a single cell in a non-dimensional sense the volume then becomes very significant and can be used as a means to distinguish one roll from the next.

Cell shape is tied to pickout ratio. Specifically, maintaining the aspect ratio of the cell is important in order to predict its pickout correctly.

The scratches on the web indicate that there is consistent contact between the roll and web but these experiments did not elucidate a specific mechanism/cause. As the contact suggests that the web is being at least partially supported, a means of accounting for it is a benefit to a numerical model.

Chapter 3   Numerical Formulation

3.1   Introduction

This chapter describes the formulation of a predictive computational model for discrete cell gravure roll coating. The model uses a two-scale approach where the large scale describes fluid flow through the coating bead and the small scale describes flow at a cell level. The progression of these length scales is illustrated in Figure 3.1 noting as well that in the laboratory scale there is also a gravure roll width component which is on the order of meters. First, theory behind multi-scale modelling is outlined followed by the formulation of the two scales.
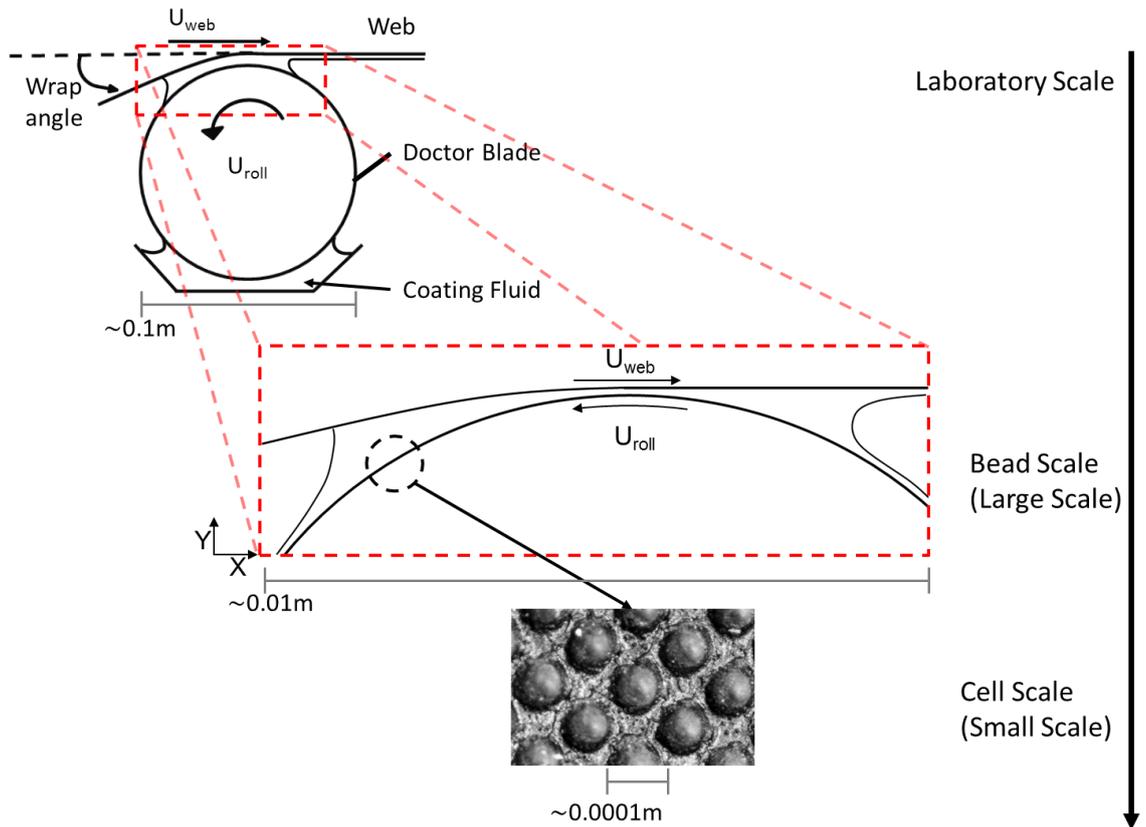
Figure 3.1: A schematic of length scales being modelled where the laboratory scale involves the entire apparatus, the bead scale is measured from the upstream to the downstream meniscus and the cell scale is that of a single cell.

3.2 Multi-scale Theory

A multi-scale approach is designed to describe problems that require mathematical descriptions of the problem on disparate spatial or temporal scales (E, Bjorn, & Zhongyi, 2003), (E, et al., 2007). The large scale defines the region of interest but the mathematical description is not explicit; it is either not valid everywhere or incomplete. The method assumes there is access to an accurate model on a smaller scale (temporal or spatial). The small scale can therefore be used to estimate the missing information at the large scale. This is made possible by the two scales sharing a given state variable.

The small scale is solved subject to boundary conditions that are set by the large scale. While these vary from one problem to the next, here, they are set by a periodic homogenization throughout the small scale. This means that the small scale contains a unit that repeats at regular intervals (i.e. periods) and as such can be homogenized by considering a unit with periodic boundaries.

In the case of gravure roll coating the region of interest in this investigation is the coating bead as this is where fluid transfer from roll to web occurs. The quantity of interest is the amount of fluid transferred to the web. In the event the roll is smooth it can be analytically solved using lubrication theory. However, the presence of the gravure cells precludes this due to the rapidly changing topography inducing complex fluid flow through the bead that is not appropriate to the lubrication assumptions (see section 1.3.1 for lubrication assumptions). A description of the fluid flow is therefore missing on the bead length scale. However, accurate models can be formulated on the cell length scale using Computational Fluid Dynamics (CFD).

In order to couple the state variables the large scale must first be written in mathematical terms. This is done by the system of ordinary differential equations in section 3.4.2. These equations are missing information that prevent them being solved (information, in this case, refers to the details of how the coating fluid is affected by the gravure topography). This information

is of the small scale and is defined in section 3.6. The small scale information is conveyed to the large scale via a lookup table. The problem can now be viewed as two distinct parts; that is the large scale defining the flow through the coating bead and the small scale pertaining to the flow through a cell.

3.3 Model Formulation

The formulation has been presented in two parts; the large scale (Figure 3.2) which considers the fluid in the coating bead and the small scale (Figure 3.3) which considers the fluid in a single cell. The large scale is described in section 3.4 and the small scale is dealt with in section 3.6.

The schematic in Figure 3.2 shows the large scale problem being considered, where the velocity of the web is given by U_{web}, the velocity of the roll is given by U_{roll}. R is the radius of the roll, G is the web-to-roll gap and H is the vertical distance from top dead centre of the roll to the web.
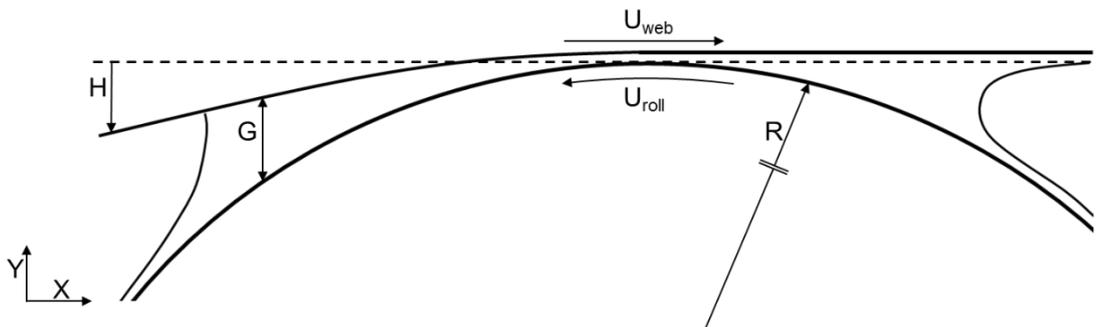
Figure 3.2: Cross section of the coating bead. This forms the large scale domain and neglects the explicit definition of the gravure cells.

The small scale problem is shown in Figure 3.3 where the web-to-roll gap is G and is measured from the gravure land to the web, the cell opening radius is R_0 and the cell depth is D. The characteristic length is the sum of L_1, L_2 and L_3 (Equation 3.1) and the periodic boundaries are shown. For an ideal roll the components L_1 and L_3 should always be equal.
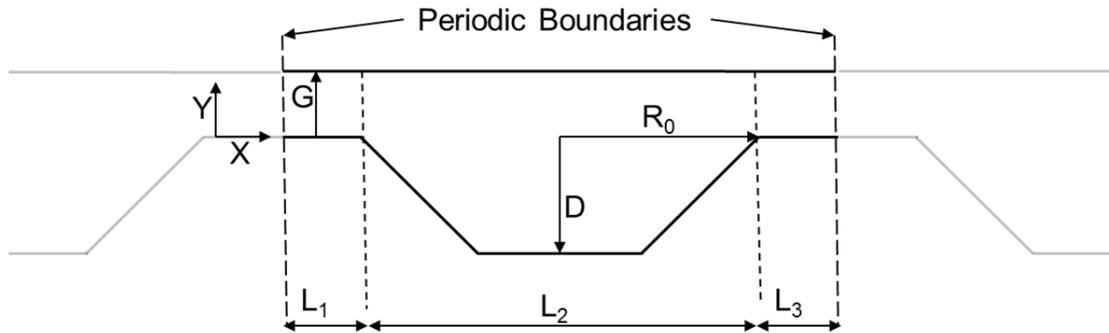
Figure 3.3: Cross section of a gravure cell forming the small scale domain. The sum of L1, L2 and L3 forms the characteristic length, the boundaries of which are periodic.

$$L = L_1 + L_2 + L_3 \qquad \textbf{3.1}$$

Where L is the distance from one periodic feature (e.g. a cell) to the next.

To simplify the formulation the parameters have been reduced to dimensionless quantities:

$$\frac{U_{web}}{U_{roll}} = S \qquad \textbf{3.2}$$

$$\frac{\{R, R_0, D, G, H, X, Y\}}{L} = r, r_0, g, h, x, y \qquad \textbf{3.3}$$

$$\frac{PL}{\eta U_{roll}} = p \qquad \textbf{3.4}$$

$$\frac{T}{\eta U_{roll}} = t \qquad \textbf{3.5}$$

$$\frac{Q}{L U_{roll}} = q \qquad \textbf{3.6}$$

The dimensional quantities are denoted by the capital letters and their dimensionless counterparts are denoted by lower case. S is the web-to-roll speed ratio, X and Y are axis coordinates in the tangential and radial roll directions (Figure 3.4). The fluid properties have also been made non-dimensional where P is the fluid pressure, T is the web tension, Q is a volumetric flow rate and η is the fluid viscosity.
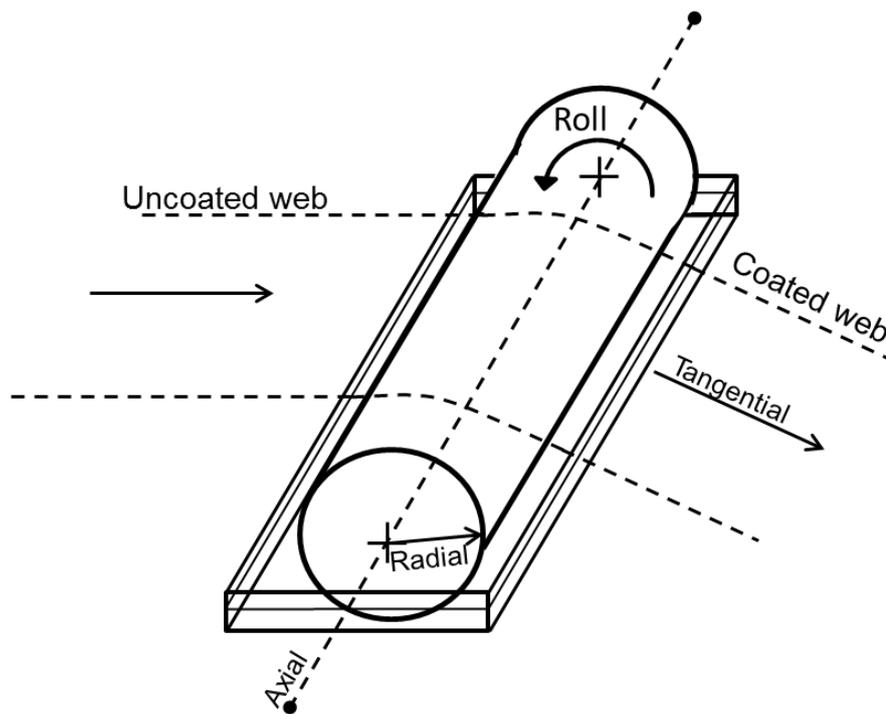
Figure 3.4: Roll and web direction definitions.

3.4 Large Scale: Theory

3.4.1 Fluid Regime

The fluid regime is governed by the cell length scale and on this scale viscous forces dominate (inertial forces are considered negligible). Under such conditions the Navier-Stokes equations of fluid flow reduce to the linear Stokes flow (3.7). Further the fluid is assumed Newtonian and incompressible allowing for the simplified conservation of volume in Equation 3.8.

$$\eta \nabla^2 \mathbf{u} - \nabla p = 0 \qquad \textbf{3.7}$$

$$\nabla \cdot \mathbf{u} = 0 \qquad \textbf{3.8}$$

The length of the coating bead in the direction of the moving web (x-direction) is on the order of millimetres while its width is on the order of metres at industry scales and is 10 cm at laboratory scales. This means most of the bead is insensitive to edge effects and can be well approximated in two dimensions (length, x, and height, y, see Figure 3.2).

The fluid transport mechanism in the large scale is solely driven by the web and roll which act in the positive and negative x-direction respectively and therefore the local velocity only varies with the distance from these surfaces and the induced pressure gradient. The pressure gradient in the x-direction can then be written in terms of the flow rate, q_x, and the web-to-roll gap (Equation 3.9).

$$\frac{dp}{dx} = f(q_x, g) \qquad \textbf{3.9}$$

3.4.2   Governing Equations of the Coating Bead

The governing equations in the large scale are derived to describe the fluid flow between a rigid curved surface (the gravure) and a flexible web. Attention is first focused on deriving the pressure gradient across the fluid domain of Figure 3.2. For the derivation process the roll will be considered smooth (the complexity of the cells will be addressed after). In the literature review (Section 1.3.1) a derivation of lubrication theory arrived at equation 3.10 which relates fluid flow rate, Q_x, to the pressure gradient, $\frac{\partial P}{\partial x}$, and the relative motion of the web (U_w) and gravure (U_g) surfaces.

$$Q_x = -\frac{G^3}{12\eta}\frac{\partial P}{\partial x} + \frac{G}{2}\left(U_w - U_g\right) \qquad \textbf{3.10}$$

Making the equation non-dimensional according to 3.2 - 3.6 gives Equation 3.11:

$$q_x = -\frac{g^3}{12}\frac{\partial p}{\partial x} + \frac{g}{2}S - \frac{g}{2} \qquad \textbf{3.11}$$

The coefficients $-\frac{g^3}{12}$, $\frac{g}{2}$ and $-\frac{g}{2}$ are therefore representative of a smooth roll coater. They do not apply to a gravure roll and therefore in the large scale these coefficients are not explicitly known (these are the missing information described in the previous section). They can be replaced by the unknown coefficients a, b and c which are some function of the web-to-roll gap (g) giving Equation 3.12.

$$q_x = a\frac{\partial p}{\partial x} + bS + c \qquad \textbf{3.12}$$

Secondly, attention is turned to the flexible web. The web curves in response to the fluid pressure as well as the web tension. The web is thin and can be treated as a membrane under tension, t, (Storey, 1996). This leads to a force balance between the web tension and the difference in fluid pressure either side of the web yielding Equation 3.13:

$$\Delta p = -\kappa t \qquad\qquad \textbf{3.13}$$

In Cartesian coordinates the curvature of a line can be written as Equation 3.14.

$$\kappa = \frac{\dfrac{d^2 y}{dx^2}}{\left(1 + \left(\dfrac{dy}{dx}\right)^2\right)^{\frac{3}{2}}} \qquad\qquad \textbf{3.14}$$

The fluid in the coating bead can now be described by the three differential equations 3.15, 3.16 and 3.17. Equation 3.15 relates the pressure gradient across the coating bead, the web-to-roll speed ratio and the large scale flux term, q_x. The coefficients a, b and c represent the missing information at the large scale and are a function of the web-to-roll gap (g). They are determined from the small scale but can be analytically approximated using lubrication theory (see section 1.3.1). The coefficients are supplied to the large scale via a lookup table.

$$\frac{dp}{dx} = \frac{q_x - Sb(g) - c(g)}{a(g)} \qquad\qquad \textbf{3.15}$$

$$\frac{dq}{dx} = 0 \qquad\qquad \textbf{3.16}$$

$$\frac{d^2 h}{dx^2} = \frac{p}{t} \times \left(1 + \left(\frac{dh}{dx}\right)^2\right)^{\frac{3}{2}} \qquad\qquad \textbf{3.17}$$

The pressure gradient in the length of the coating bead is given by $\frac{dp}{dx}$, S is the web-to-roll speed ratio. Conservation of volume (equation 3.16) dictates that under steady state conditions the change in flow rate through the coating bead remains equal to zero (the fluid is assumed incompressible, hence conservation of mass is implied). Finally, equation 3.17 describes the curvature of the web where h is the vertical distance from the web to the roll surface and $h = 0$ was chosen arbitrarily to be at the top dead centre of the roll, t is the tension in the web.

The web to roll gap (g) is calculated using equation 3.18 where the surface of the gravure roll is approximated by a parabola based on the roller radius, r.

$$g = h + \frac{x^2}{2r}$$
<div align="right">**3.18**</div>

3.4.3   Boundary Conditions

To close the problem six boundary conditions are required because as the initial position of the menisci are unknown the problem is solved in a moving coordinate frame which is described in section 3.5.1. Each boundary condition is implemented at the upstream (us) and downstream (ds) meniscus locations shown in Figure 3.5. Equations 3.19 and 3.20 are used to set the wrap angle, β, of the web entering and leaving the coating bead.
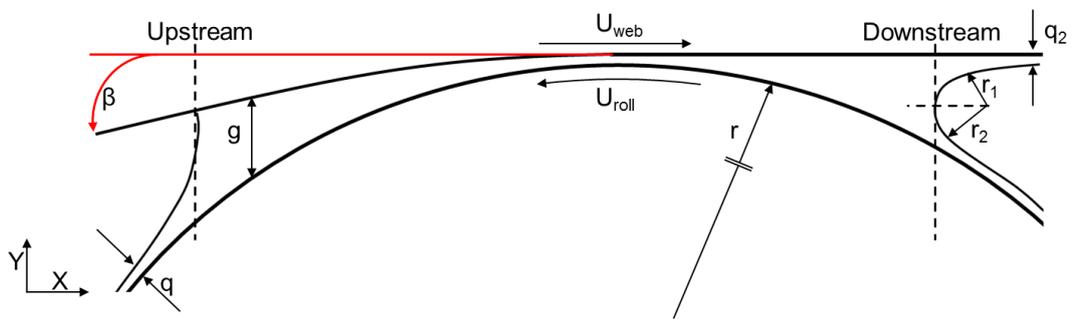
Figure 3.5: Location of the up and downstream boundary conditions. The wrap angle β is the upstream wrap angle. In practice the wrap angle is applied at the upstream while at the downstream it is equal to zero.

$$\frac{dh}{dx_{us}} = -\beta \qquad\qquad \textbf{3.19}$$

$$\frac{dh}{dx_{ds}} = 0 \qquad\qquad \textbf{3.20}$$

The location of the meniscus is not a known parameter but is approximated by relating the meniscus radius of curvature to the web-to-roll gap and the simplifying assumption of a 90 degree contact angle. This radius of meniscus curvature is approximated using the Bretherton equation (1961). The x axis relates to the web-to-roll gap via equation 3.21 which has been rearranged from equation 3.18. The menisci locations are then given by equations 3.23 and 3.25 where the web-to-roll gap at the upstream and downstream locations is specified in equations 3.22 and 3.24 which are

derived from equation 1.21 in the literature review. The terms in equations 3.21 to 3.25 are defined in Figure 3.5 and relate to the subscripted meniscus location upstream (us) or downstream (ds).

$$x = \sqrt{2r(g - h)} \qquad \text{3.21}$$

$$g_{us} = \frac{q}{1.34(Ca)^{\frac{2}{3}}} \qquad \text{3.22}$$

$$x_{us} = -\sqrt{2r\left(\frac{q}{1.34(Ca)^{\frac{2}{3}}} - h\right)} \qquad \text{3.23}$$

$$g_{ds} = \frac{2q_2}{1.34(SCa)^{\frac{2}{3}}S} \qquad \text{3.24}$$

$$x_{ds} = \sqrt{2r\left(\frac{2q_2}{1.34(SCa)^{\frac{2}{3}}S} - h\right)} \qquad \text{3.25}$$

Where q_2 is the volumetric flow rate leaving on the web and is equal to the difference between the volume of fluid entering the coating bead (determined by cell volume and roll speed) and that moving through the coating bead (from equation 3.16). The capillary number is defined by $Ca = \frac{\eta U_{roll}}{\gamma}$, where γ is the surface tension. At the upstream meniscus there is only one wetted surface and therefore only one radius of curvature. At the downstream there are two wetted surfaces, that from the fluid entering the bead on the roller and that which is leaving on the web. The two components, r_1 and r_2, in Figure 3.5 represents these two radii of curvature and are measured from the point of film splitting. In equation 3.25 these two components are assumed to be equal to the radius formed by the meniscus and the web.

The final two boundary conditions arise from the Young-Laplace equation which specifies the pressures at the menisci (Landau & Levich, 1942) and

again the radius of meniscus curvature was approximated by the web-to-roll gap. The surface tension (γ) component of the Young-Laplace equations was made non-dimensional with the product of viscosity and roller velocity leaving it in terms of the capillary number.

$$p_{us} = \gamma \times \frac{1}{r_{us}} = \frac{\gamma}{\eta U_{roll}} \times \frac{1}{r_{us}} \cong \frac{1}{Ca} \times \frac{1}{g} \qquad \textbf{3.26}$$

$$p_{ds} = \gamma \times \left(\frac{1}{r_1} + \frac{1}{r_2}\right) = \frac{\gamma}{\eta U_{roll}} \times \left(\frac{1}{r_1} + \frac{1}{r_2}\right) \cong \frac{1}{Ca} \times \frac{2}{g} \qquad \textbf{3.27}$$

3.4.4   Contact Pressure

Contact between the web and roll occurs when the gap closes to zero. Evidence for contact can be seen experimentally as scratches on the web. The scratches can only form when the web is dragged along the roll. At this point the pressure through the coating bead has two components. The first is the hydrodynamic forces of the fluid, p_f. The other is the effect of two contacting solids, p_c. The total pressure supporting the web is the sum of the two components such that the web curvature equation (3.17) takes the form of Equation 3.28.

$$\frac{d^2h}{dx^2} = \frac{p_f + p_c}{t} \times \left(1 + \left(\frac{dh}{dx}\right)^2\right)^{\frac{3}{2}} \qquad \textbf{3.28}$$

Justification for a contact model can be found in the form of experimentally observed web scratching where measuring from the highest to the deepest point of the scratch is on the order of 1s of microns (in Figure 2.16 the depth is 5 µm though this varies along the length of the scratch).

The term p_c grows exponentially as the web-to-roll gap approaches zero and is approximated by Equation 3.29.

$$p_c = 10^{\frac{-g}{0.00001}}$$

<div align="right">**3.29**</div>

Equation 3.29 was constructed to supply a large pressure force term in equation 3.28 when the web-to-roll gap is zero. Similarly the contact pressure term must be negligible wherever the web-to-roll gap is larger than zero. There are other formulations that can approximate this contact but here equation 3.29 will be used throughout.

3.5   Large Scale: Numerical Implementation

3.5.1   Moving Mesh

As the location of the bounding menisci is not known a priori the system of differential equations was solved on a moving mesh in order solve on a constant number of grid points but with a grid spacing that varies between iterations. This moving mesh is defined by equations 3.30 and 3.31 where ζ is the mesh axis and Ψ is the first order derivative of the coating bead axis (x) with respect to ζ. Equations 3.32 to 3.35 are the governing equations written in terms of this coordinate system. The inclusion of equation 3.34 is required to reduce equation 3.35 to a first order differential which was solvable numerically in MATLAB.

$$\frac{d^2x}{d\zeta^2} = 0$$

<div align="right">**3.30**</div>

$$\frac{dx}{d\zeta} = \Psi$$

<div align="right">**3.31**</div>

$$\frac{dp}{d\zeta} = \left[\frac{dp}{dx} \times \frac{dx}{d\zeta}\right] = \Psi\left(\frac{dp}{dx}\right)$$

<div align="right">**3.32**</div>

$$\frac{dq}{d\zeta} = \left[\frac{dp}{dx} \times \frac{dx}{d\zeta}\right] = \Psi \times 0$$

<div align="right">**3.33**</div>

$$\frac{dh}{dx} = \Psi^{-1}\frac{dh}{d\zeta}$$

<div align="right">**3.34**</div>

$$\frac{d\left(\Psi^{-1}\frac{dh}{d\zeta}\right)}{d\zeta} = \Psi\frac{p}{t}\left(1 + \left(\Psi^{-1}\frac{dh}{d\zeta}\right)^2\right)^{\frac{3}{2}}$$

$$\textbf{3.35}$$

3.5.2 Coating Bead Boundary Value Problem

The structure of the coating bead, that is a fluid body which is bound upstream and downstream by a meniscus interface between fluid and air, is well suited to be modelled as a Boundary Value Problem (BVP). Solutions exist to approximate the values at the meniscus locations which form convenient boundary conditions for the BVP.

The solution of a BVP requires a general solution to fully define the problem. When this is implemented numerically it is referred to as an initial guess or initial solution. The BVP can have an infinite number of solutions or alternatively zero and therefore finding a general solution can be difficult.

A sequential solving process was used (Figure 3.6) to obtain an initial guess.

This was accomplished by first relaxing the boundary conditions to represent a flooded system where the meniscus location was an infinite distance away, the pressure and web gradient were set to zero. The ODEs were approximated by initially setting the pressure field to zero everywhere while the web was considered horizontally flat (i.e. also zero everywhere).

After generating the first solution the problem lends itself well to a continuation method. Such methodology greatly increased the stability of the overall simulation. Continuation also serves as a convenient method to simulate over a large parameter space (i.e. increasing/decreasing speed ratio).
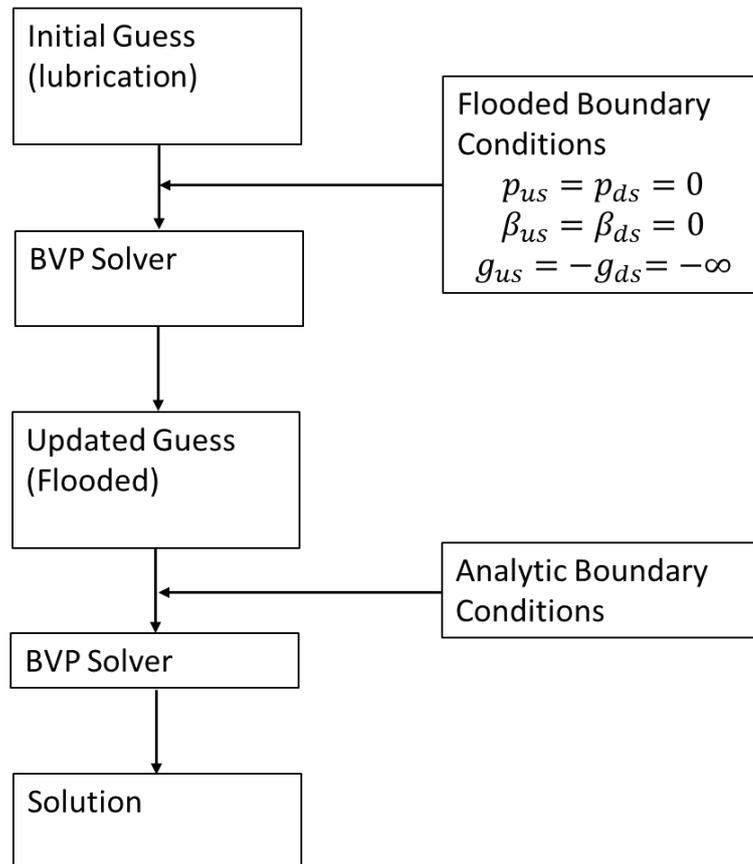
Figure 3.6: Flow chart describing how to obtain an initial solution over the coating bead.

3.6   Small Scale: Theory

The purpose of the small scale model is to estimate the information missing in the large scale (Equation 3.15) thereby facilitating the large scale solution. To do this the small scale needs to be homogenised such that it is valid everywhere on the large scale. This is done by taking advantage of the periodic surface topography found on a discrete cell gravure roll. The small scale then only varies with the web-to-roll gap as shown in Figure 3.7 where g defines the column of fluid above the gravure cell (shown as a square section in Figure 3.7). The characteristic length is the distance from one cell centre to the next and is at least one order of magnitude smaller than the large scale (this varies from one roll to the next and is typically 2 or more orders of magnitude).
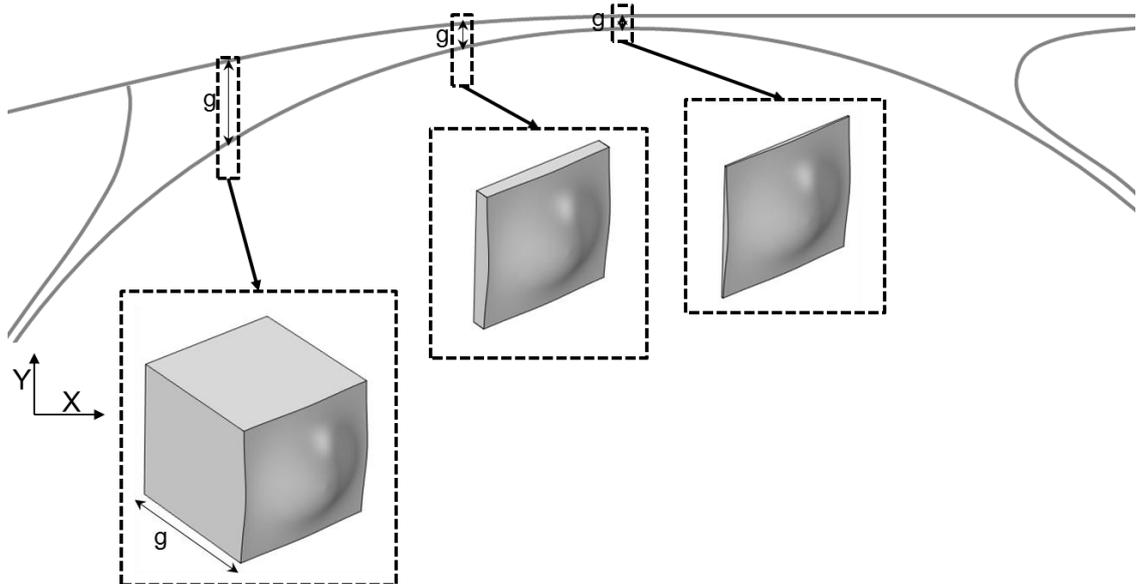
Figure 3.7: Small scale domain (dashed boxes) varying with the web-to-roll gap along the large scale domain.

The small scale model is bound on the upper surface by a smooth web, on the lower surface by a representation of the gravure and finally by four periodic fluid interfaces. The fluid interfaces correspond to the periodic bounds and it is this periodicity that makes the small scale homogeneous.

On the cell length scale inertial forces are negligible and viscous forces dominate, i.e. Stokes flow, an assumption that is commonly applied to problems with a low Reynolds number ($Re = \frac{\rho u_{roll}L}{\eta}$) [(Gaskell et al, 1994), (Gaskell et al 1998), (Hewson et al, 2009)]. Here the Reynolds number is calculated to be 15.7 for Roll A and 32.5 for Roll B.

$Re = \dfrac{\rho u_{roll}\left(\frac{V_{cell}}{A_{cell}}\right)}{\eta} = \dfrac{1000 \times 0.5 \times \dfrac{8.9 \times 10^{-13}}{\pi(75 \times 10^{-6})^2}}{0.0016} = 15.7$	**36**
$Re = \dfrac{1000 \times 0.5 \times \dfrac{7.5 \times 10^{-12}}{\pi(150 \times 10^{-6})^2}}{0.0016} = 32.5$	**37**

Due to the linearity of Stokes flow the flux through the small scale domain only varies with the web-to-roll gap. The flux through the domain is governed by equation 3.38.

$$q_x^* = a(g)\frac{dp}{dx} + Sb(g) + c(g)$$

3.38

The terms a, b, and c vary with web-to-roll gap and Equation 3.38 couples the large and small scales. Equation 3.38 can be solved numerically subject to the boundary conditions in Table 3:1 to simultaneously determine the coefficients. Solutions are sought over the web-to-roll gap range of 0.001-5. The coefficients are then implemented into the large scale via a look up table.

Solving the coefficients subject to the boundary conditions in Table 3:1 requires two simulations for each web-to-roll gap. Solving the pressure driven flow problem (Poiseuille flow) yields coefficient a. Solving the wall driven shear flow (Couette flow) gives coefficient b. The final coefficient, c, can be found analytically based on the domain volume and in the roll centric reference frame is equal to a zero flow condition. When translated into the laboratory frame coefficient c is given by the difference in coefficient b and the domain volume.

Table 3:1: Boundary conditions in the laboratory reference frame for the solution of the small scale coefficients in equation 3.38.

Coefficient	$\dfrac{dp}{dx}$	S
a	-1	0
b	0	-1
c	0	0

3.7   Small Scale: Numerical Implementation

3.7.1   Overview

The purpose of the small scale solutions is to supply missing information about the influence of the gravure cells on the fluid flow to the large scale. Therefore small scale must find an approximate solution to this problem and then communicate it to the large scale. The approximate solution is found using CFD methodology and it is then communicated to the large scale via a lookup table. A flow chart summary is shown in Figure 3.8 of the solution process.

The solution process requires first defining a physical model for the fluid domain (Section 3.7.3) and the representation of the gravure surface (Section 3.7.4). The second step creates a generic baseline mesh and the third step deforms it to the starting shape (Section 3.7.5). The problem is then solved using a Finite Element Method (FEM) using a Multigrid solver (Section 3.7.6). The height of the domain is sequentially decreased and a continuation method is employed until the minimum height of 0.001 is reached (see Figure 3.8). The final step extrapolates the small scale coefficients from a height of 0.001 until the zero flow point (Section 3.7.7). The small scale coefficients are used to populate a lookup table for use in the large scale.

```
┌─────────────────────┐
│   Physical Model    │
└─────────────────────┘
          │
          ▼
┌─────────────────────┐
│  Create Baseline Mesh │
└─────────────────────┘
          │
          ▼
┌─────────────────────┐
│  Deform Mesh to     │
│  Topography and Height=5 │
└─────────────────────┘
          │
          ▼
┌─────────────────────┐
│  FEM: Solve for a, b │ ──────────────────────────┐
│  and c              │                            │
└─────────────────────┘                            │
          │                                        │
          ▼                                        │
       Height=0.001                                │
┌──────────────┐   ┌────┐  ◇                       │
│ Reduce height │◄─│ No │◄─ Height=0.001            │
└──────────────┘   └────┘                          │
          │                                        │
          ▼ Yes                                    │
        ┌─────┐                                    │
        │ Yes │                                    │
        └─────┘                                    │
          │                                        │
          ▼                                        │
┌─────────────────────┐                            │
│  Extrapolate to Zero │ ──────────────────────────┤
│  Flow Condition     │                            │
└─────────────────────┘                            │
                                                   ▼
                                    ┌──────────────────────┐
                                    │  Record in lookup table │
                                    └──────────────────────┘
```
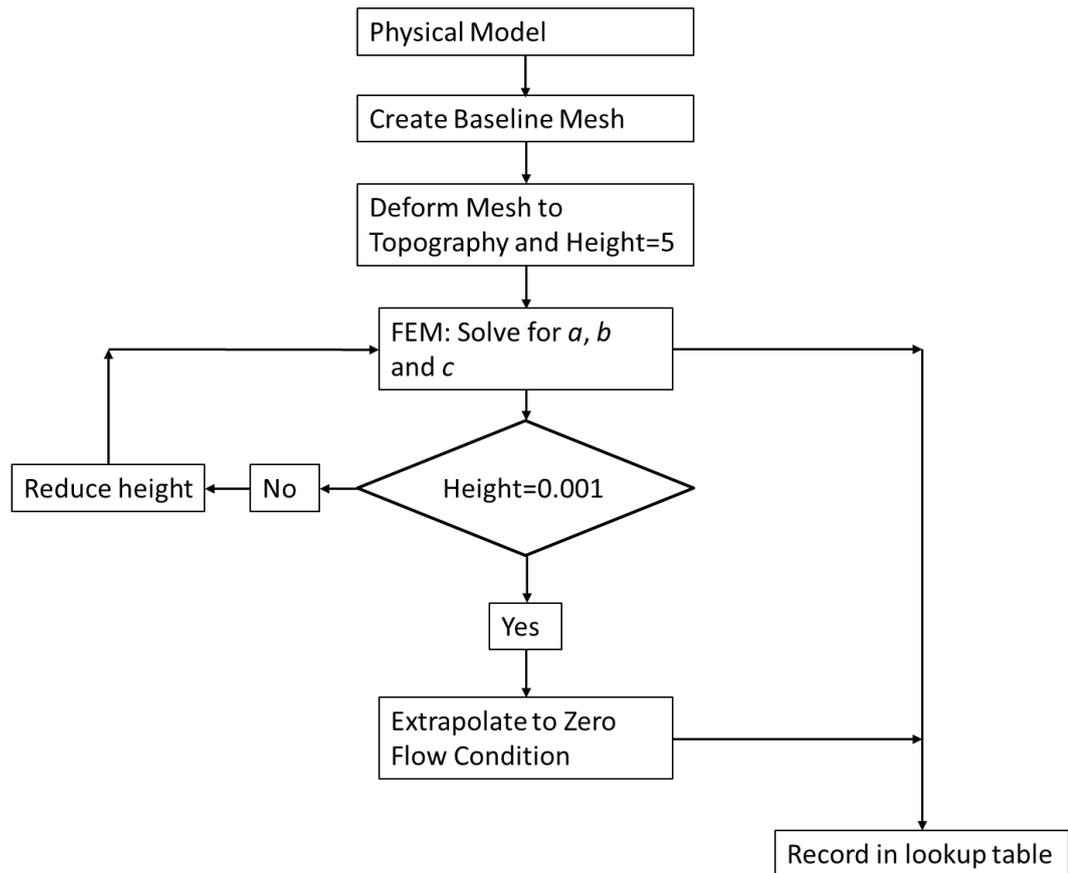
Figure 3.8: Flow chart summarizing the small scale solution process.

3.7.2 The Small Scale Reference Frame

The cell domain has two moving surfaces, the roll and the web. In order to avoid modelling a moving topographical surface a change in reference frame is required that will separate how the large scale and small scale are considered.

In the laboratory frame of reference (large scale) the web and roll move in opposing motion relative to each other. Changing the reference frame to one which is roll centric (small scale) allows the roll to be modelled as stationary with a moving web (Figure 3.9). In this frame the web is moving at a speed of $S + 1$. This simplifies the problem because the web is smooth and therefore simulating it in motion is trivial.
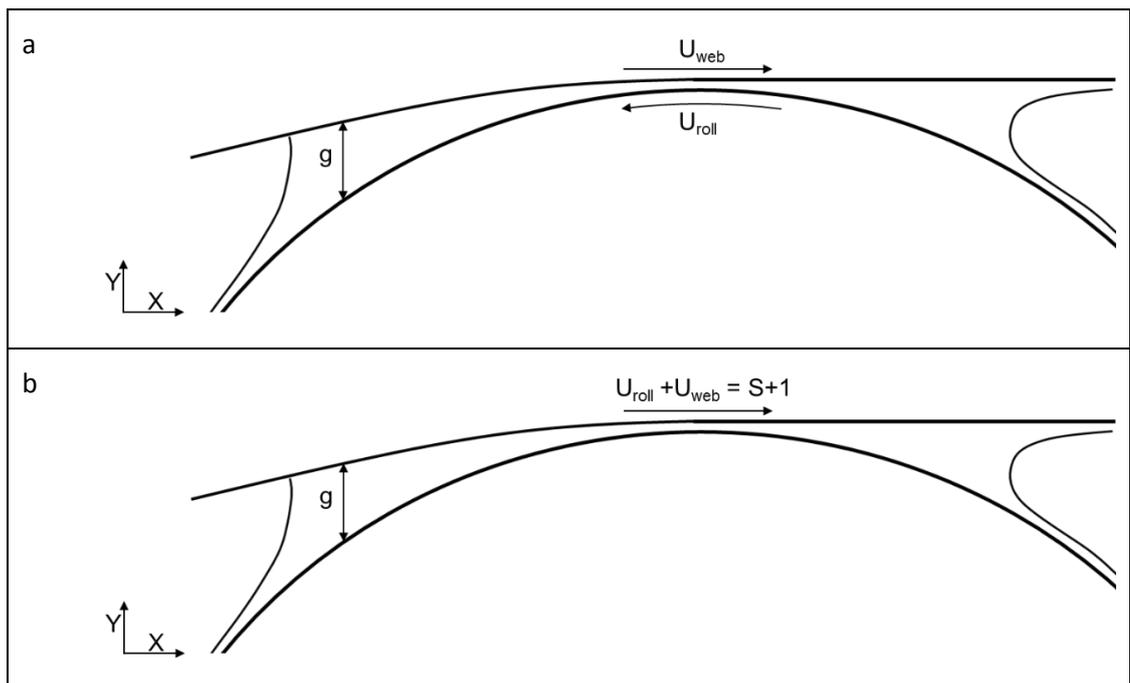
Figure 3.9: Difference between the laboratory reference frame (a) and the roll centric reference frame (b).

3.7.3 Fluid Domain

The fluid web interface is modelled using a no-slip moving wall and the lower surface with a stationary no-slip representation of the gravure surface topography. The four fluid interfaces used periodic boundary conditions such that in the roll axis direction $V_1 = V_2$, $P_1 = P_2$ and in the direction tangent to the roll surface $U_{us} = U_{ds}$, $P_{us} = P_{ds} + \delta P$ (Figure 3.10) where δP is the pressure gradient along the domain.
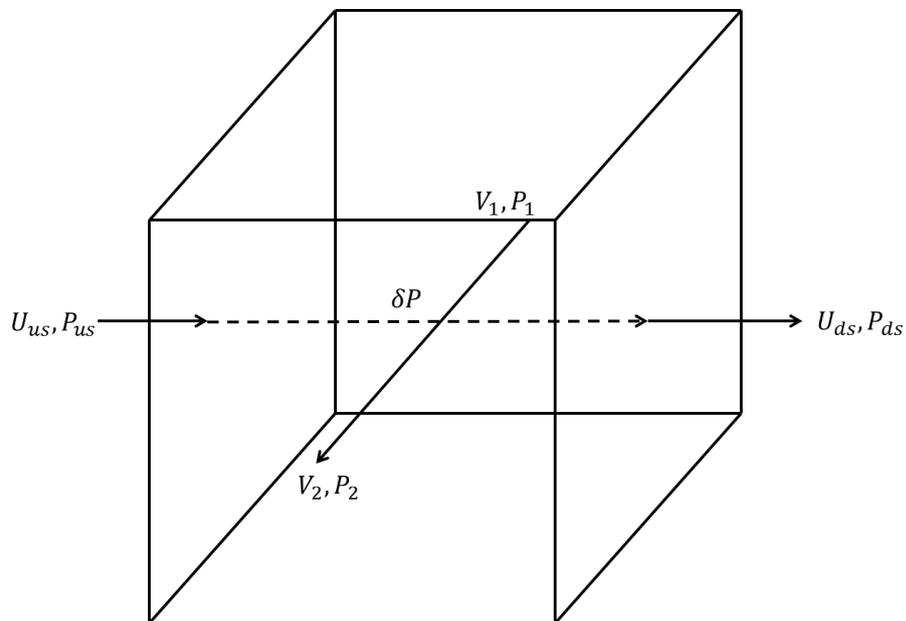
Figure 3.10: Diagram showing the velocity and pressure terms were implimented in the small scale model. A pressure gradient term is only present in the tangential direction. The gravure surface topography has been removed for clarity.

The fluid is modelled as a steady, incompressible and Newtonian flow in the Stokes regime. The implementation is governed by Equation 3.39 and follows the continuity law in Equation 3.40.

$$\nabla \cdot \left[-p\mathbf{I} + \left(\nabla \mathbf{u} + (\nabla \mathbf{u})^{\mathrm{T}} \right) \right] \qquad \textbf{3.39}$$

$$\nabla \cdot \mathbf{u} = 0 \qquad \textbf{3.40}$$

3.7.4 Method for Creating Cell Topography

The creation of the cell topography has been divided into two sections for clarity where the first describes a generic process and the second shows how it models the experimental phase from Chapter 2.

3.7.4.1 Method: Generic Topography

The small scale is represented by a cell with a circular opening and is parameterised by a radius and cell depth value. The shape of the cell is created using a hyperbolic tangent as described by Equation 3.41.

$$d = \frac{d_{max}}{2}(-1 - \tanh\{\alpha r - \alpha f[x, z]\})$$

3.41

Where d_{max} is the maximum cell depth, r_0 was the radius of the cell, α is a factor that determined the '*steepness*' of the cell wall and $f(x, z)$ determines the radial distance from the cell centre in the local cell.

Equation 3.41 forms the profile shown in Figure 3.11. Rotating this profile through 360° creates the cell geometry. The zero depth corresponds to the roll land.
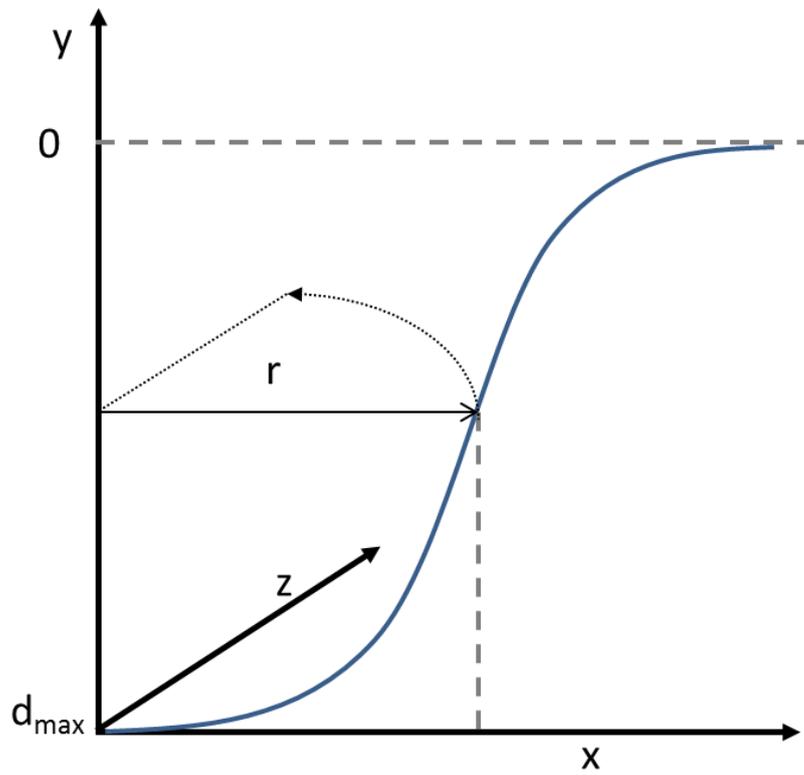
Figure 3.11: Diagram showing the parameters used in Equation 3.41 to create the hyperpolic tangent for the cell geometries. The profile in blue is created by Equation 3.41 and is implemented through the x-z plane

The mesh angle, θ, in the large scale is caused by one row of cells being off-set from the next; this is shown in Figure 3.12. For this to be consistent between the two scales the small scale must be skewed as in part b of Figure 3.12 such that the area on the small scale domain remains constant. Equations 3.42 and 3.43 determine the displacement in the x and z axis directions.
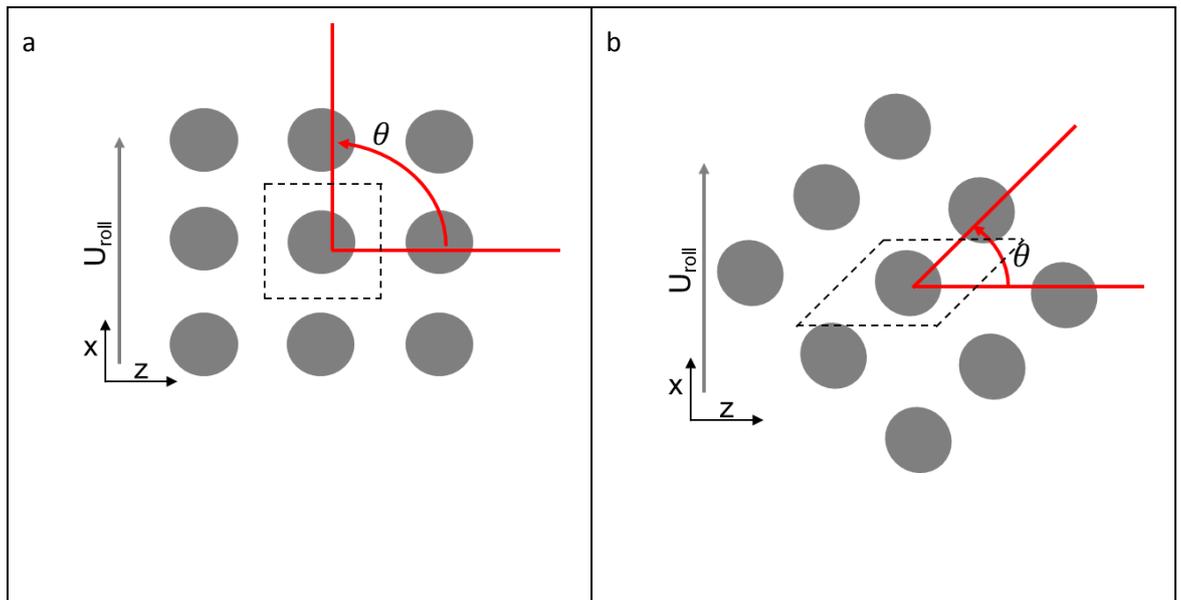
Figure 3.12: Variation of mesh angle as seen from top down on roll surface. In diagram a the mesh angle is 90° and in diagram b the mesh angle is 45°. In both diagrams the small scale is highlighted by the dashed lines.

$$\Delta x = x(\cos\theta - 1) \qquad \textbf{3.42}$$

$$\Delta z = (x \times \sin\theta) + z\left(\frac{1}{\cos\theta} - 1\right) \qquad \textbf{3.43}$$

3.7.4.2   Method: Topography for Experimental Comparison

For comparison with the experimental results it is important that the cell shapes represent what was tested experimentally. These parameters are shown in Table 3:2 for rolls A and B which were used in the experimental phase. Figure 3.13 shows a side-by-side comparison of the implemented topography with a white light interferometer image of the roll. The surface of

the idealised model is significantly smoother than the interferometer data suggests and also neglects any non-periodic features.

The cells on both rolls are at a 45 degree mesh angle. This was captured by skewing the domain subject to Equations 3.42 and 3.43. The small scale representation shown in Figure 3.13 has a cross-sectional area of one (through the x-z plane) and the cell volume was maintained to that measured by the white light interferometer (see Section 2.3.2). Inspection of the contour plots show that aspects of the upstream and downstream cells are present.

Table 3:2: Key cell parameters

Average Cell Values	A		B	
Characteristic Length	250 um		450 um	
Cell Diameter	150 um	0.6	300 um	0.67
Cell Depth	80 um	0.32	175 um	0.39
Cell Volume	9E-13 m^3	0.055	7.5E-12 m^3	0.083
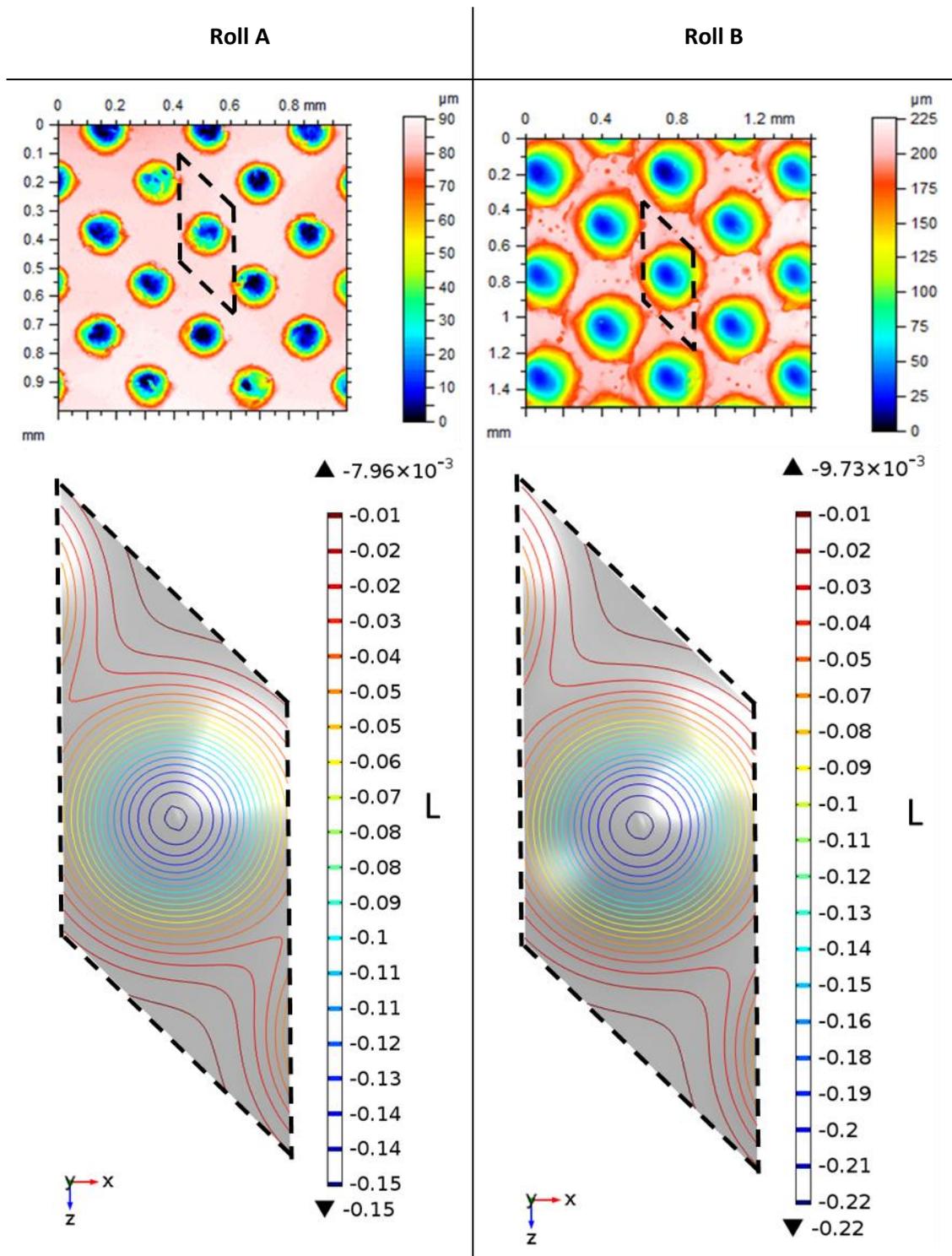
Figure 3.13: Cell topography for rolls A and B. Roll motion is in the x-axis direction. The length units, L, are the characteristic length of each roll. The small scale representation is highlighted by the dashed line on the large scale white light interferometer images. The small scale (bottom) is the approximation of the images using Equation 3.41 to 3.43.

3.7.5   Meshing and Geometry Creation

A deformed mesh was used to represent the geometry. For this process it means that a mesh must first be generated on a given shape (Figure 3.14) and then the nodes and elements are transformed to meet the desired shape (Figure 3.15).

In this case the process started with a cube of dimension 1. Two surface meshes of square elements were produced on opposite faces. This was then swept through to form a regularly meshed cube. The sweeping distribution was altered such that element density was larger at the bottom than at the top, this is where the gravure topography is represented and therefore would experience the most non-linear flow, and is therefore a more efficient use of the fixed number of elements. This formed the meshed cube shown in Figure 3.14.
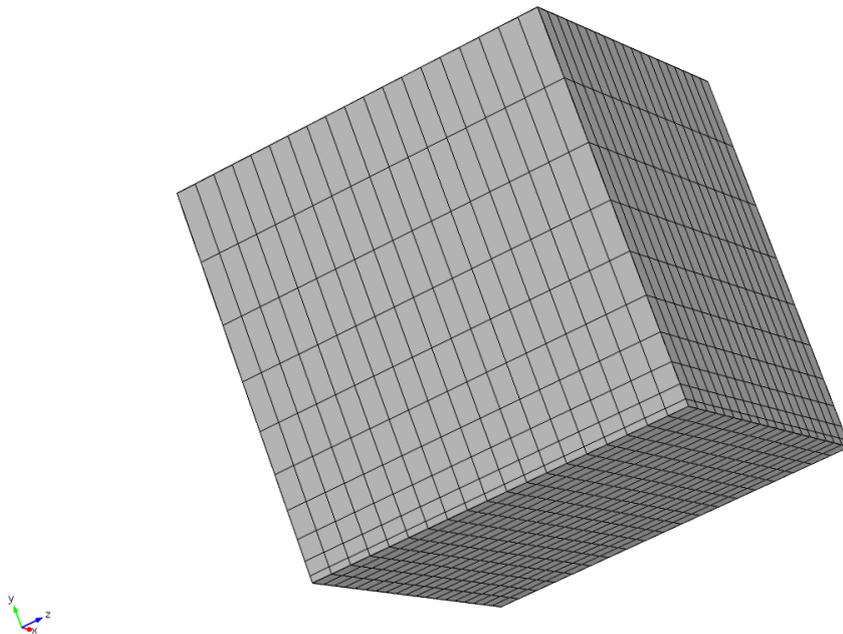
Figure 3.14: Basic cube with an off-set swept mesh which has had its elements skewed towards the base to increase the density at the bottom. This forms the baseline mesh in Figure 3.8.

The moving mesh implementation was designed to a) adjust the height of the cube to meet the web-to-roll gap specified in the lookup table over the range of 0.001-5 times the characteristic length; b) move the base of the

cube to form the cell topography and c) execute the skewing process to represent the large scale cell patterning (the angular offset from one row of cells to the next). An example result is shown in Figure 3.15. In this diagram it is clearer why additional elements are desired towards the gravure surface.

The mesh deformation process scales the total required displacement amongst all the elements such that x-z plane running through y=0 remains stationary. The elemental displacement is defined in Equation 3.44 for the creation of the cell where d is the result of Equation 3.41.

$$\Delta y_{element} = \frac{y}{d_{max}} d \qquad \textbf{3.44}$$
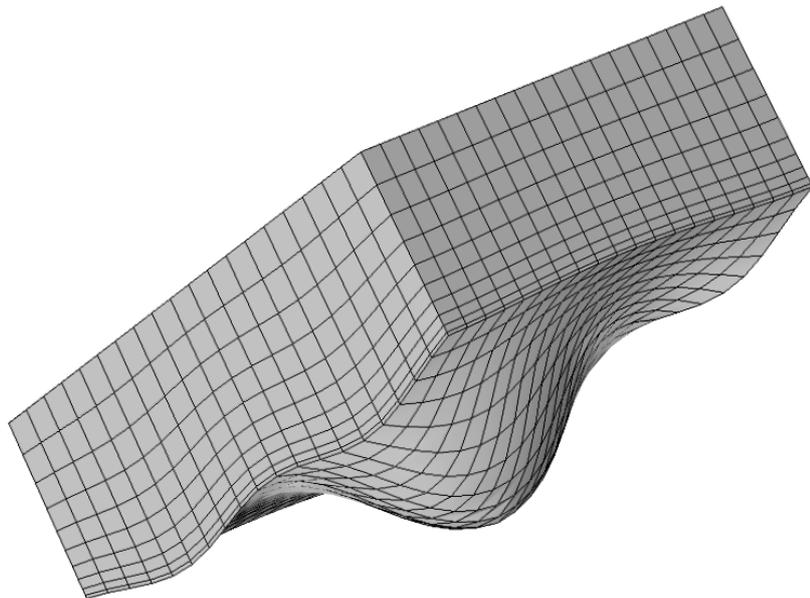
Figure 3.15: Mesh deformed into a example small scale geometry. The web-to-roll gap in this example is 0.5 and the mesh angle is 45°. This forms the deformed mesh in Figure 3.8.

3.7.5.1 Mesh Sensitivity

Mesh sensitivity results on a cell geometry with a web-to-roll gap of one is shown in Figure 3.16. The element count was varied from 320 elements to 25168 elements and over that range showed a volumetric flow rate change of 0.00128 which corresponds to a 0.1% change. The solution time increased linearly with the number of elements (Figure 3.17) from 6 seconds to 405 seconds. The point marked in red on both figures indicates the element count used for the small scale models.
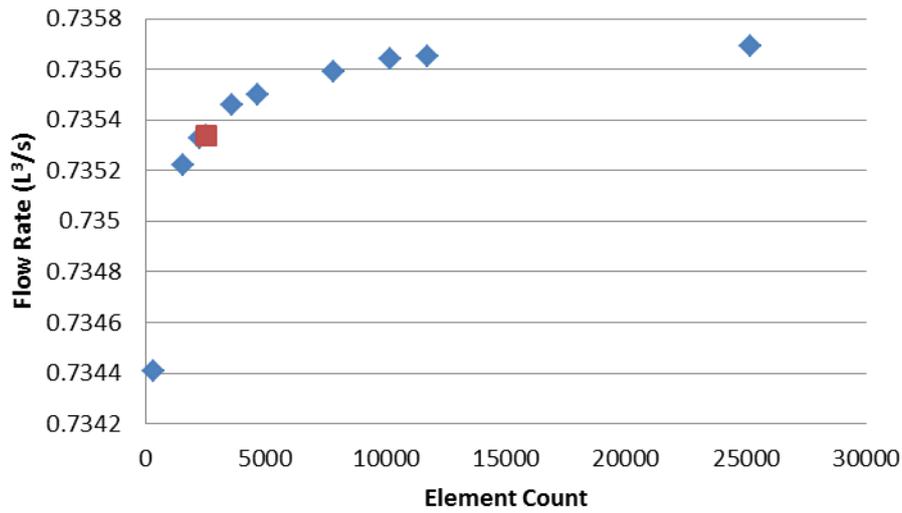
Figure 3.16: Volumetric flow rate where L is the characteristic length. Shown in blue are study point and the red point marks the mesh count used create the small scale models.
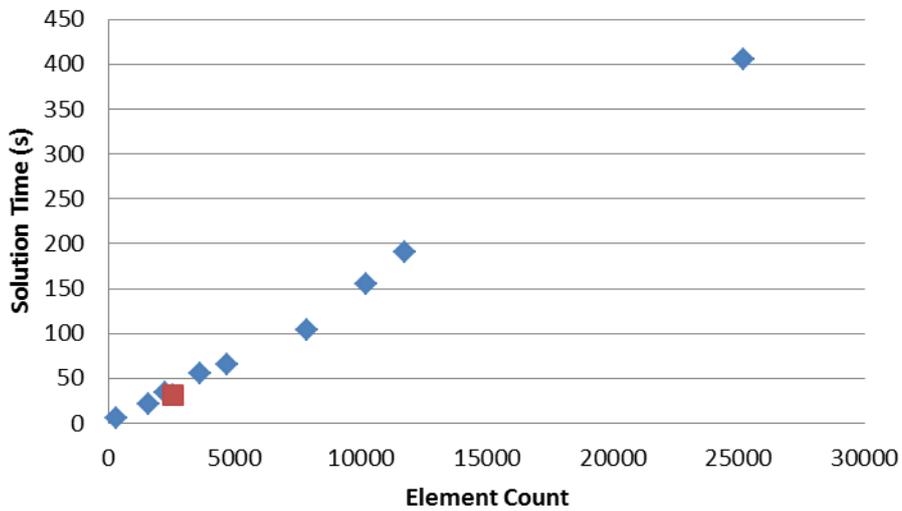
Figure 3.17: Solution time in seconds increasing linearly with element count. The point in red marks the element count used to create the small scale models.

3.7.6 Solver: Multi-Grid

The problem was solved using a multi-grid solver (Briggs & McCormick, 2000). This is an iterative solver that breaks the initial dense grid into a series of coarser grids (a process called restriction) to obtain an initial solution and then using interpolation methodology achieves a solution on the dense grid (a process called prolongation), the process is outlined in Figure 3.18. This type of solver is more memory efficient than using a direct solver on the initial grid. The effect of this is to allow for a higher mesh density to be used than would have been possible using direct solver.
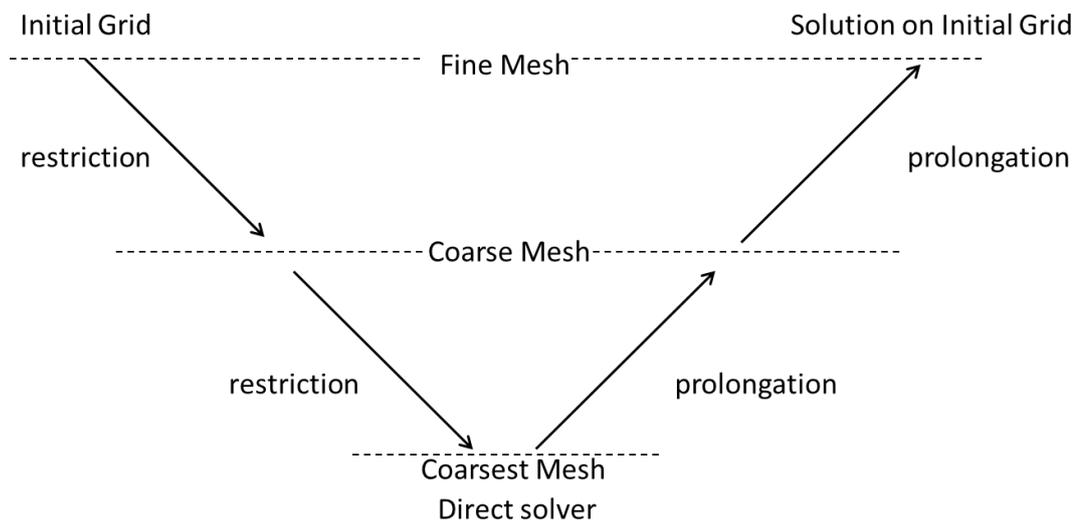
Figure 3.18: Multi-grid V-cycle.

3.7.6.1 Solver: Multi-Grid Implementation

The multi-grid solver was used in conjunction with a continuation method to sequentially solve over the range governed by the lookup table. Solutions at large web-to-roll gaps could be supplied with an initial guess approximated by lubrication theory. By continuing the problem the solution at a large web-to-roll gap could be applied as the initial guess to the next smaller web-to-roll gap problem. This process made achieving solutions over the whole lookup table consistent. In the event a solution could not be readily achieved it was

required that the gap be increased such that the solution from the previous iteration better fit the new problem.

3.7.7 Zero Flow Rate Geometry

Zero flow geometry represents the point at which the web-to-roll gap is so small it allows no fluid to flow from one boundary to the other. For a cell that has perfectly idealised land then this occurs at a gap of exactly zero. The hyperbolic tangent used in equation 3.40 asymptotically approaches land of the gravure (i.e. where cell depth equals zero) and for certain formulations of this equation there can be a significant gap below zero. In practice many cells also have features that allow flow through the geometry when the web-to-roll gap is less than zero (e.g. large cell radius so the peripheries of the cells meet forming a channel between the cells). Modelling these types of geometries is difficult for two reasons. First, predicting exactly where the zero flow rate occurs is difficult as it varies for every geometry. Second, modelling at a negative web-to-roll gap causes mesh inversions using the generic deformed mesh method described in section 3.7.5.

It is necessary to have a representation of this region to prevent the large scale requesting values outside of the lookup table. The extrapolation to negative gap produces an impossible situation where the web is inside the roll. The web-to-roll contact would normally prevent this but it does allow comparisons to be made in the large scale without the contact model (this allows the importance of the contact model to be assessed).

The first step is to determine at what web-to-roll gap zero flow occurs. This is the same gap for all three flow coefficients a, b and c with b and c being the most linear. By linearly extrapolating b to zero along the height axis the minimum height can be estimated (see example results in Figure 3.20). Coefficient a is cubic and can be extrapolated by fitting a curve to the computational data (see example results in Figure 3.19).

Coefficient c is a function of the domain volume. Below a web-to-roll gap of zero this changes non-linearly because the web is below the land, a situation which in reality is impossible, and therefore the volume below the web is a

partial cell volume rather than the fluid column (this transition point is seen as a break in the example results shown in Figure 3.21). Therefore it needs to be extrapolated numerically by integrating the volume remaining below the web location Figure 3.21.
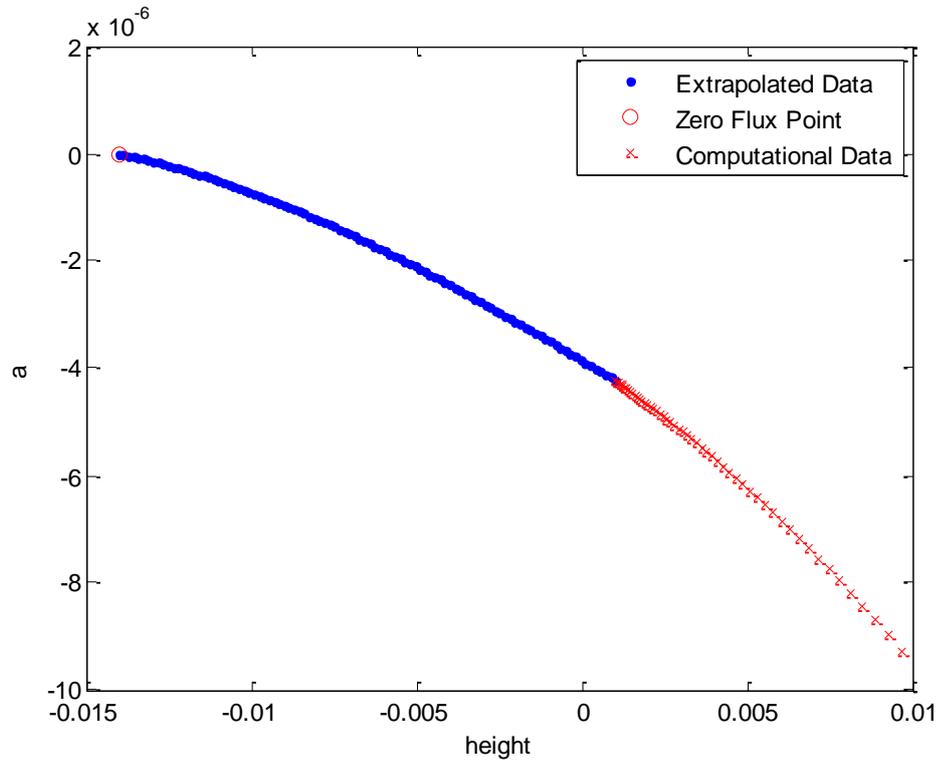
Figure 3.19: Extrapolated data (blue ·) from the computational results for coefficient a (red x).
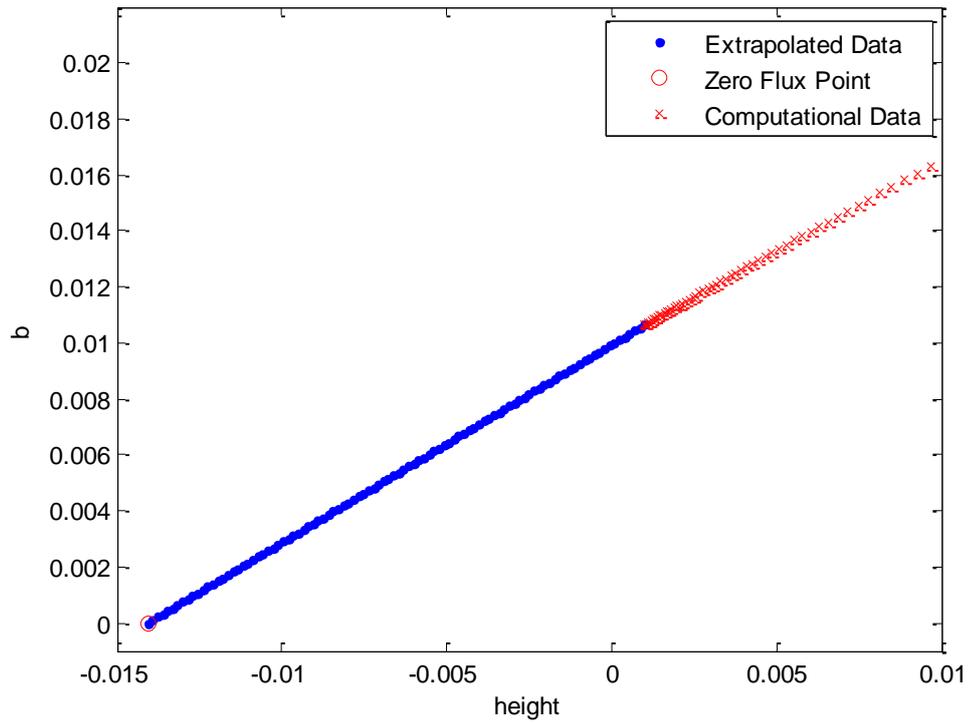
Figure 3.20: Extrapolated data (blue ·) from the computational results for coefficient b (red x).
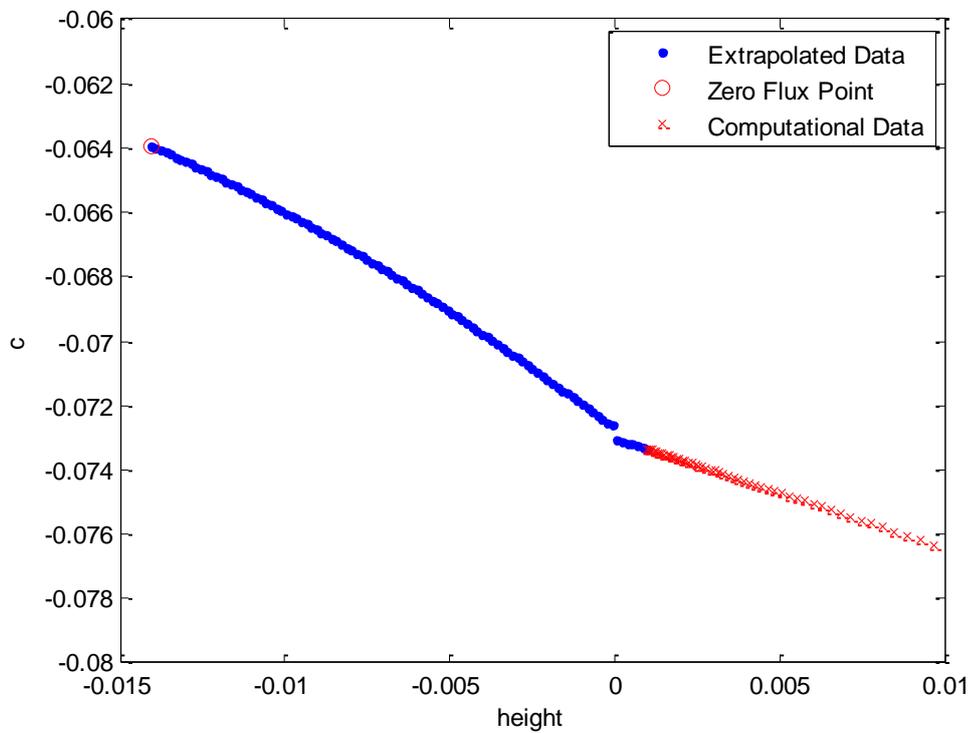
Figure 3.21: Numerically extrapolated data (blue ·) and computational results (red x). The break in the graph at height=0 occurs as the web moves through the land.

3.7.8 Validating the Small Scale with Lubrication Theory

Comparing the computational result in the small scale to the analytic result of lubrication theory offers a means of validation. Though comparison with experimental data would be preferable the cell length scales make this impractical.

Computational results over the web-to-roll gap range of 0.001-5 for the coefficients in Equation 3.38 are compared against their analytic lubrication values in Figure 3.22 and Figure 3.23 for rolls A and B respectively. The lubrication values are calculated using Equations 3.45, 3.46 and 3.47. The difference between the computational and analytic results becomes more apparent when looking at the percentage difference between the two. This percentage difference is found using Equations 3.48 to 3.50

$$a_{lube} = -\frac{h^3}{12} \qquad \textbf{3.45}$$

$$b_{lube} = \frac{h}{2} \qquad \textbf{3.46}$$

$$c_{lube} = -\frac{h}{2} \qquad \textbf{3.47}$$

$$\%\Delta_a = 100 \frac{a_{comp} - a_{lube}}{a_{lube}} \qquad \textbf{3.48}$$

$$\%\Delta_b = 100 \frac{b_{comp} - b_{lube}}{b_{lube}} \qquad \textbf{3.49}$$

$$\%\Delta_c = 100 \frac{c_{comp} - c_{lube}}{c_{lube}} \qquad \textbf{3.50}$$

The lubrication height terms are calculated such that the total volume of fluid in the domain is the same as that in the computational gravure case. This makes the numerical difference between the computational and analytic results only due to topography rather than from some difference in volume. By plotting the percentage difference between the computational and

analytic results it is clear that when the web-to-roll gap is large lubrication theory is a good approximation to the small scale flow field. As the web-to-roll gap tends toward zero the solutions diverge up to a 100% difference in the coefficients of both rolls.

Considering the relative volume of the cell and the fluid column can help elucidate the reason for this difference. At the minimum value of the web-to-roll gap of 0.001(L) the volume of the fluid column is $0.001(L^3)$ (recall that the cross-section area is equal to unity). The cell volume for Roll A is 0.055 (L^3) and for Roll B is 0.083 (L^3). Therefore the volume of the cell is 55 (Roll A) and 83 (Roll B) times larger than the fluid column making it the dominant flow feature at this web-to-roll gap.

Column two in Figure 3.22 and Figure 3.23 shows the extrapolated values from the minimum computed web-to-roll gap of 0.001 to a zero flow condition which occurs at a negative gap of -0.016. This allows gaps all the way to zero to be modelled without exceeding the lookup table. This is an issue which arises when using a contact model requiring gaps approaching zero.
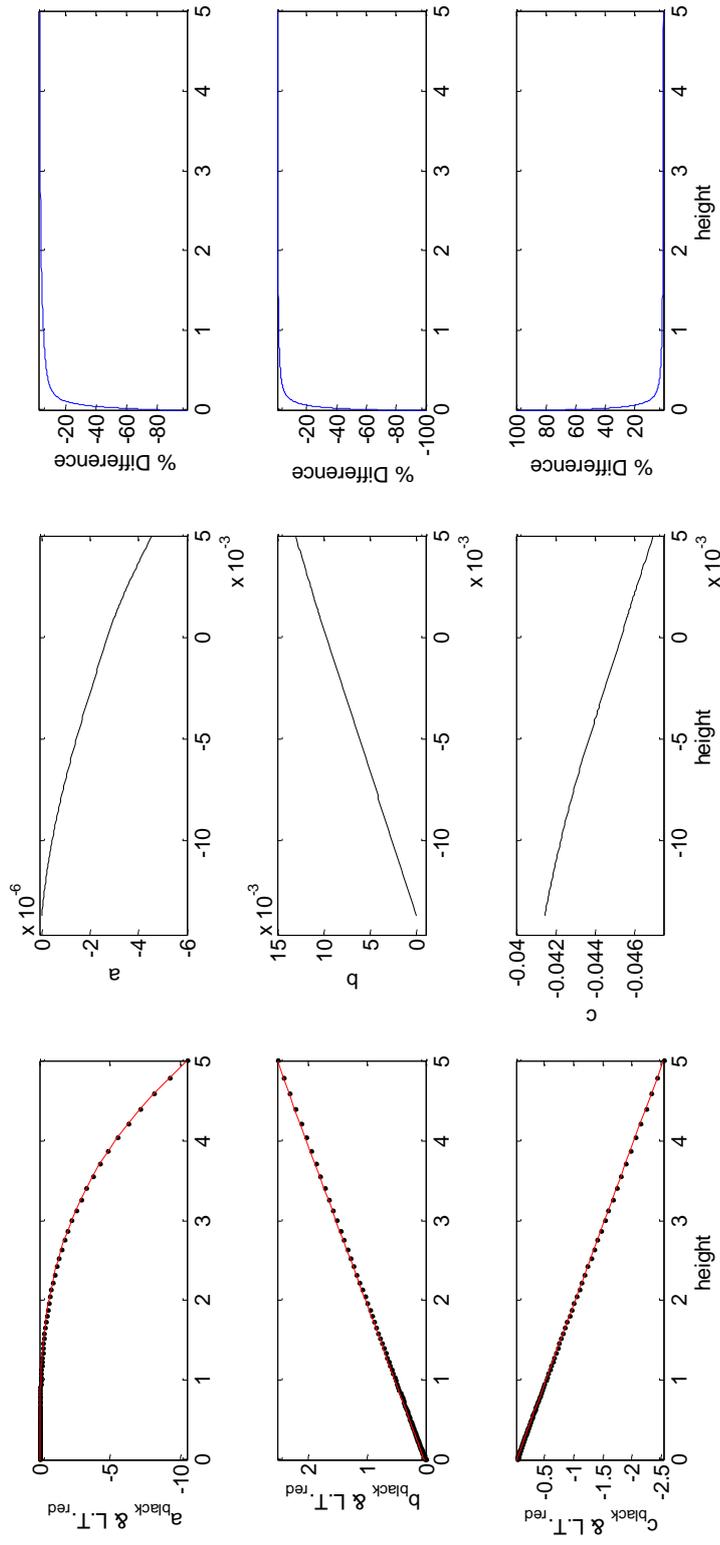
Figure 3.22: Small scale lookup table data for Roll A. Column one shows a comparison between computational results (black) and lubrication theory (L.T. red) over height range 0 to 5. Column two is zoomed in to show web-to-roll gaps less than 0.005. Column three shows the percentage difference between the computational data and lubrication theory.
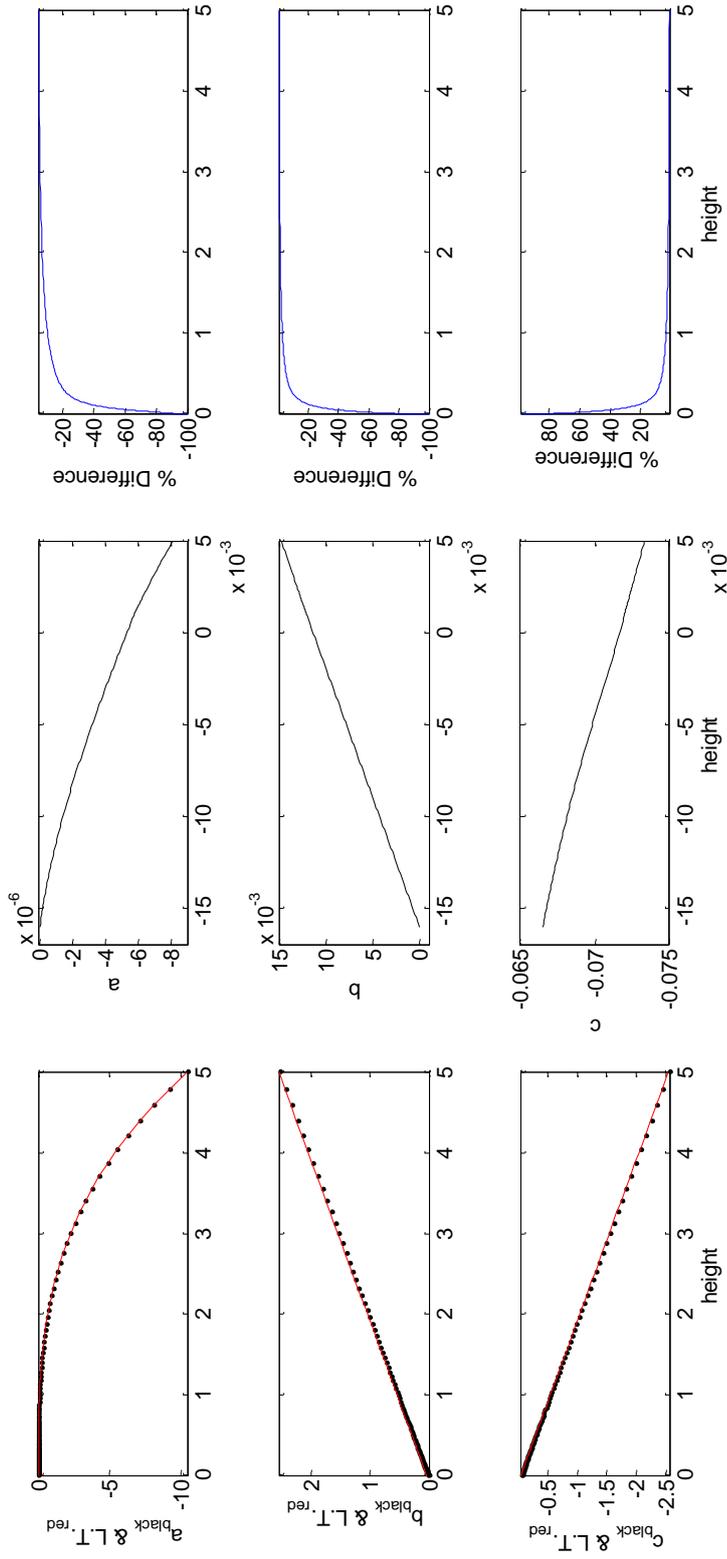
Figure 3.23: Small scale lookup table data for Roll B. Column one shows a comparison between computational results (black) and lubrication theory (L.T. red) over height range 0 to 5. Column two is zoomed in to show web-to-roll gaps less than 0.005. Column three shows the percentage difference between the computational data and lubrication theory.

By examining the flow field within the small scale domain further evidence is found to explain the difference in Figure 3.22 and Figure 3.23. The two flow components are the pressure driven flow (Poiseuille) and the wall driven flow (Couette).

Examples of the two fluid flow components are shown in Figure 3.24 to Figure 3.31. Figure 3.24 to Figure 3.27 depicts the smallest web-to-roll gap at 0.001 and Figure 3.28 to Figure 3.31 is for the much larger gap of 1. A comparison of the two shows that the fluid is less affected by the cell when the gap is large. The fluid flow when the gap is small is dominated by the cell topography, including the formation of an eddy in the Couette component. Comparing these with Figure 3.22 and Figure 3.23 helps to form a complete picture as to why lubrication theory is a poor representation when the gap is small.

The Couette components in Figure 3.24 and Figure 3.25 show the axial flow that was captured by the small scale. This process transfers fluid axially across the domain and is caused by the mesh angle. There is also some evidence of this axial transfer in the Poiseuille component in Figure 3.26 and Figure 3.27.
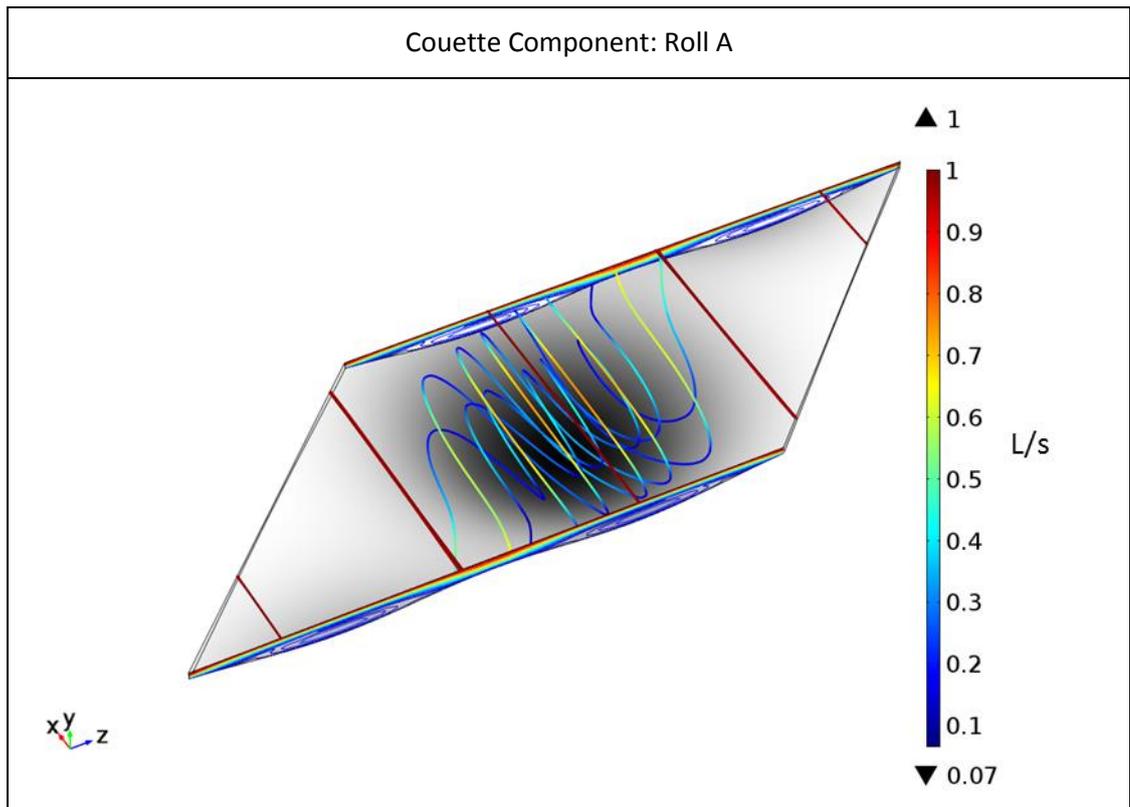
Figure 3.24: Gap of 0.001. Contour plot at walls with streamlines in the fluid domain and scale showing dimensionless velocity.
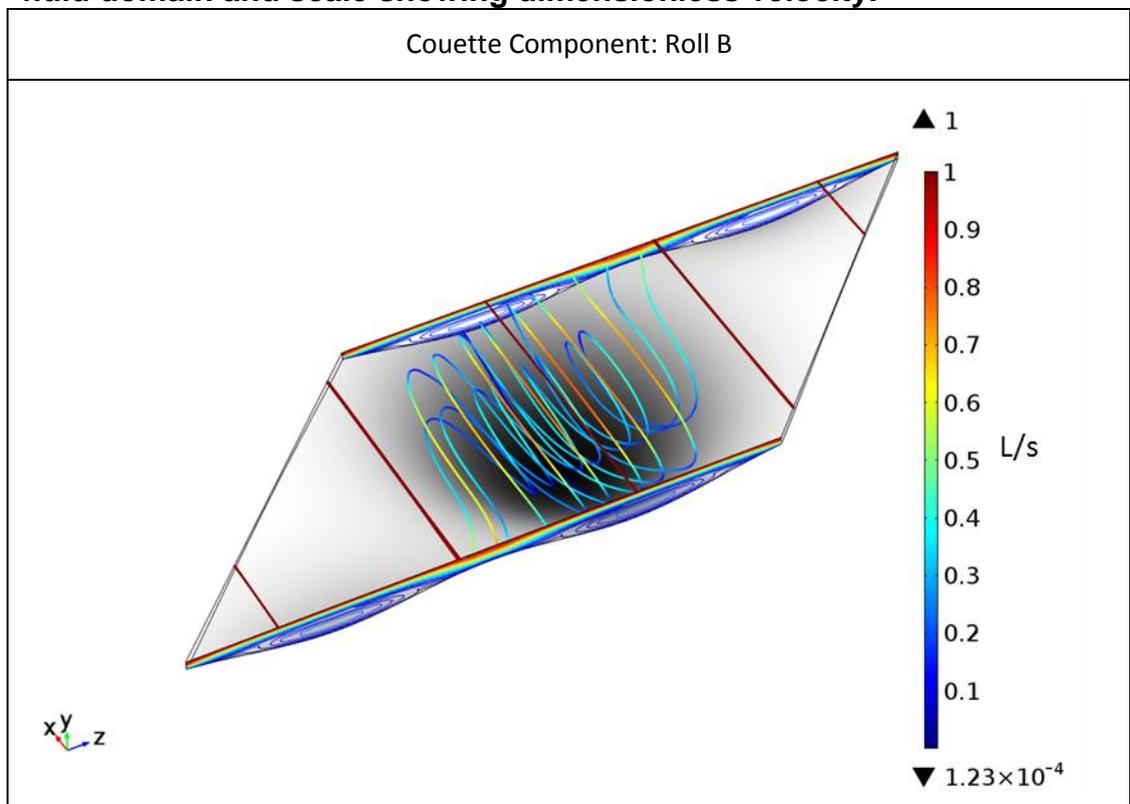
Figure 3.25: Gap of 0.001. Contour plot at walls with streamlines in the fluid domain and scale showing dimensionless velocity.
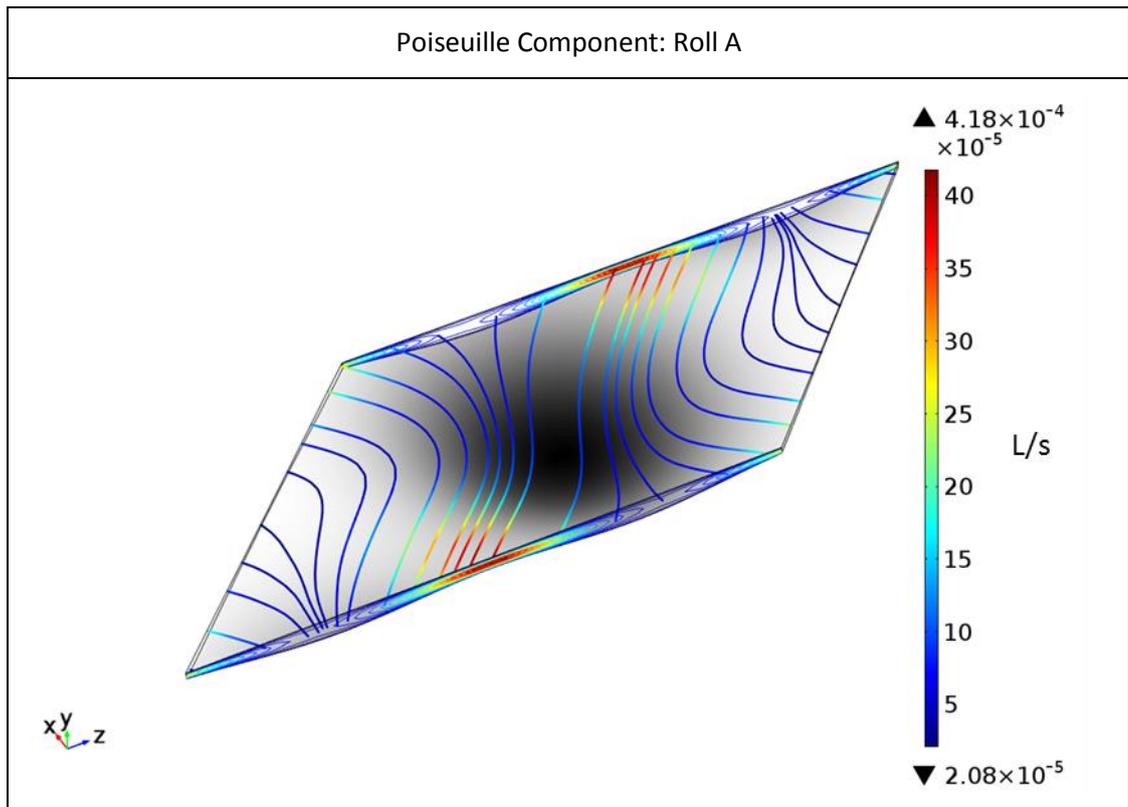
Figure 3.26: Gap of 0.001. Contour plot at walls with streamlines in the fluid domain and scale showing dimensionless velocity.
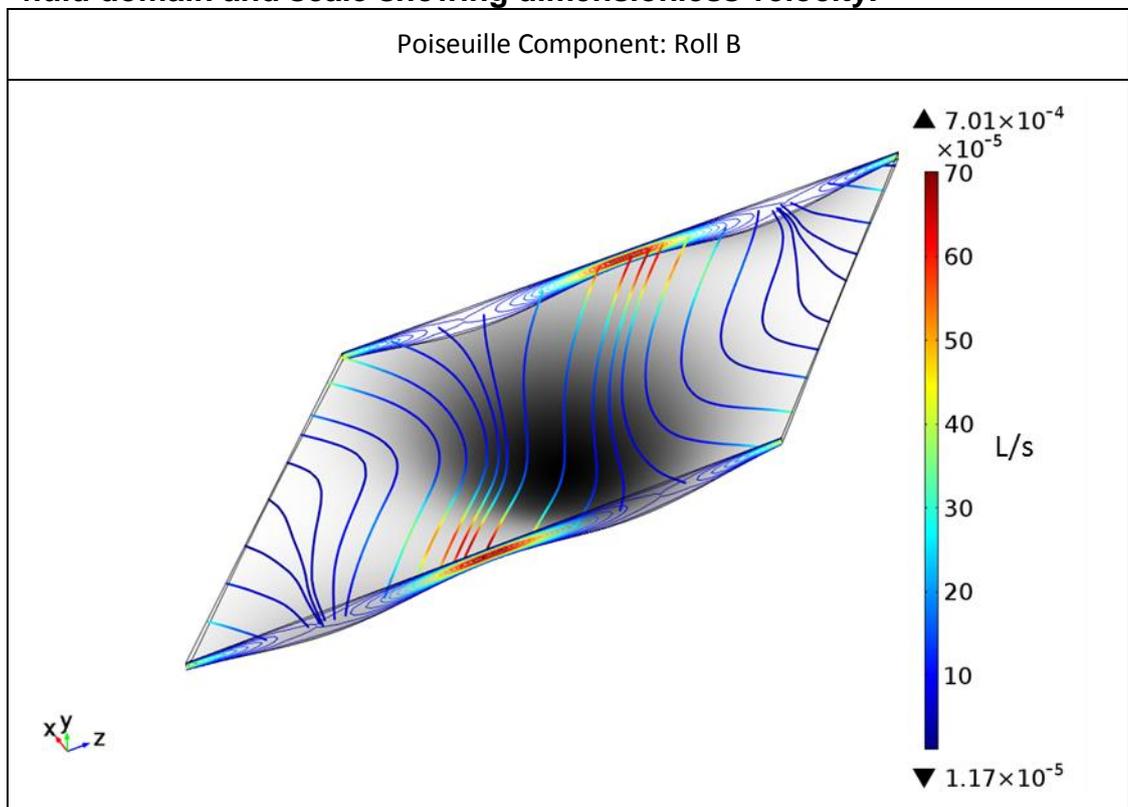
Figure 3.27: Gap of 0.001. Contour plot at walls with streamlines in the fluid domain and scale showing dimensionless velocity.
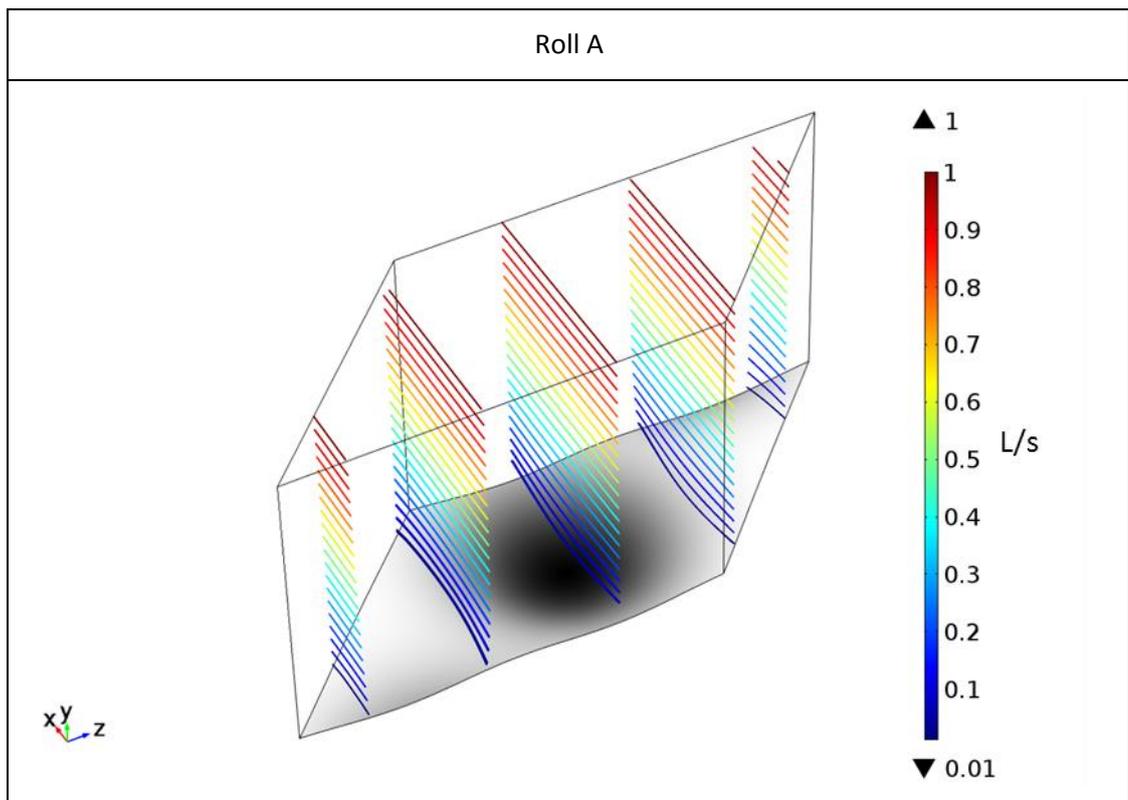
Figure 3.28: Roll A at a web-to-roll gap of 1. Streamlines in the fluid domain and scale showing dimensionless velocity.
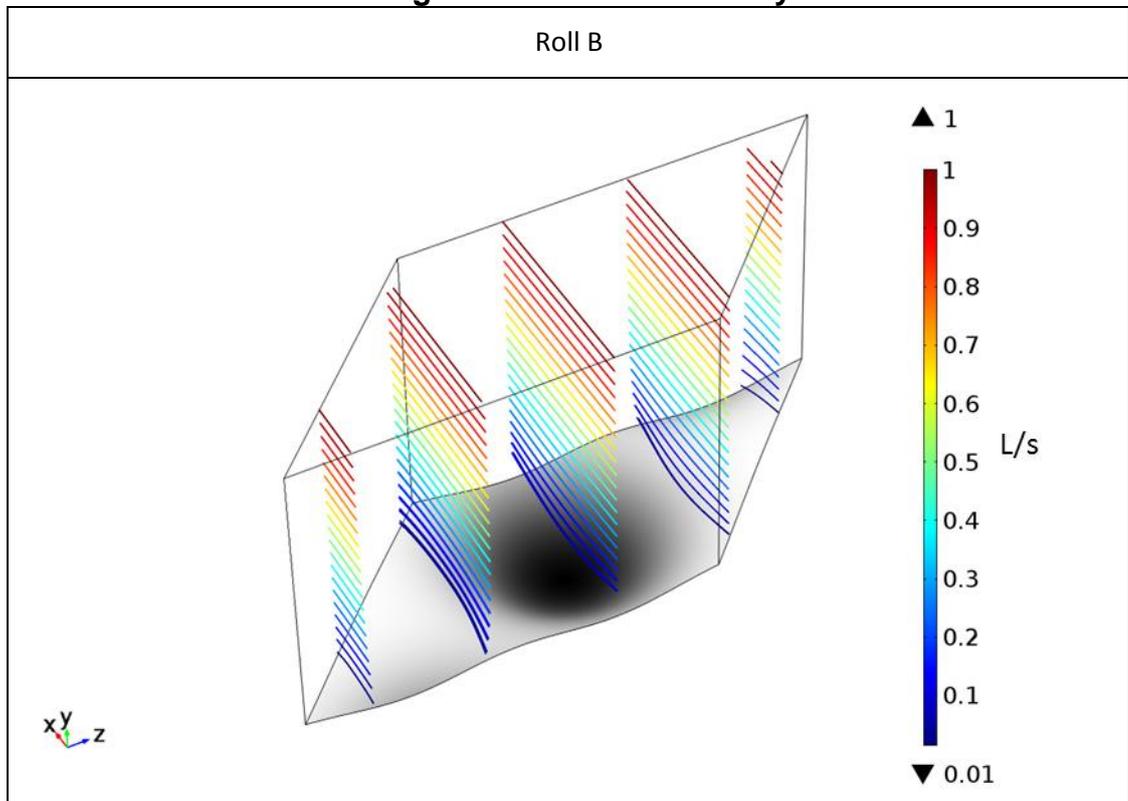
Figure 3.29: Roll B at a web-to-roll gap of 1. Streamlines in the fluid domain and scale showing dimensionless velocity.
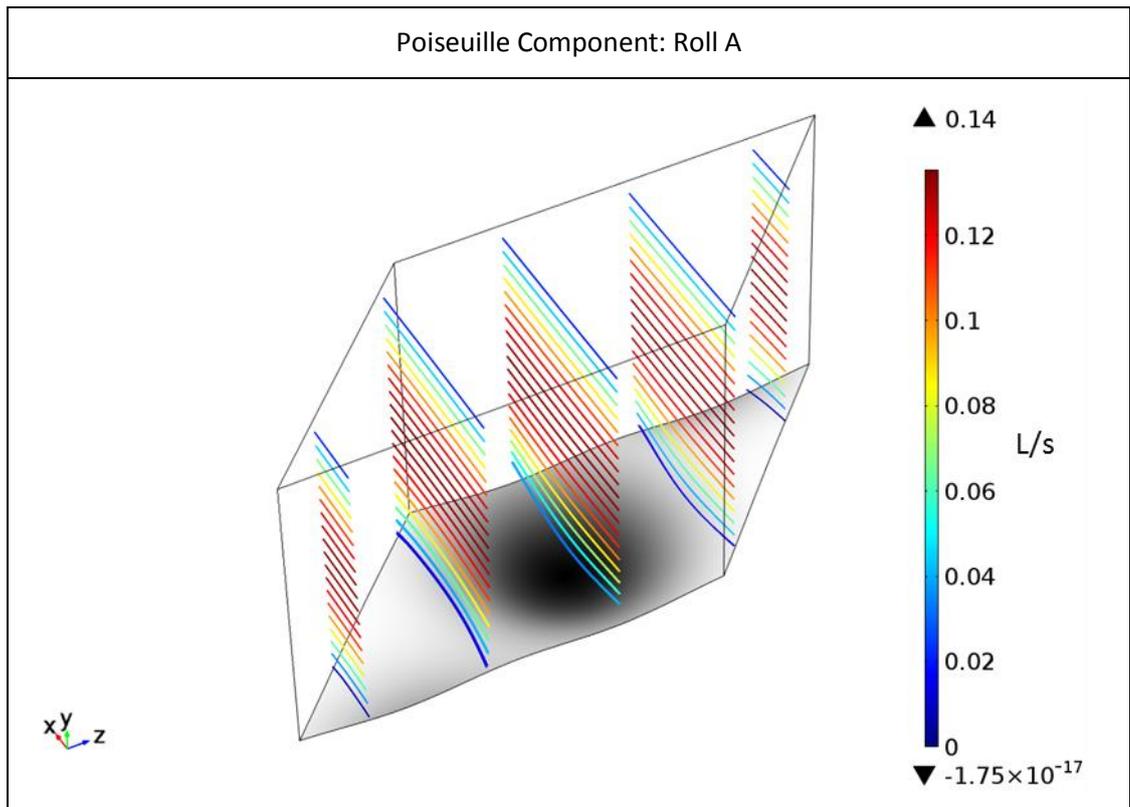
Figure 3.30: Roll A at a web-to-roll gap of 1. Streamlines in the fluid domain and scale showing dimensionless velocity.
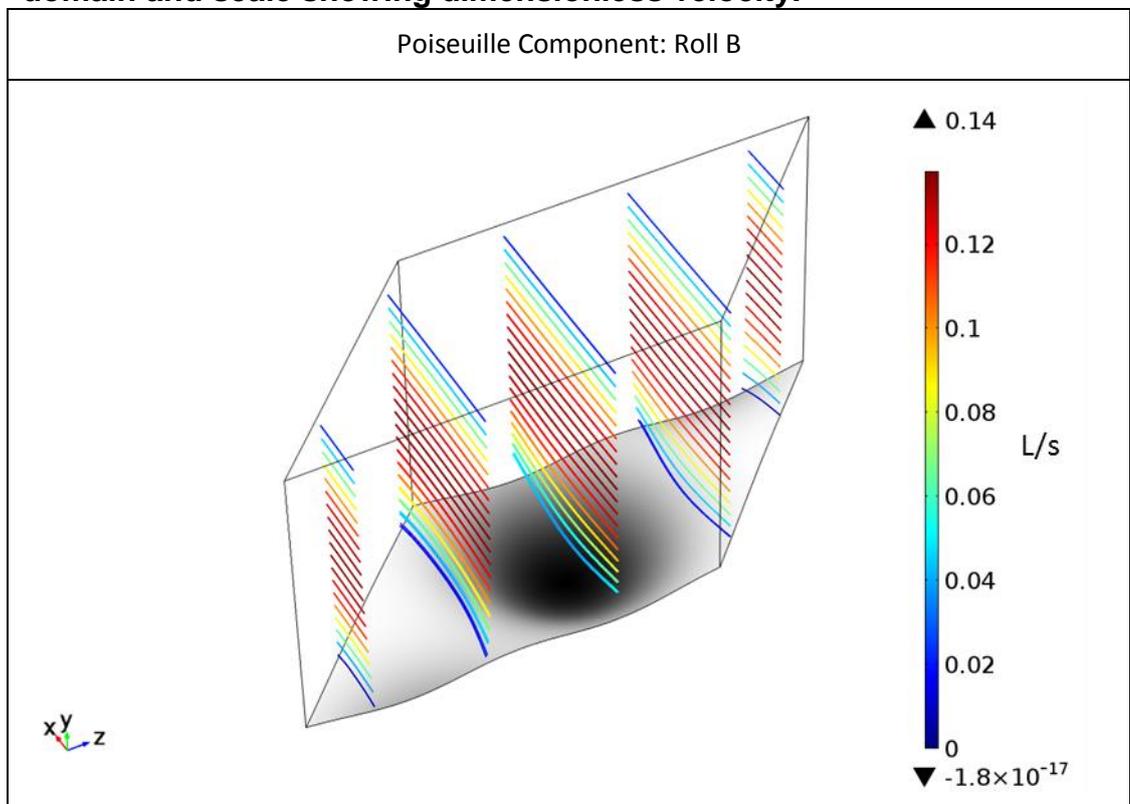
Figure 3.31: Roll B at a web-to-roll gap of 1. Streamlines in the fluid domain and scale showing dimensionless velocity.

Chapter 4   Computational Results

The results from the multi-scale model are presented with the results obtained via experiment in Chapter 2. The parameter space for both sets of results are summarised in Table 4:1. The purpose of this is to allow for a direct comparison between computation and experiment. This comparison is first done using pickout ratio as a metric at varying speed ratios. The second section (4.2) assesses the importance of web-to-roll contact in the computational model with reference to the scratches observed during experiment. The third section (4.3) assesses the sensitivity of the model to the boundary conditions.

Table 4:1: Parameter space for experiemental and computational results.

Parameter	Experiment Value	Computational Value
Web Tension	1000 N/m	1203700
Web Thickness	23 μm	neglected
Wrap Angle	2.5°	2.5°
Capillary Number	0.0204	0.0204
Viscosity	0.00163 Pa·s	-
Surface Tension	0.0400 N/m	-
U_{roll}	0.500 m/s	-
Speed Ratio	0.5-1.25	0.5-1.25
Roll Radius (Roll A/Roll B)	0.05 m /0.05 m	200/111
Mesh Angle	45°	45°
Characteristic Length, L, (Roll A/Roll B)	$2.5 \times 10^{-4}/4.5 \times 10^{-4}$ m	1/1

4.1   Comparison of Computational and Experimental Results

Pickout ratio (ϕ) versus speed ratio results are shown in Figure 4.1 and Figure 4.2 for rolls A and B respectively. Computational and experimental results show a nearly linear gradient which is under predicted by computation in both cases. For rolls A and B the gradients of the Best Fit lines for the experimental results are 0.50 and 0.38 while the computational gradients are 0.23 (Roll A) and 0.21 (Roll B). The experimental and computational lines intersect at S = 1.18 and ϕ = 0.44 for Roll A; and S = 1.09 and ϕ = 0.33 for Roll B. At S = 1 pickout ratios are separated by 0.027 (Roll A) and 0.018 (Roll B). The largest difference occurs at S = 0.5 with a difference of 0.13 (Roll A) and 0.086 (Roll B).
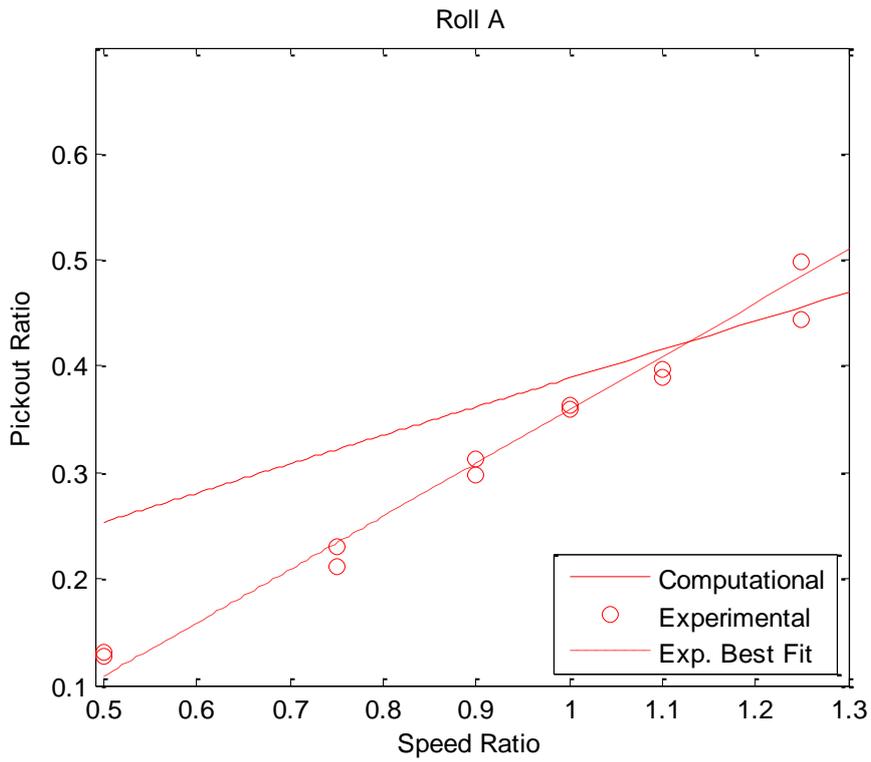
Figure 4.1: Numerical and experimental pickout ratios plotted against the web-to-roll speed ratio for Roll A.
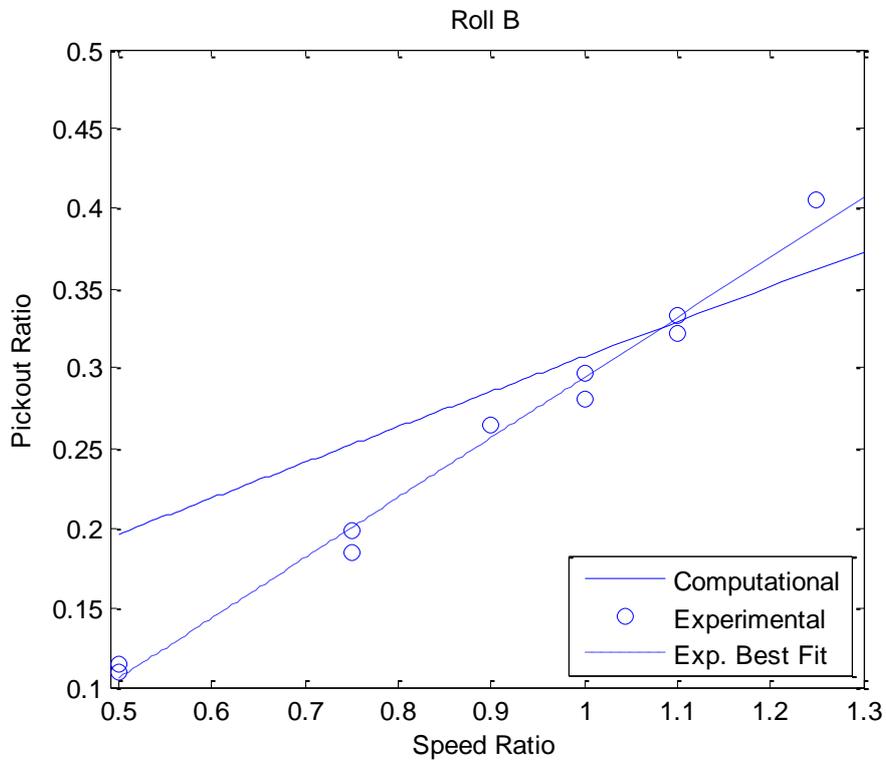
Figure 4.2: Numerical and experimental pickout ratios plotted against the web-to-roll speed ratio for Roll B.

4.2   Contact Model Results

Figure 4.3 and Figure 4.4 demonstrate the influence of the contact model at a speed ratio of one. The primary region of contact is immediately downstream of x=0 (top dead centre of the roll), which corresponds to the region of minimum gap (see parts (b) and (c) of Figure 4.3 and Figure 4.4). The fluid pressure is shown to be too small to support the web as can be seen in part (a) of Figure 4.3 and Figure 4.4 in the form of a spike of contact pressure. The length of the contact area is approximately 0.8 for Roll A and 0.4 for Roll B making it less than the length of the small scale domain.

Directly comparing the coating bead pressures on the two rolls in Figure 4.5 and Figure 4.6 shows that the fluid pressure on Roll B is smaller than that of A. This translates to a higher contact pressure required to support the web in Figure 4.6. The scale of these differences is highlighted in Table 4:2.

Table 4:2: Comparison of non-dimensional pressure.

Roll	Max Fluid Pressure (P_f)	Max Contact Pressure (P_c)	Difference in Pressure	$\dfrac{P_c}{P_f}$
A	768	6016	5248	7.8
B	362	10800	10438	29.8

a

b

c
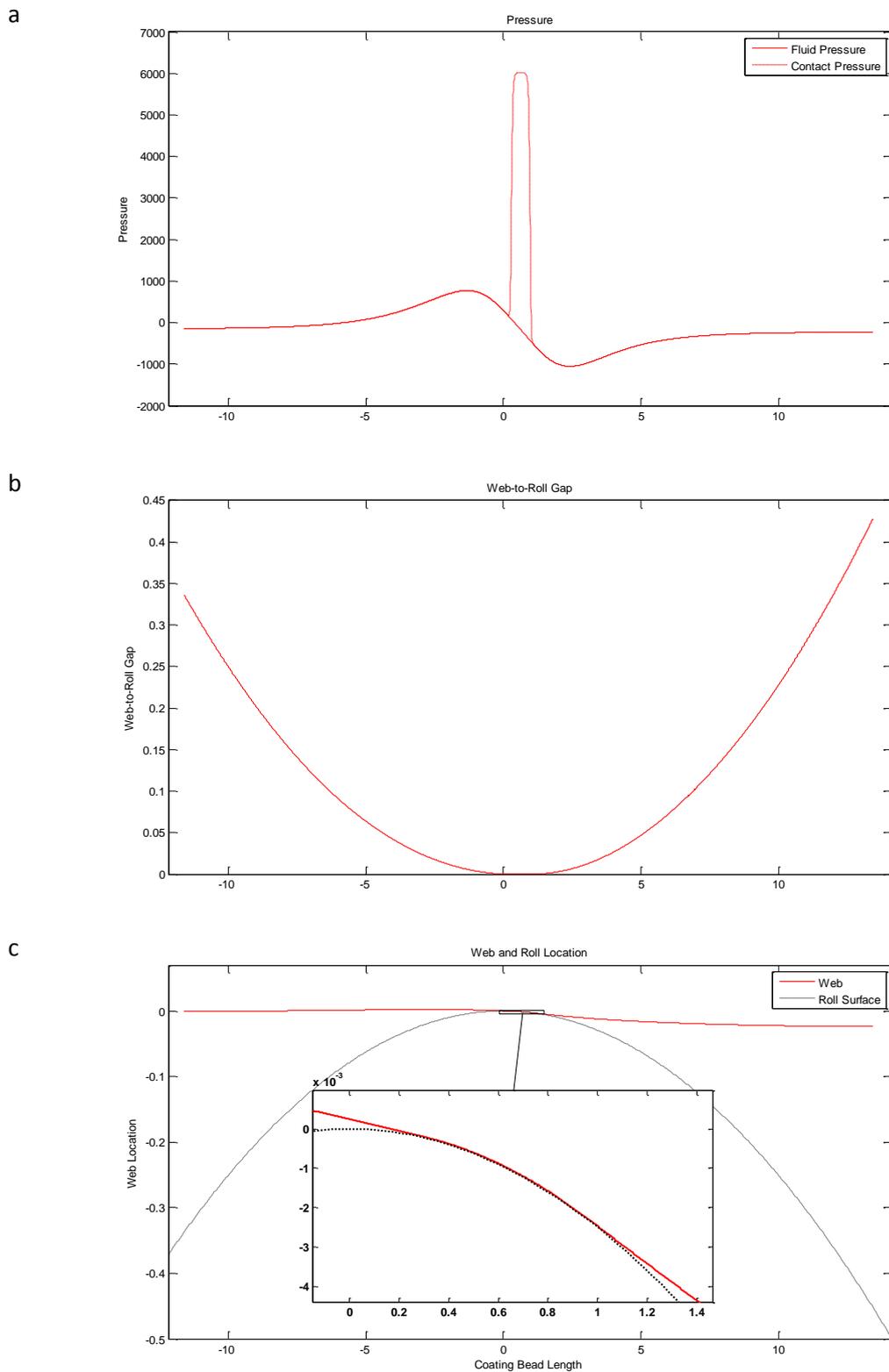
Figure 4.3: Plots with the x axis showing the coating bead axis. The top plot (a) is the sum of the fluid pressure and the contact pressure. Second plot (b) indicates the web-to-roll gap and the third (c) is the web location relative to the surface of the roll.
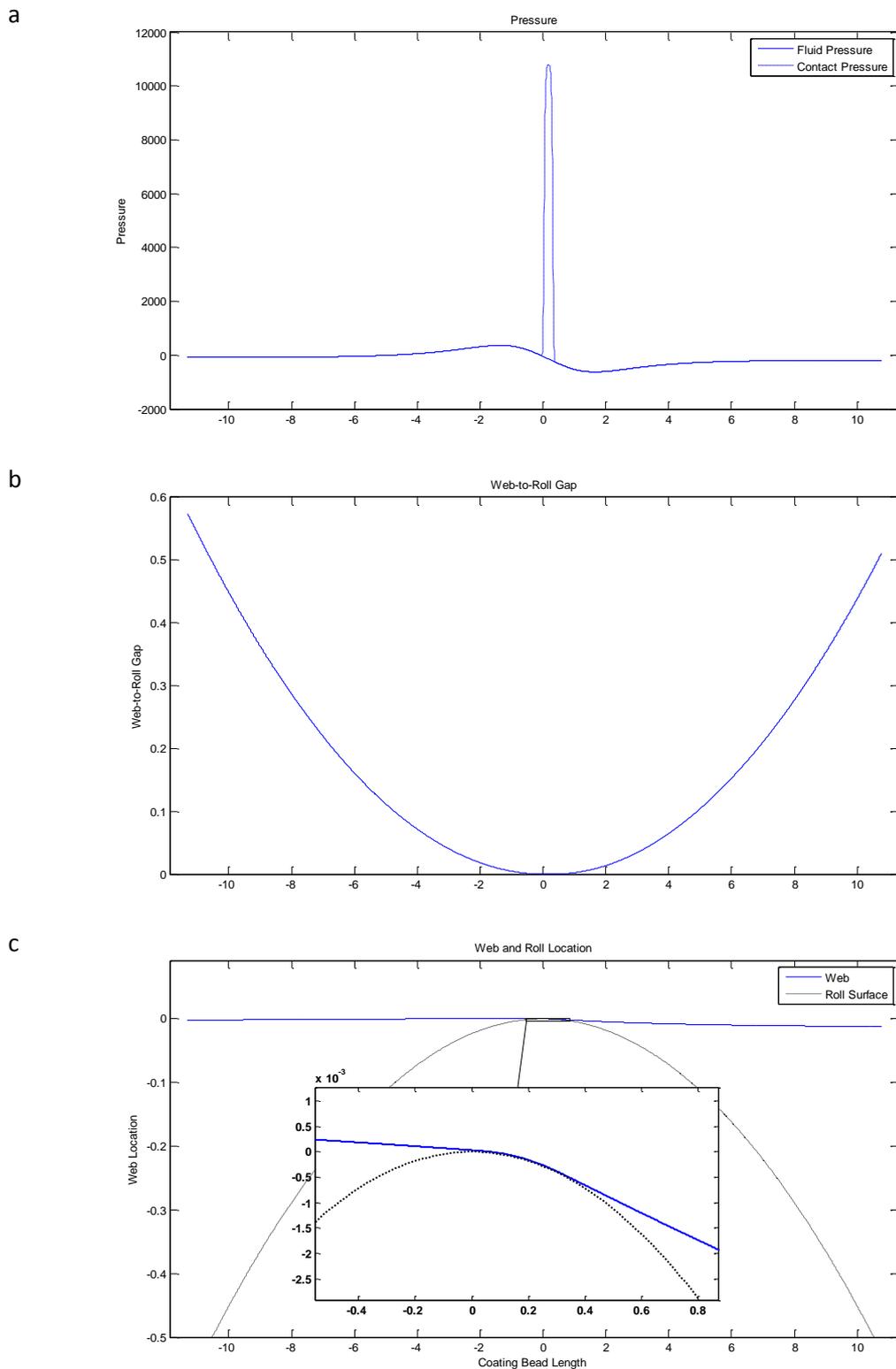
Figure 4.4: Plots with the x axis showing the coating bead axis. The top plot (a) is the sum of the fluid pressure and the contact pressure. Second plot (b) indicates the web-to-roll gap and the third (c) is the web location relative to the surface of the roll.
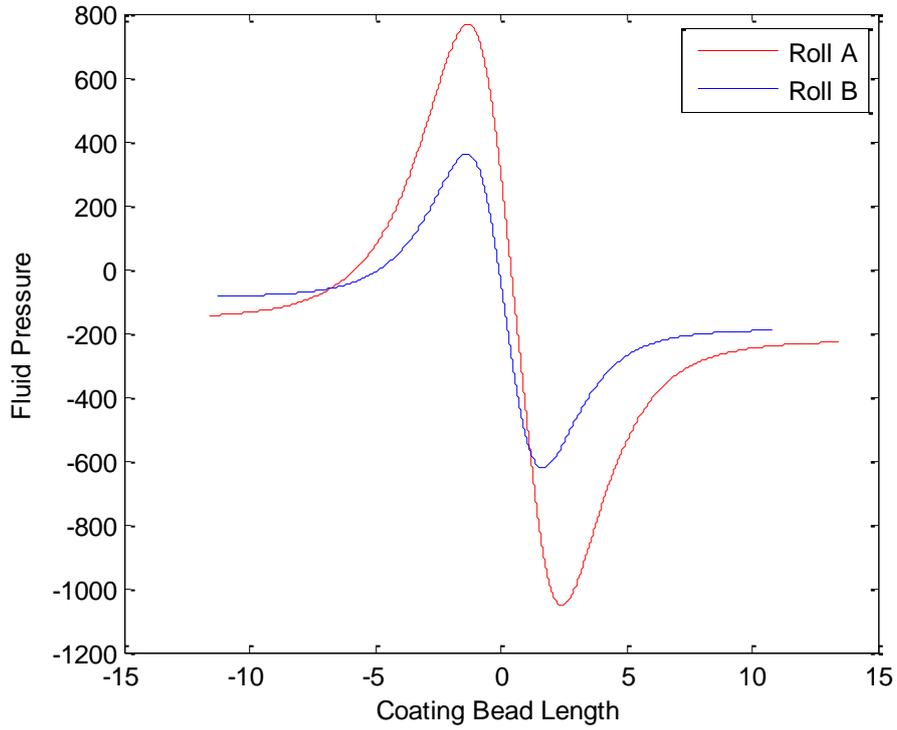
Figure 4.5: Comparison of fluid pressure at S = 1 for rolls A and B.
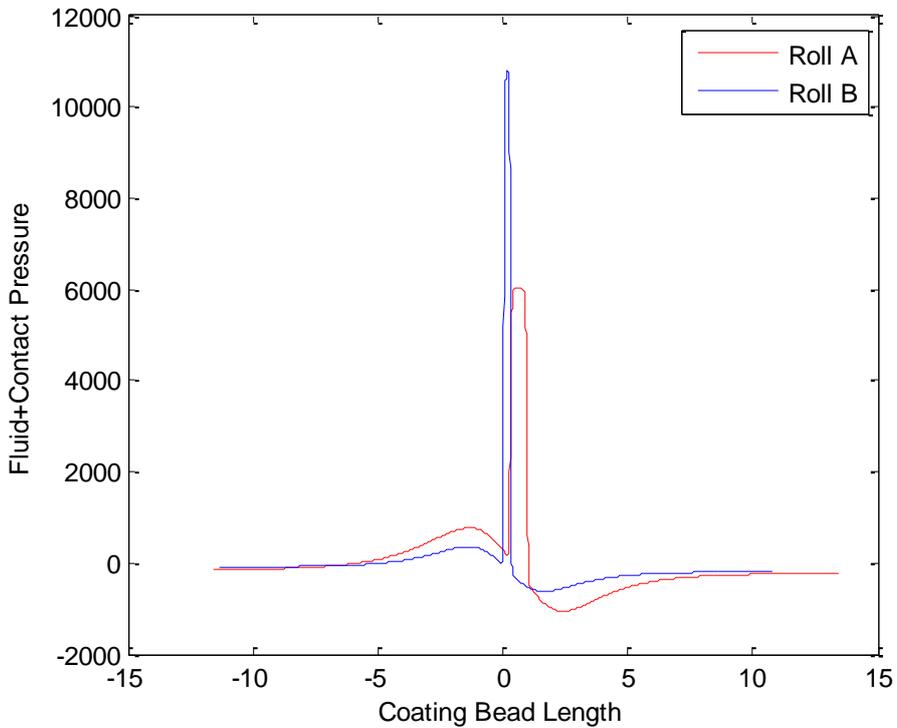
Figure 4.6: Comparison of fluid plus contact pressure at S = 1 for rolls A and B.

4.3   Boundary Condition Results and Analysis

This section investigates the limitations of the boundary conditions. This is accomplished by the introduction of scaling variables into the boundary conditions equations (3.23, 3.25, 3.26 and 3.27). Section 4.3.1 outlines what simplifications are present at the menisci. The later sections vary the scaling variables (α) to determine how the pickout ratio responds to these changes. Ultimately this section concludes that the model is relatively insensitive to the simplifications at the menisci.

4.3.1   The Smooth Roll Assumption: Meniscus Locations

The boundary conditions neglect the gravure topography by assuming the meniscus travels along a smooth surface (this simplification is illustrated in Figure 4.7). This simplification is required for the implementation of Equations 3.23, 3.25, 3.26 and 3.27 which govern the meniscus location and pressure. These boundary conditions relate the meniscus radius of curvature to the web-to-roll gap.
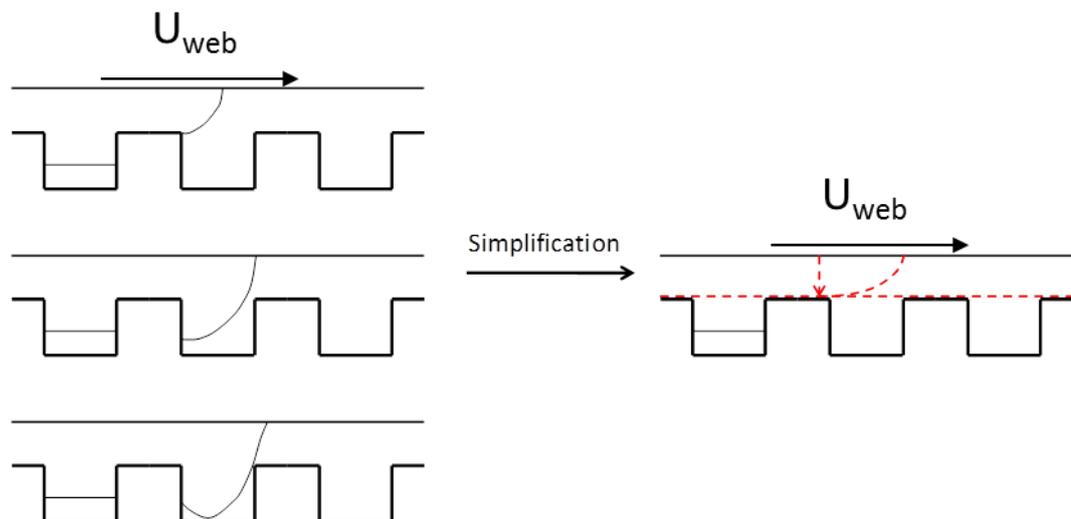
Figure 4.7: An illustration of the smooth roll assumption at the upstream free surface and how it is simplified in section 3.4.3. While dry contact angle is shown in the cell this may not always (or even ever) be the case.

First considering the meniscus location boundary conditions (Equations 3.23 and 3.25), which are calculated using the Bretherton equation (4.1). This equates the meniscus radius of curvature (r) to the web-to-roll gap (Equation 4.2). The ratio of planar film thickness, λ, and meniscus radius of curvature are related by a function of capillary number.

$$\frac{\lambda}{r} = 1.34(Ca)^{2/3}$$ **4.1**

$$g \cong r = \frac{\lambda}{1.34(Ca)^{2/3}}$$ **4.2**

On a gravure topography the assumption that b is planar breaks down at both meniscus to gravure interfaces. These occur at r_2 and r_3 in Figure 4.8 while at r_1 the meniscus forms on the smooth web.

At the upstream position the gravure surface exits the coating bead with partially filled cells, a process that is dynamic with the position of the roll. At the downstream the meniscus with radius r_2 is travelling over a mixture of land, where the film is thin, and over cells where the film is much thicker. Both of these situations are not strictly valid in Equation 4.1 (Bretherton, 1961).
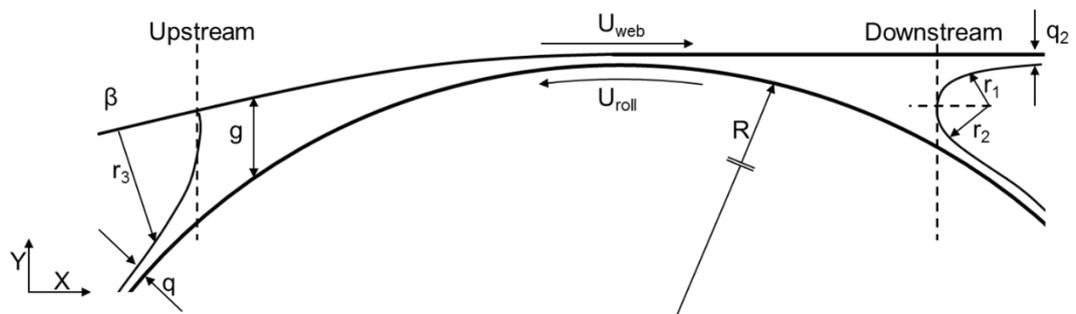
Figure 4.8: Schematic defining the meniscus radii of curvature in the context of the coating bead.

Secondly, considering the Young-Laplace (Equation 4.3) equation is used to obtain the pressure at the menisci. These equations relate the meniscus radius of curvature and the capillary number to determine the pressure across a fluid-fluid interface (here the fluids are air and the coating liquid). The implementation used for Equations 3.26 and 3.27 first assumes that the contact angle at the upstream web interface is 90°. At the downstream location the assumption is that $r_1 = r_2 = 2r_1$. These radii of curvature are then approximated using the web-to-roll gap (Equation 4.4). The dynamic nature of a meniscus passing over a gravure surface means that the actual separation of the web and meniscus changes with the roll.

$$p = \frac{1}{Ca} \times \frac{1}{r} \qquad\qquad \textbf{4.3}$$

$$p \cong \frac{1}{Ca} \times \frac{1}{g} \qquad\qquad \textbf{4.4}$$

As it is clear that the boundary conditions are being poorly represented it is important to quantify what impact this has on the model as a whole. In all cases the relation of web-to-roll gap and meniscus curvature is poor. This is addressed via a sensitivity test which artificially scales the web-to-roll gap and looks at the changes to pickout ratio.

The section investigates the sensitivity of these meniscus boundary conditions looking separately at the upstream and downstream meniscus locations and then at the upstream and downstream meniscus pressure conditions. In each case a scaling variable, α, is introduced that increases/decreases the web-to-roll gap.

4.3.2   Meniscus Location: Upstream

The upstream meniscus features one dry contact angle at the meniscus to web interface. The implementation is defined by Equation 3.23 where the web-to-roll gap is approximated using Equation 4.2. The sensitivity test is

conducted such that the scaling variable, α, is introduced to increase/decrease the web-to-roll gap, g, subject to Equation 4.5.

$$x_{us} = \sqrt{2R(\alpha g - h)}$$

4.5

The limits of the scaling variable are conducted varying α from 0.5 to 5. The results are plotted in Figure 4.9. Over the entire range the pickout ratio is insensitive to α. Physically increasing α becomes increasingly similar to a flooded boundary condition where the meniscus location is very far from the centre of the roller.
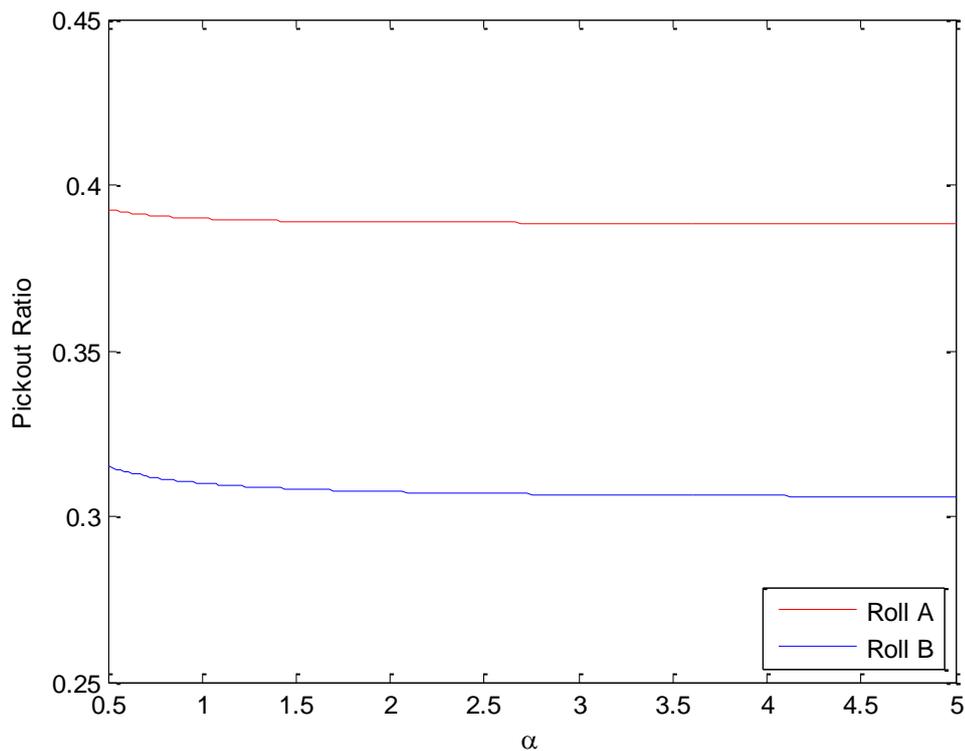
Figure 4.9: Pickout ratio plotted versus scaling variable α. The implemented value of α in the model was 1.

4.3.3 Meniscus Location: Downstream

The downstream meniscus location represents a flow leaving the coating bead on the web (q_2 on Figure 4.8) and an incoming flow in the cells. The web flux component, q_2, forming meniscus curvature r_1 is planar and is well approximated by 4.1. The menisci radius, r_2, which measures to the roll is not planar due to the roll topography. The model approximated these two components by considering both equal to r_1 and equating this to the web-to-roll gap via Equation 4.6.

$$g \cong 2r_1 = \frac{2 \times q_2}{1.34(SCa)^{2/3}S}$$
<div align="right">**4.6**</div>

The scaling variable, α, was implemented to scale the web-to-roll gap over the range 0.1-10 where initially it was equal to two. This adjusts the downstream meniscus boundary condition to the form seen in Equation 4.7 (this is the addition of α to equation 3.22).

$$x_{ds} = \sqrt{2R(\alpha g - h)}$$
<div align="right">**4.7**</div>

The pickout results have been shown in Figure 4.10. The implemented boundary condition is at $\alpha = 2$. With increasing values of α the pickout tends towards an asymptote. With decreasing α there is a reduction in pickout of 6% (Roll A) and 3% (Roll B) from the baseline model. The simulation for Roll B reached a minimum α value of 0.18 instead of the desired 0.1.
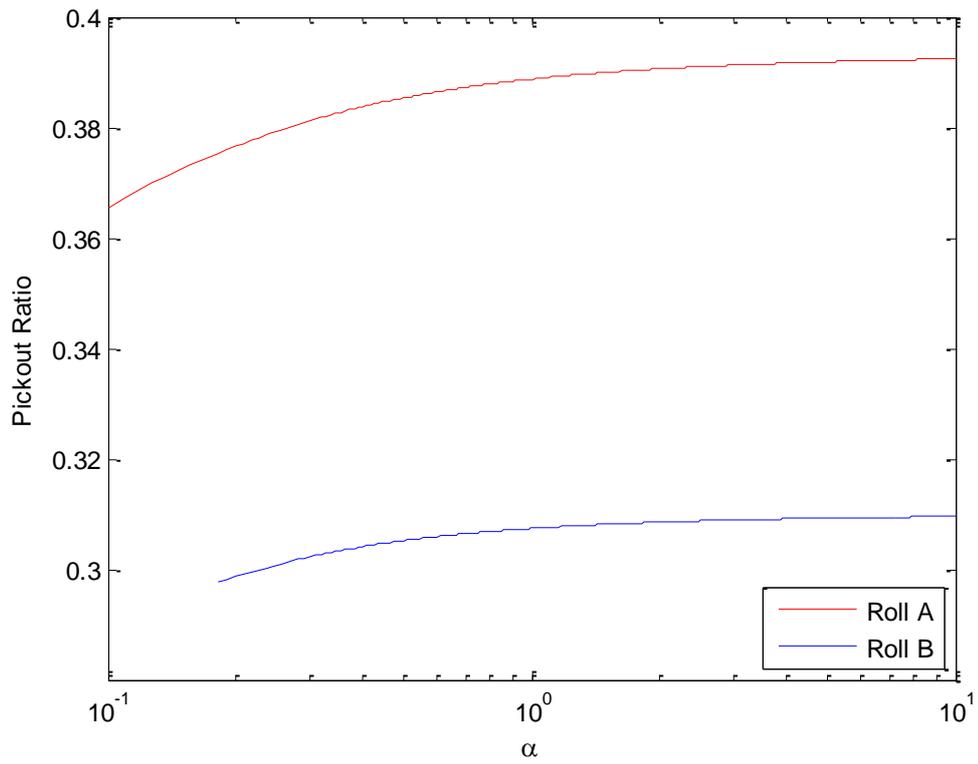
Figure 4.10: Comparison of pickout ratio against α for Rolls A and B. This is implemented into the model at α = 2.

4.3.4   Meniscus Pressure: Upstream

The meniscus pressure is defined by Equation 3.26 at the upstream meniscus. This meniscus has a dry contact angle at the web-air-coating liquid interface. The implementation assumes this contact angle is 90° and that the meniscus radius of curvature can be approximated by the web-to-roll gap as shown by Equation 4.8.

$$p_{us} = \frac{1}{Ca} \times \frac{1}{r_3} \cong \frac{1}{Ca} \times \frac{1}{g} \qquad \textbf{4.8}$$

The topography of the gravure surface means that the validity of equating r_3 and g changes depending on whether the meniscus is over a cell (in which case r_3 is large) or over land (in which case r_3 is small). The scaling variable, α, is used to vary the web-to-roll gap to establish the effect of poorly approximating r_3. The implementation of α is done according to Equation 4.9.

$$p_{us} = \frac{1}{Ca} \times \frac{1}{\alpha g} \qquad \textbf{4.9}$$

The results of varying α over the range 0.5-5 are shown in Figure 4.11. The pickout ratio is shown be insensitive to changes in α above one. Increasing α tends towards a flooded condition where there meniscus pressure approaches zero.

Reduction in α corresponds to a fall in pickout ratio and an asymptotic increase in the magnitude of the pressure while physically this corresponds to a smaller web-to-roll gap.
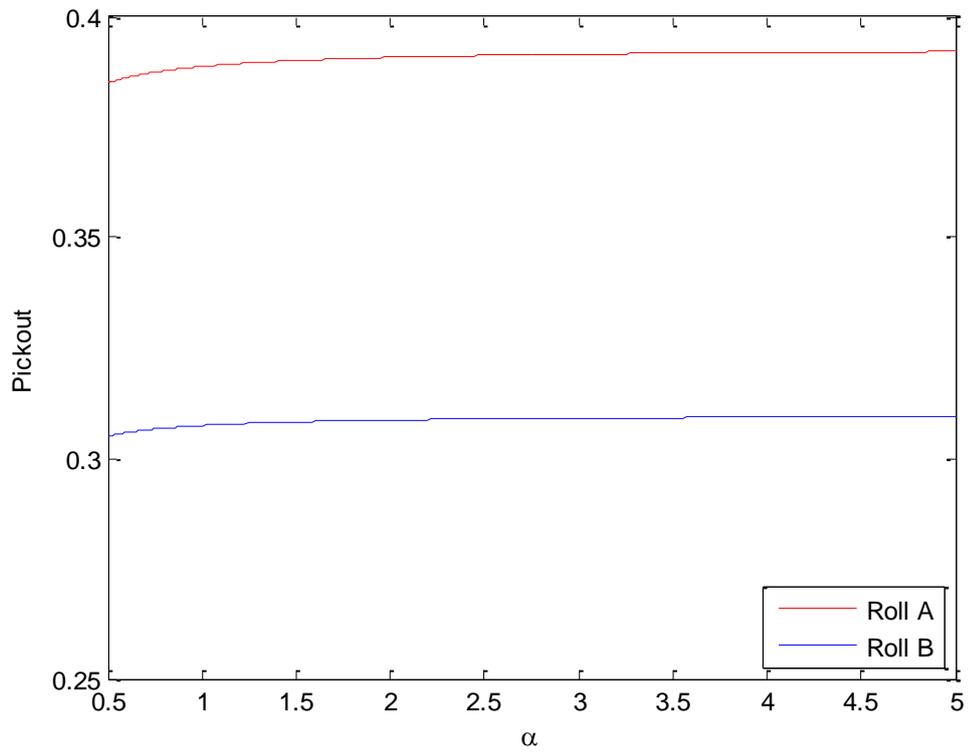
Figure 4.11: The effect of scaling parameter α on the pickout ratio of Roll A and B.

4.3.5   Meniscus Pressure: Downstream

The downstream meniscus location contains the two menisci radii of curvature r_1 and r_2. These are implemented in the model by assuming that $r_1 = r_2 \cong 2r_1 = g$. The r_2 component is affected by the gravure topography because the pool of fluid in cell is inconsistent with an asymptotically thin film which underpins the Young-Laplace equations.

The scaling variable is implemented into the downstream boundary condition according to Equation 4.10.

$$p_{ds} = \frac{1}{Ca} \times \frac{2}{\alpha g} \qquad \textbf{4.10}$$

The results of scaling α over the range of 0.5-5 show that pickout ratio is insensitive to changes in downstream meniscus pressure (Figure 4.12). The result for Roll B was terminated at $\alpha = 0.78$ as it became unsteady.
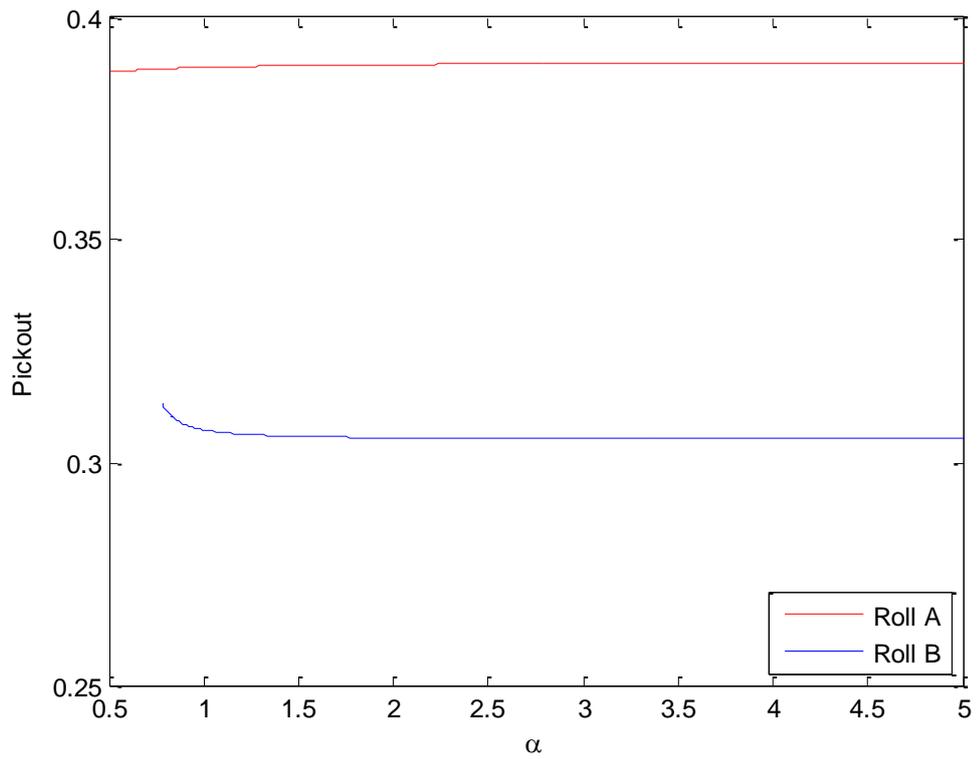
Figure 4.12: Influence of scaling variable, α, on the pickout ratio.

4.4 Discussion

Computational results are presented for a multi-scale model of two discrete cell gravure rolls (A and B). The results show a near linear relationship between pickout ratio and speed ratio. This relationship was also found in a like-for-like comparison with the experimental results from Chapter 2. Despite predicting this relationship the magnitude of the gradient is under predicted by the computational model. The model does qualitatively agree with the experimental results.

The contact model is shown to play an important role in the fluid transfer process with the maximum contact pressure being 7.8 and 29.8 times larger than the maximum fluid pressure for rolls A and B respectively. Roll B has a larger cell size than that of Roll A (refer to Figure 3.13) and corresponding larger small scale coefficients, the most significant of which at very small web-to-roll gaps is the pressure gradient coefficient, a. This is found in the denominator of the governing equation 3.15 which determines the fluid pressure. It also scales approximately cubically with the web-to-roll gap. It therefore suggests that small cells produce a higher fluid pressure in the coating bead than larger ones because they naturally have smaller values of coefficient a. Roll B is more likely to produce low fluid pressure flows due to its larger cells, rough surface and narrow cell walls. To illustrate why coefficient a is smaller for Roll A, consider the comparison between rolls A and B in Figure 4.13. The opening radius of the cells and the cell depth is larger in Roll B. This can also be interpreted as Roll B having less land area.
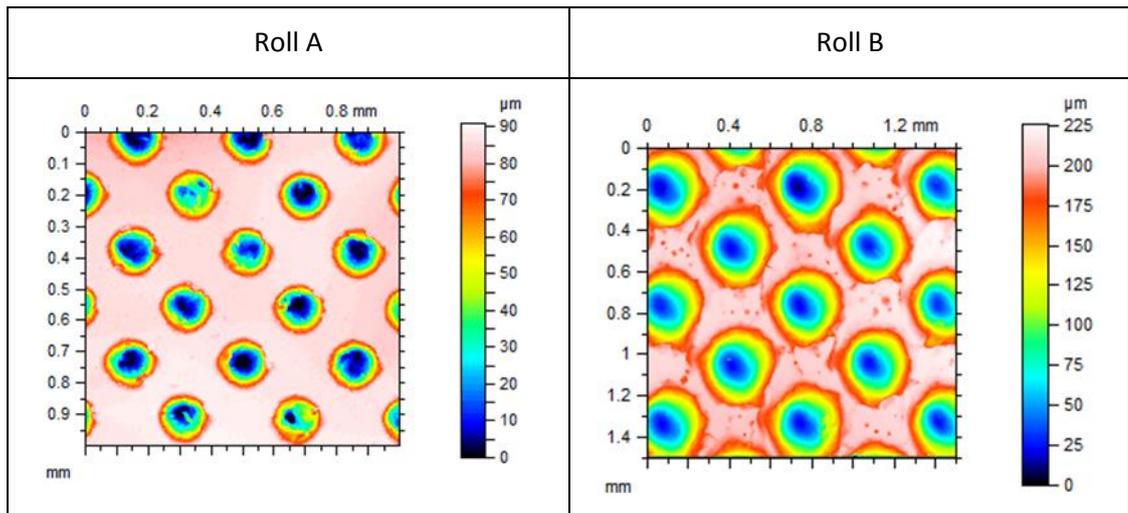
Figure 4.13: Side by side comparison of the surfaces of Roll A and Roll B.

The difference in surface area between the two rolls has been highlighted by digitally removing the lowest components of each roll and only keeping the surface layers. A side by side comparison shows Roll A to have more surface area (Figure 4.14) than Roll B. In the event of web to roll contact it is only the upper surface that will actually be in contact. Consider that the contact length is greater for Roll A (see the length of the contact pressure spike in Figure 4.3 and Figure 4.4) and that it inherently has a greater surface area. Since the pressure gradient coefficient, a, scales approximately cubically with the web to roll gap, Roll A has a higher portion of its surface area at that gap (remembering that web-to-roll gap is measured to the land and not to the base of a cell).
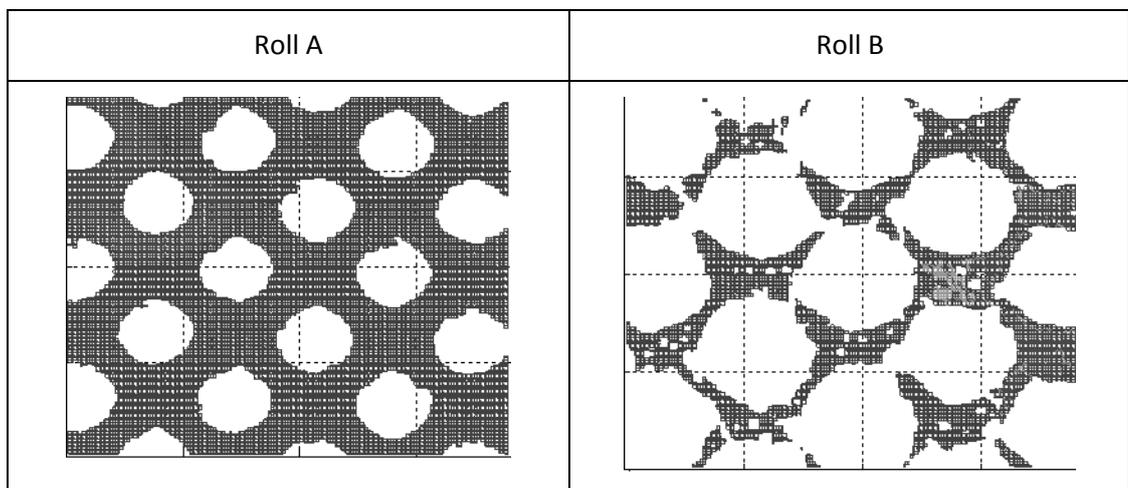
Figure 4.14: Side by side illustration Roll A and Roll B where all but the surface layer has been removed from Figure 4.13.

This is of interest in the context of web scratching because if the fluid can fully support the web then the contact pressure drops to zero and an unscratched web would be expected.

The advantage of the multi-scale model is that it allows the complex topography of the gravure roll to be accounted for in a more robust way than lubrication theory would allow. This advantage does not extend to the boundary conditions, which as implemented still maintain a smooth roll approximation. By considering the sensitivity of the pickout ratio to changes in the boundary conditions it can be highlighted that even though this discrepancy exists at the meniscus boundaries, it does not have a significant impact on the predictive results for common industrially relevant applications where the speed ratio is near unity.

Chapter 5   Parametric Results

5.1   Introduction

In this chapter key parameters are systematically varied to investigate how sensitive the model is to these parameters, with a specific focus on the pickout ratio result. In the first section (5.2), attention is focused on coating parameters (wrap angle, capillary number etc.) which are dealt with in the large scale. The second section (5.3) varies the gravure cell geometry which is dealt with in the small scale. The final section is an investigation of the sensitivity of the large scale boundary conditions to establish the importance of neglecting cell geometry at the boundaries.

For convenience the following sections refer back to an initial set of results, termed the "baseline results".

5.1.1   The Baseline Results

As this chapter presents results over a changing parameter space, it is useful to have a constant set of data for comparison. These are drawn from the baseline model presented here. The parameters for the baseline model are shown in Table 5:1. Each parameter variation in the following section will assume to have started from these results unless otherwise stated. The pickout ratio against speed ratio graph for the baseline model is shown in Figure 5.1.

Table 5:1: Baseline parameters

Parameter	Value	Value (dimensionless)
Web Tension	1000 N/m	1227000
Wrap Angle (β)	0°	0
Capillary Number (Ca)	-	0.0204
Roll Radius (Roll A/Roll B)	0.05m/0.05m	200/111
Mesh Angle (Cell Patterning)	45°	45°
Characteristic Length, L, (Roll A/Roll B)	$2.5 \times 10^{-4}/4.5 \times 10^{-4}$ m	1/1
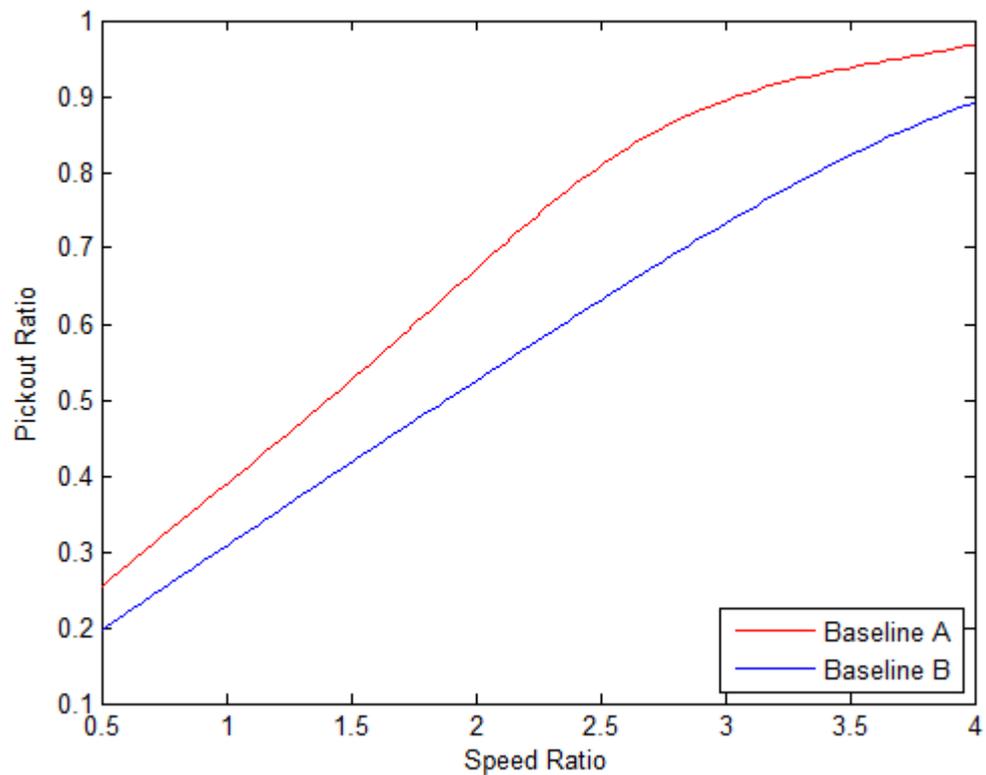
Figure 5.1: Pickout against speed ratio for the baseline models A and B. These results have been taken from Chapter 3 where the upstream wrap angle has been set to zero.

5.2   Coating Parameters (Large Scale)

5.2.1   Web Tension

The non-dimensional web tension was varied from $t = 10000$ (8.15 N/m) to $t = 10,000,000$ (8150 N/m) which have been made non-dimensional using Equation 3.5. A typical tension used in industry is 1000 N/m (Kapur, 1999) which corresponds to $t = 1,227,000$ in non-dimensional units. On an industrial scale the web tension is not used to control the film thickness, but is determined by upstream and downstream web stretching.

The results are shown in Figure 5.2. It is clear that for industrially relevant tensions there is no significant effect on the pickout ratio. This remains the case as web tension increases. Figure 5.3 shows a corresponding increase in the contact pressure component, that is pressure from web-to-roll contact rather than fluid pressure in the coating bead.

The pickout ratio becomes sensitive to changes in web tension when it is much smaller than the baseline model. These points are at $t = 515602$ and $t = 132661$ for Roll A and B respectively.
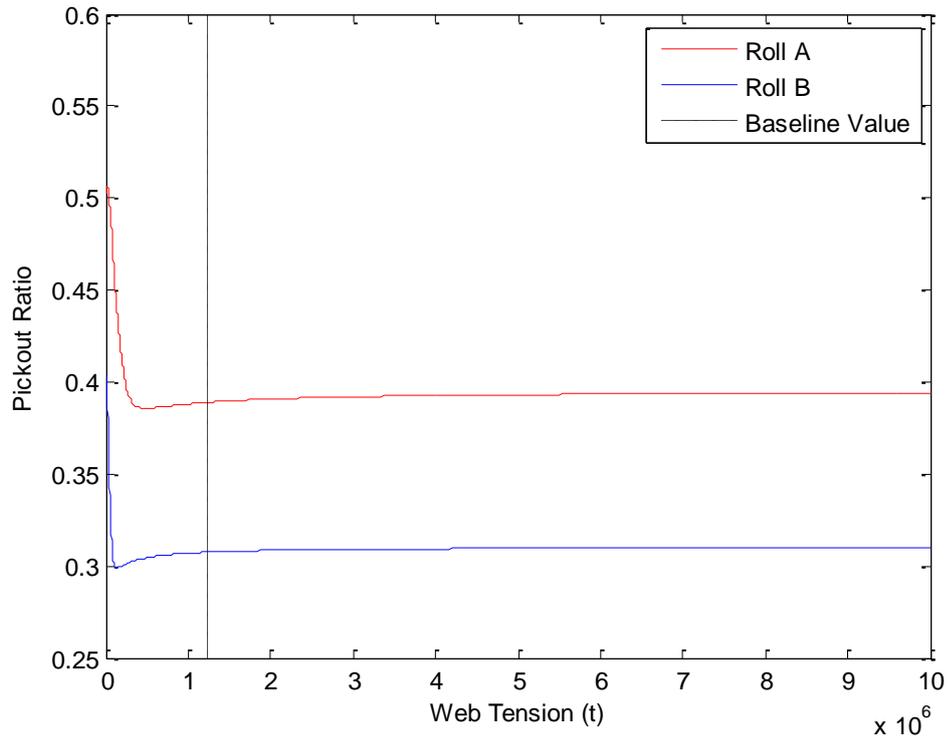
Figure 5.2: Depicts how the pickout ratio varies with web tension for rolls A and B.
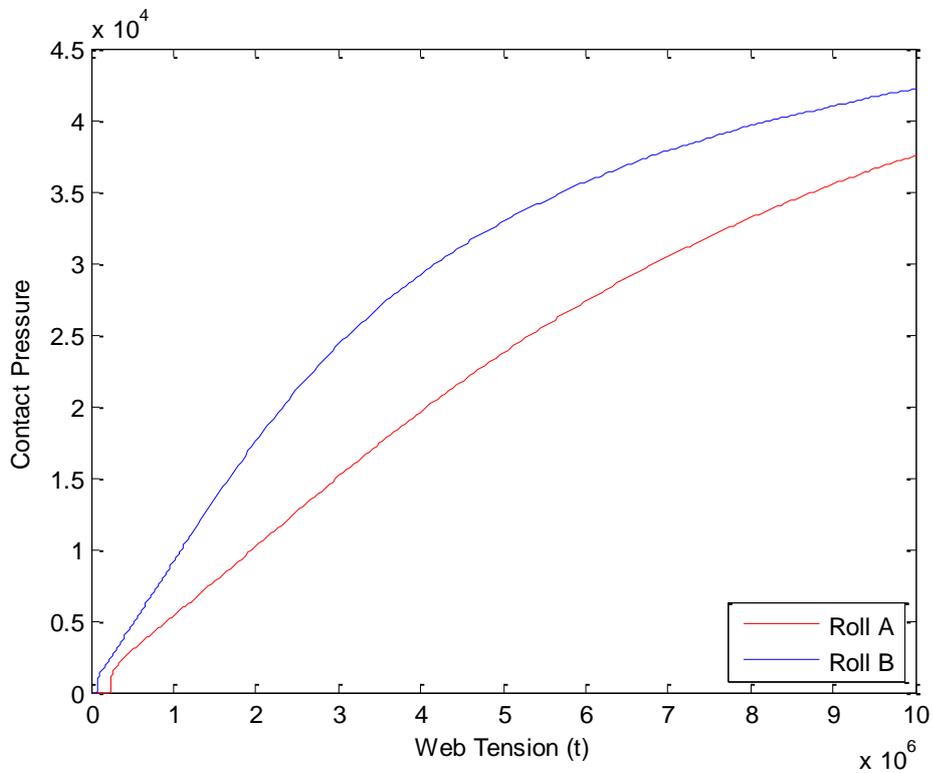
Figure 5.3: Contact pressure varying with web tension for rolls A and B. Very low web tensions experience no contact.

An examination of the pressure profile (i.e. an indication of how the pressure varies along the length of the coating bead) is useful in determining at what tension web-to-roll contact occurs. Figure 5.4 shows how the coating bead pressure profile varies with web tension for rolls A and B. The minimum pickout value is marked by A2 and B2, A3 and B3 correspond to the baseline result. The limits of the simulation are marked by A1, B1 and A4, B4.

As web tension increases beyond the minimum point (A2, B2) the fluid pressure profiles through the coating bead remains mostly constant (a decrease in maximum fluid pressure from 900 to 700 occurs from points A2 to A4 and from B2 to B4). The additional load induced by the increase in web tension is supported by the gravure roll in the form of contact pressure (Figure 5.5) which experiences an order of magnitude increase from points A2, B2 to A4, B4.

At points A1 and B1 the fluid pressure is large enough to support the web. With reference to Figure 5.6 and Figure 5.7, which show the relative position of the web and the gravure roll surface, it is shown that the web-to-roll gap is maintained at points A1 and B1. A region of constant positive bead pressure forms. This result bears a striking resemblance to that found by Hewson et al (2011) whom also modelled low pressures in a gravure coating bead. The results presented in that study are for cells 80%-90% smaller than those here but both cases suggest a coating bead pressure profile containing a long region of constant gap followed a downstream pressure ripple indicating that the web is being deformed by the fluid pressure. As web tension increases at points A2 and B2 this gap drops to zero signifying that the fluid pressure is insufficient to maintain a separation of web and roll and leads to the onset of contact pressure.
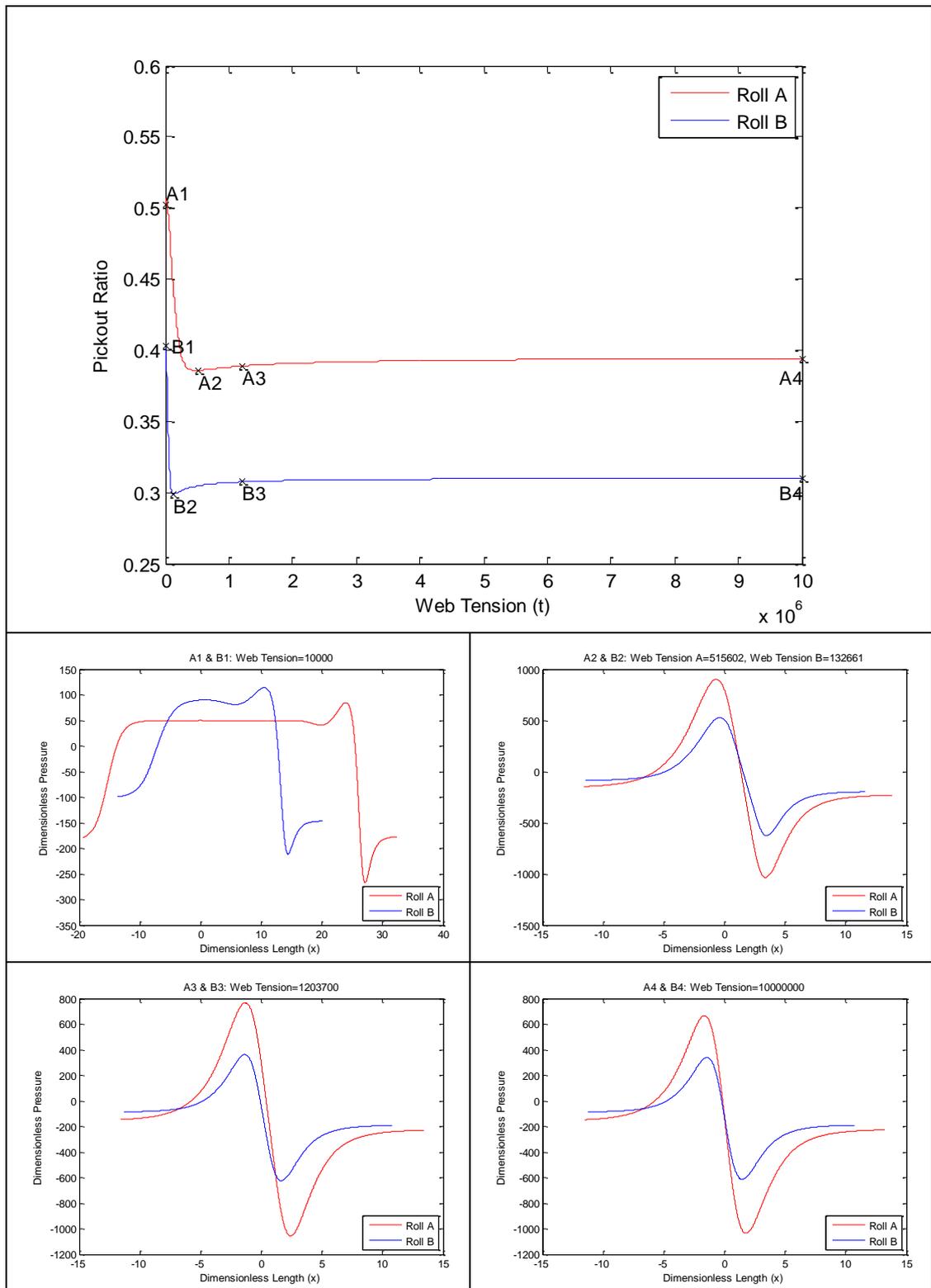
Figure 5.4: The top diagram indicates the change in pickout ratio with web tension; the subsequent four graphs depict how the fluid pressure profile in the coating bead varies as the tension changes. A2 and B2 are the minimum pickout condition; A3 and B3 correspond to the baseline result. A1, B1, A4 and B4 are the limits of the simulation.
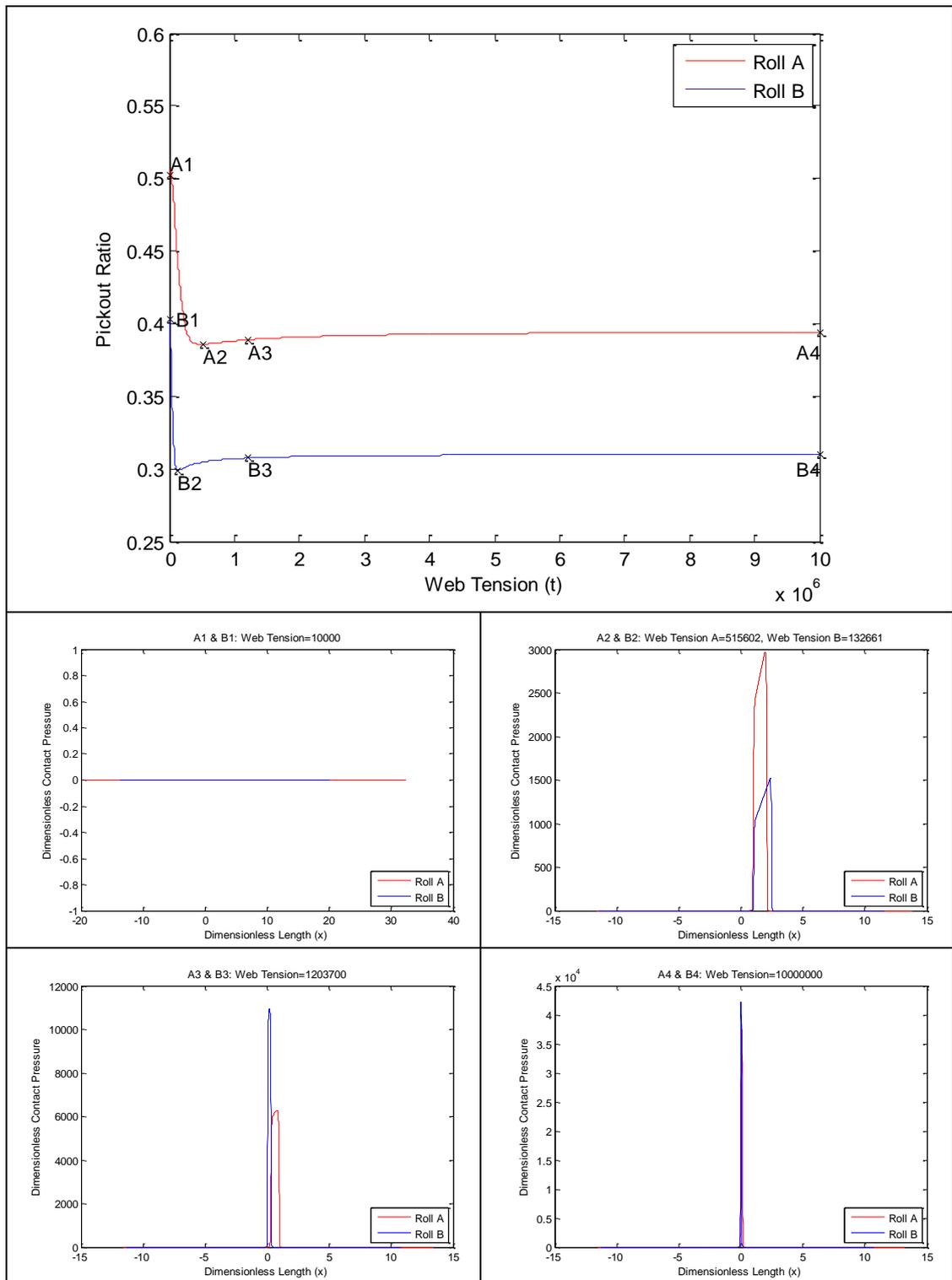
Figure 5.5: The top diagram indicates the change in pickout ratio with web tension; the subsequent four graphs depict how the contact pressure increases with increasing tension. A1 and B1 have no contact component. A2 and B2 are the minimum pickout condition; A3 and B3 correspond to typical industrial values. A1, B1, A4 and B4 are the limits of the simulation.
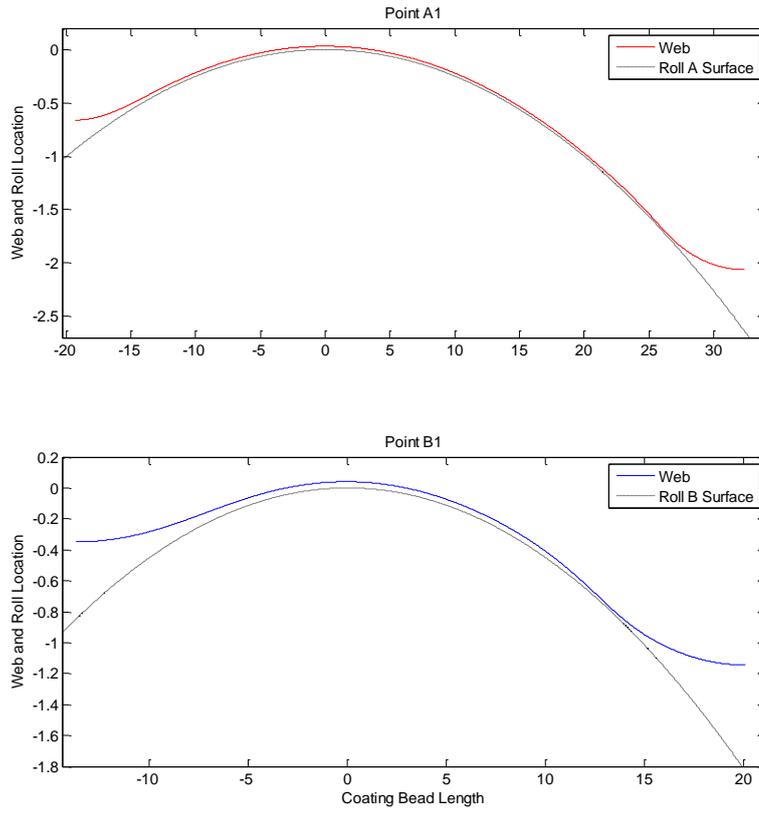
Figure 5.6: Web and roll locations at points A1 and B1 on Figure 5.4 (t =10000).
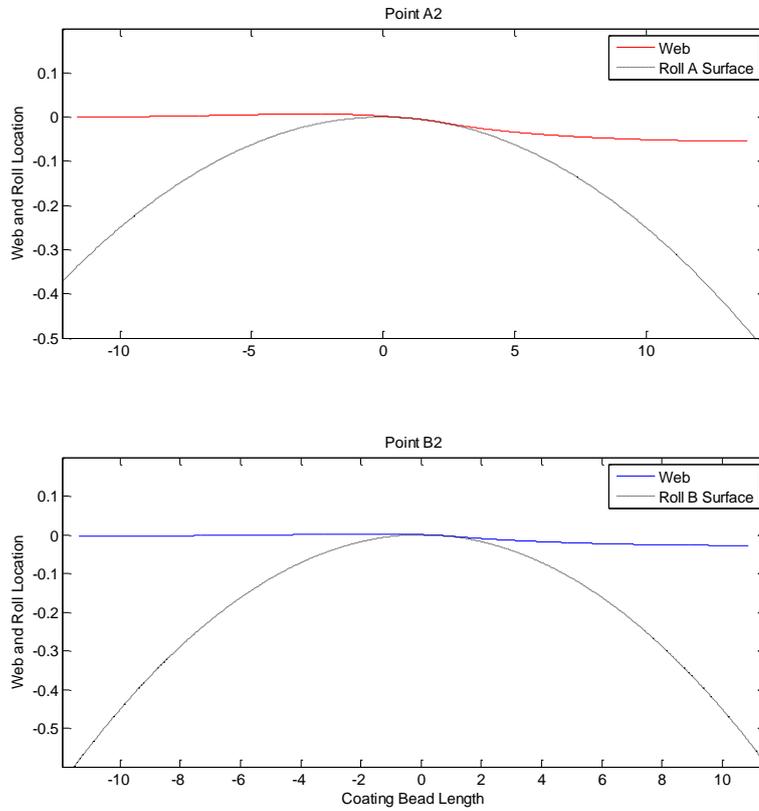
Figure 5.7: Web and roll locations at points A1 and B1 on Figure 5.4 (t =10000).

5.2.2 Wrap Angle

The wrap angle was adjusted at the upstream web entering the coating bead. An increase in wrap angle corresponds to an increasing web induced load on the roll given by $T sin(\beta)$ where β is the wrap angle and T is the web tension. Figure 5.8 shows the web location along the length of the coating bead for the range of wrap angles simulated in this parametric study.

For both rolls the upstream wrap angle was varied from 0 to 5 degrees. This changes the gradient of the web entering the coating bead at the upstream (note: wrap angle is only ever applied in practice at the upstream). Any downstream changes were negligible.
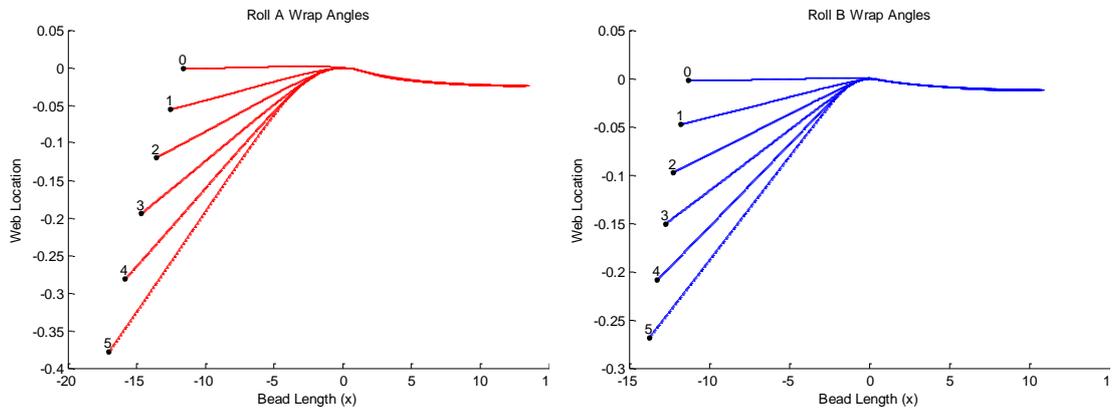
Figure 5.8: Both plots depict the web location at wrap angles from 0 to 5 degrees (as indicated on each graph) with Roll A on the left and Roll B on the right.

Referring to Figure 5.9 and Figure 5.10 it can be seen that both fluid and contact pressures increase with wrap angle. The effect this contact has on the coating bead is evident in Figure 5.11 with wrap angles at zero degrees and Figure 5.12 with wrap angles at 5 degrees. The contact effectively de-couples the upstream from the downstream boundary. Under similar circumstances some authors have found two isolated counter rotating flow regions (Rees (1995), Figure 1.13). The contact length also increases with the wrap angle.
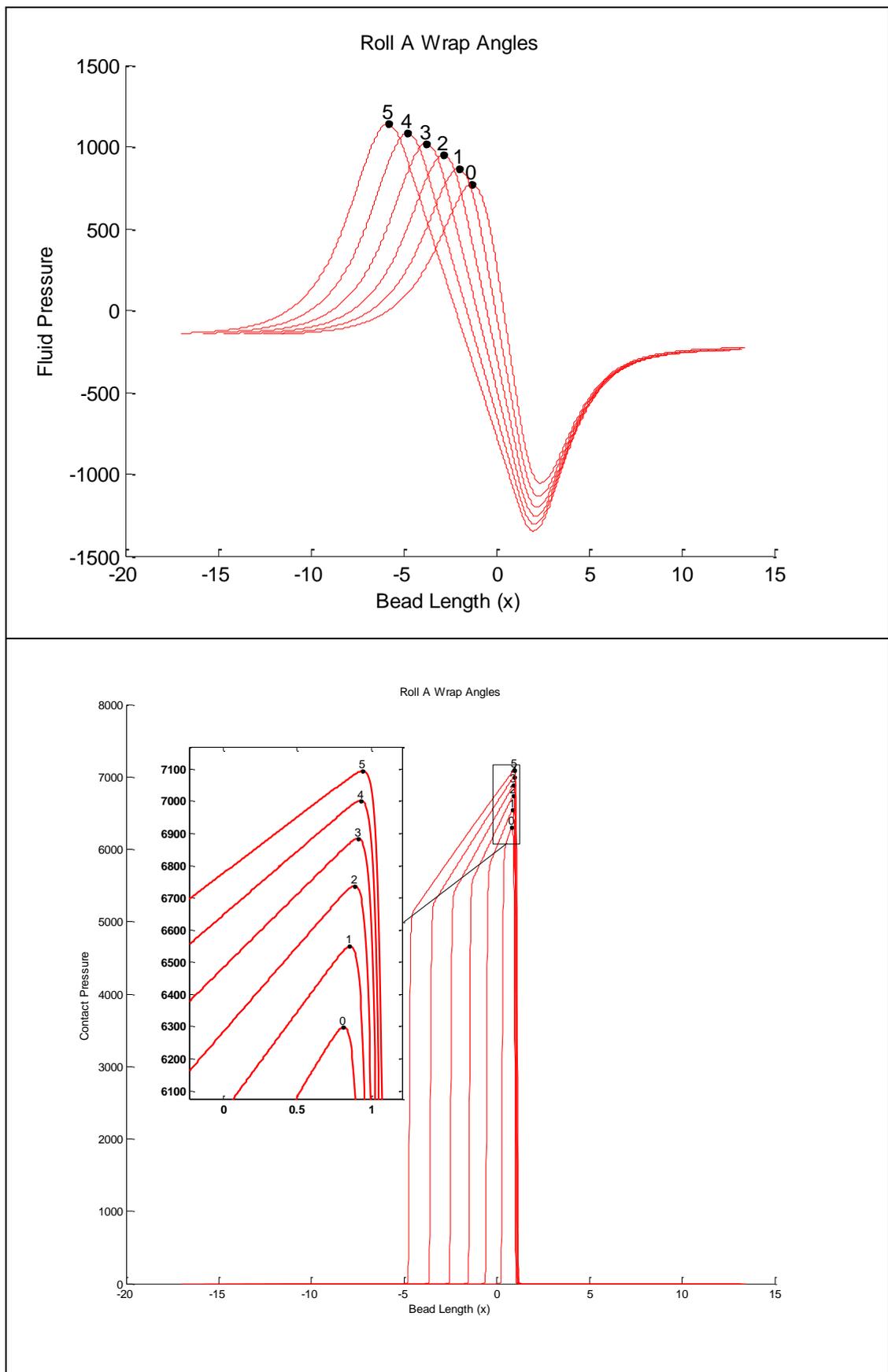
Figure 5.9: These figures depict the influence of wrap angle on fluid pressure (top) and contact pressure (bottom) for Roll A.
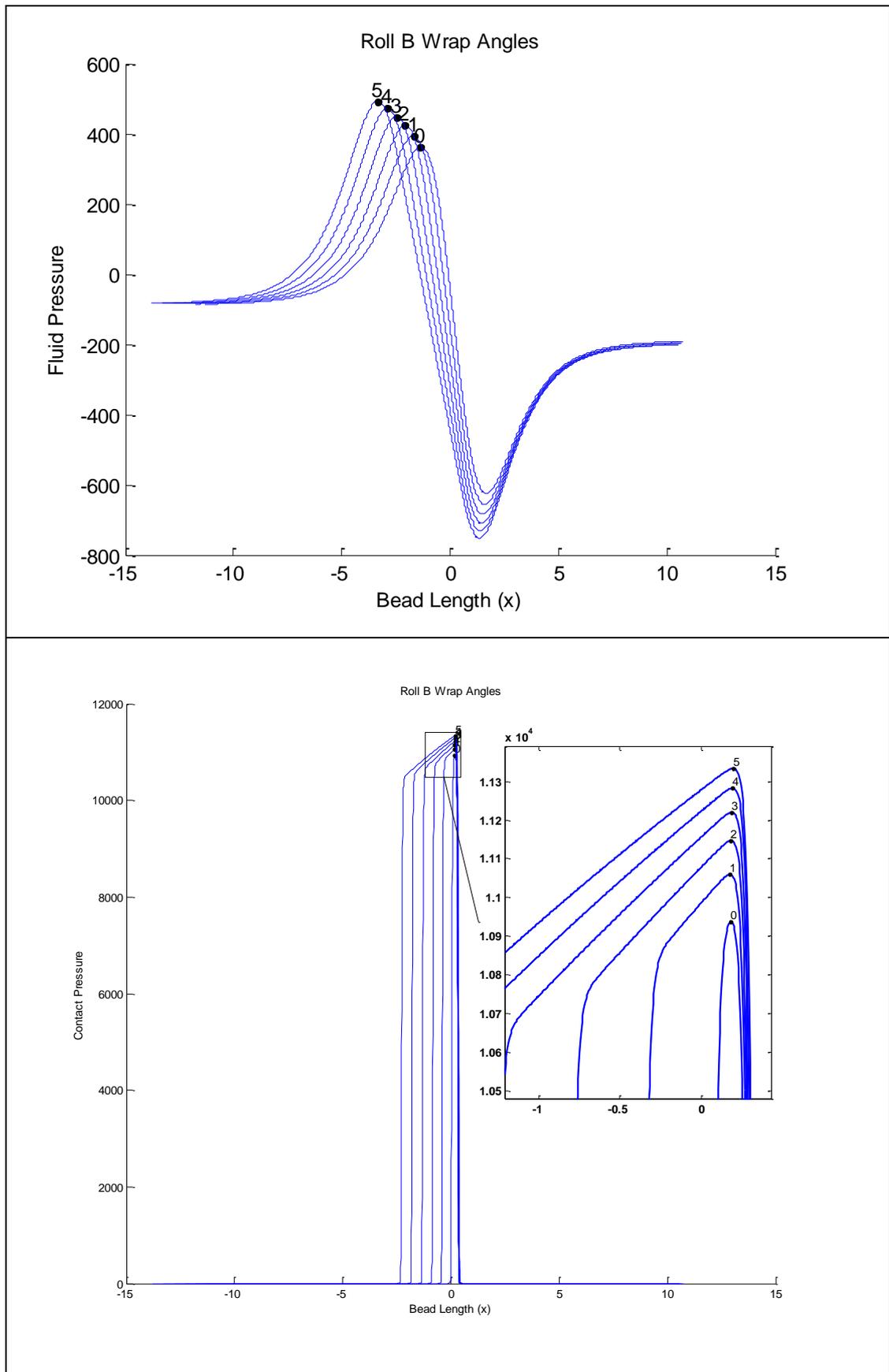
Figure 5.10: These figures depict the influence of wrap angle on fluid pressure (top) and contact pressure (bottom) for Roll B.
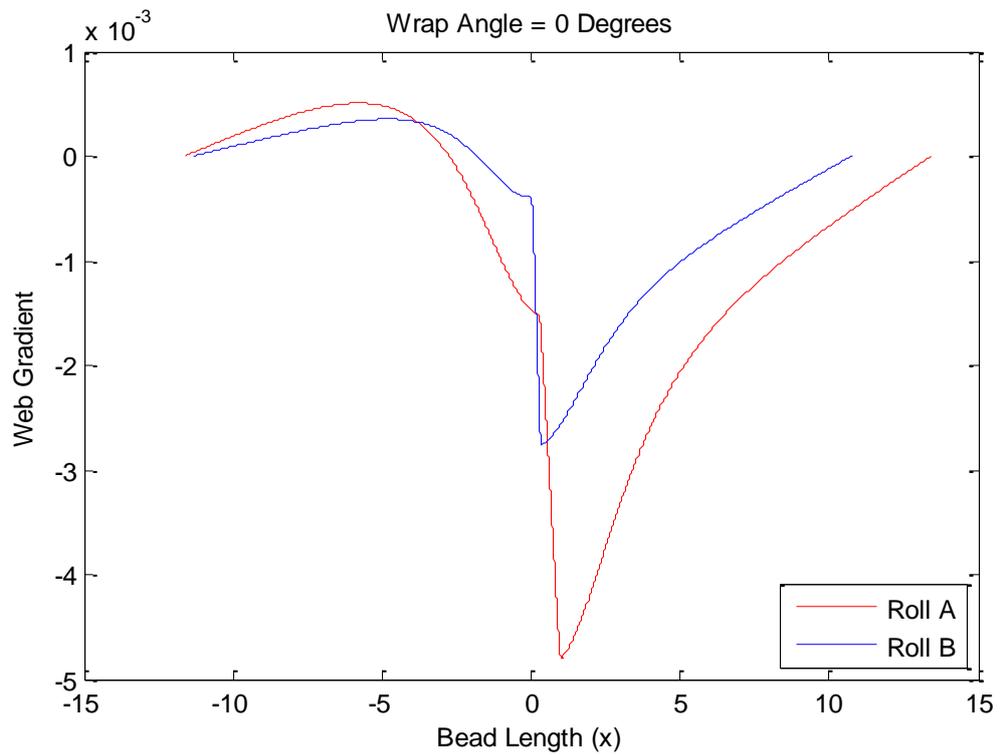
Figure 5.11: Web gradient against coating bead length. The central linear region indicates the contact region.
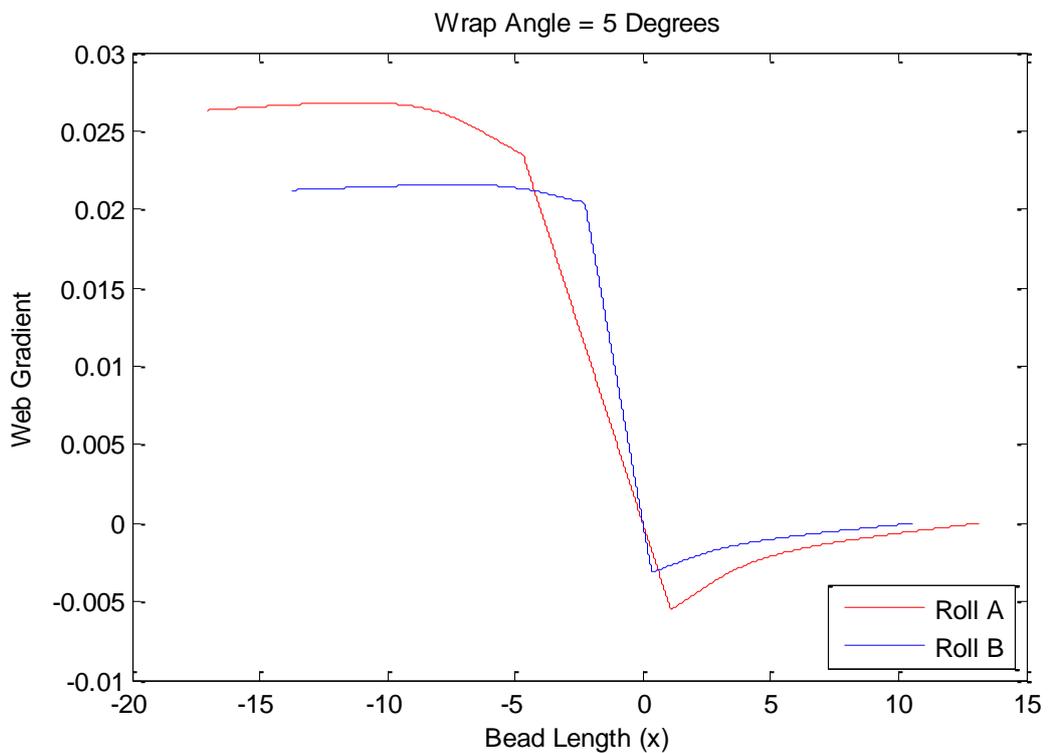
Figure 5.12: Web gradient against coating bead length. The central linear region indicates the contact region.

The pickout ratio shows a very small decrease with increasing wrap angle. This result was also found experimentally by Kapur (1999). Benkreira & Patel (1993) tested a range of 0-12 degrees wrap angle and found no significant change in film thickness.
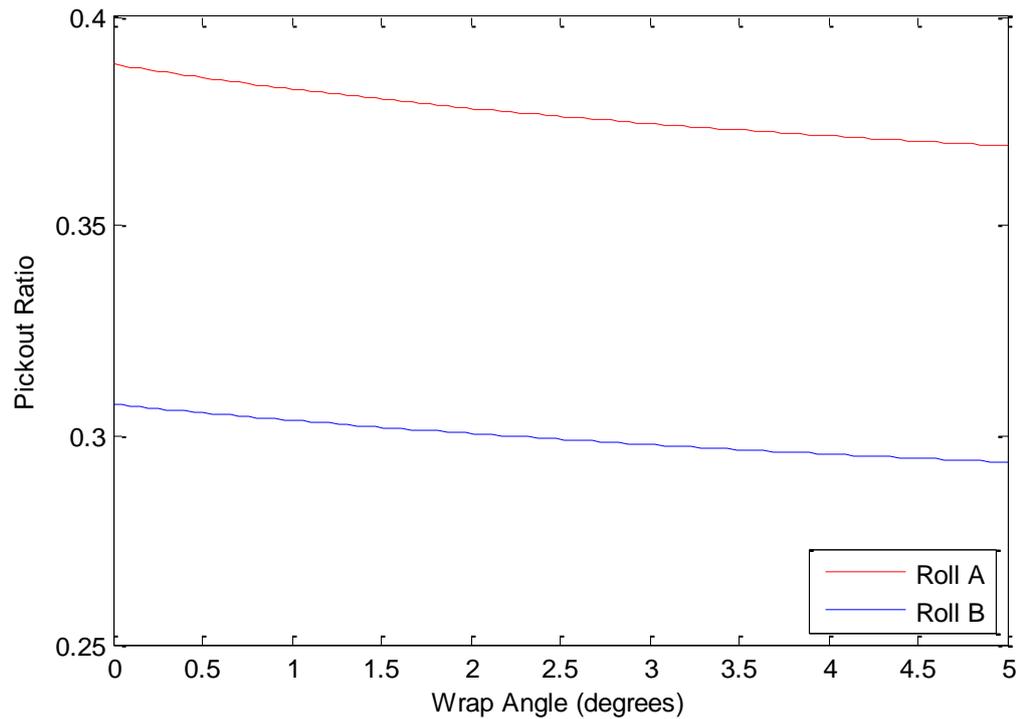
Figure 5.13: Pickout ratio variation with wrap angle for Rolls A and B.

5.2.3   Capillary Number

The capillary number (equation 5.1) is the non-dimensional number relating the relative effect of fluid viscosity (η), surface tension (γ) and some characteristic speed (U_{roll}). It is currently employed in the Landau-Levich and Bretherton boundary conditions to find both the meniscus pressure and location (equations 3.23, 3.25, 3.26 and 3.27). Viscosity terms are also used to make the web tension and the pressure terms non-dimensional while the characteristic speed is used in the non-dimensional speed ratio term. Industrially the viscosity is varied by changing the concentration of solid particles in the coating solution. This allows the dry coat thickness to be scaled.

$$Ca = \frac{\eta U_{roll}}{\gamma} \qquad \textbf{5.1}$$

Here, the capillary number was varied from 0.001 to 0.1. At small capillary numbers (i.e. below 0.01) the pickout ratio is predicted to increase with increasing capillary number. For all larger capillary numbers the change in pickout ratio is negligible (Figure 5.15 and Figure 5.18). This trend is exhibited by both rolls.

The experimental investigation by Patel & Benkreira (1991) suggested a relation between capillary number and film thickness that increases rapidly when the capillary number is low and plateaus at higher capillary numbers. However, it is unclear what influence other parameters had on this result. Subsequent work by Kapur (2003) removed this ambiguity and observed a secondary relationship between increasing pickout ratio with increasing capillary number (web-to-roll speed ratio being the primary relation between the two). At a speed ratio of one the study varied capillary number from 0.02-0.08 and observed that a 1% increase in capillary number caused an approximate 0.3% increase in pickout ratio.

The use of Landau-Levich and Bretherton boundary conditions has been shown to predict appropriate sensitivity to capillary number in rigid smooth roll cases [(Benjamin, et al., 1995) (Gaskell, et al., 1995), (Summers, et al., 2004)], smooth roll cases with a tensioned web (Gaskell, et al., 1998) as well as smooth cases with a deformable roll (Carvalho & Scriven, 1997). The ability of these equations to predict appropriate sensitivity to capillary number does not appear to extend to the gravure case observed by Kapur.

Interestingly the fluid pressure in the coating bead shows the same trend exhibited in the earlier work of Gaskell et al (1998) where the maximum and minimum value of fluid pressure decreases with increasing capillary number Figure 5.16 and Figure 5.17.
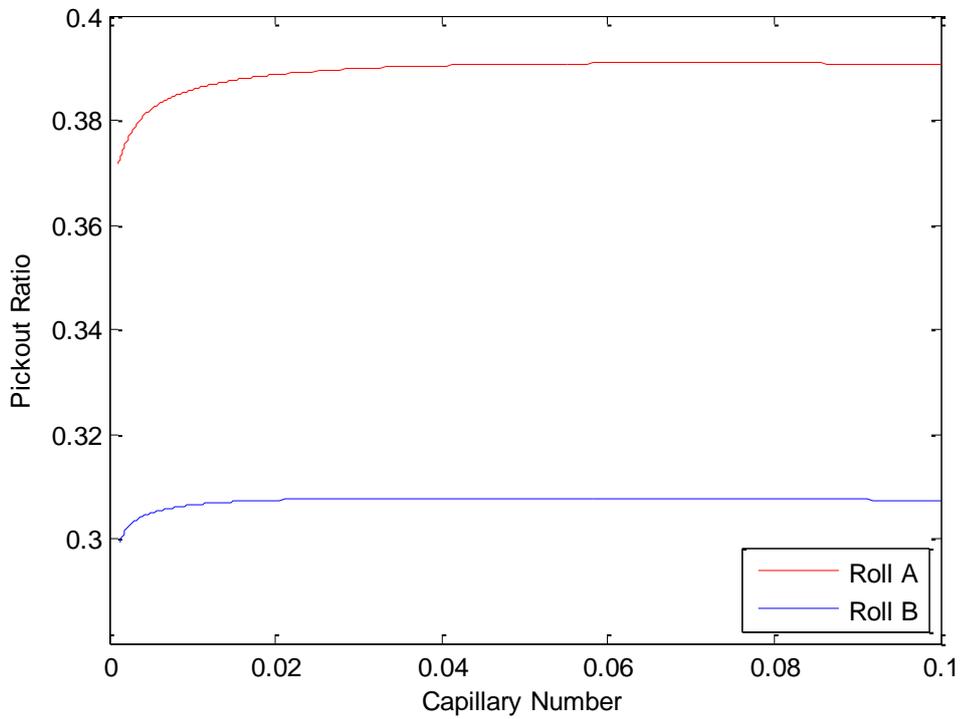
Figure 5.14: Pickout ratio against capillary number for rolls A and B at a speed ratio of one.
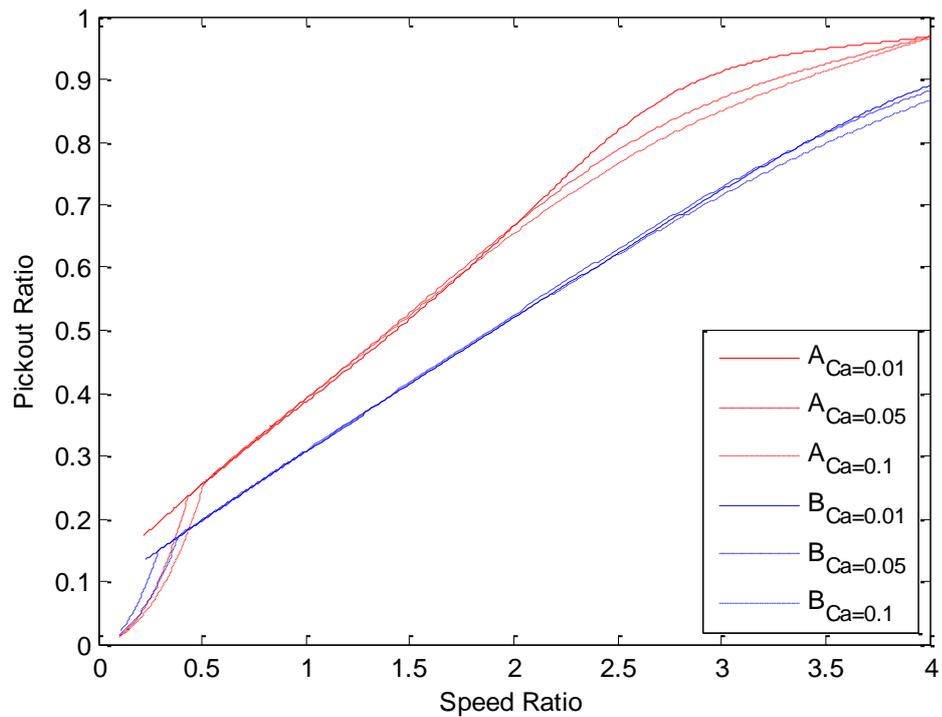
Figure 5.15: Pickout ratio against speed ratio for rolls A and B at capillary numbers of 0.01, 0.05 and 0.1.
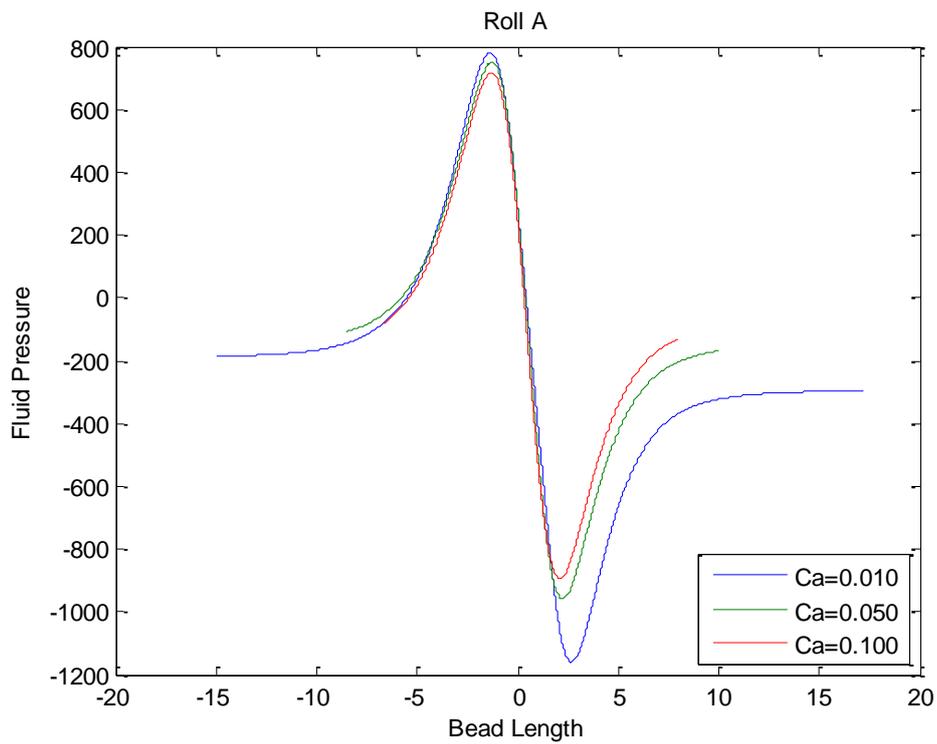
Figure 5.16: Fluid pressure varying along the coating bead for Roll A at S=1.
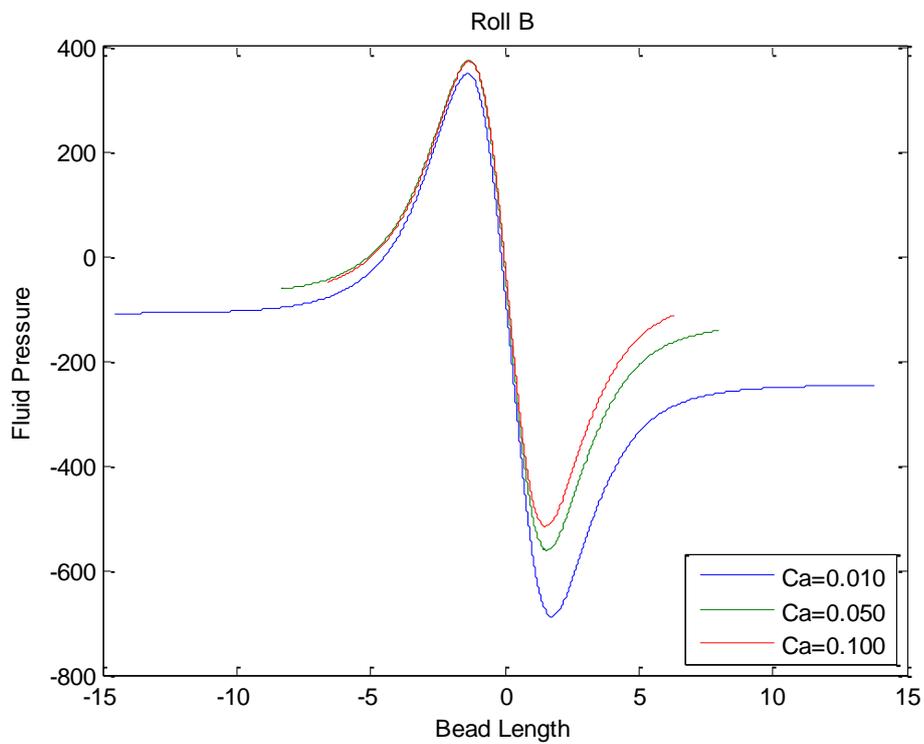
Figure 5.17: Fluid pressure varying along the coating bead for Roll B at S=1.

There is a sharp change in the gradient of Figure 5.15 below S=0.5 which corresponds to the contact pressure dropping to zero. The contact pressure at a given speed ratio can be seen in Figure 5.19.

With reference to the results below a speed ratio of 0.5 in Figure 5.15 it is unclear from that diagram if the capillary number has an effect when there is no contact pressure. To clarify this Figure 5.20 was created to show pickout ratio over the range of speed ratios 0.5 to 4 at a web tension of $t = 10000$. At this reduced web tension there is no contact (see Figure 5.19). However, even at this web tension value the capillary number has a negligible effect on the pickout ratio (Figure 5.20).
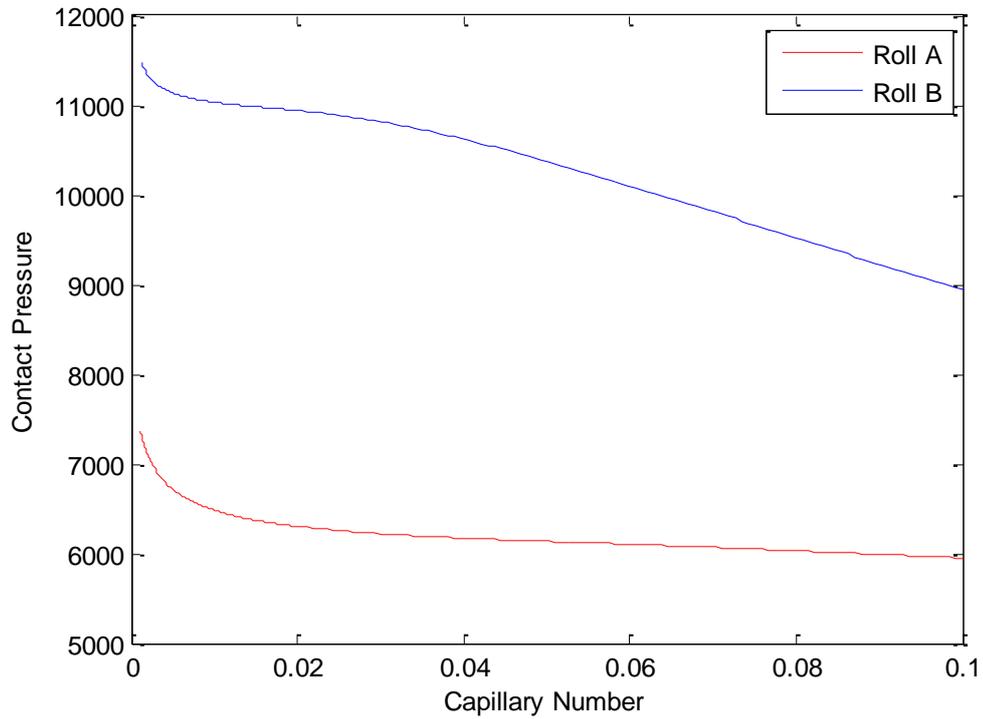
Figure 5.18: Contact pressure between the web and roll against capillary number at a speed ratio of one.
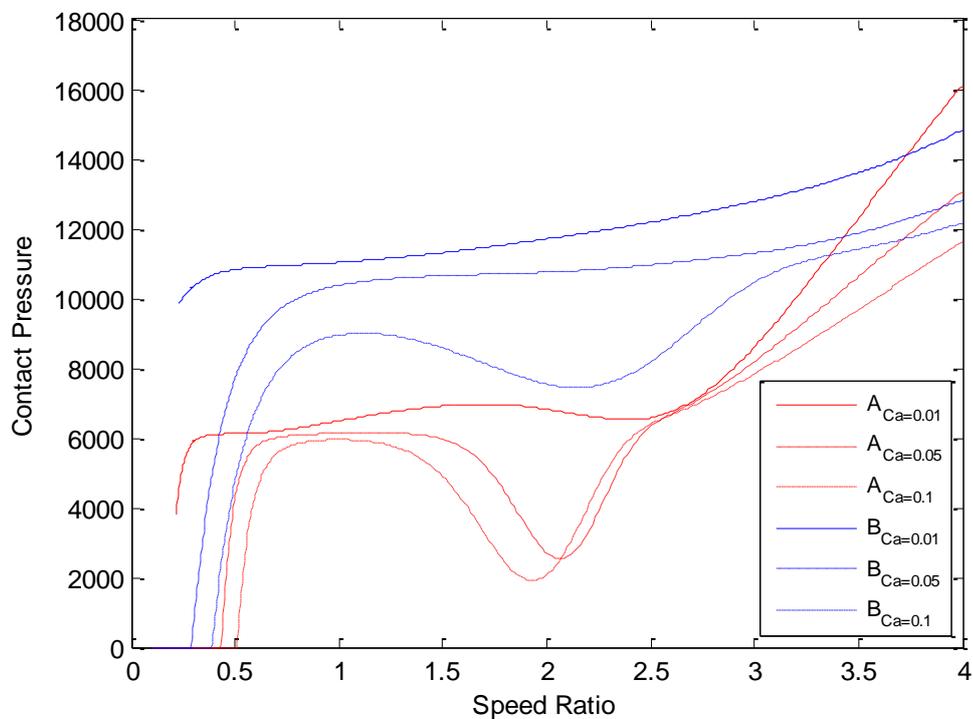
Figure 5.19: Contact pressure against speed ratio at capillary numbers of 0.01, 0.05 and 0.1. The wrap angle was zero and the web tensions was t =1203700 (1000 N/m).
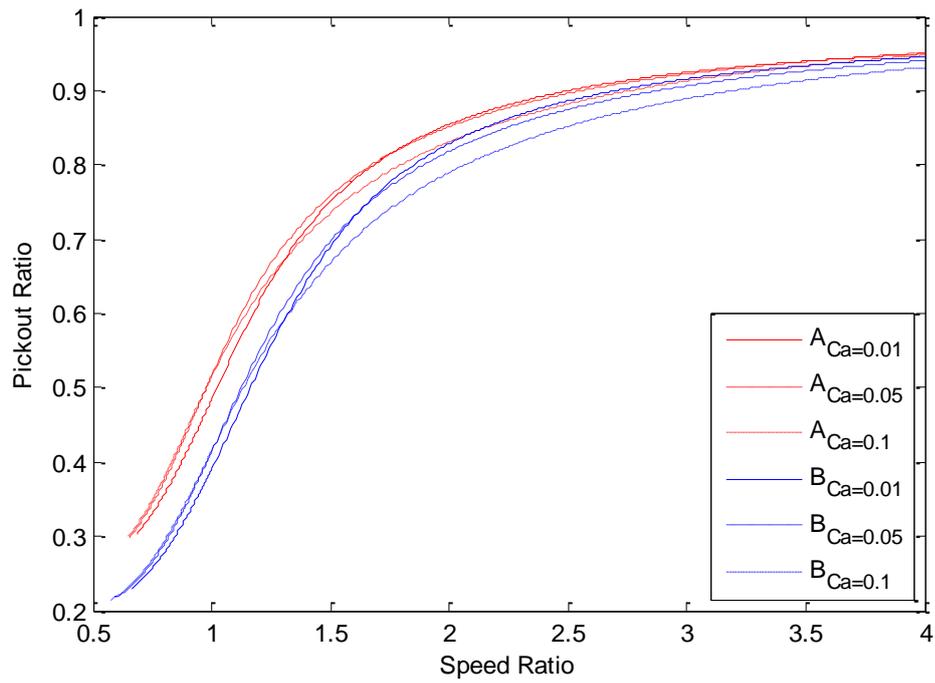
Figure 5.20: Pickout ratio against speed ratio for rolls A and B at the indicated capillary numbers. The web tension has been set to $t = 10000$ which reduces the contact pressure to zero near speed ratios of one.

5.2.4   Roll Radius

The baseline model approximates the cylindrical roll surface using the parabolic expression in Equation 5.2. The impact on pickout ratio of varying the roll radius is shown in Figure 5.21. The pickout response is insensitive until the contact pressure drops to zero (also shown in Figure 5.21), after which pickout increases with increasing roll radius.

There are two different ways of looking at a change in roll radius. The first (and most obvious) is simply that the roll is getting larger/smaller. The second has to do with how it was made non-dimensional. An increase in the roll radius is equivalent to a reduction in the characteristic length which means these results are also relevant to having varied the cell size at a fixed roll diameter. The present simulation can be interpreted as a change in roll radius of $100L \rightarrow 1000L$ or change in characteristic length of $5 \times 10^{-4}m \rightarrow 5 \times 10^{-5}m$.

$$\text{Roll}_{\text{surface}} = \frac{x^2}{2r}$$

5.2
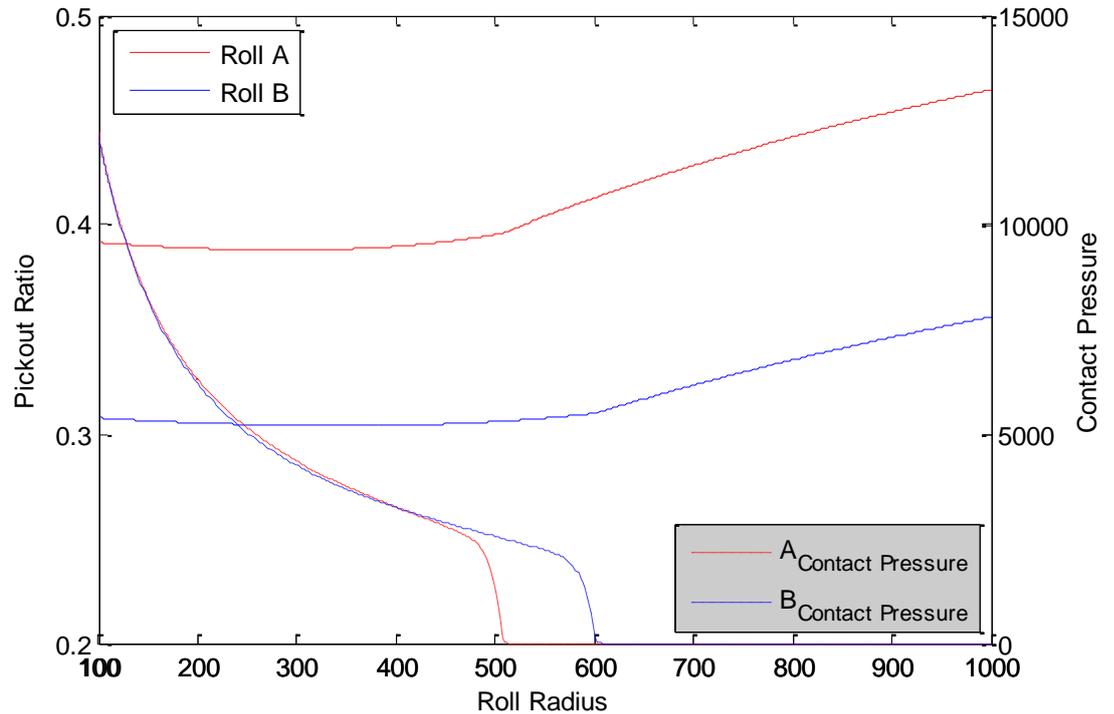
Figure 5.21: Dependence of pickout from Rolls A and B against the roll radius. Left axis shows the pickout ratio while the right axis shows the contact pressure. When contact pressure drops to zero the gradient of pickout ratio increases.

With reference to Figure 5.22 it can be seen that the length of the coating bead increases as the roll radius increases. The points P1 and P2 on Figure 5.22 indicate the two extremes of the simulation. Comparing P1 profiles (Figure 5.23, Figure 5.24 and Figure 5.25) to P2 profiles (Figure 5.26, Figure 5.27 and Figure 5.28) shows:

- Increased length of coating bead. There is no significant change in the web-to-roll gap at the up and downstream boundaries due to changing the roll radius. The coating bead extends to meet the existing boundary conditions.
- Change in shape of the profiles due to lack of web-to-roll contact while fluid pressure rises with increasing roll radius. The maximum fluid pressure doubles from P1 to P2 (see Figure 3.23 and Figure 3.26).
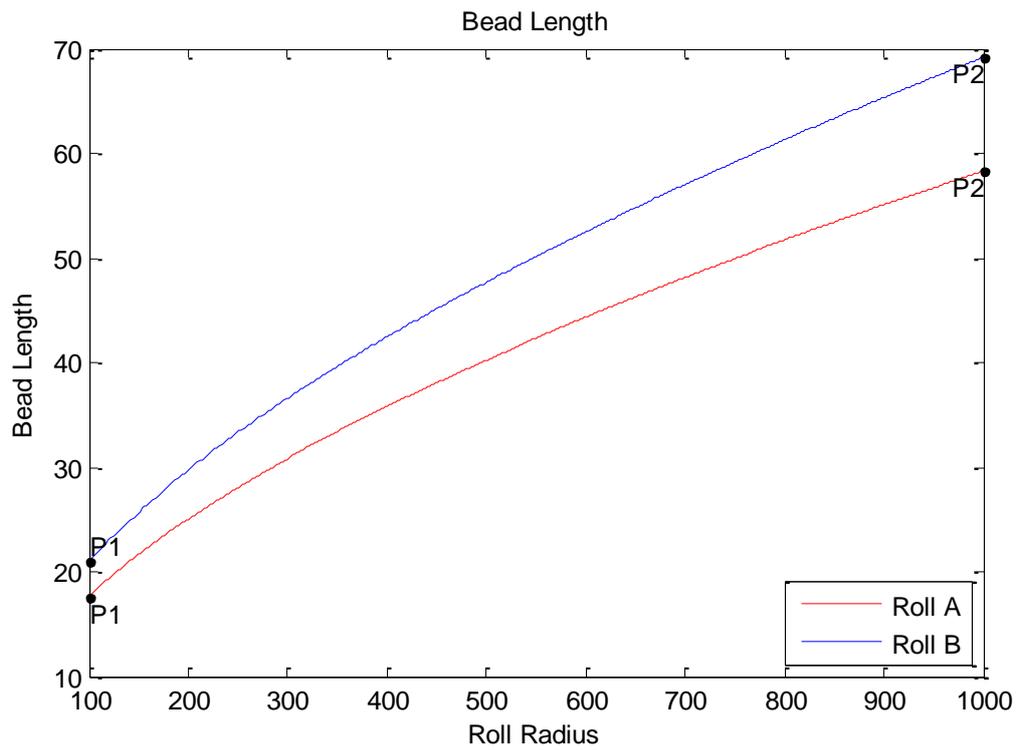
Figure 5.22: Coating bead length increasing with radius of the roll.
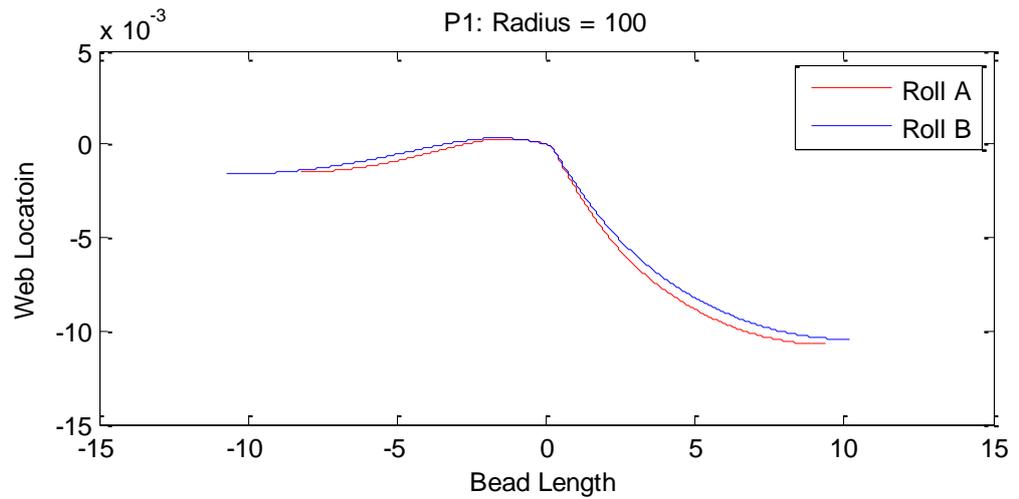
Figure 5.23: Web location profile at P1 from Figure 5.22.
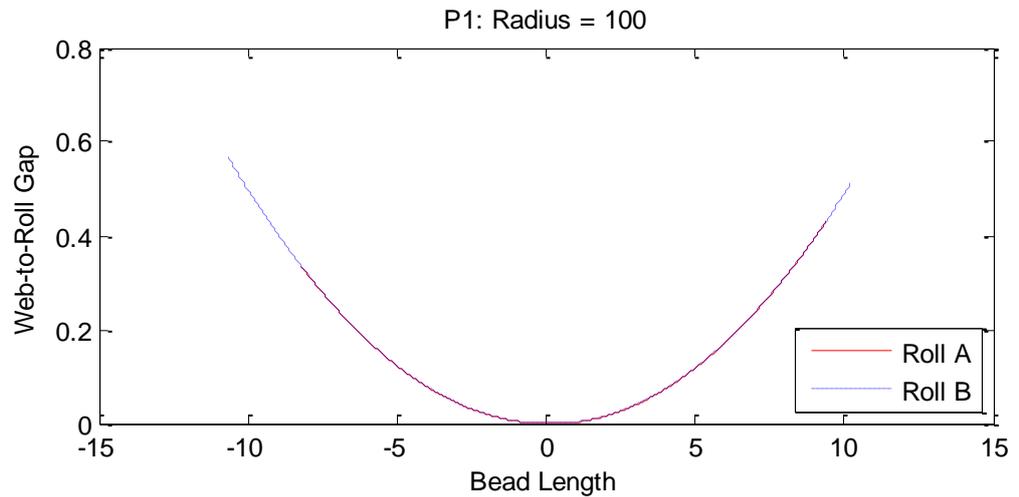
Figure 5.24: Web-to-roll gap profile at P1 from Figure 5.22.
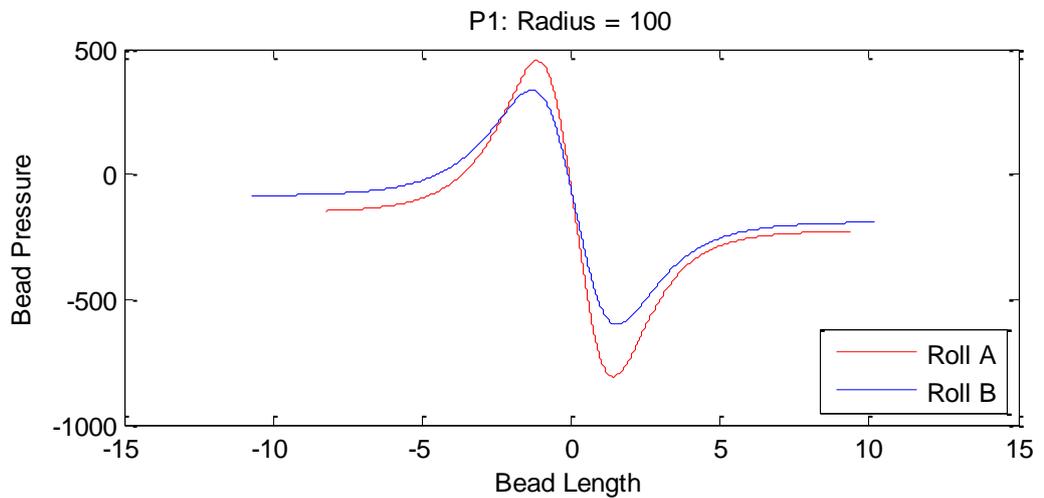
Figure 5.25: Bead pressure profile at P1 from Figure 5.22.
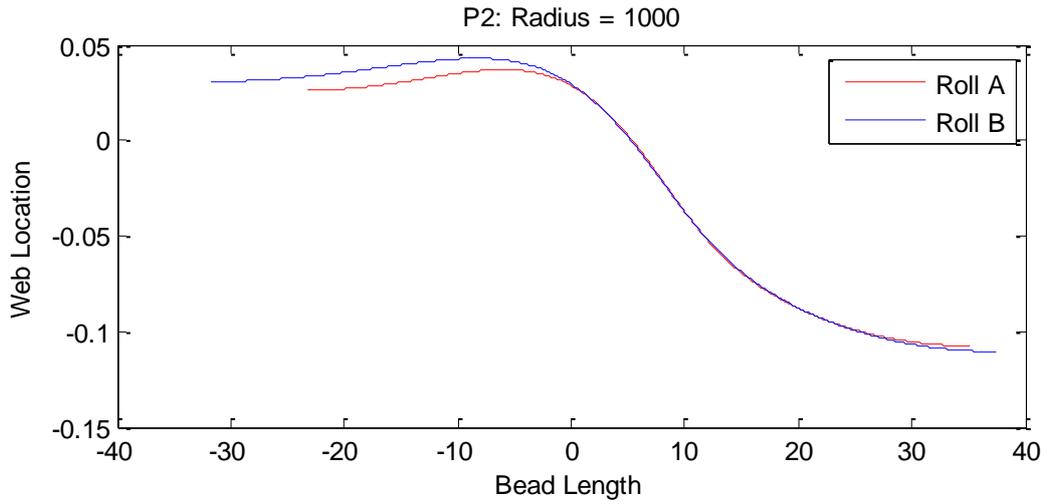
Figure 5.26: Web location profile from at P2 from Figure 5.22.
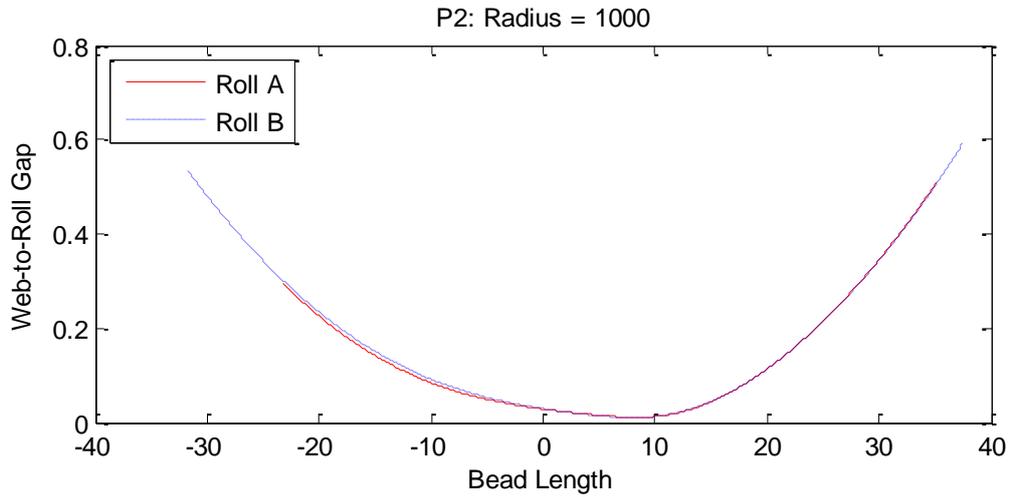
Figure 5.27: Web-to-roll gap profile at P2 from Figure 5.22.
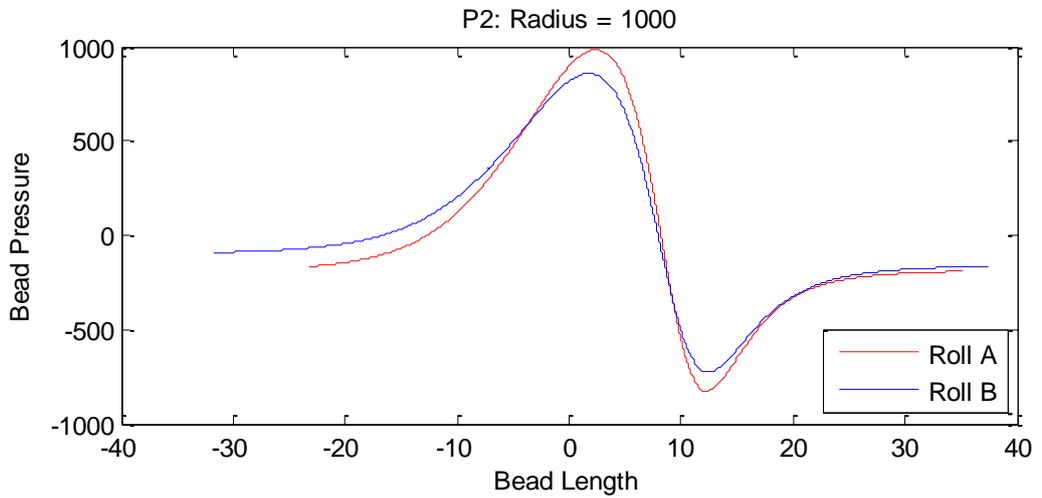
Figure 5.28: Bead pressure profile at P2 from Figure 5.22.

5.2.5 Coating Parameters: Summary

The coating parameters are entirely considered in the large scale. The parameters examined in this section were wrap angle, capillary number, web tension and roller radius. The speed ratio has been displayed in Chapter 4 and is by far the most sensitive of the coating parameters.

The web loading is determined by $T \sin \theta$ and is shown in these computational results to have no significant impact on the pickout ratio unless the web tension is very low, as was the case at points A1 and B1 in Figure 5.4. Experimental observation by Kapur (2003) also noted little change in pickout ratio with web loading. However, work by Gaskell et al (1998) on smooth roll coaters found that the coat weight did vary with web loading. This adds to the conclusion the gravure cells play an important role in the fluid transfer mechanism. This conclusion highlights the importance of web-to-roll contact. In the case of a smooth roll coater any contact would only allow fluid to accumulate downstream of the point of contact (Figure 5.29) while on a gravure roll the cells offer a means to carry fluid through the coating bead.
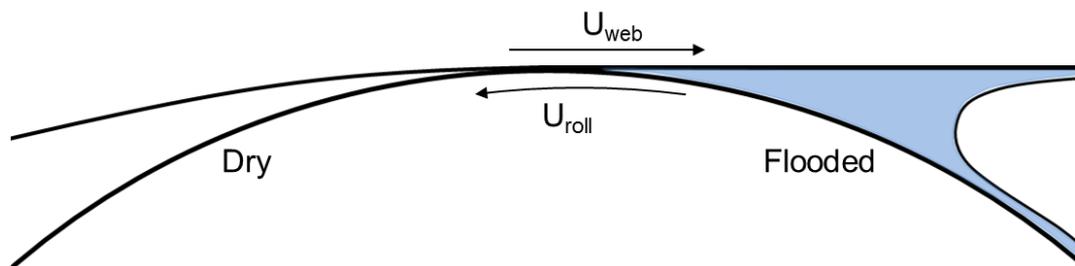
Figure 5.29: Smooth roll with contact between web and roll. Fluid is unable to transfer past point of contact.

The discussion in section 4.3 suggests that the small scale pressure gradient coefficient is the most important at small web-to-roll gaps. For example at a web-to-roll gap of 0.001 the value of the pressure gradient coefficient, a, is -4.22×10^{-6} for Roll A and -8.10×10^{-6} for Roll B. For a smooth roll coater which is well approximated by lubrication theory, the

same equivalent pressure gradient coefficient corresponds to $\frac{1}{12}g^3 = 8.3 \times 10^{-11}$. This is a difference of five orders of magnitude and implies that a smooth roll coater can achieve much higher fluid pressures than a gravure coater (the reader is referred to Equation 3.15 for clarity). Therefore, using cells as a metering device also reduces the fluid pressure such that web-to-roll contact will occur at lower web loading than that of smooth roll coating.

The cells in Roll B are larger than that of Roll A and an inspection of the pressure profiles in Figure 5.25 and Figure 5.28 shows that B has a smaller maximum fluid pressure. This suggests that Roll A is more analogous to a smooth roll than that of Roll B.

Roll radius variation shows the very interesting result of increasing fluid pressure with radius size. This can be either interpreted as the roll becoming physically larger or the characteristic length becoming smaller. This poses the interesting situation where the use of very small cells may reduce web-to-roll contact and thus reduce scratching.

5.3 Gravure Parameters (Small Scale)

In this section the small scale geometry was varied and the influence at the large scale was assessed. The geometry used was that for Roll B and all other parameters are from the baseline model. The first part varies the cell mesh angle and the second varies the aspect ratio of the cell.

5.3.1 Results: Gravure Cell Mesh Angle

The mesh angle (sometimes referred to as cell patterning) refers to the angle at which each row of cells is off-set from the next. This was approximated in the small scale by deforming the domain such that the total volume remains constant. The deformation is equivalent to rotating a square grid of cells as shown in Figure 5.30. The effect is to capture the flow field as it is influenced by the adjacent up and downstream cells. The small scale cells used here can be seen in Figure 5.31, where geometry C most clearly shows the adjacent cells. For a consistent comparison of mesh angle all the cell volumes were kept constant at 0.083.

The pickout ratio against speed ratio results are shown in Figure 5.32. A mesh angle of 0° yields the highest pickout ratio which decreases with increased mesh angle. At a speed ratio of 1 there is a 0.067 difference in pickout between 0° and 45° mesh angles which corresponds to a 17.8% change. At this speed ratio Figure 5.33 shows the bead pressure profiles for each mesh angle and in Figure 5.34 the matching contact pressures. The fluid pressure increases with increasing mesh angle.
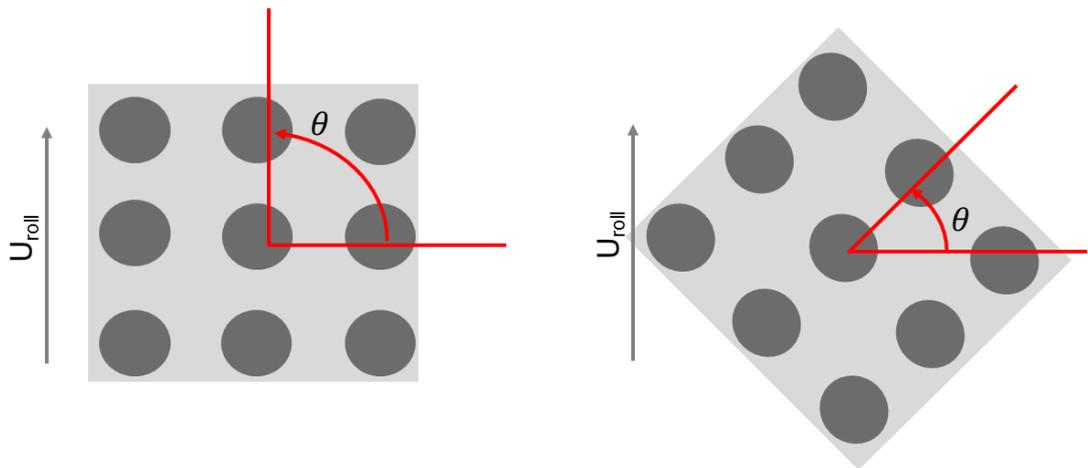
Figure 5.30 Cell grid showing rotation that is approximated by deforming a small scale geometry by 45 degrees.
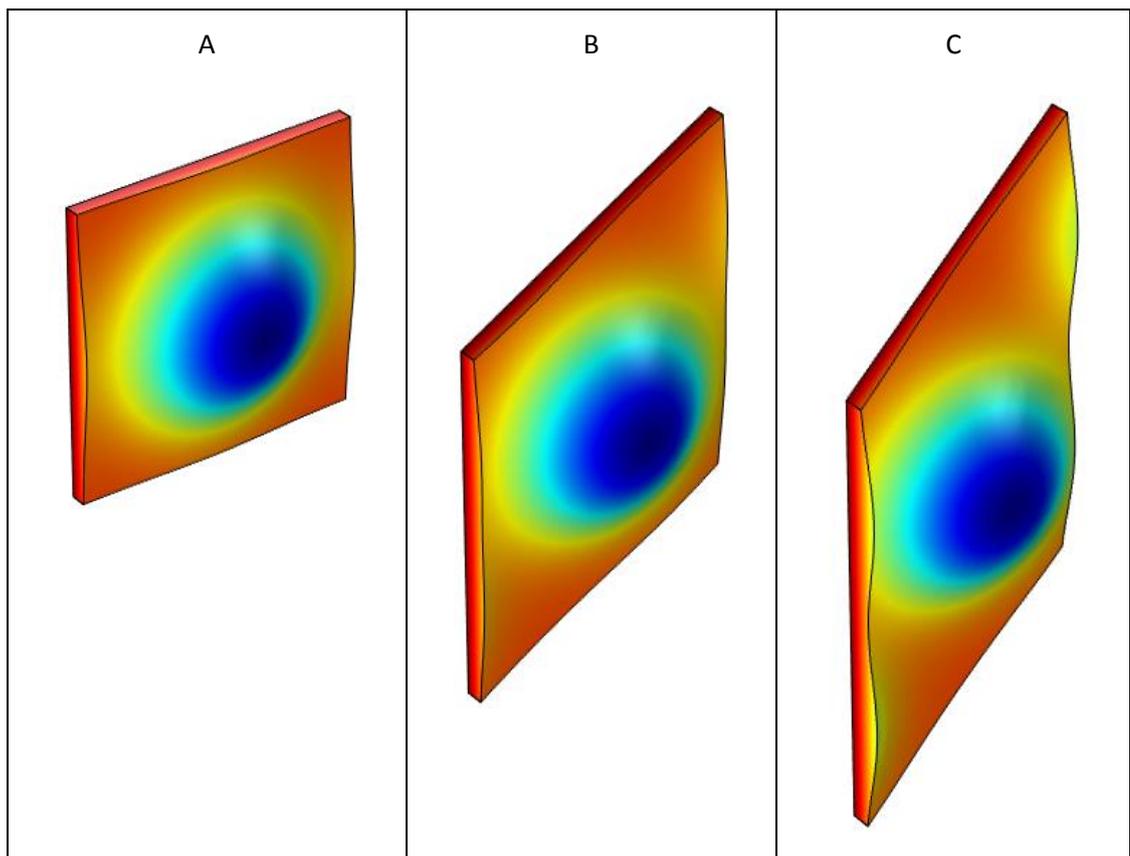
Figure 5.31: Small scale models at a web to roll gap of 0.05 where A has a mesh angle of 0°, B has a mesh angle of 30°and C has a mesh angle of 45°. In all the diagrams the direction of roll movement is left to right and the roll axial direction runs from the bottom to top.
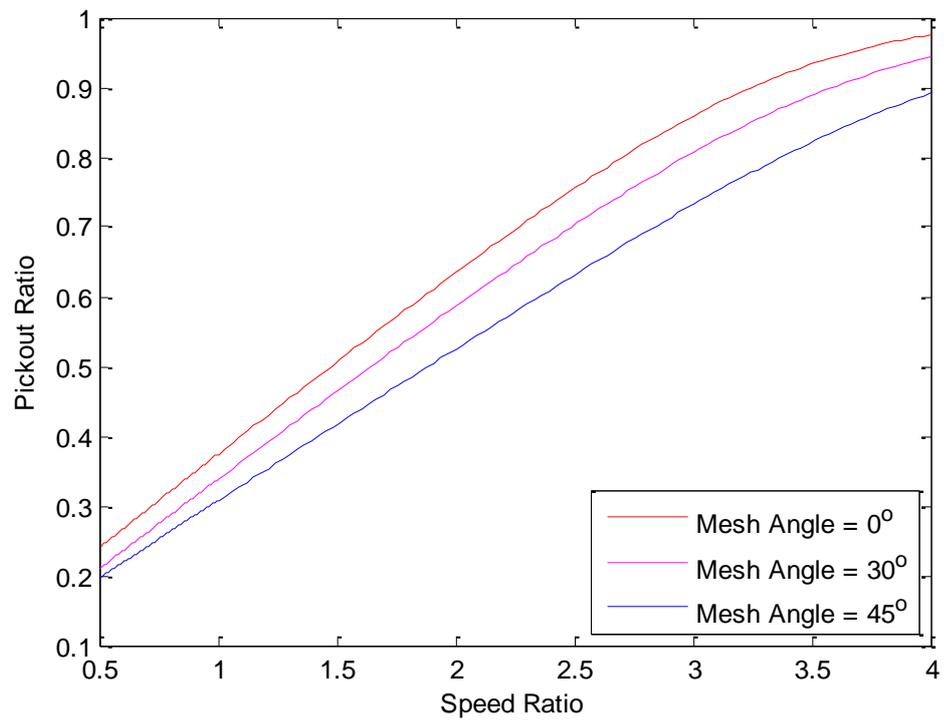
Figure 5.32: Pickout ratio against speed ratio for mesh angles of 0°, 30° and 45°.
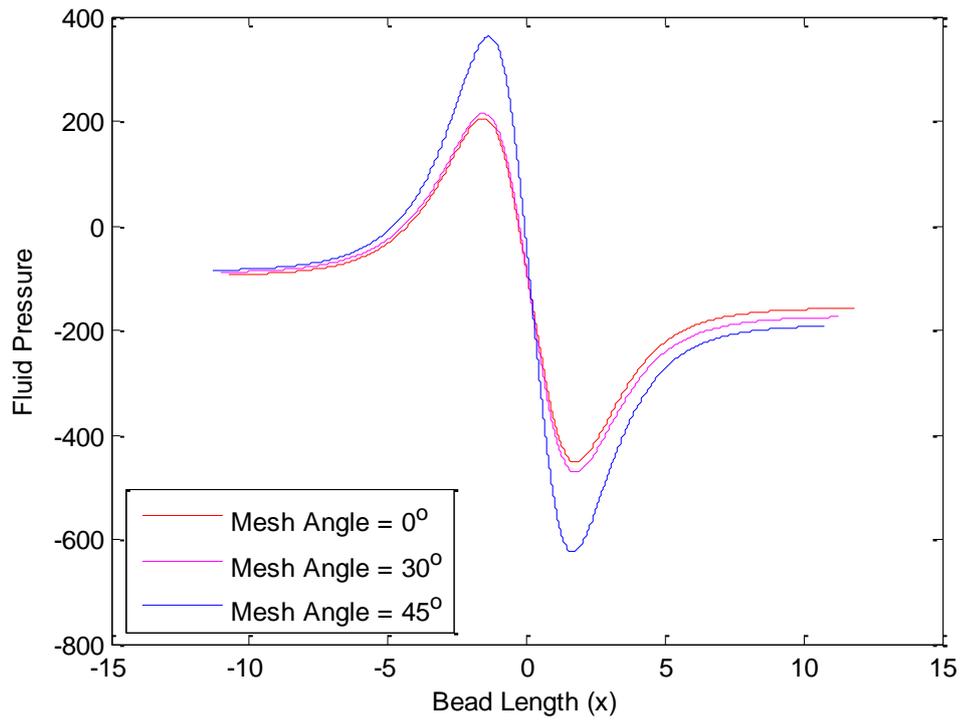
Figure 5.33: Fluid pressure against the coating bead length for mesh angles of 0°, 30° and 45°.
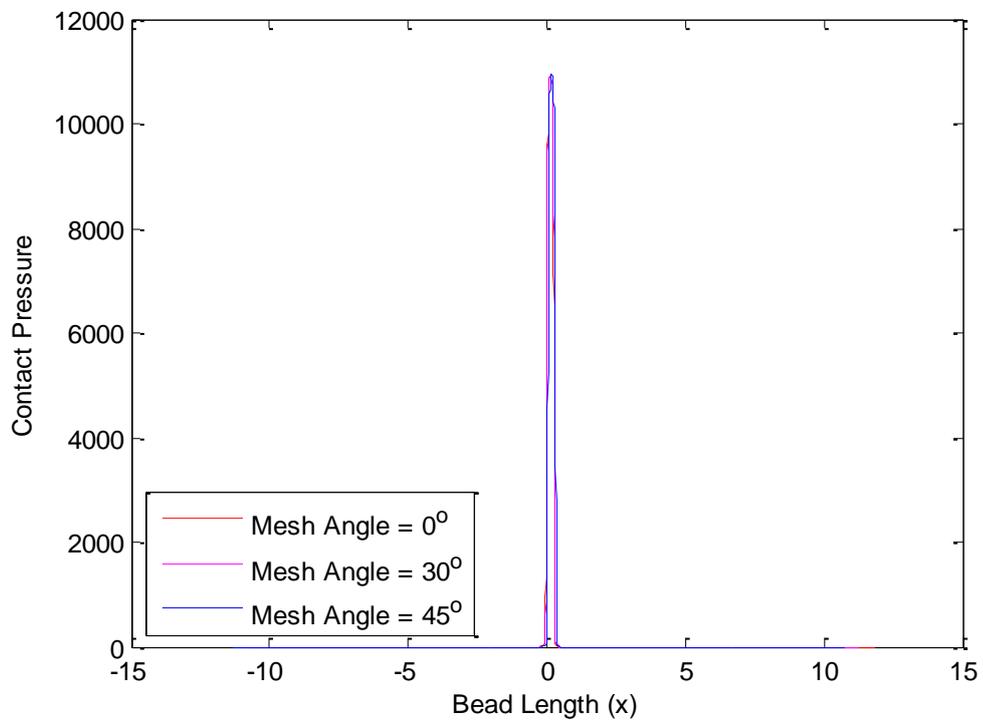
Figure 5.34: Web to roll contact pressure against bead length for reference with Figure 5.33.

5.3.2   Results: Gravure Cell Aspect Ratio

The ratio of a cell's opening area to its depth has been identified as an important parameter in determining the pickout ratio in Chapter 2 as well as in other published work [(Benkreira & Patel, 1992), (Schwartz, et al., 1998), (Kapur, 2003)]. The aspect ratio in Equation 5.3 relates the radius, r_0, to the depth, d, of the cell and these are defined in Figure 3.11 and are implemented in Equation 3.41. For this parametric study the aspect ratio is varied from 0.5 to 1 while the cell volume is held constant, these parameters for this are summarised in Table 5:2. The resulting geometries are shown in Figure 5.35 as contour plots where the aspect ratio is largest in geometry A and reduces to its minimum in geometry C. This means that geometry A has a cell which is relatively shallow and wide, while geometry C has a cell that is relatively narrow and deep. The colour axis in these figures indicates the depth at the contour.

$$AR = \frac{r_0}{d} \qquad\qquad \textbf{5.3}$$

	r_0	Depth (d)	AR
A	0.35	0.18	0.50
B	0.28	0.24	0.85
C	0.26	0.26	1.00

Table 5:2: Parameters used in parametrically varying aspect ratio.
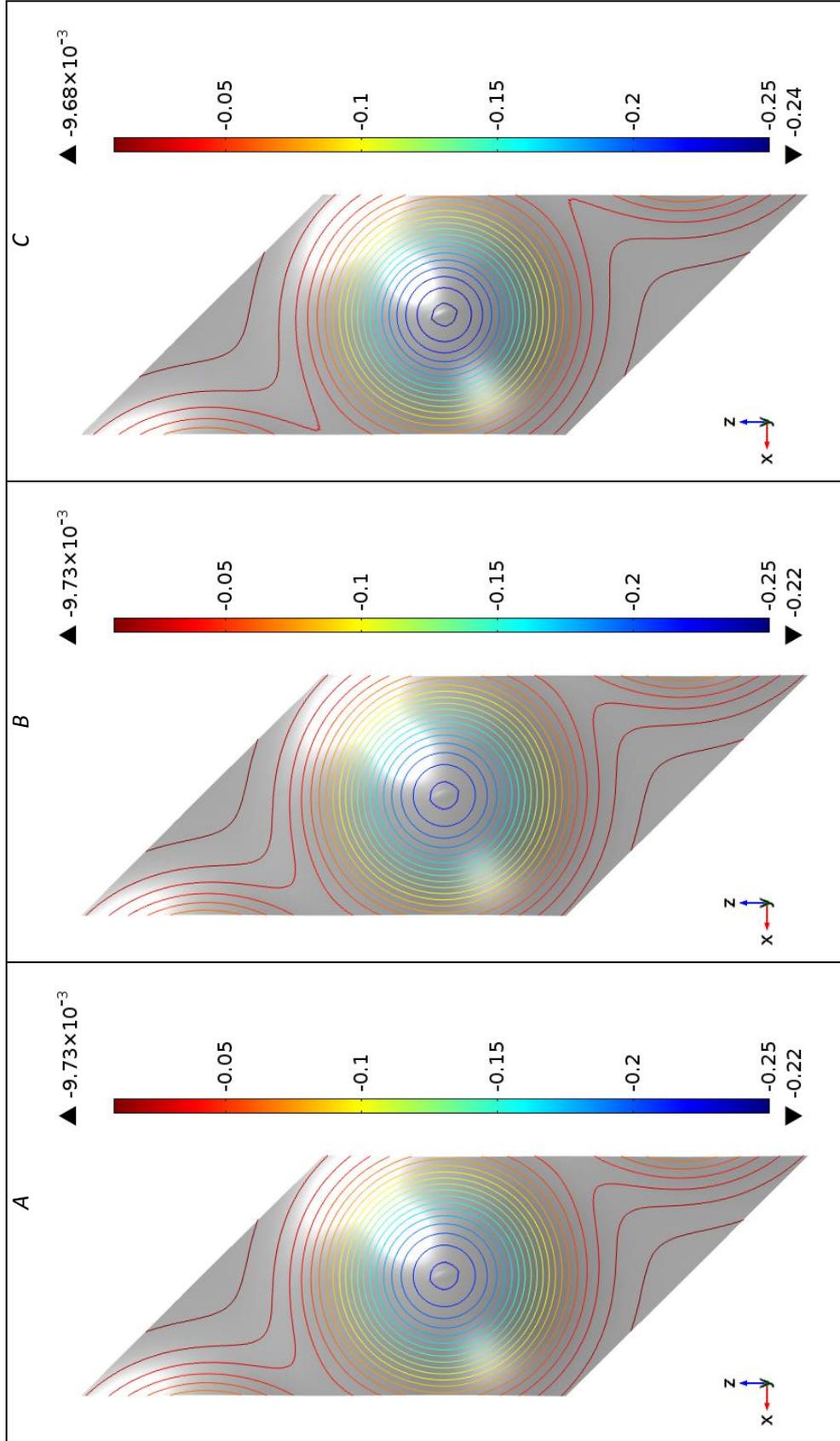
Figure 5.35: Surfaces used for the small scale model. *A* has a cell radius (r_0) of 0.35032 and a cell depth of $r_0 \times 0.5$. *B* has a cell radius (r_0) of 0.27815 and a cell depth of $r_0 \times 0.85$. *C* has a cell radius (r_0) of 0.25815 and a cell depth of $r_0 \times 1$.

Figure 5.36 shows the pickout ratio as a function of speed ratio for the three cell geometries. It is clear that aspect ratio plays an important role in the coating flow process. At a speed ratio of 1 the difference in pickout ratio between geometry A and C is 0.20 which is a 43% change in pickout ratio as the aspect ratio goes from 0.5 to 1. From the coating bead pressure profile in Figure 5.37 the highest pickout ratio also corresponds to the smallest magnitude pressure profile while the lower pickouts correspond to the higher pressures. The contact pressure does not vary significantly from one aspect ratio to the next but it is clear that the cell geometry does not change the point in the coating bead at which contact occurs (Figure 5.38).
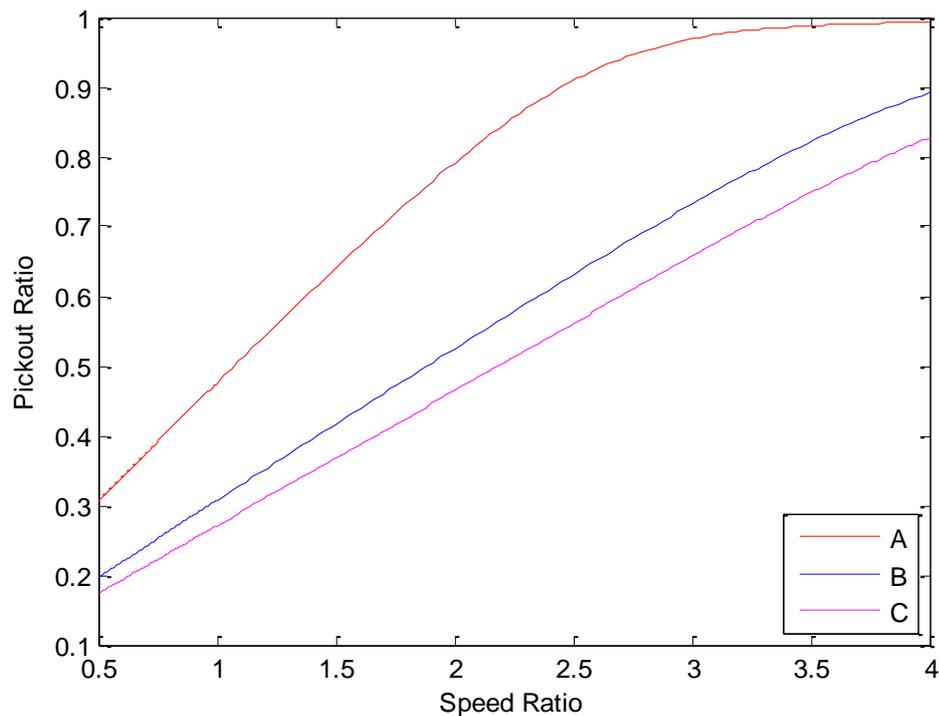
Figure 5.36: Pickout ratio against speed ratio for the three cell geometries. A has a cell radius (r_0) of 0.35032 and a cell depth of $r_0 \times 0.5$. B has a cell radius (r_0) of 0.27815 and a cell depth of $r_0 \times 0.85$. C has a cell radius (r_0) of 0.25815 and a cell depth of $r_0 \times 1$.
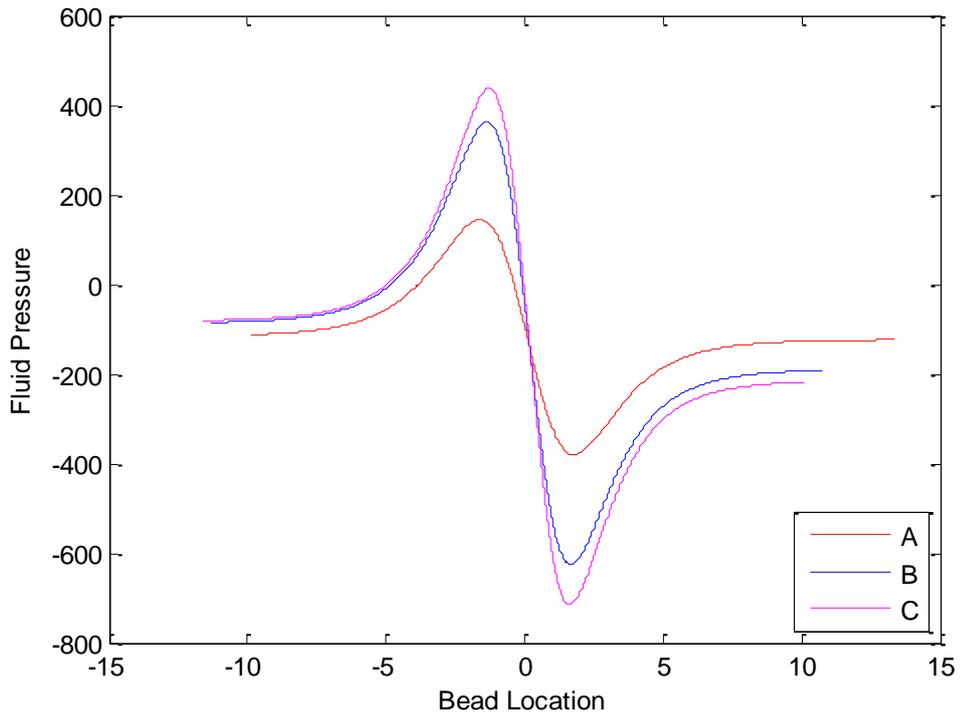
Figure 5.37: Fluid pressure against coating bead location. A has a cell radius (r_0) of 0.35032 and a cell depth of $r_0 \times 0.5$. B has a cell radius (r_0) of 0.27815 and a cell depth of $r_0 \times 0.85$. C has a cell radius (r_0) of 0.25815 and a cell depth of $r_0 \times 1$.
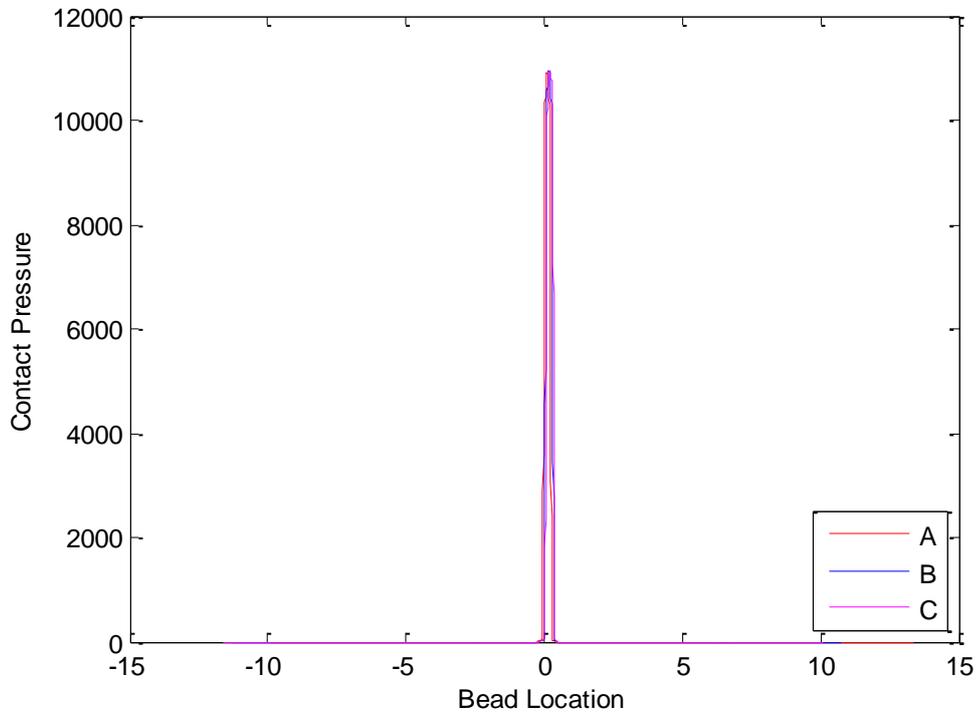
Figure 5.38: Contact pressure against bead location. A has a cell radius (r_0) of 0.35032 and a cell depth of $r_0 \times 0.5$. B has a cell radius (r_0) of 0.27815 and a cell depth of $r_0 \times 0.85$. C has a cell radius (r_0) of 0.25815 and a cell depth of $r_0 \times 1$.

5.3.3   Gravure Parameters: Summary

Two key parameters have been varied, the mesh angle and the aspect ratio. Over a change in mesh angle of 45 degrees there was a 17.8% change in pickout ratio, while a change in aspect ratio from 0.5 to 1 showed a 43% change in pickout ratio.

The pickout ratio is sensitive to the small scale geometry, much more so than the coating parameters described in section 5.2. Accurately capturing the flow physics in the small scale is vital to the accuracy of the two scale model.

5.4   Summary of Parametric Results

From the results presented in this chapter it can be seen that the coating operating parameters (web tension and wrap angle) have little effect on the coating process under normal conditions. Similarly, capillary number has only minimal effects on the pickout ratio. Only as these parameters approach zero do they begin to have significant effect on the pickout ratio. However, the surface topography has a much larger effect on the pickout ratio. In particular the cell aspect ratio which showed dramatic changes in pickout ratio.

In comparison to both the web tension and the wrap angle, pickout ratio is much more sensitive to changes in the speed ratio as shown in Chapter 4. It is also interesting that the pickout to speed ratio gradient changed when the web tension was reduced from $t = 1 \times 10^7$ to $t = 1 \times 10^4$ (see Figure 5.15 versus Figure 5.20). At these low web tensions the fluid pressure is large enough to support the web and the contact pressure drops to zero. This result is of interest when considering how to reduce web scratching.

Roll radius, which at small radii, had no significant effect on pickout ratio but did have an effect on the contact pressure. As the roll radius increased the minimum web-to-roll gap was shown to increase. The result implies that a roll with very small cells may exhibit a reduced amount of web-to-roll contact. This result is one which would benefit from experimental analysis.

Gravure patterning had a 17.8% effect on the pickout ratio over the range of 0 to 45 degrees. This is a greater sensitivity than was found from the variable coating parameters. The pickout was shown to be sensitive to the aspect ratio of the gravure cells. As the aspect ratio decreased (i.e. the radius increased and cell depth was reduced) the pickout ratio became larger for a constant volume. This is tending towards the theoretical lubrication result for a smooth roll which will transfer all the coating fluid to the web.

The implemented large scale boundary conditions neglect the influence of the cells, but it was shown in section 4.3 that the pickout ratio under normal

operating conditions is not sensitive to them. This is similar to many of the coating parameters and it should be noted that speed ratio, capillary number and wrap angle occupy a key role in the large scale boundary conditions.

5.5   Discussion

Earlier authors identified in Chapter 1 investigating the gravure coating process have experimentally established a typical operating behaviour for gravure roll coating including pickout ratio, stable operating parameters, key fluid properties and some gravure surface properties, all of which affect the coat weight. The experimental results presented in Chapter 2 fall into line with those already published [(Benkreira & Patel, 1992), (Kapur, 2003)]. However, unlike other published data these results can be linked to a specific gravure roll for a like-for-like comparison with the computational model. While similar experimental data is published elsewhere the real value of the experiments conducted here comes from the ability to make these comparisons.

The two-scale model has extended the work published in Hewson, et al (2011) where the representation of the small scale has been extended to three-dimensions as well as the inclusion of a contact pressure term in the large scale. The present work also moves the web tension into a realistic parameter space. Previously, tension had been underestimated and hence prior to this work no contact model was required.

5.5.1   Model Validation

The results predicted by the two-scale model have been compared with those determined by experiment to find a correlation between the pickout ratios for two separate rolls. The model was able to predict the linear relationship between the pickout ratio and the speed ratio.

A look at the fluid structure of the coating bead revealed similarities between the computational predictions and the observations in earlier work [(Gaskell, et al., 1998), (Hewson, et al., 2006)]. These observations are important because they are influenced by a flexible web and add more information from that of earlier fixed gap simulations. The presence of a flexible web introduces the relationship between fluid pressure and web tension and therefore when the force of web tension is much higher than that of the fluid

pressure it presents the possibility of contact. The two scale model suggests that contact between the web and roll is important in the fluid transfer process for a given parameter space (namely realistic web tensions). This contact is then evidenced by the observation of web scratches during the experimental coating phase (Chapter 2).

For both rolls the small scale representation was created such that the aspect ratio, the cell volume and the mesh angle were representative of the roll used in the experiment. This required specific images taken using a white light interferometer for each roll. A comparison of these images with the small scale implementation has shown that the main features are represented (i.e. cell volume, aspect ratio, mesh angle) but much of the detail is lost in going from the image to the computational model (small scale), specifically the surface is much smoother than it should be.

5.5.2   Scratching

Scratches on the web appear as a result of the gravure coating process. These are caused by contact between the web and the harder, rough surface of the gravure. Evidence of these scratches was experimentally observed in Chapter 2 where the scratches form a long and relatively shallow trough of plastically deformed PET web.

The inclusion of web-to-roll contact in the large scale and neglecting the same roughness in the small scale is a troublesome contradiction. The presence of web scratching is most readily explained by local peaks on the gravure surface. However, the spacing of these peaks is unknown and varies from one roll to the next as well as varying around the circumference of the roll. This is inconsistent with a multi-scale modelling method as it violates the key assumption that the small-scale is periodic. By applying an ad hoc contact pressure term in the large scale this violation is avoided, but it does imply that there is continuous contact between the web and the roll and that this contact is present at a constant load which means the predicted contact cannot be related to individual scratches.

The contact pressure is seen to be an important component in the gravure fluid transfer process. Over much of the parameter space identified in Chapter 5 the contact pressure is very high relative to the maximum fluid pressure. What is most interesting to the coating engineer is when the contact pressure drops to zero as this suggests a condition that will avoid web-to-roll contact and therefore prevent scratching.

One such situation occurs at very low web tensions but the industrial relevance of this is limited because the web tension is set by other production parameters rather than the coating operation (such as web stretching, etc.). This sensitivity to roll radius highlights a problem between the laboratory roll size and the industry roll size. Laboratory sized rolls used here are 10 cm in diameter while those at industry are often twice as large, though this does vary from one coating line to the next.

The second such condition occurs when the cells are very small. The contact pressure was shown to respond to absolute cell size in Chapter 5. It has also been shown (both in Chapter 5 and in the literature) that the pickout ratio is sensitive to the cell shape. The combination of very small cells with tailored aspect ratios to achieve a pickout ratio that gives a desired film thickness is a promising direction of research into the production of scratch free coatings.

5.5.3 Relevance to Industry

The two-scale model has applications in the design process of these new types of rolls. Physically creating and experimentally testing rolls is an expensive process, while computationally doing this is cheaper and faster.

The cells size has also been shown to correlate to the pressure in the coating bead. Smaller cells are more analogous to a smooth roll and correlate with a higher pressure.

Computational investigations of the surface topography captured in the small scale simulations showed the formation of eddys in the cells (Figure 3.24 and Figure 3.25). In these regions not all of the fluid is being replaced as the cell passes through the coating bead. This alludes to a common industrial

problem of solid particulate build-up in the cells (these particulates are often part of the coating fluid). The build-up changes the cell volume over time and results in a reduction in coating weight requiring the roll to be cleaned. Any particles trapped in the eddy have no obvious path exiting and will therefore have an increased likelihood of becoming attached to the roll surface.

Chapter 6   Conclusions and Future Work

This thesis presented both experimental and computational work. The conclusions drawn from this work are:

- The two scale model correlates with experimental results and predicts a nearly linear relationship between pickout ratio and speed ratio. Successfully predicting the gradient of this relationship remains elusive. At industrially relevant speed ratios (i.e. within 10% of S=1) the pickout ratio predicted by computation is consistent with the results from experiment. The formulation of the model allows for a variety of cell geometries and roll coating conditions to be accounted for.

- Web-to-roll scratching has been observed to occur during the coating process. The fluid pressure at normal operating conditions is computationally predicted to be insufficient to support the web and therefore a contact pressure component between the web and gravure takes the additional load. The inclusion of contact in the computational model is supported by experimentally observed scratching on the web. Contact is of particular interest for discrete cell gravure roll coating because contact does not stop the fluid transfer process. Coating fluid can be transported through the coating bead during contact because the presence of the cells. The inclusion of web to roll contact is entirely novel and provides a valuable insight into the web scratching phenomena.

- The magnitude of the contact pressure correlates with the web tension and the cell size/roll radius. At sufficiently low web tensions the contact pressure is reduced to zero suggesting there is no web-to-

roll contact. At sufficiently small cell size (or equally large roll radius) the contact pressure drops to zero suggesting no contact. In the reduced tension case there are increases in the pickout ratio. In the reduced cell size/increased roll radius case there is a nominal effect on pickout but also implications in film thickness due to the change in characteristic length.

- Wrap angle has only a nominal effect on the pickout ratio. In accordance with what has been shown elsewhere in the literature the wrap angle increases the web loading on the gravure. This has been extended here to show that this additional loading is not always supported by the fluid but instead increases the contact pressure between the web and roll.

- At web tensions below the point of web-to-roll contact the pickout ratio is sensitive to changes in web tension. At web tensions above where web to roll contact occurs the pickout ratio becomes unaffected by further increasing the web tension. This is due to the roll supporting the additional load.

- The small scale has been extended from a two dimensional representation of topography in earlier work (Hewson, et al., 2011) to a three dimensional representation of the topography.

- The surface topography is important to the fluid transfer process. This has also been observed experimentally in the literature. Correctly implementing features such as the cell aspect ratio and volume are important when representing the small scale. Cells with larger aspect ratios will have a larger pickout ratio.

- Capillary number is computationally predicted to have a nominal effect on the pickout ratio. This is in contrast to what other authors have experimentally observed.

- The pickout ratio is affected by the layout of the cells which as been observed elsewhere in the literature (Schwartz, 2002).

6.1   Future Work

The predictive two-scale model discussed in this thesis provides a computational representation in a realistic parameters space for discrete cell gravure roll coating and qualitatively validates it against experimental results. It does not quantitatively predict the pickout ratio as it changes with speed ratio. This an important detail to the coating engineer as speed ratio is a common method of scaling the production process.

The parametric study in Chapter 5 showed that the pickout ratio is strongly influenced by the small scale results. The idealised small scale models presented here neglect surface non-uniformities. Inclusion of these non-uniformities is not a trivial task as these features are much smaller than the cell itself. They open the exciting possibility of creating third smaller scale of the model.

A small scale representation of a real roll would be an improvement to the model. Instead of idealising the surface topography it would be beneficial to create it directly from some surface data, such as an image obtained from white light interferometry. An example of this is shown in Figure 6.1. This would more closely capture the opening area and the depth of a cell allowing for a more realistic representation of not only the cell but the land as well. It presents challenges in maintaining periodicity as one end of the domain will no longer be of the same opening area as the other on a cell by cell basis.
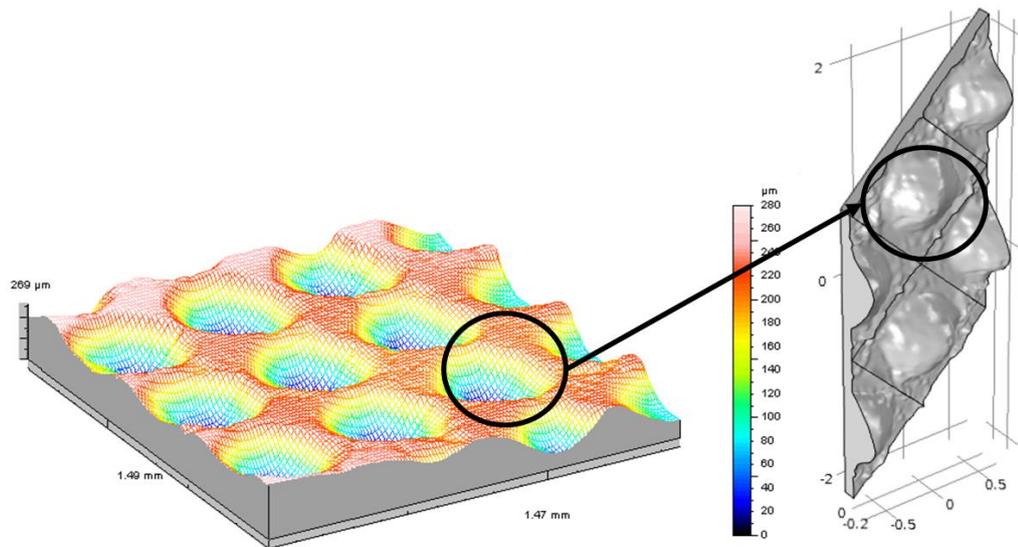
Figure 6.1: Example of a numerical geometry created from a white light interferometer image of a gravure surface. One cell is modelled and then mirrored to maintain periodicity.

The problems caused by web-to-roll contact currently prevent gravure coating from being used for coating products that require a scratch free surface. Such products are becoming more common with the miniaturization of electronics towards the micro and nano scales, for example the mass production of micro-scale transistors (Tobjörk D. et al (2008), Maenosono et al (2003)). Results in Chapter 5 point to gravure rolls with very small cells as a promising direction for further work on the question of web-to-roll scratching.

The large scale boundary conditions could be further refined so that they more correctly represent coating bead menisci. They do not have significant effect on the pickout ratio at normal industrial operating conditions but it was shown that as the web-to-roll gap approaches zero they become significant. At extremes of speed ratio (i.e. below 0.5 and above 2 with some variation from one roll to the next) the web-to-roll gap does approach zero as the upstream or downstream meniscus is drawn into the narrow central location of the coating bead.

During the industrial coating operation the rolls experience a build-up of solid particulates that change the shape of the cell and other surface features. Each roll is affected slightly differently by this build up but in all cases there is a reduced cell volume and a corresponding drop in coated film thickness over time. These changes limit the time a given gravure roll can operate. Measurements of the coat weight during the industrial coating process decline over the length of time used and upon reaching a predetermined minimum the coating process must be stopped and the roll cleaned. Obviously, this is a source of inefficiency. Gravure roll coating is particularly susceptible to this due to its topography. The re-circulation that forms in the cells means that once material becomes trapped in a cell there is not a clear path for escape. It presents a couple of interesting areas for research. Firstly, an understanding of the build-up process is required. Secondly, a means of preventing or delaying the onset of the build-up is needed. The former requires a means of experimental study. The latter can be well addressed via a numerical investigation looking specifically for conditions at

which the streamlines sweep through the base of the cell. Both situations require an understanding of the flow physics at the cell scale.

Bibliography

Benjamin, D. F., Anderson, T. J. & Scriven, L. E., 1995. Multiple roll sytems: Steady-state operation. *Fluid Mechanics and Transport Phenomena,* 41(5), pp. 1045-1060.

Benkreira, H. & Cohu, O., 1998. Direct forward gravure coating on unsupported web. *Chemical Engineering Science,* 53(6), pp. 1223-1231.

Benkreira, H. & Patel, R., 1992. Direct Gravure Roll Coating. *Chemical Engineering Science, Vol. 48, No. 12,* 48(12), pp. 2329-2335.

Benkreira, H., Patel, R., Edwards, M. F. & Wilkinson, W., 1994. Classification and analyses of coating flows. *Journal of Non-Newtonian Fluid Mechanics,* Volume 54, pp. 437-447.

Booth, G., 1970. *Coating equipment and processes,* New York: Lockwood Publishing Company.

Bretherton, F., 1961. The motion of long bubbles in tubes. *Journal of Fluid Mechanics, 10,* 10(2), pp. 166-188.

Briggs, W. L. & McCormick, S. F., 2000. *A multigrid tutorial.* s.l.:Siam.

Cameron, A., 1981. *Basic Lubrication Theory.* Chichester: Ellis Horwood Limited.

Carvalho, M. S. & Scriven, L. E., 1997. Deformable roll coating flows: steady state and linear perturbation analysis. *Journal of Fluid Mechanics,* Volume 339, pp. 143-172.

Coyle, D. J., Macosko, C. W. & Scriven, L. E., 1990. A simple model of reverse roll coating. *Ind. Eng. Chem. Res.,* Volume 29, pp. 1416-1419.

Coyle, D. J., Macosko, C. W. & Scriven, L. E., 1990. The fluid dynamics of reverse roll coating. *AIChE,* Volume 339, pp. 161-174.

Coyne, J. & Elrod, H., 1970. Conditions for the rupture of a lubricating film-Part 2: New boundary conditions for Reynolds equation. *Journal of Lubrication Technology,* 93(1), pp. 156-167.

Coyne, J. & Elrod, H. G., 1967. Conditions for the rupture of a lubricating film. Part 1: Theoretical Model. *J. Tribol,* 92(3), pp. 451-456.

Dowson, D., 1979. History of Tribology. In: New York: Longman Inc., pp. 499-500.

E, W., Bjorn, E. & Zhongyi, H., 2003. Heterogeneous multiscale method: A general methodology for multiscale modeling. *Physical Review,* 67(9), pp. 1-4.

E, W. et al., 2007. Heterogeneous multiscale methods: a review. *Commun. Comput. Phys,* 2(3), pp. 367-450.

Gaskell, P. H., Innes, G. E. & Savage, M. D., 1998. An experimental investigation of meniscus roll coating. *Fluid Mech.,* Volume 335, pp. vol. 255, pp. 17-44.

Gaskell, P. H. & Kapur, N., 2001. Bead-break instability. *Physics of Fluids,* Volume 13, pp. 1243-1253.

Gaskell, P. H., Savage, M. D., Summers, J. L. & Thompson, H. M., 1995. Modelling and analysis of meniscus roll coating. *Journal of Fluid Mechanics,* Volume 298, pp. 113-137.

Gaskell, P., Rees, S., Savage, M. & Storey, S., 1998. A Mathematical Model of Roll-to-Web Kiss Coating. *IChemE,* 76(1), pp. 29-37.

Gostling, M. J., Savage, M. D., Young, A. E. & Gaskell, P. H., 2003. A model for deformable roll coating with negative gaps and incompressible compliant layers. *Journal of Fluid Mechanics,* Volume 489, pp. 155-184.

Greener, J. & Middleman, S., 1979. Theoretical and experimental studies of the fluid dynamics of a two-roll coater. *Ind. Eng. chem. Fund.,* Volume 18, pp. 35-41.

Hanumanthu, R., 1999. Variation of gravure coating thickness during early stages of doctor blade wear. *AIChE,* 45(12), pp. 2487-2494.

Hariharan, P., 2006. *Basics of Interferometry (Second Edition).* San Diego: Elsevier Science Publishing Co Inc.

Hewson, R., Kapur, N. & Gaskell, P., 2011. A two-scale model for discrete cell gravure roll coating. *Chemical Engineering Science,* 66(16), pp. 3666-3674.

Hewson, R., Kapur, N. & Gaskell, P. H., 2009. Modelling the discrete-cell gravure roll coating process. *The European Physical Journal,* Volume 166, pp. 99-102.

Hewson, R. W., 2009. Free surface model derived from the analytical solution of stokes flow in a wedge. *Journal of Fluids Engineering,* 131(4).

Hewson, R. W., Kapur, N. & Gaskell, P., 2006. A theoretical and experimental investigation of tri-helical gravure roll coating. *Chemical Engineering Science,* 61(16), pp. 5487-5499.

Hoda, N. & Kumar, S., 2008. Boundary integral simulations of liquid emptying from a model gravure cell. *Physics of Fluids 20,092106,* Volume 20, pp. 1-12.

Holmes, H. N., 1922. *Laboratory Manual of Colloid Chemistry.* New York: John Wiley & Sons, Inc.

Kapur, N., 1999. *Flow phenomena in fixed-gap and gravure roll coating sytems, PHD Thesis.* s.l.:University of Leeds.

Kapur, N., 2003. A parametric study of direct gravure coating. *Chemical Engineering Science 58,* 58(13), pp. 2875-2882.

Kapur, N., Gaskell, P. & Bates, A., 2001. A parametric study of offset gravure roll coating. *Trans IChemE, Vol. 79, Part A,* 79(1), pp. 41-50.

Kistler, S. F. & Schweizer, P. M., 1997. *Liquid film coating.* London: Chapman & Hall.

Krechetnikov, R. & Homsy, G. M., 2005. Experimental study of substrate roughness and surfactant effects on the Landau-Levich law. *Physics of Fluids,* 17(102108).

Landau, L. & Levich, B., 1942. Dragging of a liquid by a moving plate. *ACTA Physicochimica U.R.S.S.,* pp. 42-54.

Maenosono, S., Okubo, T. & Yamaguchi, Y., 2003. Overview of nanoparticle array formation by wet coating. *Journal of Nanoparticle Research,* Volume 5, pp. 5-15.

Murphy, D. B., 2001. *Fundamentals of light microscopy and electronic imaging.* s.l.:A John Wiley & Sons, Inc..

Patel, R. & Benkreira, H., 1990. Gravure Roll Coating of Newtonian Liquids. *Chemical Engineering Science,* 46(3), pp. 751-756.

Patel, R. & Benkreira, H., 1991. Gravure Roll Coating of Newtonian Liquids. *Chemical Engineering Science,* 46(3), pp. 751-756.

Powell, C., Savage, M. & Gaskell, P., 2000. Modelling the meniscus evacuation problem in direct gravure coating. *IChemE,* Volume 78, pp. 61-67.

Pranckh, F. R. & Coyle, D. J., 1997. Elastohydrodynamic coating systems. In: *Liquid Film Coating.* London: Chapman & Hall, pp. 599-635.

Pulkrabek, W. W. & Munter, J. D., 1982. Knurl roll design for stable rotogravure coating. *Chemical Engineering Science,* 38(8), pp. 1309-1314.

Rees, S. R., 1995. *An experimental and theoretical investigation of gravure roll coating.* s.l.:University of Leeds.

Reynolds, O., 1886. On the theory of lubrication and its application to Mr Beauchamp Tower's experiments, including an experimental determination of the viscosity of oil. *Philosophical Transactions of the Royal Society,* Volume 177, pp. 157-234.

Schwartz, L., Moussalli, P., Campbell, P. & Eley, R., 1998. Numerical Modelling of Liquid Withdrawal from Gravure Cavities in Coating Operations. *IChemE,* 76(Part A), p. Vol 76.

Schwartz, L. W., 2002. Numerical modelling of liquid withdrawal from gravure cavities in coating operations; the effect of cell pattern. *Journal of Engineering Mathematics,* Volume 42, pp. 243-253.

Storey, S. P., 1996. *A theoretical investigation of the flow between a web and roll, with application to gravure coating. PhD Thesis.* s.l.:University of Leeds.

Summers, J. L., Thompson, H. M. & Gaskell, P. H., 2004. Flow structure and transfer jets in a contra-rotating rigid-roll coating system. *Theoretical and Computational Fluid Dynamics,* Volume 17, pp. 189-212.

Szeri, A. Z., 1998. *Fluid Film Lubrications Theory & Design.* Cambridge: Cambridge University Press.

Tobjörk, D. et al., 2008. All-printed low-voltage organic transistors. *Organic Electronics,* 9(6), pp. 931-935.

Yin, X. & Kumar, S., 2005. Lubrication flow between a cavity and a flexible wall. *Physics of Fluids,* 17(6).

Yin, X. & Kumar, S., 2006. Flow visualization of the liquid emptying process in scaled-up gravure grooves and cells. *Chemical Engineering Science,* 61(4), pp. 1146-1156.

Yin, X. & Kumar, S., 2006. Two-dimensional simulations of flow near a cavity and a flexible solid boundary. *Physics of Fluids,* 18(6).